Weifeng Shang

A survey on pattern formation
in DC gas discharge systems

2007

Experimentelle Physik

A survey on pattern formation in DC gas discharge systems

Inaugural-Dissertation
zur Erlangung des Doktorgrades
der Naturwissenschaften im Fachbereich der Physik
der Mathematisch-Naturwissenschaftlichen Fakultät
der Westfälischen Wilhelms-Universität Münster

vorgelegt von
Weifeng Shang
aus Henan, Volksrepublik China
– 2007 –

Abstract

The recent studies on pattern formation in systems driven far from thermodynamic equilibrium shed new light on our understanding about self-organization and thus provide a new perspective on a fundamental problem in philosophy and science, i.e. the origin of order. Furthermore, a better understanding of self-organization may lead to new classes of methods for fabricating ordered structures, which are important in many applications. A brief survey of the experimental study on pattern formation in various types of systems, i.e. fluid systems, chemical reaction diffusion systems, granular media, nonlinear optical systems and dielectric barrier gas discharge systems, is given in Chapter 1. As the present work focuses on pattern formation in gas discharge systems with a semiconductor cathode driven with a direct-current source, the basics of gas discharge physics are described in Chapter 2. An extensive review on the experimental results dispersed in the literature, which have been obtained on this kind of gas discharge systems, is given in Chapter 3. After describing the experimental setup in Chapter 4, the investigation on the gas discharges with conductive electrodes is presented in Chapter 5. The results of a systematic study on pattern formation in gas discharge systems with Si:Pt cathodes are given in Chapter 6. The phase diagram of various generic patterns, i.e. hexagonal spots and stripes, is quantitatively determined on the plane of the conductivity of the semiconductor σ and the source voltage U_0. The issues of a quantitative reproducibility of such phase diagrams are addressed. The influence of the gas pressure p and the inter-electrode distance d on the phase diagram is investigated. Whereas previous experimental work on this system used exclusively N_2 as the working gas, the present study extended the experimental investigation to other gases, i.e. He, Ne and Ar. In the case of Ar, hexagonally woven stripes (or negative hexagons), though already familiar in dielectric barrier discharge systems, have been observed in the present direct-current gas discharge system. The basic phenomenology and the typical phase diagram on σ-U_0 plane are described and their dependence on p and d are investigated. When He or Ne are used as the working gas, the uniform state of the discharge is stable in the investigated parameter ranges and no pattern formation is observed. Phenomenological investigations have also been made in the case of other cathode materials, i.e. Si doped with deep impurity Zn and GaAs compensated with Cr, and the results are presented in Chapter 7. Finally the major results are summarized in Chapter 8.

Zusammenfassung

Aktuelle Untersuchungen über Strukturbildung in Systemen, die weit weg vom thermodynamischen Gleichgewicht getrieben werden, werfen ein neues Licht auf unser Verständnis von Selbstorganisation und liefern gleichzeitig eine neue Sicht auf ein grundlegendes Problem in der Philosophie und in der Wissenschaft, nämlich den Ursprung der Ordnung. Darüber hinaus kann ein besseres Verständnis der Selbstorganisation zu neuen Methoden für die Schaffung geordneter Strukturen führen, die in vielen Anwendungen wichtig sind. Eine kurze Übersicht der experimentellen Untersuchungen der Musterbildung in verschiedenen Systemen, d.h. in Fluidsystemen, chemischen Reaktions-Diffusions-Systemen, granularen Medien, nichtlinearen optischen Systemen und dielektrischen Barrierenentladungssystemen, wird in Kapitel 1 gegeben. Weil diese Arbeit sich auf Musterbildung in einem Gasentladungssystem mit einer Halbleiterkathode konzentriert, das mit einer Gleichspannungsquelle getrieben wird, werden die Grundlagen der Gasentladung in Kapitel 2 beschrieben. Ein umfangreicher Review der experimentellen Ergebnisse, die in derartigen Gasentladungssystemen erhalten wurden, wird in Kapitel 3 gegeben. Nach einer Beschreibung des experimentellen Aufbaus in Kapitel 4 wird die Untersuchung von Gasentladungen mit Metallelektroden in Kapitel 5 dargestellt. Kapitel 6 enthält die Ergebnisse einer systematischen Untersuchung der Musterbildung in Gasentladungssystemen mit Si:Pt Kathoden. Das Zustandsdiagramm in der Ebene der Kontrolparameter (die Leitfähigkeit des Halbleiters σ und die Quellspannung U_0) wird experimentell bestimmt. Die quantitative Reproduzierbarkeit solcher Zustandsdiagramme innerhalb des Fehlers wird bewiesen. Der Einfluß des Gasdrucks p und des Abstands d zwischen beiden Elektroden auf das Zustandsdiagramm wird untersucht. Während vorhergehende Experimente mit diesem System ausschließlich N_2 benutzten, werden in der vorliegenden Untersuchung auch andere Gase, d.h. He, Ne und Ar, verwendet. Im Falle von Ar werden die Phänomenologie der Musterbildung und das typische Zustandsdiagramm in der σ-U_0 Ebene beschrieben und die Abhängigkeit des Zustandsdiagrams von p und d untersucht. Wenn He oder Ne verwendet wird, ist der homogene Zustand der Entladung innerhalb des untersuchten Parameterbereichs stabil und es wird keine Musterbildung beobachtet. Phänomenologische Untersuchungen werden auch im Falle von andereren Kathodematerialien, d.h. Si:Zn und GaAs:Cr, durchgeführt und in Kapitel 7 dargestellt. Schließlich werden die wichtigsten Ergebnisse in Kapitel 8 zusammengefasst.

Acknowledgements

To my family who give me their continuous and distant support, I would like to say: 我想你们，我爱你们！

Contents

Chapter 1

Pattern formation in various systems

The existence and origin of order, which is ubiquitous in nature, have been one of the fundamental problems in philosophy and science since antiquity. Whereas in the past it was generally believed that creation and existence of ordered patterns and structures requires external intervention or control, during recent times the problem has been approached in the context of self-organization. The experimental investigations of the last decades on physical, chemical and biological systems have provided convincing evidence that spatial and/or temporal order can emerge spontaneously in systems driven far from equilibrium due to continuous energy dissipation. In equilibrium systems which can be approximated with linear differential equations, the dynamics of the systems can, at least in principle, be studied analytically thanks to mathematical techniques like Fourier transformations. However, in systems far from equilibrium nonlinearity plays an essential role. Consequently, it is necessary to describe such systems with nonlinear differential equations. Due to the absence of general methods for solving nonlinear differential equations analytically, nonlinear systems can only be studied on a case by case basis with the help of numerical techniques. The widely available computational resources and advances in numerical techniques in the last half century have made important contributions to the study of nonlinear systems which can be described by a small number of variables. It has been observed that simple nonlinearities can lead to complicated dynamics, like chaos. It is no longer a surprise any more that many of the intuitions developed during the study of linear systems failed and that nonlinear systems display completely new and in some cases unexpected behaviors. Therefore, it may not be too surprising that spontaneous formation of regular spatiotemporal structures are observed experimentally in spatially extended nonlinear systems under uniform driving. In such cases, nonlinearity and energy dissipation play essential roles. It is interesting to note that in nature nonlinearity is the rule rather than the exception, and the evolution of the ecological system is accompanied by a constant energy dissipation. For example, the sun as an energy source is essential to the ecological system on the surface of earth whereas alternative ecological systems exist close to deep sea volcanic vents where the energy stored in the core of the earth serves as source of energy. In this context, a quantitative study of spatiotemporal pattern formation in well-controlled laboratory systems driven far from equilibrium could not only shed new light on the phenomena of self-organization, but also give a new perspective when considering intriguing problems like the origin of life.

(a)	(b)	(c)
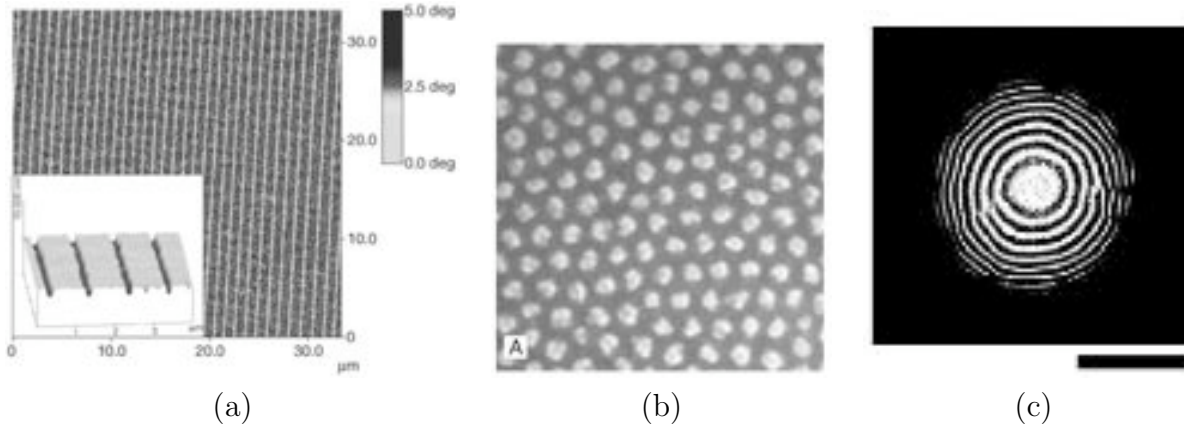
Figure 1.1: Examples of self-organization processes of technological interest. (a) Scanning force microscope (SFM) phase image and topography image (inset) of the structured surface consisting of about 200 nm wide channels separated by 800 nm wide stripes of a monomolecular L-α-dipalmitoyl-phosphatidylcholine (DPPC) film (from Gleiche et al., 2000); (b) Scanning electron microscope (SEM) image of a hexagonal quantum dot pattern with a characteristic length of 45 nm on a (100) GaSb surface induced by normal incidence of 420 eV Ar$^+$ ions (from Facsko et al., 1999); (c) Fresnel-like micro-lenses (scale bar 250 μm) prepared by a spontaneous periodic precipitation initiated by wet stamping silver nitrate onto a thin layer of a dry gel doped with potassium dichromate (from Campbell et al., 2005).

From a technological point of view, a clear understanding of self-organization may lead to entirely new classes of applications based on the concept of self-assembly. The fabrication of structures in the micron or nanometer range is increasingly difficult to achieve if one follows the so-called bottom-up principle, i.e. putting together the smaller components to form a functional object with desired structures. Therefore the "top-down" methods based on the principle of self-organization become increasingly attractive as the dimension is getting smaller. It has been shown that instabilities can be used to make regular micro-structures in various systems. For example, a structured surface consisting of 200 nm wide hydrophilic channels separated by 800 nm wide hydrophobic stripes of monomolecular film (Figure 1.1 a) can be obtained as a result of the instability of film adsorption during Langmuir-Blodgett film transfer processes (Gleiche et al., 2000). It is also shown that highly ordered and densely packed quantum dots on a nm scale (Figure 1.1 b) can be obtained by etching a (100) GaSb surface with Ar$^+$ ions under normal incidence. The regular pattern with a characteristic wavelength is believed to result from the competition between the smoothing mechanism due to diffusion and the roughening mechanism, where the erosion under sputtering is greater in a depression than on an elevation (Facsko et al., 1999). Furthermore, it was demonstrated that Fresnel-like diffractive lenses created using the mechanism of periodic precipitation in chemical systems work well to focus light. Such optically opaque concentric rings (Liesegang rings) on a μm scale (Figure 1.1 c) are formed by periodic precipitation induced from a ring-shaped source of silver nitrate on a thin layer of dry gels doped with potassium dichromate (Campbell et al., 2005).

Compared to the philosophical speculations, scientific research on self-organization

and pattern formation has a relatively recent origin. Many interesting phenomena in fluid systems, which are important for the later developments in the field of pattern formation, were studied during the last two centuries. Other pattern forming systems, e.g. chemical reaction diffusion systems, granular media, optical systems, and gas discharge systems, have only started to attract attention in recent decades.

It is more attractive, for the understanding of order in nature, to study the emergence of structures in three-dimensional space. However, because of the difficulties to drive a three-dimensional system uniformly in experiments, most of the work on pattern formation in dissipative systems so far has been done in systems with a large aspect ratio. In such so-called quasi-two-dimensional systems, the emergence and evolution of the patterns are studied in a plane while the third dimension is used to apply a uniform driving force to the system. In some cases, e.g. Taylor vortex flow, one dimension can be further eliminated due to the symmetry and a quasi-one-dimensional system is thus obtained.

1.1   Fluid systems

(a)   (b)
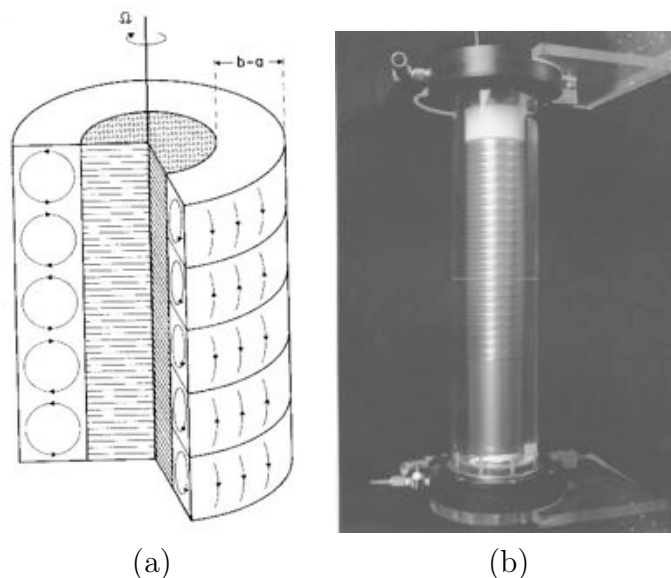
Figure 1.2: (a) Schematic Taylor vortex flow. The inner cylinder rotates against the outer wall (from Cross and Hohenberg, 1993); (b) Visualization of the Taylor vortex flow using reflective flakes which align themselves with the flow (photo from G. Ahlers, University of California Santa Barbara, USA)

The Navier-Stokes equation which describes the ideal fluid is intrinsically non-linear and it is thus perhaps not too surprising that complicated phenomena like turbulence and vortices would still not be completely understood. However, it is also not self-evident that a fluid driven out of equilibrium would form various patterns which under appropriate conditions can be highly ordered. The Taylor vortex flow, for example, is obtained when the fluid between an inner cylinder and an outer tube is driven away from equilibrium by rotating the inner cylinder. The system has been originally used by Couette in the late 1800s to study the viscous behavior of fluids. When the speed of rotation of the inner

cylinder is less than a critical value, the fluid simply rotates azimuthally around the cylinder. When it exceeds the critical value, the uniform circular flow along the vertical direction is no longer stable and periodically spaced vortex pairs are formed between the walls of the cylinder and the tube (Figure 1.2). As the speed is increased further, a sequence of increasingly complex states is observed. In the early 1900 this kind of flow instability was studied quantitatively by Taylor (1923) and the theoretical results were experimentally confirmed.

A different kind of instability in fluids which also leads to pattern formation manifests itself in the convection of a shallow layer of fluid which is heated from below. Carefully controlled laboratory experiments were carried out at the beginning of the 1900s by H. Bénard using various fluids of different viscosities. In Bénard's original experiments the lower boundary (the bottom of the container) is rigid and the upper surface is in contact with air and thus free. In this case a hexagonal pattern is typically formed (Figure 1.3). It is now known that the instability is induced by a gradient of surface tension due to temperature fluctuations. This kind of stability is called Bénard-Marangoni instability. The stability analysis made by Lord Rayleigh (1916) predicts that the heat-conducting state of the fluid layer is unstable against roll patterns with a characteristic wavenumber when the temperature difference between the lower and upper surface exceeds a threshold. Without considering the surface tension, Rayleigh's results can of course not explain Bénard's observations, but open a new field to study a different kind of instability induced by the buoyancy force due to the thermal expansion. The situation analyzed by Rayleigh is realized experimentally in convection of a fluid between two flat plates. The temperature of the lower plate is maintained above that of the upper plate by ΔT. When the stabilizing force due to the viscosity and thermal diffusion overwhelms the destabilizing buoyancy force determined by ΔT, heat is transported from the lower plate to the upper one by pure thermal conduction. In the opposite case, convection flows come into play. Later, it was predicted on the basis of the weakly nonlinear stability analysis that straight convection rolls are stable. Convection rolls as well as many other patterns (Figure 1.4) have been observed in numerous experiments (for a review see e.g. Cross and Hohenberg, 1993). After decades of intensive research, many aspects of the Rayleigh-Bénard convection are by now well understood and the system has become an important paradigm for studying pattern formation.

Early experiments on the excitation of surface waves in a shallow layer of fluid oscillated rigidly in the vertical direction were performed by Faraday (1831) and such waves are therefore also known as Faraday waves. With sufficiently large driving forces standing waves are formed and the oscillations correspond to half the driving frequency. Various spatial patterns occur as a result of the nonlinear interaction of the eigenmodes of the waves determined by the boundary conditions. The typical experimental setup consists of a fluid layer in a container which is a few millimeter thick. The lateral dimension of the container is normally between tens and hundreds of millimeter. The container is shaken vertically by a periodic driving force. The pattern of standing waves is determined by the viscosity of the fluid and the frequency and amplitude of the driving force. Besides typical patterns like squares, hexagons and stripes obtained with a single-frequency sinusoidal driving quasi-periodic patterns with 12-fold rotational symmetry are also observed with two-frequency driving (Figure 1.5). In general, when the driving amplitude or frequency is increased further, transitions to spatially and temporally dis-
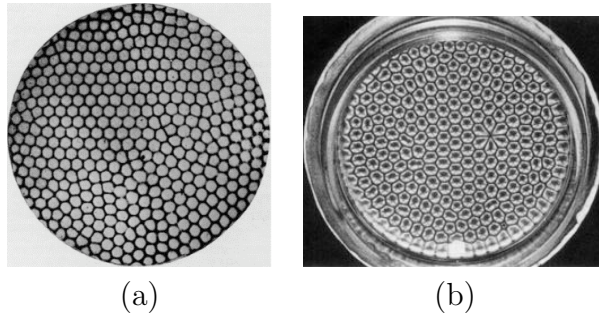
Figure 1.3: Typical patterns in Bénard convection. (a) Pattern from Bénard's original publication(Revue générale des Sciences XII, p. 1261, 1900); (b) Convection cell visualized with aluminum powder. Dark and bright regions indicate vertical and horizontal motion respectively (from Cross and Hohenberg, 1993).
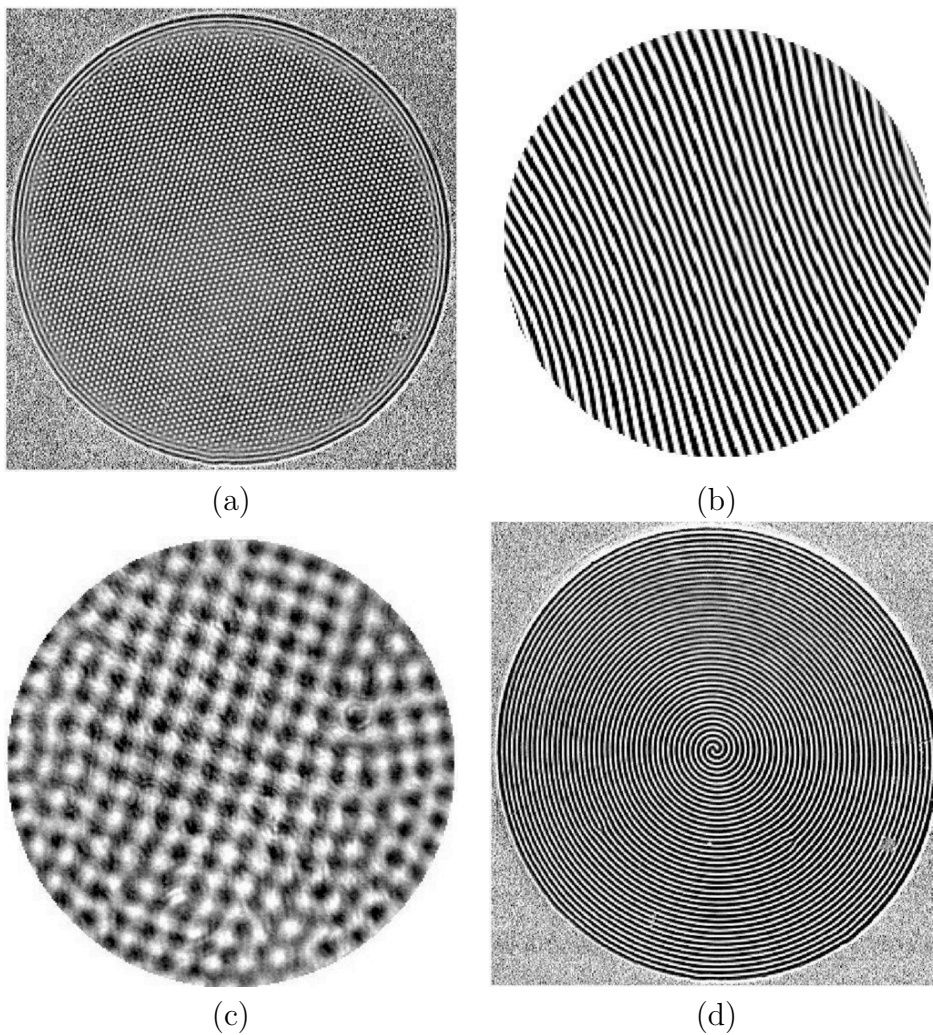
Figure 1.4: Regular patterns in Rayleigh-Bénard convection visualized through shadowgraphs. (a) defect-free hexagonal pattern near the onset of convection (from Bodenschatz et al., 1991); (b) stripes in a cell with a ramped spacing at the boundary (from Bajaj et al., 1999); (c) squares obtained when the cell is rotated around a vertical axis (from Bajaj et al., 1998); (d) Slowly rotating spirals (from Bodenschatz et al., 1991).
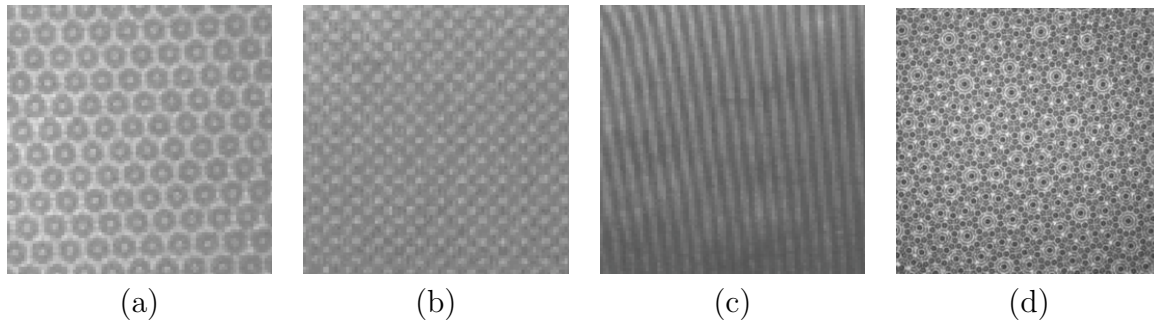
Figure 1.5: Typical patterns in a system consisting of a 3 mm layer of silicone oil in a 32 cm diameter container under vertical oscillation. The bright and dark regions correspond to larger and smaller amplitude of the standing waves. (a), (b) and (c) are obtained by using a single-frequency sinusoidal driving. (d) is obtained with a two-frequency sinusoidal driving. (from www.haverford.edu/physics-astro/Gollub/faraday/faraday1.html, J. P. Gollub, Haverford college, USA)

ordered states occur. A systematic survey of the patterns in such systems is given by Kudrolli and Gollub (1996).

1.2   Chemical reaction diffusion system

A chemical system driven far from equilibrium shows various types of instabilities which lead to spatial and/or temporal order. For example, in a continuously stirred tank reactor (CSTR) with an in- and outflow of some reagents and products, the reaction is constantly out of equilibrium because some reactive species are always in excess. In this kind of reactors the system is considered to be uniform as a result of the mixing, and thus only the temporal behaviors are studied. In the reaction of cerium catalyzed oxidation of malonic acid, chemical oscillations were first discovered by Belousov in the early 1950s and then studied by Zhabotinsky. Later, temporal chaos was also observed in the Belousov-Zhabotinsky reaction. When the reactants are not mixed by stirring, as in the case of a thin layer of solutions in a Petri dish or in a gel, beautiful target and spiral waves can be obtained. These discoveries and pioneering works have opened the new field of chemical oscillations and chemical waves in excitable media.

Parallel to these developments, a different mechanism of spatial pattern formation in chemical systems was proposed. It was found by R. E. Liesegang (1869-1947) that, periodic ring structures are formed when the insoluble product of a chemical reaction in a gel medium precipitates. Such structures are now known as Liesegang rings. Later, it was suggested by Turing that the interplay between chemical reactions and diffusion alone suffices to account for the main aspects of morphogenesis in biology (Turing, 1952). Stable spatial structures can be generated and maintained when a species which inhibits the reaction diffuses faster than a species which activates it. Despite the simplicity of the concept, it is extremely difficult to obtain genuine Turing structures in aqueous solutions for two reasons. First of all, the differences between the diffusion constants of all chemical substances in water are extremely small. Secondly, transport processes other than diffusion, like convection driven by the concentration gradient or induced by evaporative cooling at free surfaces, are unavoidable. Almost 40 years after Turing's speculation,

(a)

(b)
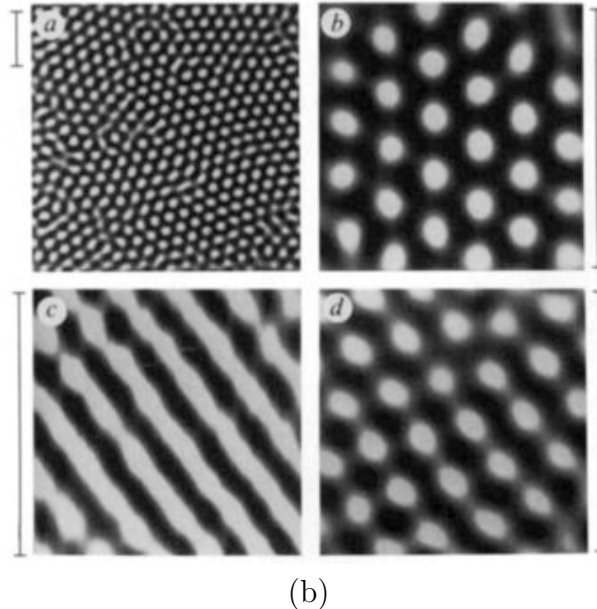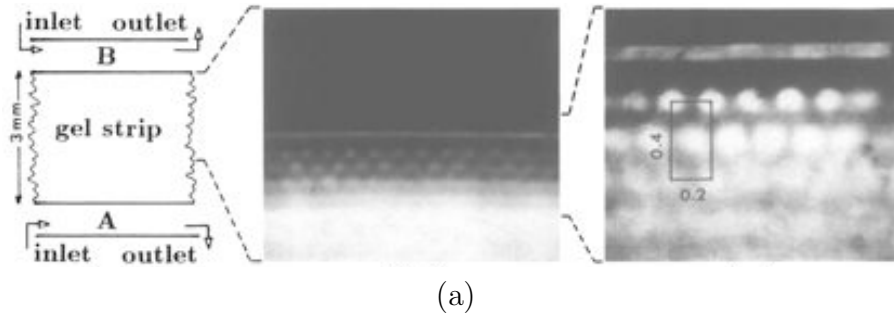
Figure 1.6: Typical patterns in chemical reaction diffusion systems. (a) First Turing structures produced in a gel reactor (from Castets et al., 1990); (b) Hexagons and stripes (scale bars 1 mm). The direction of observation is through the A and B tank indicated in the left (a) (from Ouyang and Swinney, 1991).

stable structures based on the activator-inhibitor mechanism were first observed in the CIMA (chlorite-iodide-malonic acid) reaction in a gel reactor (Castets et al., 1990). In retrospect, two factors are important to the success. First, the use of gel reactor avoids the transport of chemical substance by convection and the mass transport is only due to diffusion. Secondly, the activator molecules combine with the starch indicator to form a large macromolecular complex and the diffusion constant of the complex is therefore considerably reduced, which is essential for the fulfillment of the Turing instability criteria. Later two dimensional Turing patterns, stripes and hexagons, were obtained in a modified setup (Ouyang and Swinney, 1991).

1.3   Granular media

Besides the traditional fluid systems and chemical reaction diffusion systems, granular media as pattern forming systems have been the subject of intensive studies during the last several decades. Granular materials, e.g. sand, metal or glass spheres etc, are conglomerations of a large number of discrete macroscopic particles in vacuum or a
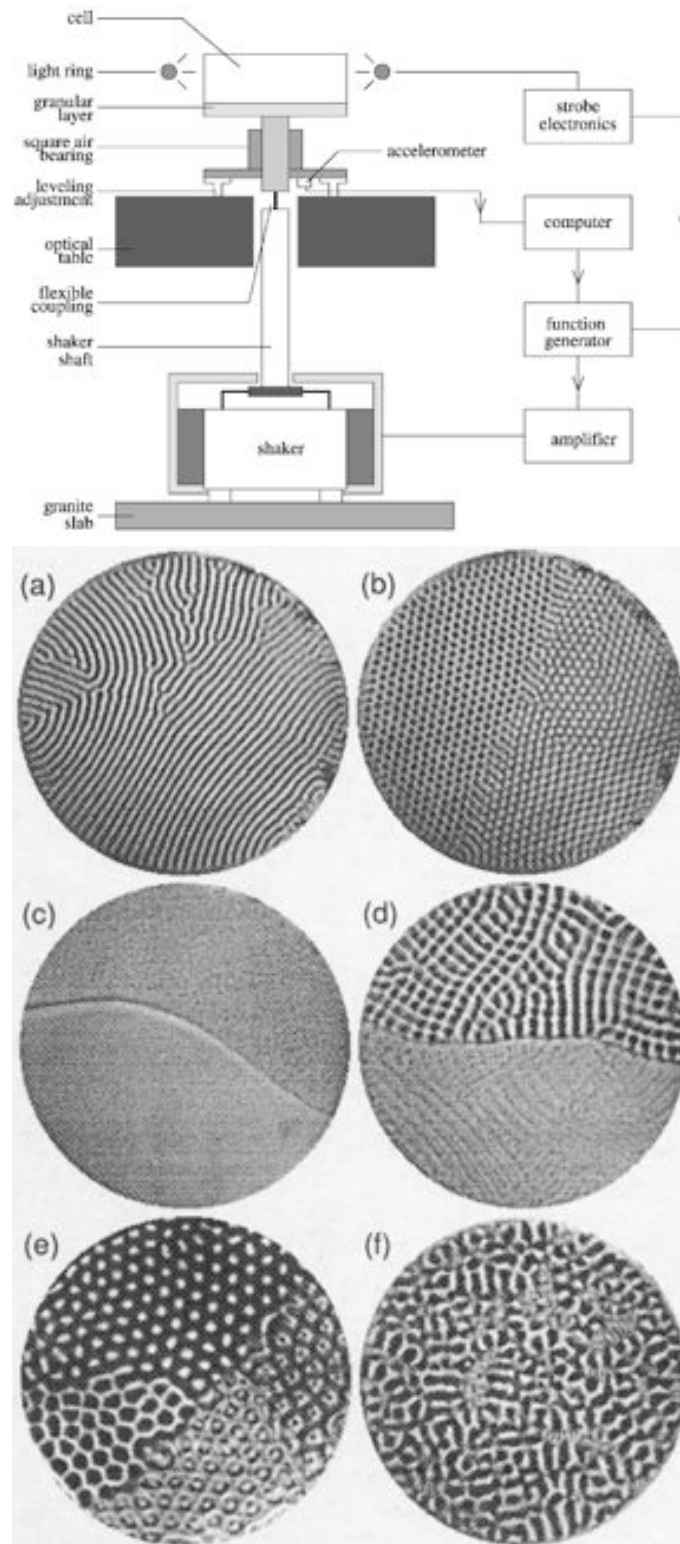
Figure 1.7: Schematic experimental setup (top) (from de Bruyn et al., 2001) used to study granular media driven by an external perturbation; Typical patterns in a layer of granular media under vertical oscillation (from Melo et al., 1995). The patterns are visualized by strobing the standing waves at half the driving frequency. Bright and dark regions correspond to higher and lower positions.

interstitial fluid like air or water. The study of granular media has a long history in engineering because of the need of handling them in industries like mining, agriculture and pharmaceutical manufacturing. Granular materials have been particularly intensively studied in recent years, with the help of measurement techniques like video analysis and computers simulations. From the physical point of view, a granular medium is a typical dissipative system due to the presence of static friction and inelastic collisions. Despite the apparent simplicity, the phenomenology in granular media under external driving is extremely rich, e.g. size segregation, avalanche phenomena, convection and self-organization etc (Jaeger et al., 1996). Therefore, granular physics has become a new frontier in the study of complex systems. Under certain conditions, granular materials behave like fluids. Faraday had already noticed the vibration-induced convection in the 1830s, for example. Furthermore, in analogy with the standing surface wave excited by vertical oscillation, standing waves at the interface of granular materials oscillate at either one-half or one-quarter of the driving frequency. The schematic setup for studying pattern formation used by H. Swinney's group (University of Texas) is given in Figure 1.7 (top) (de Bruyn et al., 2001). The cell containing a layer of spherical bronze particles with diameters of a few hundred microns is evacuated and connected to a shaker. The depth of the layer is about 20 particles. The pattern of standing waves is strobed with a ring of LEDs around the cell at half the driving frequency. The bright regions correspond to peaks while troughs appear dark due to the shadow of the particles in the peaks. Under appropriate conditions of driving amplitude and frequency, these systems form regular spatial patterns, e.g. stripes, squares and hexagons (Melo et al., 1995). Localized structures called oscillons (Umbanhowar et al., 1996) and spirals (de Bruyn et al., 2001) have also been observed in this system.

1.4 Nonlinear optical systems

Another experimental system which shows pattern forming behaviors is the single mirror feedback system in nonlinear optics (for a review see Ackemann and Lange, 2001). As illustrated in Figure 1.8 (a), the system consists of a thin layer of nonlinear medium (typically sodium vapor) placed at a certain distance in front of a mirror, which has transmission of a few percent. A single-mode laser beam with a Gaussian profile passes through the medium and is then reflected by the mirror and interacts with the medium. The spatial pattern is observed behind the mirror. The patterns can be recorded simultaneously in both real space and Fourier space. The nonlinearity of the medium lies in the dependence of its refractive index on the local intensity of the light. The major control parameters are the power of the input laser beam, the temperature of the sodium vapor (effectively the molecular density) and the polarization of the laser. When the power of the laser beam is below a certain threshold, the smooth Gaussian profile of the beam is recorded. When it exceeds the threshold, positive or negative hexagons or squares emerge spontaneously depending on the polarization of the laser. A further increase in power leads to secondary bifurcations. For example, starting from a hexagonal pattern quasi-periodic pattern of twelve-fold symmetry can be obtained (Figure 1.8 (b) and (c)). In the same system, an interplay between diffraction and nonlinear refraction gives rise to localized structures called solitons (Figure 1.8 (d)) which could in principle serve as bits in optical computations.
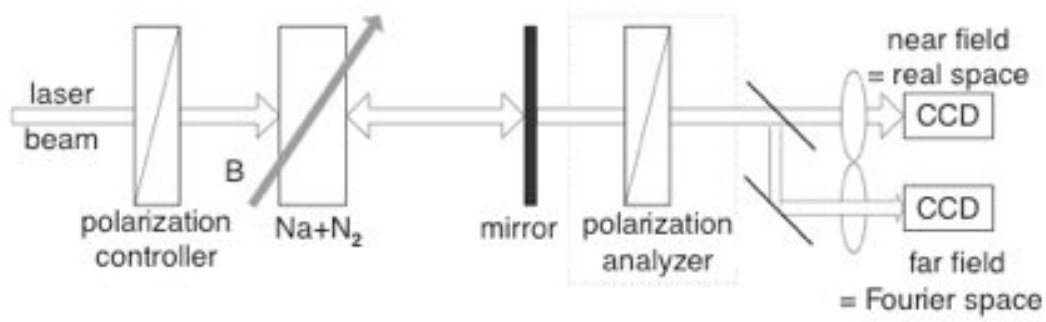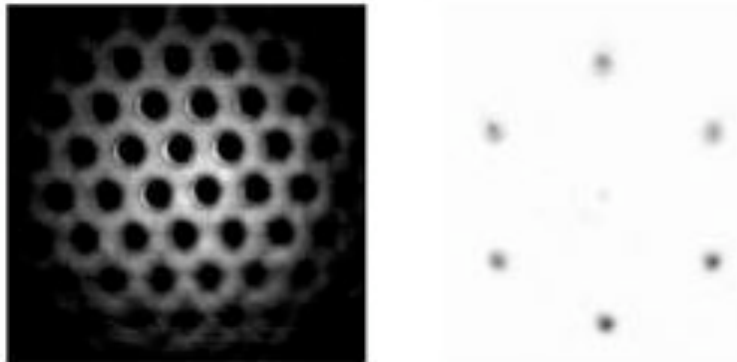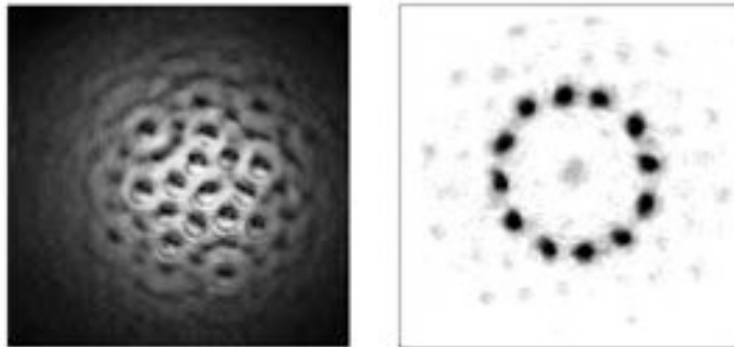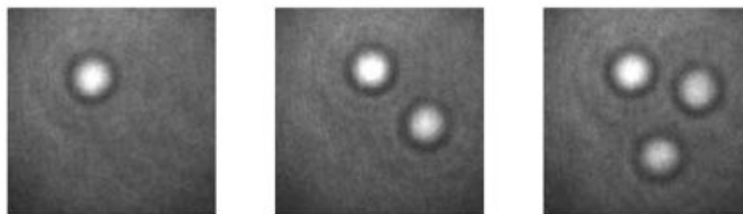
Figure 1.8: (a) Schematic experimental setup of the single-mirror feedback system; The patterns in real space (left) and Fourier space (right): (b) Hexagonal patterns; (c) Quasi-structure with 12-fold symmetry; (d) Localized structures. (from Ackemann and Lange, 2001).

1.5 Dielectric barrier discharge system

Dielectric barrier discharge (DBD) is a form of gas discharge which occurs when a system consisting of electrodes covered with dielectrics is driven periodically by an alternating high voltage source. It has been historically used to generate ozone for industrial purposes and has nowadays many applications, e.g. surface treatment, CO_2 lasers, excimer lamps, plasma displays etc. A basic description of various DBDs was given by Pietsch (2001, and references therein)

The discharge actually consists of many individual transient self-extinguishing micro-discharges. The micro-discharge emits radiation in the visible range when the gas molecules make transitions between their excited states. This allows one to observe the spatial distribution of the filaments (i.e. micro-discharges) directly when transparent electrodes are used. It has long been known that the distribution of the filaments is in general random in space. It came, therefore, as a surprise when highly ordered patterns of filaments were first observed under certain conditions in a parallel plate DBD system with large aspect ratio by Boyers and Tiller (1982). In their experiments, a 50 μm gap purge flowed with He at atmospheric pressure was driven with a 125 kHz high voltage source. With a sinusoidal wave source a hexagonal array of current filaments was observed when the peak-to-peak voltage was slightly above the breakdown voltage. An increase of the applied voltage resulted in double breakdown of the gas during the rising portion of each half cycle. The first discharge formed an array of filaments and the second discharge occurred in the interstitial spaces between the filaments of the first array. Further increases in the applied voltage eventually led to a transition to a uniform glow. The use of square wave driving gave rise to a different transition scenario: a hexagonal array changed first to stripes, then to hexagonally woven stripes (inverted hexagon) and finally to a uniform glow as the applied voltage was increased. Following this discovery, self-organized patterns in DBD system were studied, among others, by H.-G. Purwins and colleagues (University of Münster, Germany) and recently by L. Dong and colleagues (Hebei University, Baoding, China). During the last two decades, the DBD system has become a further model system for the experimental investigation of pattern formation phenomena.

Typical experimental setups used by different groups for studying pattern formation in DBD are illustrated in Figure 1.9. The discharge cell consists of two parallel glass plates separated by a distance much smaller than their lateral extension. In the case of Figure 1.9 (a) used by Purwins' group (University of Münster, Germany) and Figure 1.9 (b) used by Breazeal et al. (1995), the electrodes are glass plates coated on one side with a transparent conductive ITO (Indium-Tin-Oxide) film. The ITO film is replaced by water with a conductivity of about 0.3 S/m in the experimental setup (Figure 1.9 (c)) used by Dong's group (Dong et al., 2004). In this case, the water also serves as coolant for the glass electrodes. In the experiments published so far, the inter-electrode distance varies from 50 μm to 2 mm and the electrodes have diameters of several centimeters, giving aspect ratios ranging from 30 to 400. In some experiments, the discharge area is defined by the electric field (i.e. the area of the conductive coating where charge carriers can diffuse freely outside the plasma region), whereas in other cases the plasma is confined by rigid dielectric walls. We refer to the two kinds of boundary as free and rigid boundaries respectively. In most experiments in the literature a circular boundary
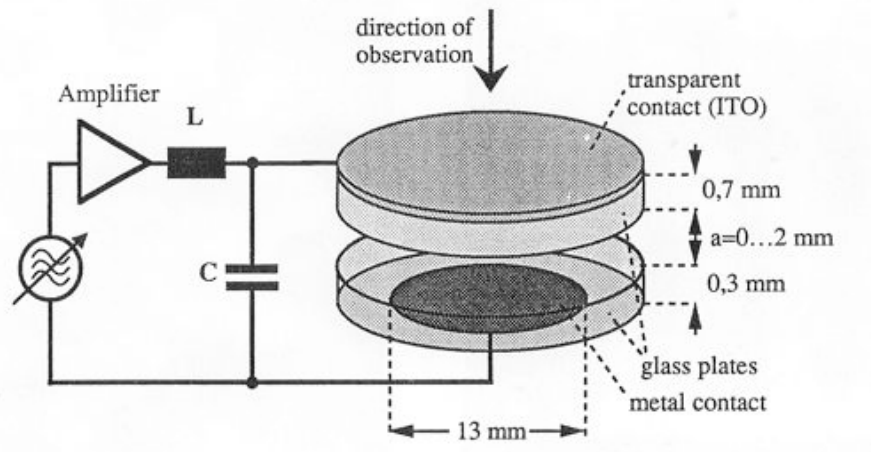
(a)
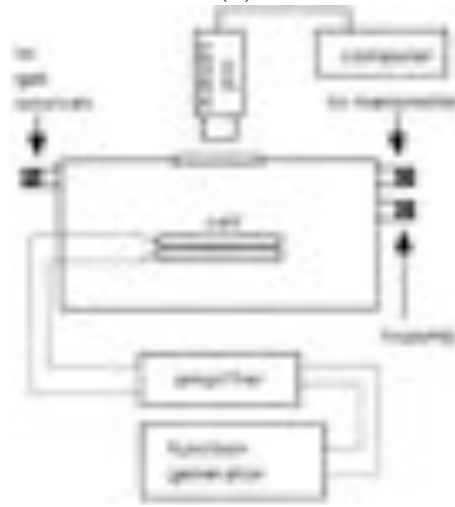
(b)
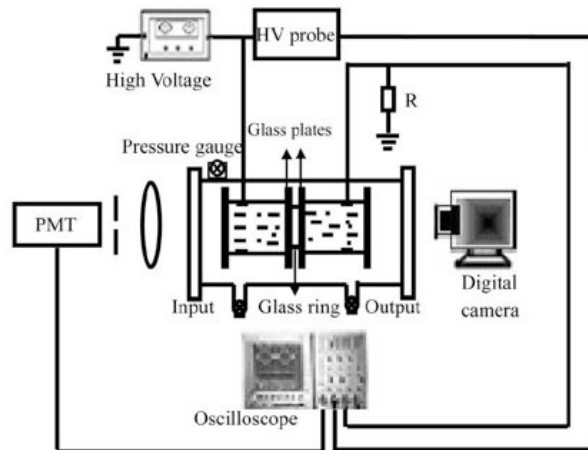
(c)

Figure 1.9: Three variants of schematic experimental setups for studying pattern formation in the dielectric barrier discharge system. (a) from Ammelt et al. (1993); (b) from Breazeal et al. (1995); (c) from Dong et al. (2005).

was used although a rectangular boundary was also used in several cases. The discharge gap is filled with He or Ar at atmospheric pressure or at several hundred hPa. Typically the high voltage source produces a sine or square wave with a frequency between 20 and 400 kHz. The experimental control parameters are gas composition, gas pressure, inter-electrode distance, peak-to-peak voltage and frequency, waveform of the high voltage source etc.

The richness of the patterns observed in this class of systems is illustrated in Figure 1.10. Typical stationary patterns are hexagonal arrays of discharge filaments, square, super square or quasi-crystalline patterns with twelve-fold rotational symmetry, stripes, inverted hexagonal arrays (also referred to as hexagonally woven stripes) and uniform glow. Various dynamic patterns are also observed, i.e. rotating hexagons, stripes with constantly changing orientations, targets which emit concentric traveling waves from the central focus, drifting hexagons annihilating at the boundary, and dynamic labyrinthine structures. The phenomenology published during the last two decades is summarized in Table 1.1. Depending on the distance between electrodes and the gas pressure, the dielectric barrier discharge may operate in the Townsend mode or in the streamer mode. In the experiments made by Dong's group with a 2mm gap filled with Ar at atmospheric pressure the transient micro-discharge occurs in the streamer mode. Other experiments conducted by different authors use a gap of several hundred micron and several hundred hPa He ensuring that the discharge is in the Townsend mode. As indicated in Table 1.1, the transition scenario, i.e. from hexagonal array of filaments to stripes and finally to uniform glow as the driving voltage is increased at fixed frequency, reported by Boyers and Tiller (1982) has been reproduced by Willebrand et al. (1991b) in systems with a larger inter-electrode distance and with a higher driving frequency. It was also noticed by these authors that the arrangement of the filaments depended on the boundary, i.e. circular electrodes lead to a hexagonal pattern while rectangular ones gives a square pattern. This effect was illustrated in the results by Ammelt et al. (1993). The closed loop structure photographed with a relatively long exposure time turned out to be a superposition of arrays of seemingly randomly distributed discharge filaments between successive breakdowns. In addition, rotating hexagonal pattern and ordered filament clusters were also reported (Ammelt et al., 1993). In the work of Breazeal et al. (1995), the effect of gas composition (i.e. the concentration of water vapor in He) was investigated and novel dynamic patterns like rotating stripes and a wave-emitting target were reported besides major patterns discovered by previous workers. Under the same geometry and gas composition, it was found that the discharge driven with a 1 kHz square wave was spatially random while regular patterns formed when the system was driven with a 100 kHz square wave. This may indicate the existence of a threshold frequency for pattern formation in this kind of system. The experiments conducted in Purwins' group (University of Münster, Germany) during the following years use a 500 μm inter-electrode distance, which is larger than the 50-125 μm used in previous work. However, the pressure of He was reduced accordingly and thus the product of pressure p and distance d was of the same order of magnitude, varying between 5 and 30 hPa·cm (Müller et al., 1997; Brauer et al., 1999; Müller et al., 1999b). In these works, the motion of solitary filaments was studied as well as the spatially extended patterns. Some exotic phenomena, i.e. breathing filaments (Müller et al., 1999a) and a pair of filaments moving in a closed loop (Brauer et al., 2000), were observed when a mixture of He and air was
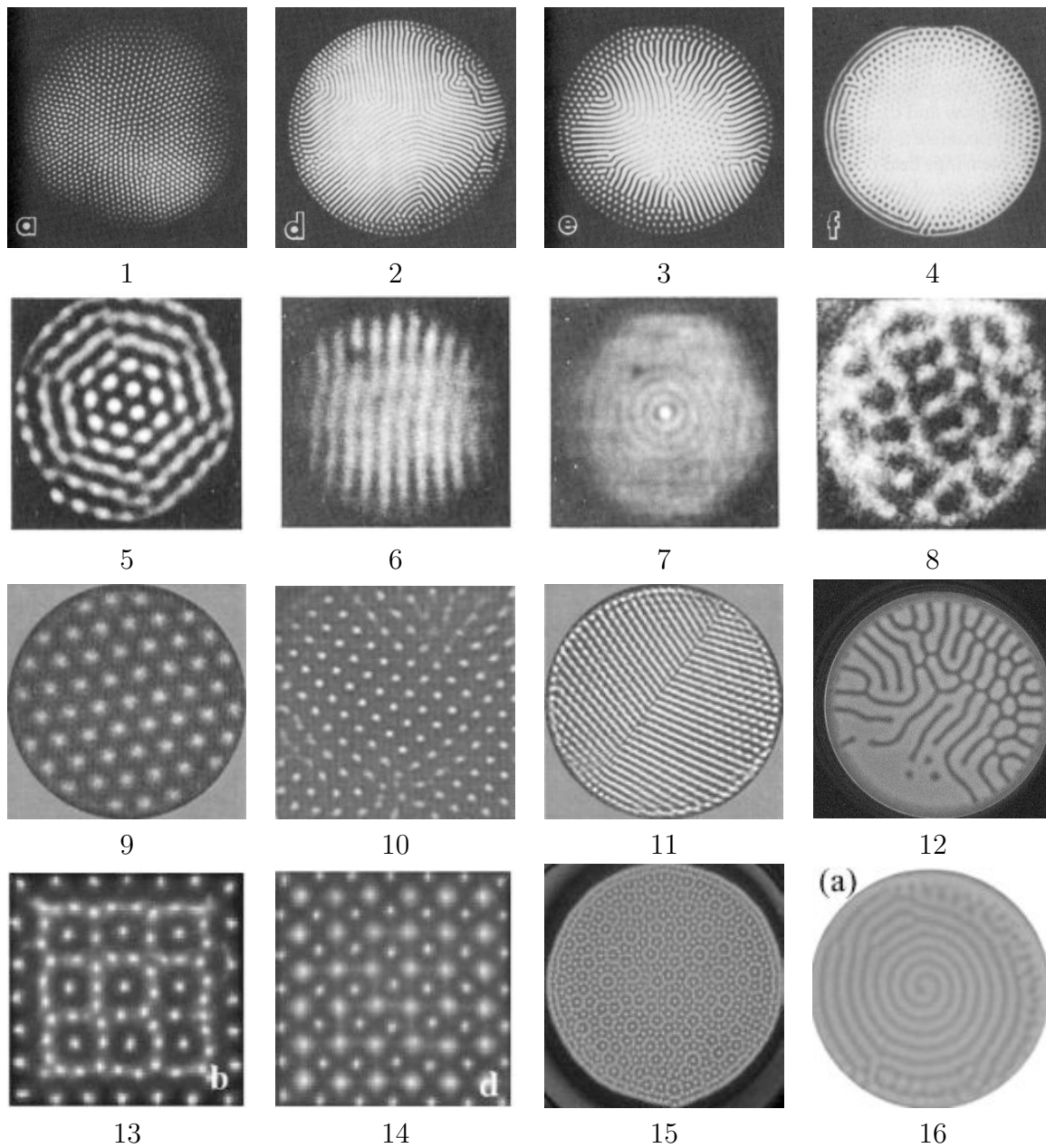
Figure 1.10: Typical patterns obtained in parallel plate dielectric barrier discharge systems. 1 hexagonal filaments; 2 stripes; 3 inverted hexagon; 4 uniform glow; 5 rotating hexagon; 6 rotating stripes; 7 target; 8 disordered discharge; 9 hexagon; 10 square; 11 drifting hexagon annihilating at the boundary; 12 labyrinth 13 super square; 14 super square; 15 quasi-crystalline pattern with twelve-fold rotational symmetry; 16 dynamic spiral. Source: 1-4 from Boyers and Tiller (1982); 5-8 from Breazeal et al. (1995); 9-12 courtesy of L. Stollenwerk (University of Muenster, Germany); 13, 14 from Dong et al. (2006); 15 courtesy of L. Dong (University of Hebei, Baoding, China); 16 from Dong et al. (2005).

14

used. With a 2 mm gap filled with 2.5 hPa N_2 Gurevich et al. (2003b) found a transition scenario from filaments to uniform and further to target pattern as the applied voltage was increased. The image sequence corresponding to four micro-discharges during a full period of the sinusoidal driving voltage showed that the target pattern consisted of two sets of concentric rings. One set corresponded to the first micro-discharge and the other to a second discharge during the rising portion of the sine wave occured at interstitial places between the previous rings. With increasing pressure, the ring pattern was destabilized and broken into filaments. Stollenwerk and Purwins (2005) found that a single discharge filament showed an intrinsic motion amid random Brownian motion and Zanin et al. (2004) studied the collective rotation of the hexagonal array in detail. When the amount of charge generated in the gas during the micro-discharge is sufficiently large, a secondary discharge on the surface of the dielectric can occur and gives a star-like halo structure around the bright spot corresponding to the filamentary form of the primary discharge in the gas. Zanin et al. (2002) pointed out that this could be a novel way of generating Voronoi diagrams which partition a plane into domains according to some set of reference points when inserting a dielectric film perforated at appropriate places into the gas layer. In contrast to the glass electrodes coated with transparent conductive films, glass cylinders filled with conductive water were used as electrodes by Dong's group (Hebei University, China). The large amount of water serves also as coolant to stabilize the temperature of the glass dielectric. With a large gap of about 2 mm and Ar at atmospheric pressure a typical $p \cdot d$ value of about 200 hPa·cm is obtained. Under these conditions, the transient micro-discharge operate clearly in the streamer mode. Typical patterns observed in systems where micro-discharge in the Townsend mode predominates, e.g. hexagons, stripes, squares etc, were reproduced in this system (Dong et al., 2003a,b, 2004). In addition, spirals and spiral defect chaos, which is similar to the case in Rayleigh-Bénard convection, were reported recently (Dong et al., 2005). It is especially interesting to note the transition from square to super square and finally to hexagon as the applied voltage is increased (Dong et al., 2006). Contrary to the claim that a rectangular boundary leads to square patterns, the hexagonal pattern appeared at high voltages despite the rigid rectangular boundary. The pattern is thus not defined by the external boundary but is selected by the internal dynamics of the system.

gap, electrode	gas	driving voltage	phenomena	reference
50-60 μm, $\varnothing$1.1 cm	1013 hPa He	125 kHz sine	hexagon;uniform glow	
		40-125 kHz square	hexagon; stripes;	
			inverted hexagon;	
			uniform glow	Boyers and Tiller (1982)
300 μm, $\varnothing$1.2 cm	1000 hPa He	300 kHz sine	hexagon; square;	
			stripes;uniform glow	Willebrand et al. (1991b)
1.7 mm, 1.2$\times$1.4 cm^2	470 hPa He	373 kHz sine 580 V	stripes	
450 μm, $\varnothing$1.3 cm	778 hPa He	200 kHz sine 578 V	rotating hexagon	
550 μm, $\varnothing$1.3 cm	419 hPa He	200 kHz sine	filament cluster	
950 μm, $\varnothing$1.3 cm	804 hPa He	250 kHz sine 636 V	loop	Ammelt et al. (1993)
75 μm, $\varnothing$0.7 cm	931 hPa He(H$_2$O)	80 kHz square 400 V	hexagon	
		45 kHz square 350 V	stripes	
		6 kHz square 320 V	inverted hexagon	
125 μm, $\varnothing$0.7 cm	399 hPa He(H$_2$O)	100 kHz square 210 V	dot array	
		100 kHz square 240 V	labyrinth	
		100 kHz square 255 V	inverted dot array	
		1 kHz square 250 V	disordered discharge	
125 μm, $\varnothing$0.7 cm	399 hPa He(H$_2$O)	190 kHz square 340 V	wave-emitting target	
		180 kHz square 260 V	rotating hexagon	
		180 kHz square 340 V	rotating stripes	Breazeal et al. (1995)
500 μm, $\varnothing$5 cm	419 hPa He	200 kHz sine 474 V	hexagon	
	243 hPa He	200 kHz sine 870 V	mixed hexagon & stripes	Müller et al. (1997)
500 μm, $\varnothing$2 cm	327 hPa He	220 kHz sine 549 V	moving solitary filaments	
		220 kHz sine 560 V	hexagon	
500 μm, $\varnothing$5 cm	667 hPa He	200 kHz sine 532 V	random filaments	
		200 kHz sine 578 V	filament domain	
		200 kHz sine 610 V	hexagon domain	Brauer et al. (1999)
500 μm, $\varnothing$5 cm	133 hPa He	200 kHz sine 470 V	hexagon	Müller et al. (1999b)

500 μm, $\varnothing$1 cm	350 hPa He (air)	180 kHz sine 605 V	breathing filaments	Müller et al. (1999a)
500 μm, $\varnothing$2 cm	50 hPa He (air)	179 kHz sine 620 V	loop (moving spot pair)	Brauer et al. (2000)
3 mm, $\varnothing$4 cm	122 hPa N_2	sine (frequency unknown)	Voronoi diagram	Zanin et al. (2002)
2 mm, $\varnothing$4 cm	2.5 hPa N_2	50 kHz sine 1050 V	target pattern	Gurevich et al. (2003b)
2 mm, $\varnothing$4.7 cm	1000 hPa Ar	26 kHz sine 2200 V	hexagon	Dong et al. (2003a)
1.5 mm, $\varnothing$5 cm	1013 hPa Ar	26 kHz sine 2000 V	hexagon	
		26 kHz sine 2400 V	square	Dong et al. (2003b)
1.65 mm, $\varnothing$ 5 cm	1011 hPa Ar	26 kHz sine 3500 V	disordered filaments	
		26 kHz sine 6000 V	hexagon	
		26 kHz sine 9000 V	stripes	Dong et al. (2004)
500 μm, $\varnothing$4 cm	113 hPa He	200 kHz sine 400 V	rotating hexagon	Zanin et al. (2004)
500 μm, $\varnothing$4 cm	200 hPa He	200 kHz sine	drift bifurcation of single moving filaments	Stollenwerk and Purwins (2005)
1.4 mm, $\varnothing$6.5 cm	1013 hPa Ar (air)	60 kHz sine 3100 V	spirals	
		60 kHz sine 8500 V	spiral defect chaos	Dong et al. (2005)
1.6 mm, rectangular	1013 hPa Ar	62 kHz sine 3200 V	square	
		62 kHz sine 3500 - 4200 V	super square	
		62 kHz sine 5000 V	hexagon	Dong et al. (2006)

Table 1.1: Summary of experimental conditions and phenomenology in a planar dielectric barrier discharge system.

1.6 summary

In the context of pattern formation, many interesting phenomena in other systems also deserve attention. For example, instability in thin films of block copolymers leads to the formation of striped patterns separating micro-domains (Harrison et al., 2000). The phenomenology of domain patterns in a variety of two-and three-dimensional physical-chemical systems in equilibrium was reviewed by Seul and Andelman (1995, and references therein). Models of pattern formation in biological systems were discussed in detail by Meinhardt (1982). In addition, spatially periodic structure of a moving nematic-isotropic interface during directional solidification of a liquid crystal (Bechhoefer et al., 1989), spiral waves in bacterial colonies and regular geomorphological structures attract also considerable interest. Pattern formation in gas discharge systems, on which the present work is focused, is reviewed in detail in the following chapter.

There has been great effort to study the universality of pattern formation as many model systems of completely different nature give rise to regular generic structures when driven out of equilibrium. During the last decades the study of the so-called dissipative structures in spatially extended nonlinear systems has been an important subject in nonlinear science (Nicolis and Prigogine, 1977; Haken, 1983, and references therein). The insight gained in the study of self-organization in nonlinear systems has also been used to tackle problems in economy and social sciences at the Santa Fe Institute (www.santafe.edu, Santa Fe, USA) and in several other groups.

Chapter 2

Basics of gas discharge physics

Gas discharge physics, the field dealing with electrical properties of partially ionized gases, is extremely broad. It covers the behavior of gases in a large range of pressure, under conditions of various electrode geometries and under the influence of electromagnetic fields with different amplitude and frequency. When gases at appropriate pressures between two parallel plate electrodes are driven by a constant voltage source, several kinds of self-sustained steady discharge, i.e. Townsend discharge, glow discharge and arc discharge, can be observed. A detailed treatment of the discharge phenomena and elementary processes related to ionized gases is available in the classical textbooks by von Engel (1993) and Raizer (1991), which also served as reference for the formulae in this chapter. Extensive experimental data dispersed in the vast literature in atomic physics and plasma physics, are compiled in a book by Brown (1993). In addition, a review on the discharge mechanism in low pressure gases is given by Druyvesteyn and Penning (1940).

Since the present work focuses on studying self-organized patterns in gas discharge systems driven by a constant voltage source, only the phenomena and mechanisms relevant to the direct current (DC) gas discharge are included here to facilitate the understanding of the basic experimental phenomena described in the following chapters. The topics in this brief introduction to gas discharge physics are limited to the phenomena occuring in the parallel plate geometry of electrodes. In the following we shall refer to "molecules" even in the case of mono-atomic gases like noble gases. It is assumed throughout that the processes of ionization leave the chemical composition of the gas unchanged, i.e. no chemical reactions.

2.1 Elemental processes in ionized gases in electric field

2.1.1 Diffusion and drift of charges in gas

When a gas is irradiated by some types of radiation, e.g. X-rays, or high energy particles, the molecules are ionized and electron-ion pairs are created. The thermal motion of the charges and the random collisions with neutral molecules lead to the diffusion of the electrons and ions on a macroscopic scale. The proportionality constant between the particle flow vector $\boldsymbol{J}$ and the density gradient of charged particles (∇n) defines the

diffusion coefficient D:

$$\boldsymbol{J} = -D\nabla n \tag{2.1}$$

D is further related to the microscopic properties of the particles by:

$$D = \frac{lv}{3} \tag{2.2}$$

where l is the mean free path and v the mean velocity. In the absence of electric field, the charges finally disappear from the gas volume through the processes like recombination or attachment to the walls. In a constant electric field, the charged particles are accelerated between successive random collisions. When the field is sufficiently weak, only elastic collisions between charged particles and neutral molecules occur and there are no excitations or ionizations. In this case, on a macroscopic scale the particles move with a certain drift velocity along the direction of the electric force. When the velocity gained from the electric field is small compared to the mean thermal velocity, the drift velocity v_d is collision-limited and related to the electric field $\boldsymbol{E}$ by:

$$v_d = \frac{q}{m\nu}\boldsymbol{E} = \mu_i \boldsymbol{E} \tag{2.3}$$

where m is the mass of the particle, q its charge, ν the effective collision frequency and μ_i the mobility of the particle. This, however, applies only to the drift of ions which have a mass close to that of the neutral molecules. In contrast, the electrons can be accelerated to a velocity significantly larger than their thermal velocity even during the interval of one mean free time. The drift velocity can thus not be treated like that of ions. A simple treatment assuming the loss of a constant fraction of its energy in each collision gives the square root dependence of v_d on the reduced field E/p:

$$v_d \propto \sqrt{\frac{E}{p}} \tag{2.4}$$

where p is the pressure. For weak fields the experimental electron drift velocity is proportional to $\sqrt{E/p}$ as expected from the theory. Above a certain value of the reduced field, inelastic collisions with the neutral molecules come into play and excitations and ionizations occur. In such cases there are no reliable theoretical predictions and experimental values must be used in simulations or calculations.

2.1.2 Ion Saturation

The electric field is uniform in the gas between two parallel conductive electrodes which are connected to a constant voltage source. In such a field, the electrons and ions created through ionization by irradiation (e.g. by X-rays) are separated by the electric force and drift to the anode and cathode respectively. When the gas is irradiated continuously, a steady current is registered in the external circuit as a result of the dynamic equilibrium between the generation of charge and the charge collection by the electrodes. When the applied voltage U is gradually increased in the setup illustrated by Figure 2.1 (left), the current rises slowly at first and then reaches a plateau. This effect can be qualitatively understood in the following way: When the voltage is small, only part of the charges
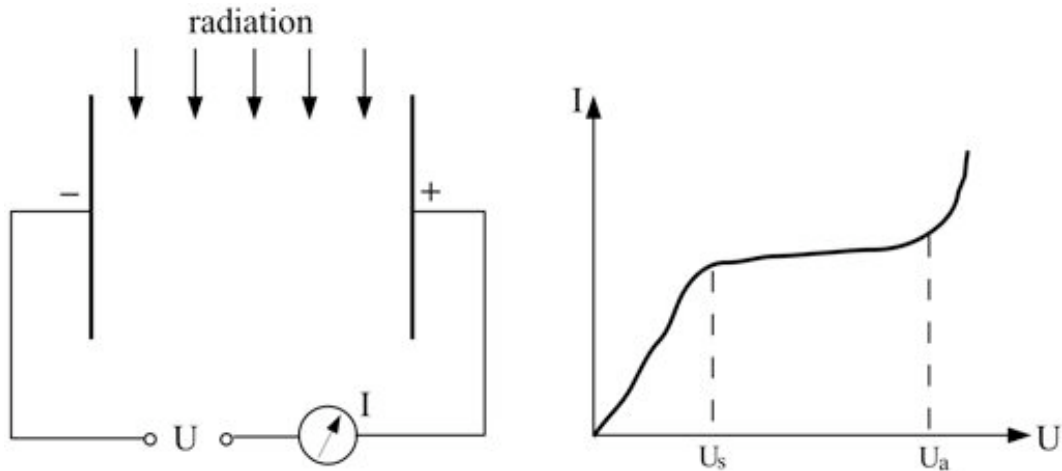
Figure 2.1: Schematic circuit for measuring voltage-current characteristics in a weakly ionized gas (left) and the typical voltage-current curve (right).

contributes to the current conduction while others disappear from the gas volume due to recombination or attachment to the lateral walls. As the voltage is increased, the electrons and ions obtain a larger drift velocity so that the probability of recombination and diffusion to the walls is reduced. Above a certain voltage, U_s, the charge loss processes become insignificant. Thus almost all the charges created by the radiation contribute to the current conduction and a plateau appears in the voltage-current characteristics. This phenomenon is known as ion saturation. In the plateau region the current, which is independent of the applied voltage in a wide range, is determined only by the generation rate of the charges due to the incident radiation. Therefore, the value of the saturated current is a measure of the intensity of the radiation. This effect is used for the construction of radiation detectors. For example, ionisation chambers consisting of two parallel plane electrodes in air are widely used to measure the intensity of monochromatic synchrotron radiation beams.

2.1.3   Townsend Avalanche and secondary effects

If the voltage is increased above U_a, the current rises rapidly as illustrated in Figure 2.1 (right). This is due to impact ionization by collision of the electrons produced by the incident radiation with the gas molecules. A rough picture of the physical processes is as follows: The electrons are accelerated between successive collisions and therefore acquire energy from the field. Their kinetic energy of the electrons is proportional to the field strength E and the mean free path, which is related to the inverse of the pressure p and consequently depends on the reduced electric field E/p. As the applied voltage is increased, the higher reduced electric field leads to an increase of the kinetic energy of the electrons. The probability of inelastic collisions between electrons and neutral molecules is thus higher. When the electrons acquire sufficient energy to ionize the gas molecules during subsequent collisions, additional electron-ion pairs are generated and the number of electrons increases. The autocatalytic process characterized by an exponential multiplication of the electron-ion pairs is called Townsend avalanche. Single avalanches developed in an uniform electric field can be visualized in cloud chambers (Fig.
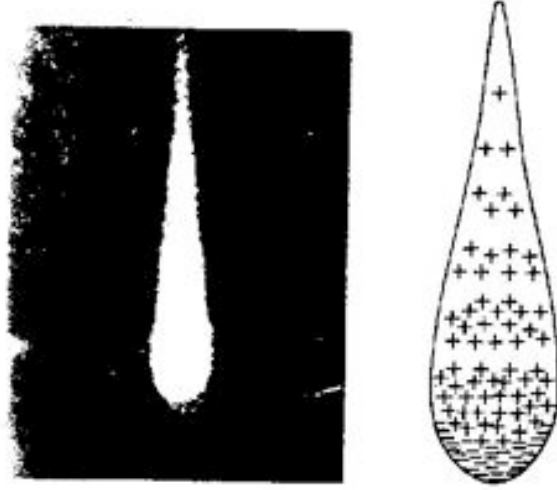
Figure 2.2: Shape of an avalanche visualized in a cloud chamber (left) and the corresponding schematic charge distribution (from Sauli, 1977, Fig. 46).

2.2). The shape and charge distribution of the avalanche result from the following facts: As half of the ions are produced over the last mean free path of the electrons, the number of ions decreases along the direction of the electric field. Due to their high mobility, in the same field the drift velocity of electrons is about several hundred times that of the ions, which drift in the opposite direction. Consequently, the electrons are always at the front of the avalanche while the ions are in the tail. An important application of Townsend avalanches is in gas-filled radiation and high energy particles detectors. In proportional counters the signal depends linearly on the intensity and energy of the incoming radiation whereas in Geiger-Müller counters the signal reaches saturation and the information about the energy and the cause of the initial ionization is lost.

Since the separation between the electrodes is usually much larger than the mean free path of the electrons, electron impact ionization can be treated as occurring continuously throughout space. The increase in the number of electrons dn produced by n electrons drifting over a distance dx along the direction of the electric force is given by:

$$dn = n\alpha dx \tag{2.5}$$

where α is the first Townsend ionization coefficient. It corresponds to the number of electrons produced by one electron per unit path length along the direction of the electric force. A semi-empirical formula describing the dependence of α on pressure p and electric field E can be justified by the following argument. An electron with free path l acquires an energy eEl from the electric field. In order to be capable of ionizing another molecule during the next collision, the kinetic energy of the electron has to be larger than the ionization energy of the gas molecules eV_i. Hence the shortest distance l the electron must move in the direction of the electric force is V_i/E. The probability that an electron would have a free path l larger than the mean free path λ is $e^{-l/\lambda}$. Since the number of collisions per unit length (e.g. 1 cm) in the direction of the force is $1/\lambda$, the number of collisions leading to ionizations per unit length, which defines the first Townsend

22

ionization coefficient α, is given by:

$$\alpha = \frac{1}{\lambda} e^{-\frac{l}{\lambda}} \tag{2.6}$$

The mean free path λ is proportional to the inverse of the gas pressure p, or λ_0/p where λ_0 is λ at unit pressure. Substituting λ and l yields the semi-empirical relationship:

$$\alpha = Ape^{-B\frac{p}{E}} \tag{2.7}$$

where $A = 1/\lambda_0$ and $B = V_i/\lambda_0$ are constants for a specific gas. It is is valid for many gases in a given range of E/p.
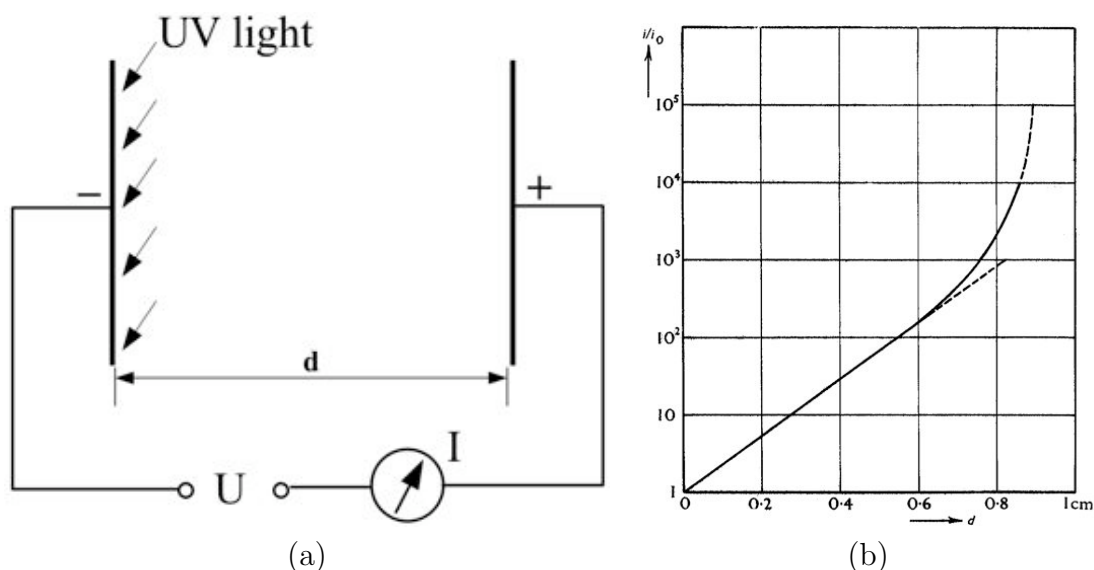
Figure 2.3: (a) Schematic experimental setup for the determination of the first Townsend ionization coefficient in electron impact ionization; (b) Multiplication ratio i/i_0 as a function of the inter-electrode distance d when the electric field is kept constant by increasing U proportionally with d (from von Engel, 1993, Fig. 89).

The experimental setup illustrated in Figure 2.3 (a) has been used in early quantitative experimental studies of electron impact ionization in a gases. Irradiation of the cathode with UV light releases electrons due to the photoelectric effect. When an appropriate voltage is applied so that the device is operated in the ion saturation mode, the value of the photoelectric current i_0 can be determined. This is the initial current before gas multiplication. When the voltage is increased further, Townsend avalanches come into play and the measured current i is larger than the initial current i_0. In a uniform electric field the ionization coefficient α is constant. Given the same pressure and electric field, the gain of this gas amplification G defined as the multiplication ratio of the current is given by:

$$G = \frac{i}{i_0} = e^{\alpha d} \tag{2.8}$$

where d is the separation between the parallel electrodes. An example of the dependence of the multiplication ratio on the inter-electrode distance d for a constant field E_0 in air at 5.2 hPa is shown in Figure 2.3 (b). The ratio i/i_0 gives a straight line in a

semi-logarithmic plot with d less than 0.5 cm when the electric field is kept constant by increasing U proportionally with d. The value of α can be determined from the slope of the line.

As illustrated in Figure 2.3 (b), the multiplication ratio i/i_0 obeys the exponential law only up to a certain value of d (0.6 cm in the given case) in a constant electric field E_0. Beyond this value the current increases faster than exponentially with the voltage $E_0 d$ (or d as shown in the figure). The sharp rise of the curve is due to secondary effects. In the avalanche processes, positive ions, photons and metastable molecules are created simultaneously besides free electrons. These ions drift toward the cathode, neutralize there, and then return to the gas volume. The bombardment of these particles on the cathode leads to the release of secondary electrons into the gas. The effective secondary emission coefficient γ, defined as the number of electrons liberated by one positive ion, ranges from 10^{-6} to 10^{-2} depending on the cathode material and the nature of the gas. When the voltage across the gap ($E_0 d$) is small, the number of ions created in avalanches is small and the probability of releasing secondary electrons is negligible. The ions can be considered as charge carriers and their interaction with the cathode corresponds solely to neutralization. However, at higher voltage (larger d in the same electric field), secondary electrons cannot be neglected any more. For simplicity, we suppose that the secondary electrons are liberated through the impact of positive ions on the cathode. The cycle consisting of the Townsend avalanche (α process) and secondary emission of electrons (γ process) is illustrated in Figure 2.4. Starting with a seed electron introduced by ionization in the gas due to the incident radiation (Figure 2.4 a), $(e^{\alpha d} - 1)$ ions are produced as the avalanche ends with the absorption of the free electrons by the anode (Figure 2.4 b). After that, the ions drift to the cathode (Figure 2.4 c). The $\gamma(e^{\alpha d} - 1)$ secondary electrons enter the gas and serve as seed electrons for the next cycle (Figure 2.4 d). As the cycle goes on indefinitely, the sum of all electrons entering the anode for one seed electron is thus

$$e^{\alpha d}(1 + z + z^2 + \cdots) = \frac{e^{\alpha d}}{1 - z} \tag{2.9}$$

where $z = \gamma(e^{\alpha d} - 1)$. Therefore the multiplication ratio including the secondary effects on the cathode is:

$$\frac{i}{i_0} = \frac{e^{\alpha d}}{1 - \gamma(e^{\alpha d} - 1)} \tag{2.10}$$

which is verified by analysis of the curved part of the plot with the value of α determined from the slope of the linear part of the same plot in Figure 2.3 (b).

2.2 Self-sustained DC discharge

2.2.1 Electric breakdown and Townsend Discharge

Obviously, Eq. 2.10 breaks down when $\gamma(e^{\alpha d} - 1)$ is unity, indicating some kind of qualitative change of the phenomena. The transition of the discharge from a state sustained by the incident radiation to a self-sustained state is referred to as the electric breakdown of the gas. It results from the interplay between the primary process (Townsend avalanche, or α process) and the secondary electron emission at the cathode under the bombardment of the incident ions (γ process). The breakdown voltage U_b of a gas between two
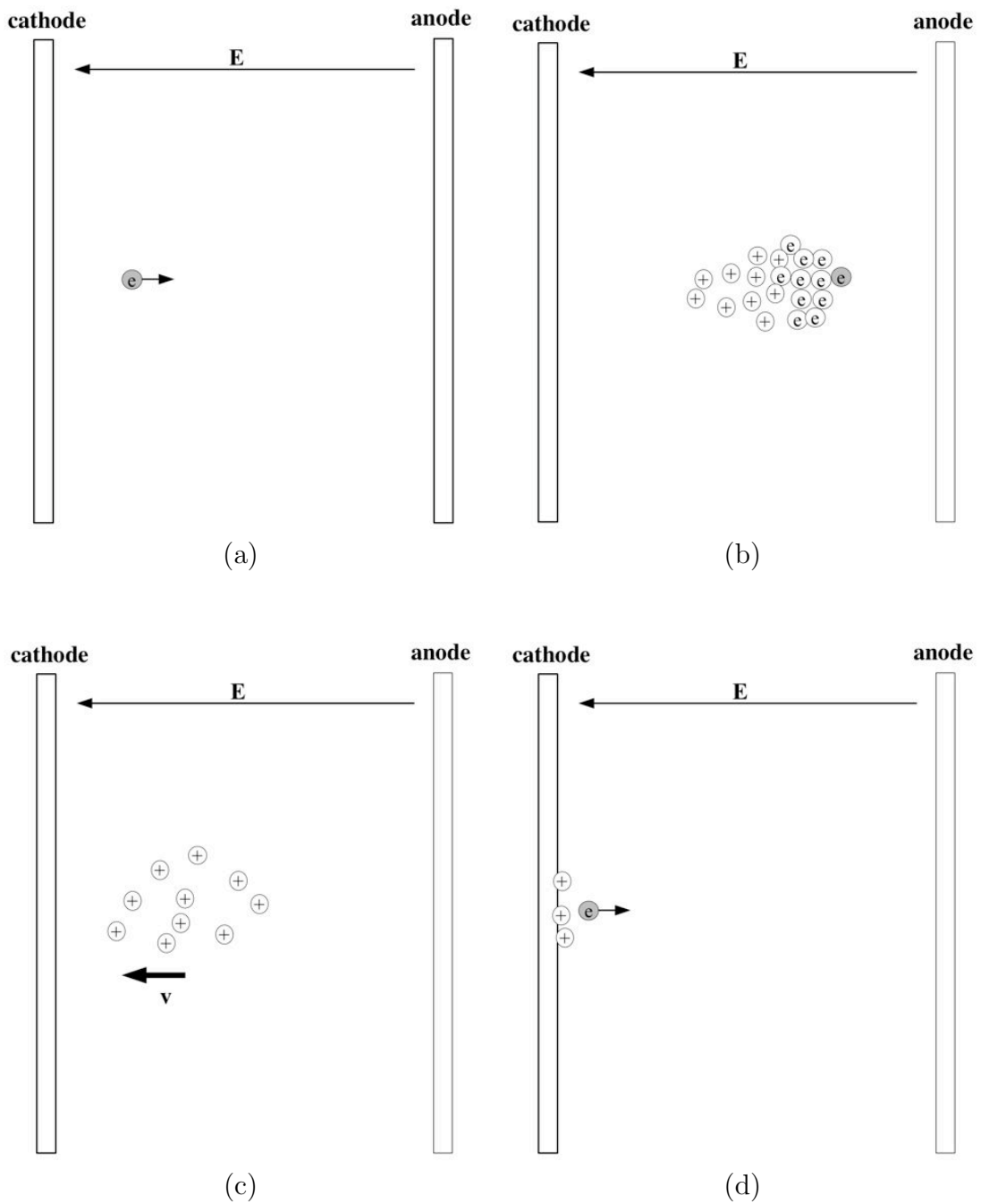
Figure 2.4: Schematic diagram illustrating the temporal sequence of a multiplication cycle consisting of the Townsend avalanche and secondary effect (i.e. the emission of electrons from the cathode under the bombardment of energetic ions).

parallel electrodes can be determined experimentally by increasing the applied voltage to a point where the discharge is self-sustained after turning off the UV illumination on the cathode. The physical meaning of the self-sustaining condition of the current, $\gamma(e^{\alpha d} - 1) = 1$, is that a sufficient number of ions must be produced in the avalanche induced by a seed electron so that at least one electron is liberated from the cathode to replace the seed electron. If one substitutes the ionization coefficient α with the help of the semi-empirical relation, the Paschen's law is obtained, which gives the breakdown voltage U_b as a function of pd.

$$U_b = \frac{Bpd}{C + ln(pd)} \quad \text{with} \quad C = ln\frac{A}{ln(1 + 1/\gamma)} \tag{2.11}$$
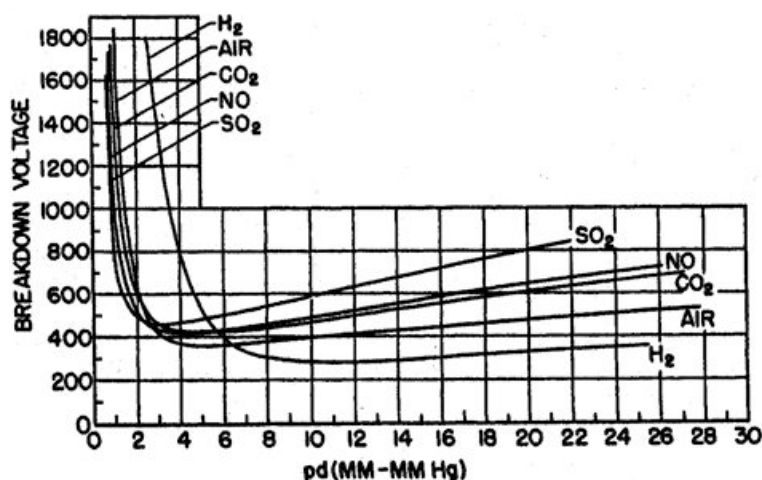
Figure 2.5: Paschen curves for various gases. (from Brown, 1993, Fig. 11.33).

Examples of typical Paschen curves for various gases are shown in Figure 2.5. With decreasing pd, the breakdown voltage decreases, reaches a minimum, and then rises rapidly. The minimal breakdown voltage can be understood in the following way: At very low pd, most of the electrons impinge on the anode after relatively few ionizations because the mean free paths are large (proportional to the inverse of p) and the number of gas molecules in the gap is not very high (proportional to pd). In order to have a sufficiently large number of ionizations to satisfy the self-sustaining condition, the voltage U_b must be larger. At very high pd values, however, the mean free path is small and few electrons acquire sufficient energy over the distance of a mean free path to ionize the gas molecules. Consequently, in order to produce enough ionizations in the gap, the voltage U_b must be higher for gases at very high pressures. Therefore the minimum of the Paschen curve corresponds to an optimal pd for ionizations in the gas.

The steady state of the gas discharge in a uniform electric field based on the α-γ mechanism is called Townsend discharge. As mentioned earlier, the structure of the avalanches shows that most of the ionizations occur very close to the anode, i.e. half of the ionizations occur in the last mean free path of the electron before it is collected by the anode. Therefore, the electrons enter the anode immediately while the ions, which have a significantly lower mobility, drift slowly to the cathode. The whole volume between the electrodes is thus positively charged. At very low current density the distortion of

26

the electric field due to space charge is negligible. As a result of the very low current density the light emitted from the gas is normally too weak to be seen with the unaided eyes. This form of discharge is therefore also known historically as dark discharge.

When the current density is sufficiently high, the space charges start to play an important role. It reduces the field near the anode and enhances the field near the cathode. The steady Townsend discharge becomes unstable. An upper limit of the current density j_c of the stable Townsend discharge is given by:

$$j_c = \frac{\mu_+ U_b^2}{8\pi d^3} \tag{2.12}$$

where μ_+ is the mobility of the ions, U_b the maintaining voltage of the Townsend discharge across the gas gap and d the inter-electrode spacing.

2.2.2 Glow Discharge

Glow discharge is a steady state of the discharge sustained by the secondary electron emission of a cold cathode under the bombardment of energetic ions. In contrast to the Townsend discharge, the current density is significantly higher and a space charge layer in front of the cathode plays a vital role to sustain the discharge. Historically, glow discharge has been studied in long tubes (tens of centimeter in length) filled with gases at pressures of a few hPa driven with a DC voltage source. The most prominent feature of glow discharge in a discharge tube is the well-defined dark and luminous layers filling the space between the electrodes. As illustrated in Figure 2.6, the following layers caused by the light emission from the discharge are found with increasing distance from the electrode: Aston dark space, cathode glow, cathode dark space, negative glow, Faraday dark space, positive column, anode dark space and anode glow. The distribution of potential is shown in Figure 2.6 b. The potential rises rapidly with increasing distance from the cathode, then increases gently in the positive column with another rapid increase in the region close to the anode. The large potential drop between the negative glow and the cathode is called cathode fall V_C. Similarly, the anode fall V_A is formed in front of the anode as a result of the buildup of negative space charge because the electrons are attracted and the positive ions are repelled by the anode. Note that a significant part of the potential drop between the electrodes is the cathode fall. The cathode fall is a result of the accumulation of a positive ions in this region (Figure 2.6 e and f). The electric field at the cathode (Figure 2.6 c) is strong and ions are accelerated toward the cathode and secondary electrons released from the cathode induce avalanches in the cathode fall region, giving the density profile for electrons and ions illustrated in Figure 2.6 (e). Whereas the cathode fall region is essential for a stable glow discharge, the positive column is not. When the inter-electrode distance is not too large, the positive column may be absent. However, when there is no sufficient distance for the formation of the cathode fall, glow discharge cannot be started. In the positive column, the electric field is constant and the concentration of electrons at any point is equal to that of positive ions (Figure 2.6 c and e). This is a typical weakly ionized non-equilibrium plasma. The ionic current dominates in the cathode fall region while in the positive column the electrons carry practically all the discharge current because of their large mobility (Figure 2.6 d).

A qualitative physical picture of the interaction between electrons and gas molecules explains the structure of the light emission. An electron usually starts at the cathode
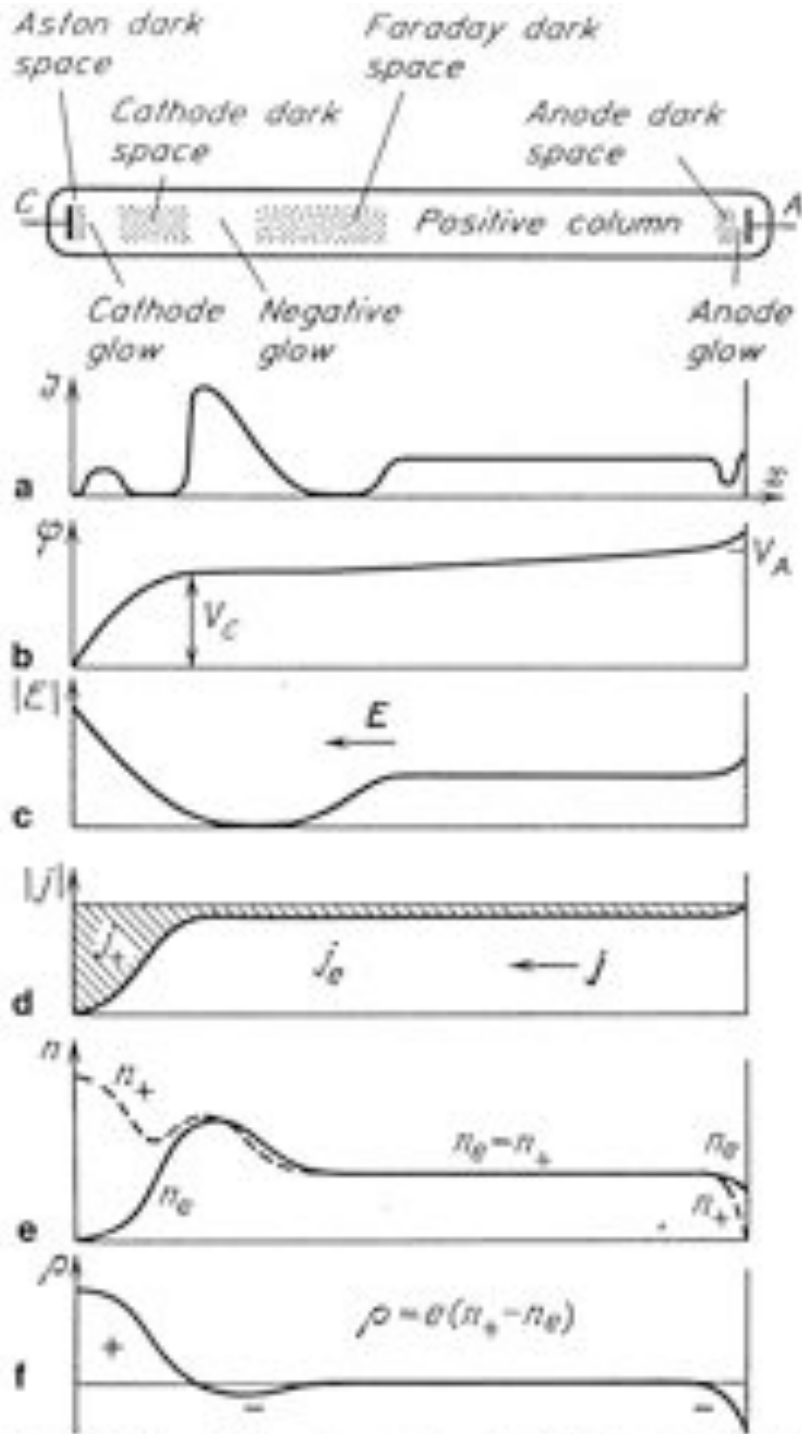
Figure 2.6: Schematic illustration of the typical distribution in a glow discharge of light emission (a), potential (b), electric field (c), current densities j_+ and j_e (d), charge density n_+ and n_e (e), and space charge density ρ (f). (from Raizer, 1991, Fig. 8.2).

with a very small initial energy of the order of 1 eV, and is not able to excite gas molecules before its energy reaches the excitation potential. This results in the formation of the Aston dark space. The cathode glow is due to the fact that the electron acquires an energy corresponding to the maxima of the excitation functions. Further from the cathode most electrons have energies well above the maximum of the excitation functions and little visible light is thus emitted from the cathode dark space. At the negative glow boundary the number of electrons which have energies below the ionization maximum but above or at the excitation maximum has become very large. The negative glow is produced by the many collisions leading to excitations. Afterwards the energy of the electrons becomes sufficiently small for recombination with positive ions to occur in and beyond the negative glow region since the concentration of ions and electrons in that region is large and the electric field is low. With increasing distance from the boundary fewer fast electrons are found and less visible light is emitted. The field increases slowly, the probability of recombination decreases, and the Faraday dark space develops. In the uniform positive column a small part of the energetic electrons generate the luminescence in the plasma. Electrons emerging from the positive column entering the anode fall region with a small initial energy are accelerated towards the anode. After having crossed the anode dark space they have acquired sufficient energy to excite and ionize the gas in front of the anode. The anode is therefore covered with a luminous sheath: the anode glow.

In the case of normal glow discharges, the negative glow does not cover the entire surface of the cathode. As the current is varied over a range of two or three orders of magnitude, the voltage drop across the gas is constant and the area of the cathode covered by the glow increases proportionally to the current. The constant current density is called normal current density. A theory similar to the α-γ theory of the dark discharge describes the self-sustained generation of charge carriers in the cathode fall region. The predicted values of the normal cathode fall and normal current density have the same order of magnitude as the experimental ones. When the current is increased up to the point where the entire surface of the cathode is covered by the glow, a further increase in current can only be achieved by an increase in current density and thus also of the cathode fall. This is the so-called abnormal glow discharge characterized by a larger cathode fall. In contrast, if the current is decreased such that the area covered by the glow has a diameter of the order of the thickness of the cathode fall, the loss of charge due to the radial diffusion and attachment to the walls becomes significant. Consequently, a larger cathode fall is required to sustain a steady glow discharge. This is the sub-normal glow discharge.

2.2.3   Arc discharge

Compared to glow discharge, arc discharge is a kind of discharge with a significantly higher current density at the cathode but a rather lower cathode fall. In the arc discharge, electrons are released from the cathode through mechanisms other than γ-process, e.g. thermionic emission or field emission etc. In the case of tungsten or carbon arcs, the cathode is heated to above 2000 K either externally or by the discharge itself so that the thermionic emission is sufficiently high to sustain the arc. In contrast, in mercury arcs the electrons are liberated from the cathode by the high field strength at the surface due

to the space charge.

As the experiments described in the present work are not in the regime of arc discharge, a detailed discussion of its properties is not included here and we refer to the textbooks by von Engel (1993) and Raizer (1991) instead.

2.3 Summary
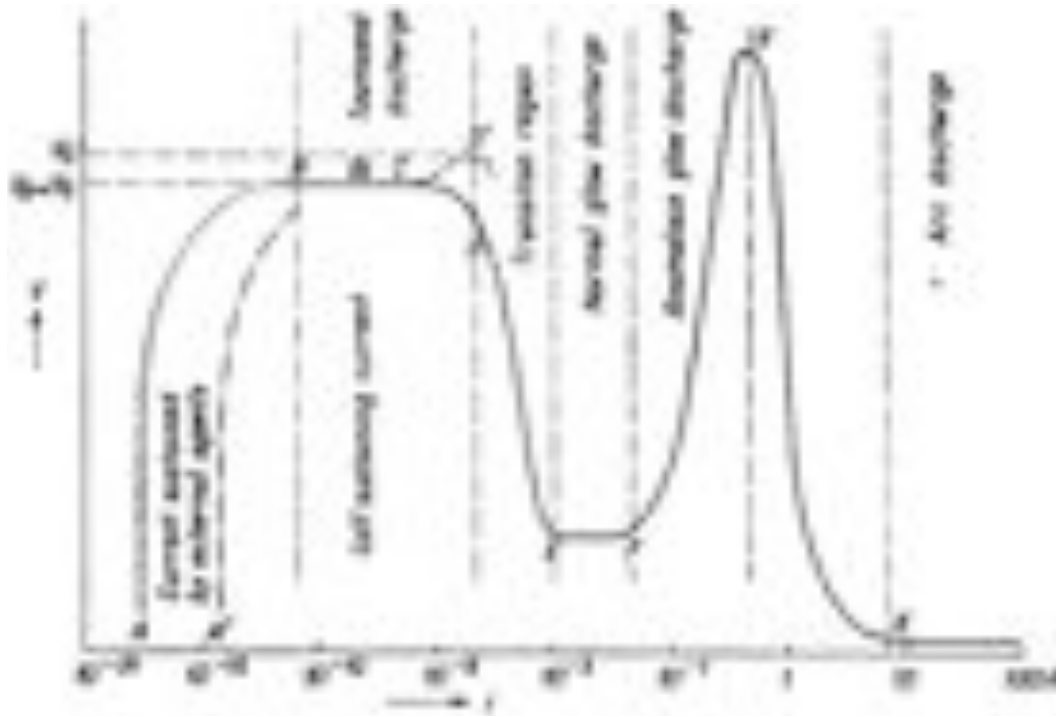
Figure 2.7: Schematic voltage-current characteristic of a gas discharge between two parallel plates (from Druyvesteyn and Penning, 1940, Fig.1).

The schematic voltage-current characteristic of the gas discharge given in Figure 2.7 illustrates the classification of the phenomena occuring in ionized gases between two parallel plate electrodes connected to a constant voltage source. The gas-filled detectors, i.e. ionization chambers, proportional counters and Geiger-Müller counters, function in the region where the current flow in the gas is sustained by the incident radiation. Two types of self-sustained discharges relevant to the present work, Townsend discharge and glow discharge, are briefly discussed. The Townsend discharge is characterized by the constant sustaining voltage which is independent of the current over a range of several orders of magnitude. The transition region from Townsend discharge to glow discharge accompanies the rearrangement of the electric field in the gas and is not always steady. Depending on the experimental parameters of the gas and the properties of the external circuit, the current is sometimes oscillatory during the buildup of the positive space charge layer which is essential for glow discharge. In the case of a steady transition, the current-voltage characteristics shows a negative differential resistance. A further increase of the current lead to the regime of glow discharge, first normal glow discharge

and then abnormal glow discharge. With even higher current, a glow to arc transition finally occurs and an arc discharge is obtained.

Chapter 3

Self-organized structures in direct current gas discharge systems

Gas discharge (e.g. lightning) has been a familiar experience for humans since ancient times. Electric sparks and glow discharge, among other forms of discharge, were only studied in laboratories since the middle of the 18th century. It was noticed by G. C. Lichtenberg that the discharge induced by a sharp conducting electrode close to a dielectric plane created intricate patterns on the surface of the dielectric which could be visualized by dust particles (1777). Lichtenberg was probably the first to relate discharge with the creation of nontrivial structures. These fractal patterns are nowadays known as Lichtenberg figures.

Glow discharge has been traditionally studied in long tubes, typically tens of cm long, filled with gases at pressures below 1 hPa. In such systems, various regions can be defined along the axis of the tube, i.e. the cathode layer, the positive column and the anode layer. At the very early stage of the research on gas discharge, it was found by M. Faraday that under certain conditions the positive column of a glow discharge consisted of a series of stationary or traveling luminous and dark zones (striations). This is now described in almost every textbooks on gas discharge physics (e.g. section 43 in Francis, 1956, etc.). The dynamics of such structures and the nature of the bifurcation were recently studied by Ammelt et al. (1992) with the help of fast cameras. Self-organization in the glow discharge close to electrodes gives rise to ordered patterns consisting of luminous spots. Experimental results on cathode spots (Moselhy and Schoenbach, 2004) and anode spots (Müller, 1988) are summarized in the following section.

As the emphasis of the present work is on the ordered patterns, a discussion on spots in arc discharge will not be included because they do not have a regular shape, nor form ordered patterns. For more about arc spots, we refer to a review by Jüttner (2001). We have also limited our discussion to the formation of ordered patterns in the direction transversal to the current flow. In the following, an extensive review on pattern formation in gas discharge systems is given. The works were done in gas discharge systems with rather large aspect ratio, i.e. the lateral extension of the electrode was larger than the inter-electrode distance by an order of magnitude.
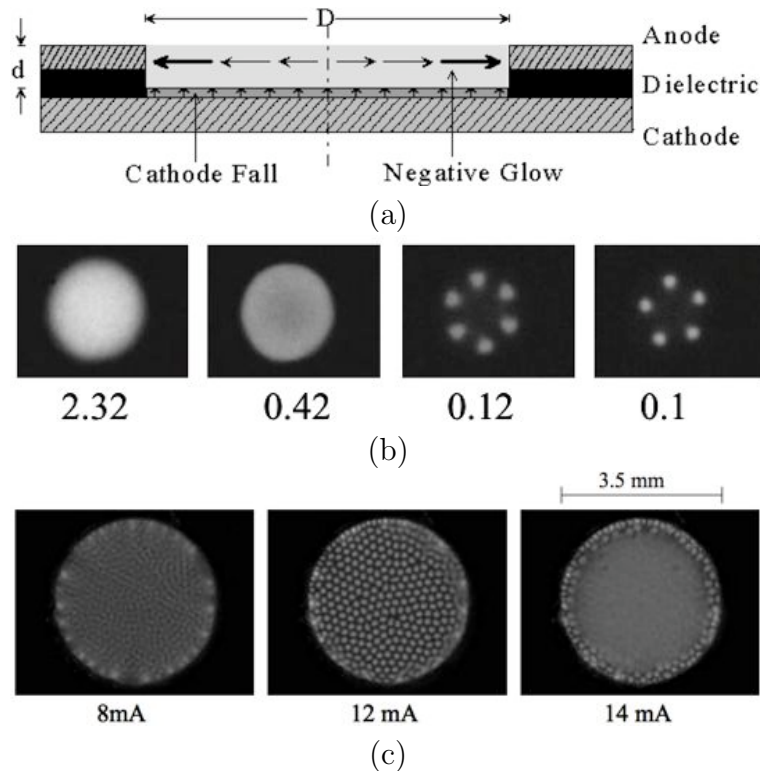
Figure 3.1: (a) Experimental setup of the cathode boundary layer discharge (from Moselhy and Schoenbach, 2004, Fig. 1); (b) Filamentation and self-organization of the filaments in a xenon discharge at 100 hPa with an opening of 0.7 mm diameter (from Moselhy and Schoenbach, 2004, Fig. 3); (c) End-on images of the discharge with a larger opening (3.5 mm diameter) at 266 hPa (Courtesy of K. H. Schoenbach, Old Dominion University, Norfolk, USA).

3.1 Gas discharge systems with conductive electrodes

Filamentation and regular distribution of the filaments in a special kind of glow discharge (which is referred to as cathode boundary layer discharge by the authors) were observed by Moselhy and Schoenbach (2004) during their study of excimer emission from xenon discharges. As illustrated in Figure 3.1 (a), the electrodes used in their work consist of a planar cathode (molybdenum) and a ring-shaped anode separated by a 250 μm thick dielectric (alumina). The diameter of the opening of the anode and dielectric is about 0.75 mm. The discharge chamber is filled with Xe at pressures between 100 and 1010 hPa. The glow discharge operated with such an electrode configuration shows only the cathode fall and the negative glow, which serves as a virtual conductive layer carrying the current from the ring-shaped anode to the cathode fall. A CCD camera in combination with a microscope lens was used to record the end-on images of the discharge. The images of the discharge at different currents for a pressure of 100 hPa were given in Figure 3.1 (b). The abnormal glow discharge is uniform and covers the entire surface of the cathode when the current is high. At 100 hPa, the discharge takes a form of diffuse spots symmetrically distributed in the active area when the current is reduced to 0.12 mA. A further reduction of the current to 0.1 mA leads to not only a change of the spot configuration, but also of its appearance. The boundary of the spots

changes from diffuse to more distinct and the spots have a well-defined diameter between 80 and 100 μm. The current density in the spot is approximately 0.3 A/cm^2. It was noticed by Takano and Schoenbach (2006) that the self-organization and filamentation occurred only when molybdenum or tungsten cathodes and high purity xenon (no less than 99.999%) were used. In contrast, such behaviors were absent when copper cathodes or argon were used. This observation leads to the assumption that the electron emission processes at the cathode play an important role in the filamentation process. One of the possible mechanisms is the enhanced photo-emission of electrons from the cathode due to the increased excimer formation accompanying the transition from homogeneous to filamentary glow. However, thermal instability associated with changes of gas density as a result of gas heating cannot be excluded. Although the mechanism of filament formation is still an unresolved issue, their spatial distribution can be well explained by a balance of Coulomb forces among the filaments and the positively charged surface of the surrounding dielectric spacer (Takano and Schoenbach, 2006). As illustrated in images recorded in a 266 hPa xenon discharge (Figure 3.1 c), patterns consisting of a large number of filaments were observed with a larger diameter of the anode opening (3.5 mm) when the current was gradually decreased.. At pressures higher than 532 hPa, the self-organization is less pronounced and the patterns lose symmetry when the current is lowered (Moselhy and Schoenbach, 2004).
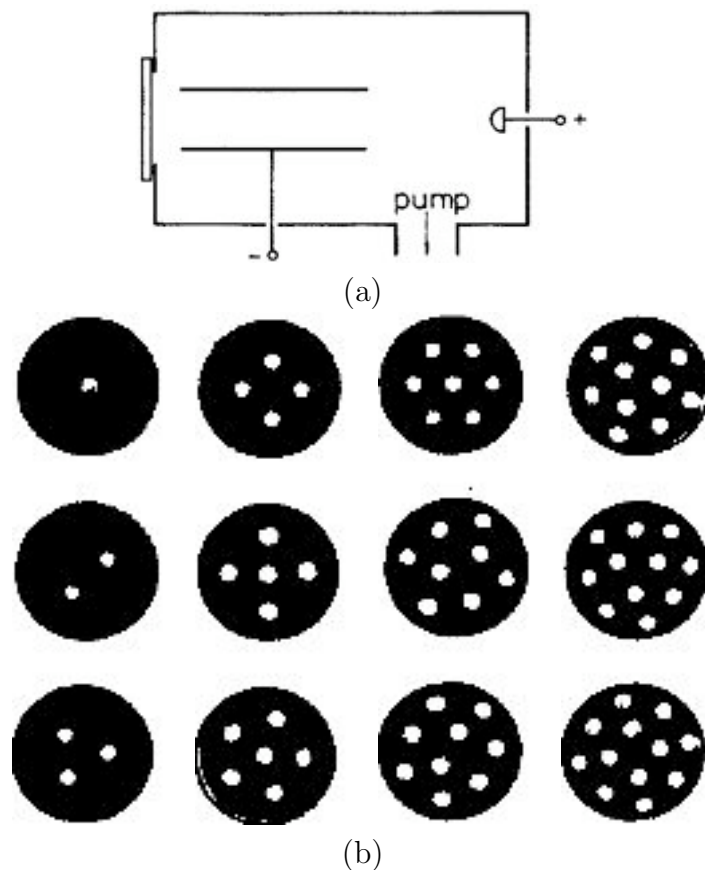

(a)

(b)

Figure 3.2: (a) Schematic experimental setup for studying anode spots; (b) Examples of self-organization of anode spots. (Müller, 1988).

Besides the observation of self-organization in the cathode region of the glow dis-

charge, regular patterns of spots close to the anode were also obtained (Müller, 1988). The experimental setup for studying anode spots (illustrated in Figure 3.2 a) consists of a hemispherical anode with a diameter of 1.5 cm and a cylindrical cathode (4 cm inner diameter and 12 cm in length). The chamber is filled with 10 hPa H_2 and the images of the discharge close to the anode is recorded side-on through the window in front of the cathode. When a glow discharge is established between the cylindrical cathode and the anode, symmetrical patterns of bright spots were observed on the background of a faint anode glow (Figure 3.2 b). According to the model proposed by Müller (1988), the existence of such kind of spot can be attributed to the typical S-shaped voltage-current characteristics of the bistable layers close to the electrodes, i.e. the cathode fall region and the anode fall region. The bulk of the glow discharge (i.e. Faraday's dark space and the positive column) can be modeled as a resistive layer. When the bistable layer is in contact with a resistive medium, patterns of spots may occur. The interaction between the spots is repulsive and their stable configuration corresponds to the minima of a generalized potential (or Lyapunov functional).

3.2 Quasi-one-dimensional gas discharge systems with semiconductor anodes

Before discussing self-organization in DC discharge systems with resistive electrodes, it is helpful to mention the original work on electrical networks of coupled nonlinear oscillators which motivates the use of resistive electrodes in gas discharge systems (Berkemeier et al., 1986; Purwins and Radehaus, 1988; Dirksmeyer et al., 1990). The governing equation of the electrical network is a set of two reaction diffusion equations of the activator-inhibitor type studied by Maginu (1975) and Rothe (1979). In a one-dimensional network a periodic structure can be obtained by changing the coupling resistance. The bifurcation from a uniform state to the periodic state is supercritical and the amplitude of the periodic structure has a square root dependence on the distance to the bifurcation point of the control parameter, in this case the coupling resistance. In this system, a quantitative agreement can be achieved between the experimental observations and the numerical simulations of the reaction diffusion models under appropriate parameters (Purwins and Radehaus, 1988). These results motivate the search for a physical system which is the continuum analog of the discrete network. From this perspective, the physical system will consist of two layers, i.e. a linear layer corresponding to the resistive coupling of the network and a nonlinear layer demonstrating a S-shape voltage-current characteristics. A special kind of gas discharge system is thus built by using a resistive semiconductor electrode. At an early stage of investigating such systems, it was found that the discharge took a form of irregular sparks with chaotic spatiotemporal dynamics when a Si cathode and a conductive anode were used (Willebrand et al., 1991b). In the subsequent work, a Cu cathode was used and the Si wafer served as anode.

As shown in Figure 3.3, the experimental system consists of a copper cathode and a silicon anode. The surface of the electrodes (i.e. the edge of a copper plate and that of a Si wafer) is about 30 mm long and 0.3 mm thick. The active volume for gas discharge is defined by the electrodes and two glass plates and is filled with He or Ar mixed with a few percent air. The gas pressure varies between 10 and 250 hPa.The separation of the
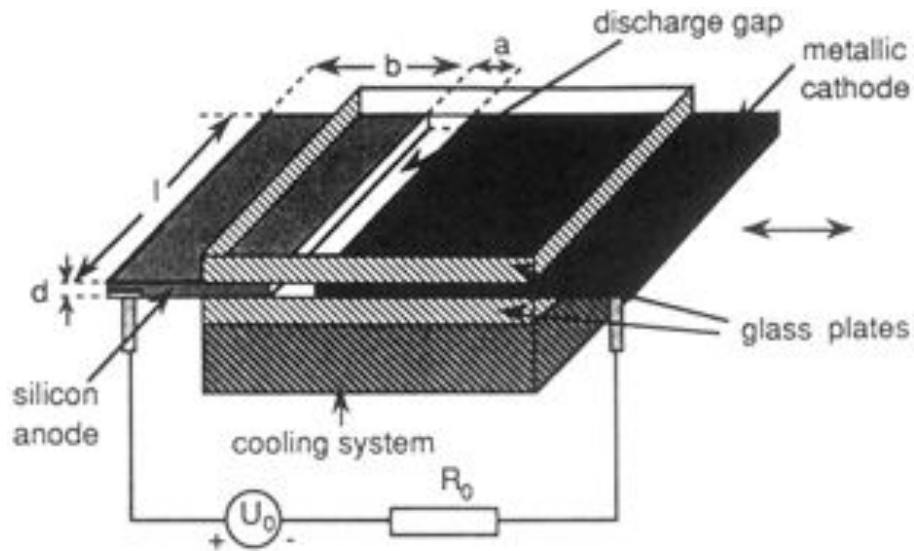
Figure 3.3: Schematic setup of the quasi-one-dimensional gas discharge system with a semiconductor anode (from Willebrand et al., 1992, Fig.1).

electrodes can be adjusted between 0.5 and 6 mm. The resistivity of the Si anode ranges from 0.5 to 2.6 kΩ·cm. A water cooling system is coupled with the lower glass plate to sink the heat produced by the discharge. The visible light emitted from the discharge can be observed through the upper glass plate.
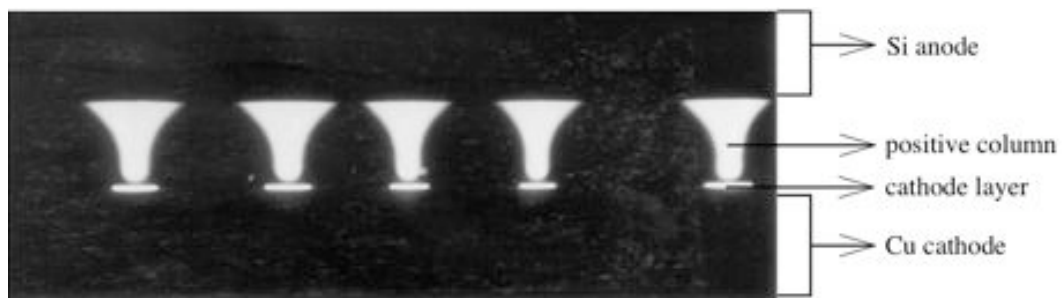
Figure 3.4: Current filaments in the quasi-one-dimensional gas discharge system with a Si anode and a Cu cathode. Experimental parameters: resistivity of Si $\rho = 1.5$ kΩ·cm; serial resistor $R_0 = 164$ kΩ; $U_0 = 750$ V; gas gap d = 3.8 mm; 170 hPa mixture of 80% Ar and 20 % air. (Willebrand, 1992).

Given the above discharge parameters, glow discharge is established when the electrical breakdown of the gas gap occurs. There are two kinds of structures observed in this system: solitary discharge filaments and spatially periodic patterns. A typical form of the discharge filament is illustrated in Figure 3.4 where the typical layer structure of glow discharge can be observed. The thin bright region close to the Cu cathode is the cathode layer which includes the Aston dark space, cathode glow, cathode dark space and negative glow (see section 2.2.2 for more about glow discharge). The cathode layer is separated from the positive column by the Faraday dark space. The end of the positive column spreads a bit on the surface of the Si anode , which gives the funnel shape of the

positive column. The discharge filaments are considered to be solitary structures due to their characteristics: First, they are of the same size and each carry the same amount of current, which is supported by the linear relation between the total current and the number of filaments (see Willebrand et al., 1990, Fig. 9). Secondly, the shape of the filament is preserved after different kinds of interactions, e.g. reflection by the boundary and elastic collisions between filaments etc. The number of discharge filaments obtained in the gap increases with the source voltage U_0.
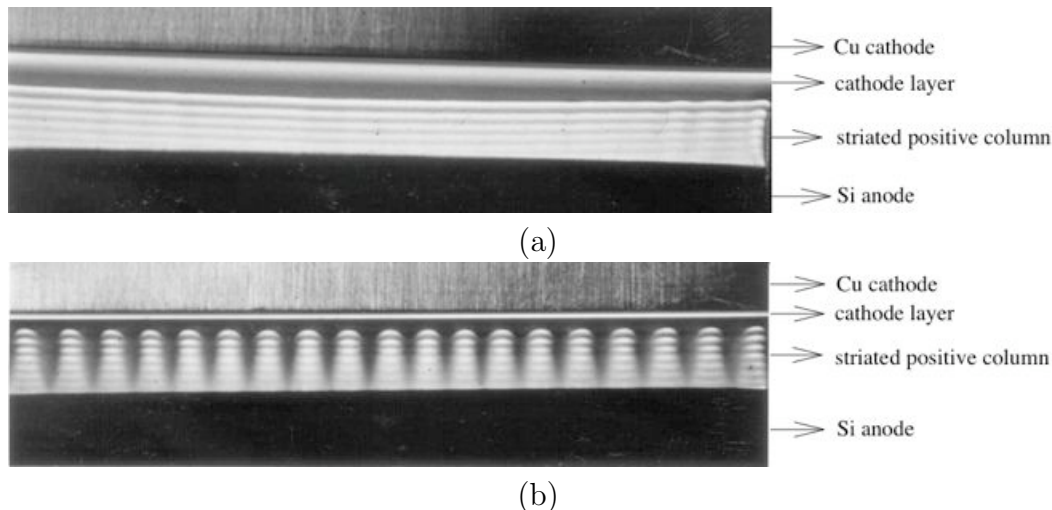

(a)

(b)

Figure 3.5: (a) Uniform state of the glow discharge in the direction perpendicular to the applied field at $U_0 = 1500$ V; (b) Periodic structures in the lateral direction at $U_0 = 800$ V. Experimental parameters: resistivity of Si $\rho = 0.9$ kΩ·cm; serial resistor $R_0 = 25$ kΩ; gas gap d = 4.5 mm; 90 hPa He. (Radehaus et al., 1992).

The other type of structures in the lateral direction are spatially periodic patterns. As a comparison the homogeneous state of the glow discharge is given in Figure 3.5 (a). The typical features of the glow discharge is evident here, there is a homogeneous cathode layer in front of the Cu cathode. The positive column contains striations in the direction of the current flow and is uniform perpendicular to the applied field. As the control parameter is varied, a periodic modulation of the positive column in the lateral direction is observed (Figure 3.5 b). The cathode layer, however, stays uniform. As the distribution of the luminosity in the lateral direction is of our interest, a single line of the signal from the video camera which is parallel to the electrode surface and cuts the positive column of the glow discharge, is recorded with an digital storage oscilloscope for further data analysis.

3.2.1 Filamentary structures

In the normal glow discharge obtained in systems with conductive metal electrodes, the area covered by the discharge increases with the total current and the current density thus remains constant. In that case, only a single filament exists and its extension is variable. In contrast, in the system with a semiconductor anode described above, the increase of the total current does not lead to the expansion of the discharge filament in size, but to a multiplication of the filaments. In the early work by Radehaus et al.
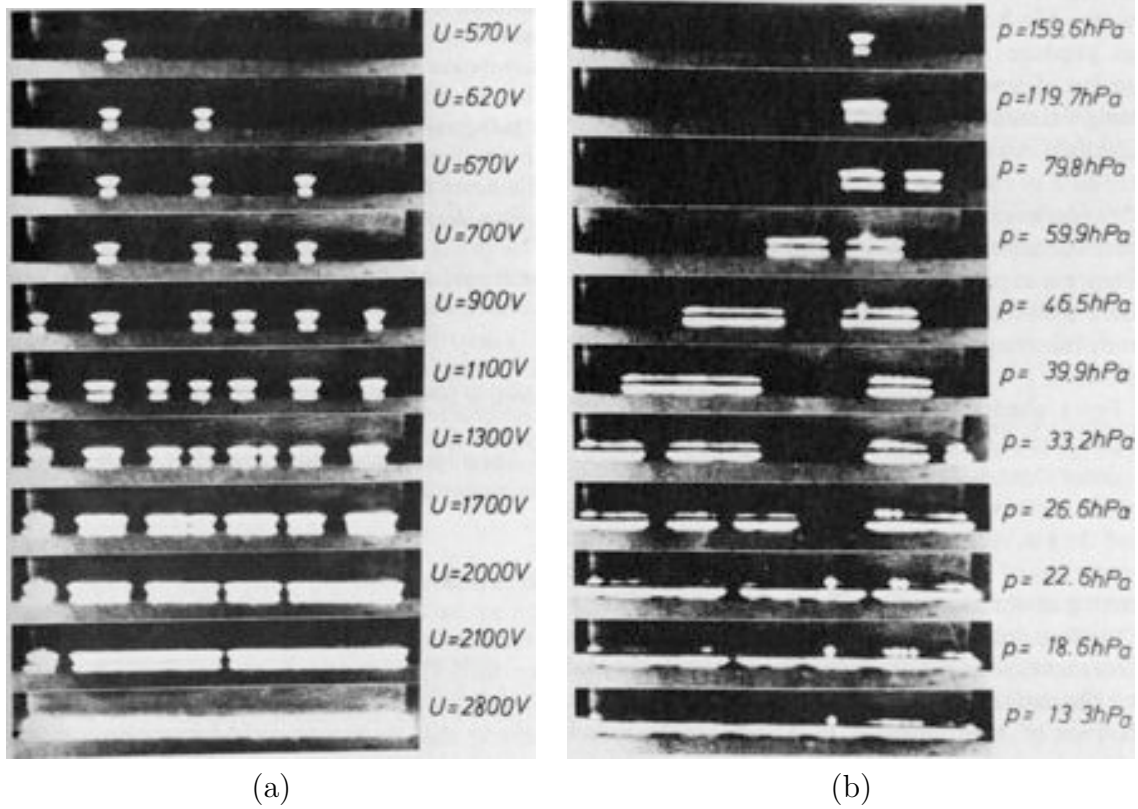
(a)   (b)

Figure 3.6: (a) Evolution of the current filaments in glow discharges using a Si anode and a mixture of 144 hPa He and 16 hPa air with increasing source voltage; (b) Evolution of the filaments with decreasing pressure at a constant source voltage. Experimental parameters: specific resistivity of Si $\rho = 1.6$ kΩ·cm; serial resistor $R_0 = 82$ kΩ; gas gap d = 1.5 mm; 90% He and 10% air. (Radehaus et al., 1987).

(1987), a Si:Au anode with a resistivity of 1.6 kΩ·cm and a mixture of 90% He and 10% air were used. In this system the control parameters are the source voltage U_0, the gas pressure p and the inter-electrode distance d. The successive creation of new filaments was observed when U_0 reached a certain value. In the example given in Figure 3.6 (a), p and d are 160 hPa and 1.5 mm respectively. The number of filaments increases from 1 to 6 as U_0 is increased from 570 V to 900 V. The size of an individual filaments remains unchanged, indicating the solitary nature of the filamentary structure. At U_0 above 1100 V, the size of the filaments starts to increase and their number continuously increases. Finally all filaments merge together and a homogeneous glow covers the entire surface of the electrodes at 2800 V. When U_0 is kept constant and the pressure is lowered, the total current increase and a broadening of the filaments and the generation of new filaments are observed simultaneously (Figure 3.6 b). The broadening of the filaments is related to the increase of the mean free path of charge carriers as the pressure is decreased.

The typical voltage-current characteristics of the glow discharge in the system with a Si anode is shown in Figure 3.7 (a). The voltage U_v in the figure corresponds to the voltage drop across the discharge cell. There are several branches separated by well-defined jumps in the voltage-current characteristics. The first jump to branch 1 as the source voltage is increased corresponds to the electrical breakdown of the gas gap and
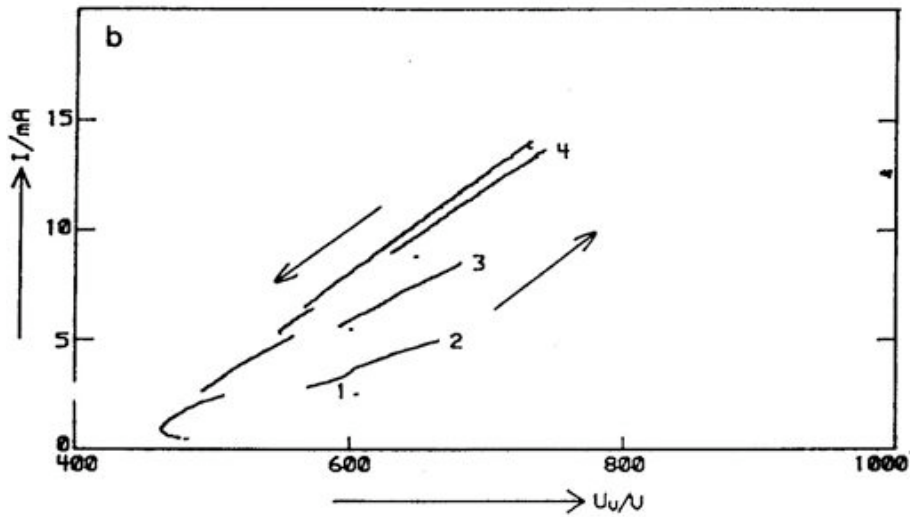
(a)
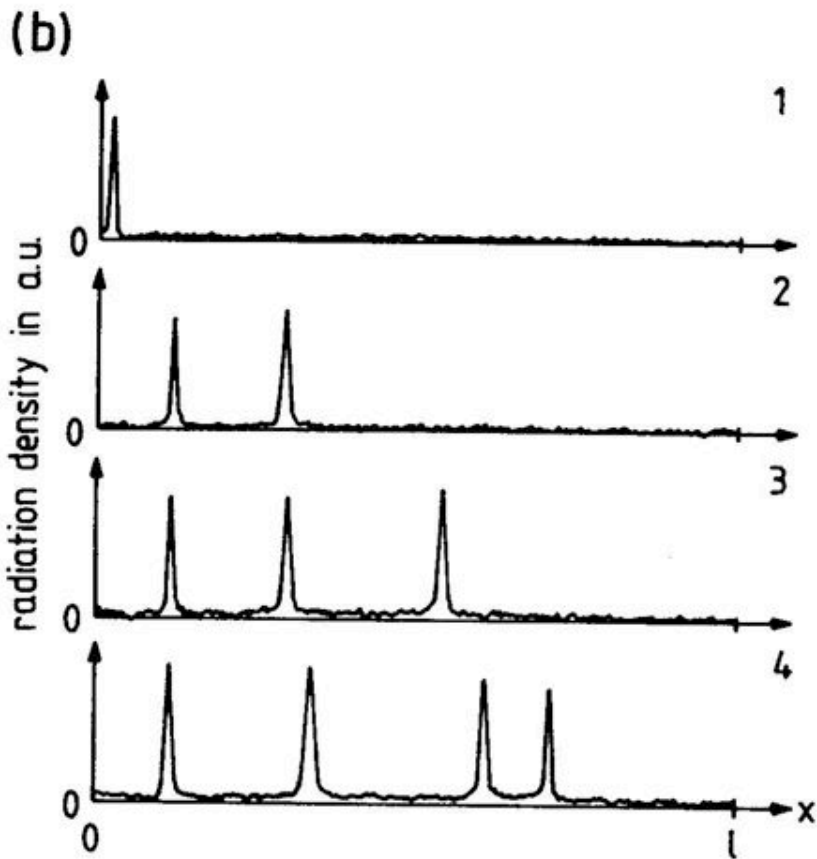
(b)

Figure 3.7: (a) Voltage-current characteristics of the gas discharge with Si anode; (b) Spatial distribution of luminosity of the discharge filaments. Experimental parameters: resistivity of Si $\rho = 0.9$ kΩ·cm; serial resistor $R_0 = 165$ kΩ; gas gap d $= 3$ mm; 144 hPa Ar and 16 hPa air. (from Willebrand et al., 1990, Fig7, Fig8).

a discharge filament is formed. The spatial distribution of the luminosity from the glow discharge corresponding to the four branches in the I-U$_v$ curve is illustrated in 3.7 (b). It is obtained by recording a single line of the video signal from the camera which is parallel to the electrode surface and cuts the positive column of the glowing discharge filaments as illustrated in Figure 3.4. In branch 1 of the I-U$_v$ curve, there is a single filament. Increasing the source voltage further drives the system to jump to branch 2 and the number of current filaments increases. Further increase of the source voltage leads to the jumps to branch 3 and 4 and the filament number increases accordingly. Decreasing the source voltage makes the system follow the four upper branches and the filaments successively disappear. In the case of a smaller shunt resistor R$_0$, which allows a larger total current, more than one filament is created immediately after the breakdown of the gas gap. A linear relationship between the total current and the number of the filament was observed, indicating that each discharge filament carries the same amount of current.
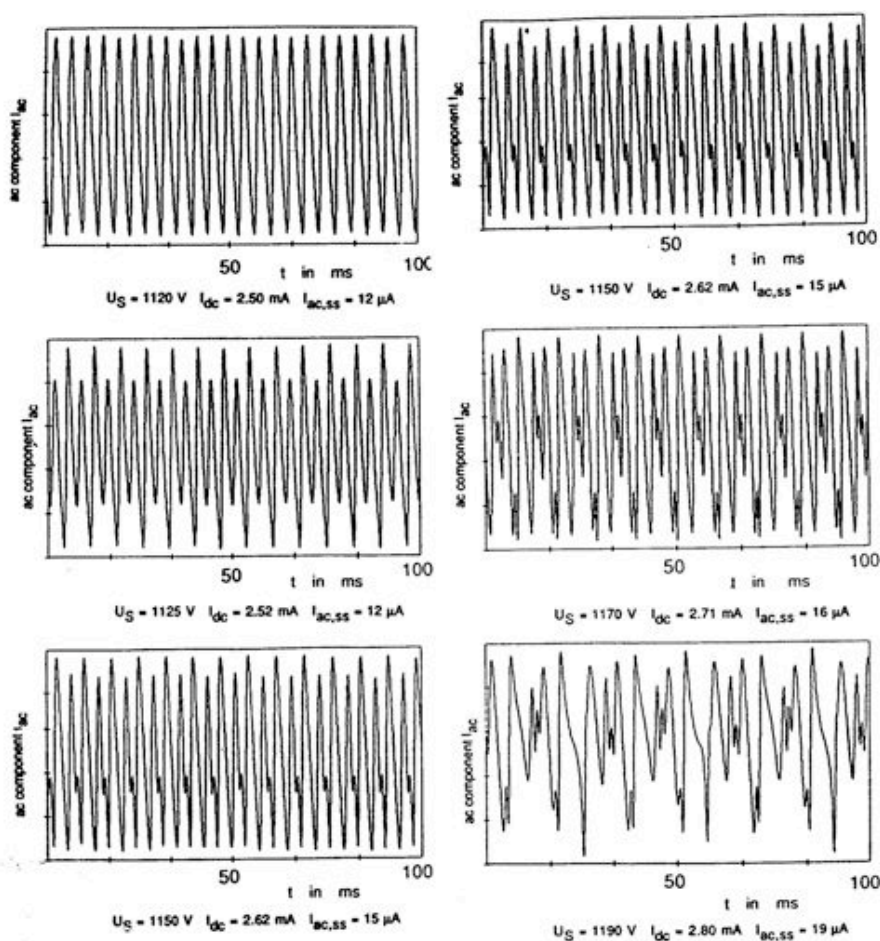

Figure 3.8: Current oscillations of the glow discharge as the source voltage is increased from 1120 to 1190 V. Experimental parameters: resistivity of Si $\rho = 1.7$ kΩ·cm; serial resistor R$_0$ = 150 kΩ; gas gap d = 3.4 mm; 200 hPa mixture of 90% Ar and 10 % air. (Willebrand et al., 1991b).

Once a current filament is established, the discharge is stable and a constant current

flows through the gas gap. This kind of stationary state corresponds to the situation of each branch of the voltage-current characteristics illustrated in Figure 3.7 (a). Temporal oscillations of the current, however, are observed during the generation of a new filament, e.g. in the jump from branch 1 to branch 2 in Figure 3.7 (a). As soon as the new filament is established, the current oscillations disappear and the current becomes constant again. It is found that a new filament is generated via the splitting of one of the existing filaments as the source voltage is increased. The current oscillation and the filament splitting process have been investigated by Willebrand et al. (1991b) in detail. The current oscillation during the transition from a stationary one-filament state to a two-filament state was studied in the discharge with a 3.4 mm gap filled with 200 hPa gas mixture of 90% Ar and 10% air. A transition of the time course of the current oscillation during the splitting of a filament was followed as the source voltage was increased from 1120 to 1190 V (Figure 3.8). At 1120 V, the oscillation is nearly sinusoidal. The frequency is about 233 Hz and the amplitude is 12 μA compared to the average DC component of 2.5 mA. Period doubling is observed for a slight increase of the source voltage (5 V) and the fundamental frequency was 140 Hz. With increasing source voltage, the period doubling process continues. The DC component of the current increases whereas the amplitude of the oscillation remains nearly unchanged. The fundamental frequency is 93 Hz at a source voltage of 1170 V. At 1190 V, the dynamics of the oscillation becomes chaotic. Beyond 1190 V, the current becomes constant and a second filament is formed. Study of the light emission from the discharge during the splitting process with a streak camera indicates that the current oscillation is accompanied by the generation and the extinction of the newly formed filaments. A new filament first branches out from an existing filament at its immediate neighboring region. It exists for a few ms and then disappears. Only at sufficiently high source voltages can the new filament be stable and separate from the old one. When the stable state of multiple filaments is established, a decrease of the source voltage leads to the successive extinction of the filaments. There is no oscillation in the current during this process.

In the case of discharges with Ar (or mixed with air) at pressures above 20 hPa the filaments are stationary and an increase of source voltage leads to an increase in their number. At a pressure between 10 and 20 hPa, interesting dynamics of the filaments, which best illustrates their behavior as solitary structures, is observed within a certain range of current (Willebrand et al., 1992). A typical dynamics of a single filament is illustrated in Figure 3.9. In this example the source voltage is slightly above the breakdown voltage and the breakdown process and the following motion of the discharge filament was recorded with a streak camera during a period 700 μs. The space coordinates 0 and 28 mm correspond to the two lateral boundaries of the discharge gap. At the instant of the breakdown (t $\approx$ 100 μs), two filaments are generated at the two boundaries and moved to the center. After about 70 μs, the one traveling from the upper boundary l = 28 mm extinguishes while the other one moves towards the upper boundary. Then it is reflected by the boundary and moved towards the lower boundary, and then bounces back and forth between the two boundaries. The velocity of the filament is constant, e.g. about 320 m/s at a gas pressure of 19 hPa. It increases to a value above 400 m/s as the pressure decreases to 10 hPa. The behavior of the filament reminds us of its particle-like nature, i.e. the elastic collision with the boundary and the annihilation. There are oscillations in the total current as the filament swept back and forth. The
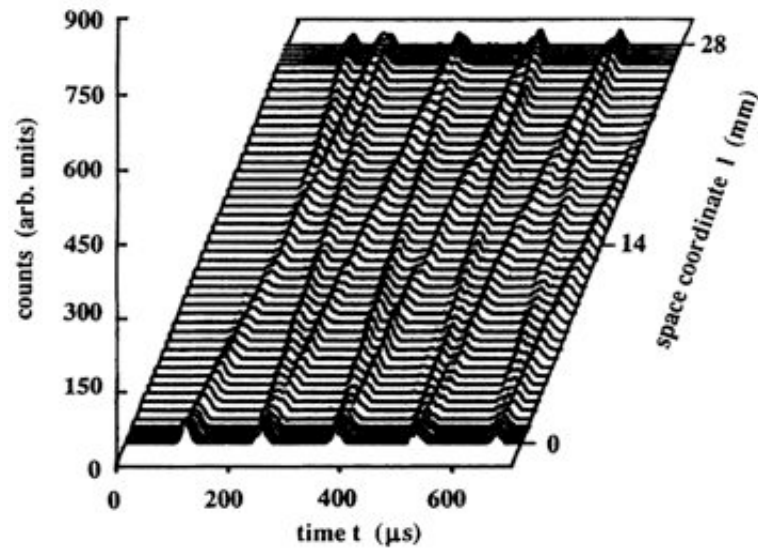
Figure 3.9: Three-dimensional plot of the streak camera images showing a current filament bouncing back and forth between the two rigid boundaries at a source voltage slightly above the breakdown voltage. Experimental parameters: resistivity of Si $\rho = 2.6$ kΩ·cm; serial resistor $R_0 = 1$ MΩ; gas gap d = 3.4 mm; 18 hPa Ar. (from Willebrand et al., 1992, Fig. 4).
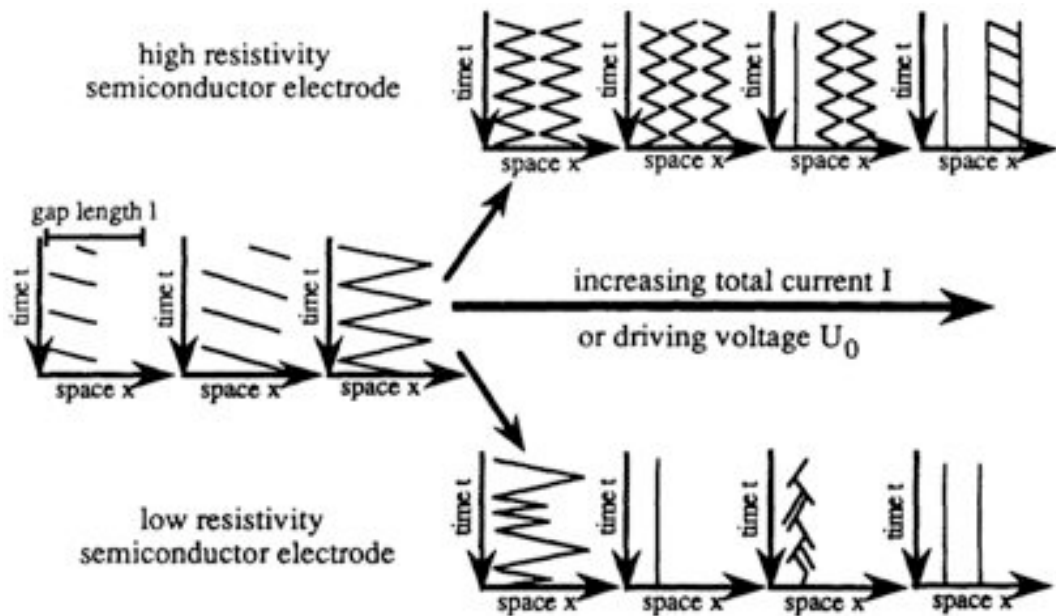
Figure 3.10: Schematic representation of the streak camera images showing the dynamics of the current filaments as the driving voltage is increased. (from Willebrand et al., 1992, Fig. 9).

current always reached a minimum when the filament was reflected at the boundaries.

Two kinds of Si wafers with different resistivity, 0.9 and 2.6 kΩ·cm, were used in the work by Willebrand et al. (1992). In the following, the former is referred to as low-resistivity electrode and the latter as high-resistivity electrode. The schematic streak camera images in Figure 3.10 summarizes the experimental observations. At low average currents the phenomena are the same for both kinds of electrodes. As illustrated in the two left plots in Figure 3.10, a filament is generated at one of the boundary, moves towards the other boundary with constant velocity, but disappears before reaching it. This process is repeated periodically in time. When the average current is sufficiently large, the motion between boundaries can be obtained. In the case of a high resistivity semiconductor, two filaments are obtained as the driving voltage is increased. The filaments move back and forth within a part of the gap at the same velocity. The filament is reflected by elastic collisions with the boundary and with the other filament. A further increase of the driving voltage leads to the generation of a third filament and each one seems to try to claim a part of the gap to move back and forth. However, the dynamics becomes irregular as the collision, generation and annihilation of the filaments occur more frequently. At very high voltages, stationary filaments are observed among the dynamic filaments as illustrated in the two top-right plots in Figure 3.10. When the resistivity of the semiconductor is low, an increase of the driving voltage leads to a decrease of the spatial area occupied by the moving filament. With increasing voltages the filament first becomes stationary and then the typical filament splitting process as described for higher pressures can be observed.

3.2.2 Spatially periodic structures

So far the particle-like behavior of the current filaments observed in the discharge system with Ar is discussed. The transition from a uniform state to a spatially periodic state has been studied in the discharges with He (Willebrand et al., 1990; Radehaus et al., 1992). When the total current of the discharge is sufficiently large, the entire active area is filled with discharge as illustrated in Figure 3.5 (a). This is referred to as a uniform state of the system as the discharge is homogeneous in the lateral direction. Starting from the uniform state, period structures can emerge spontaneously when the current is reduced by decreasing the source voltage, by increasing the serial resistance or by increasing the gap width. The evolution of the lateral structures under the change of various parameters is illustrated in Figure 3.11. In the first experiment, the source voltage is used as the control parameter (Figure 3.11 a). At 1050 V, the spatial distribution of the luminosity of the discharge is nearly homogeneous. A decrease of 25 V leads to the development of ripple structures close to the boundaries whereas the center region remains homogeneous. Reducing the voltage further causes the growth of the wavy regions. At voltages below 942 V, a periodic pattern with a characteristic wave number dominates. When the source voltage is increased at this point, the structure evolves in the reversed way and finally disappears without any evident hysteresis. In the second experiment (Figure 3.11 b), the serial resistor is gradually increased while keeping the source voltage constant. The total current is thus reduced and the periodic structure develops accordingly. In the third experiment (Figure 3.11 c), the gap width is increased continuously while the voltage and serial resistance remains unchanged. In this case, the general features of the transition

44
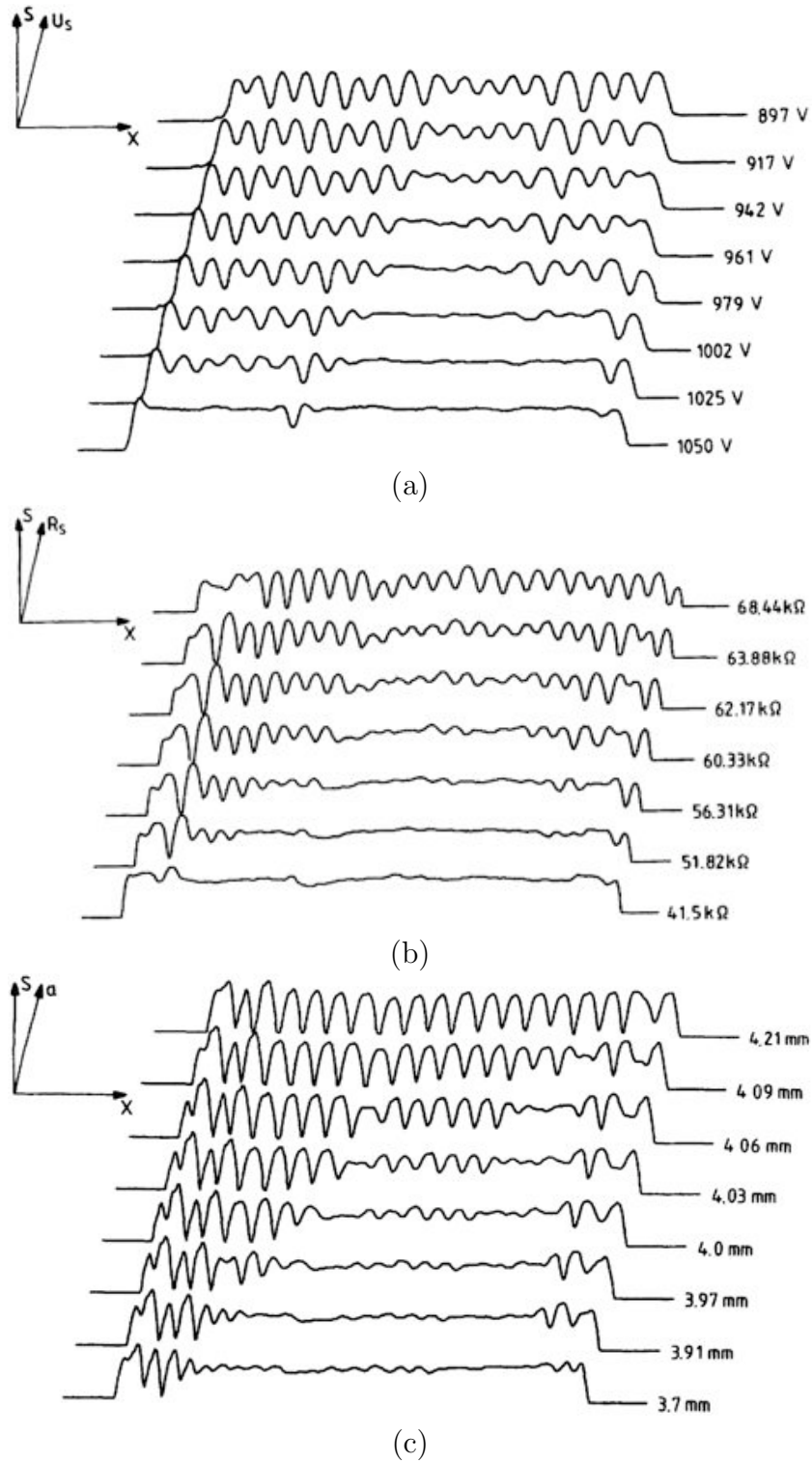
Figure 3.11: Transition from the uniform state to a spatially periodic state in gas discharges with a Si anode ($\rho = 0.53$ kΩ·cm) and 120 hPa He under variation of the source voltage (a), the serial resistance (b) and the gap width (c). Experimental parameters: (a) serial resistor $R_S = 35.2$ kΩ; gap d $= 3$ mm; (b) source voltage $U_S = 1616$ V; gap d $= 3.2$ mm; (c) source voltage $U_S = 1478$ V; serial resistor $R_S = 35.2$ kΩ. (from Radehaus et al., 1992, Fig. 8, 9, 10).

are qualitatively the same as those in the other two experiments. When the gap width is increased beyond 4.21 mm, the discharge enters the filamentary mode. The transition illustrated in these three experiments is characterized by a continuous growth of the spatially periodic modulation of the luminosity distribution. The amplitude of the spatial modulation can be determined from the average value of the difference between the minimum and maximum of the luminosity distribution. The square root dependence of the amplitude on the source voltage in the bifurcation diagram indicates its supercritical nature. This transition corresponds to the case of region b indicated in Figure 3.12.

Figure 3.12: Various kinds of bifurcations on the parameter plane of the gas pressure and the gap width when the uniform state of the discharge is destabilized by decreasing the source voltage. Experimental parameters: resistivity of Si $\rho = 1.5$ kΩ·cm and He. (from Willebrand et al., 1991a, Fig. 4).

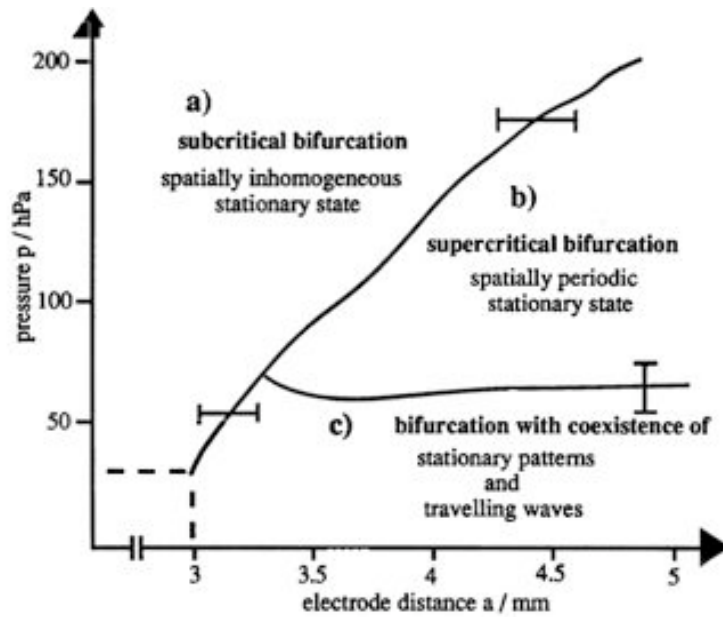As shown in Figure 3.12, besides the supercritical bifurcation, there are two other different bifurcation behaviors. In the parameter range indicated by the region a in Figure 3.12, the transition is accompanied by the abrupt appearance of dark regions out of the uniform bright background when the source voltage is reduced. A continuous decrease of the source voltage leads to the growth of the existing dark region and the formation of new dark regions. Finally a non-homogeneous state consisting of bright filaments separated by dark regions is obtained. However, at lower pressures corresponding to the region c in Figure 3.12, traveling waves are observed during the transition from the homogeneous state to the periodic state with a decreasing source voltage. An example of this kind of transition scenario is illustrated in the image sequence recorded with a streak camera. At a voltage of 2111 V (Figure 3.13 a), the discharge is homogeneous in space and stationary in time. When the voltage is decreased to 1115 V, two regions of traveling waves separated by a small stationary region appear. The waves propagate from the stationary region towards the boundaries of the discharge gap. It is interesting to note that the speed of the propagating wave is different for the two regions. In the left and right regions the velocity is estimated as 1.5 and 3.5 m/s respectively. As the

46

voltage decreases, the velocity of the traveling waves diminishes. At 1086 V, a stationary periodic state is reached for the left part of the discharge gap whereas the right part is still dominated by the traveling waves. The stationary periodic state is finally established when the voltage is reduced to 1032 V.

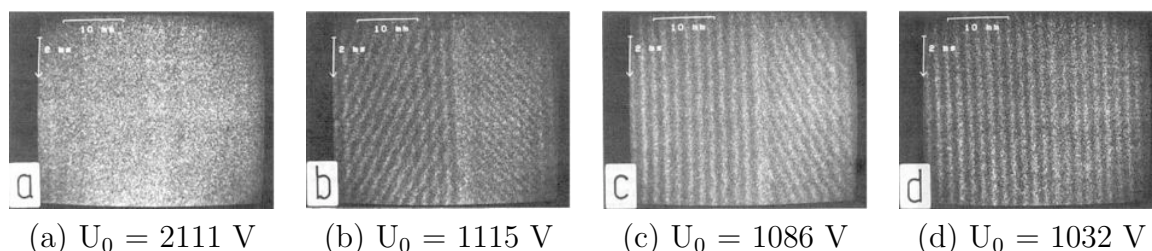(a) $U_0 = 2111$ V   (b) $U_0 = 1115$ V   (c) $U_0 = 1086$ V   (d) $U_0 = 1032$ V

Figure 3.13: Sequence of streak camera images showing the transition from the homogeneous state to stationary periodic structures via a state of dynamic waves. Experimental parameters: specific resistivity of Si $\rho = 1.5$ kΩ·cm; serial resistor $R_0 = 23.5$ kΩ; gas gap d = 3.1 mm; 51 hPa He. (Willebrand et al., 1991a).

3.3 Quasi-two-dimensional gas discharge systems with semiconductor cathodes

3.3.1 Si:Zn cathode at cryogenic temperature

The experimental setup used in the work described in this section has its origin in a special type of infrared-visible converter, which is based on the gas discharge with a semiconductor cathode. As illustrated in Figure 3.14 (a), the converter consists of a semiconductor cathode sensitive to infrared radiation and a transparent Indium-Tin-Oxide (ITO) glass anode separated by a gas gap. The diameter of the cathode is typically about 25 mm and the gap is about 100 μm. The working gas is Ne or Ar at pressures of several hundred hPa. The cathode is cooled down to about 90 K with liquid nitrogen in order to obtain a resistivity of the order of 10^{10} Ω·cm. When the cathode is not illuminated, a dark current below 0.1 A/m^2 is obtained in the case of a discharge with a Si:Zn cathode. The self-sustained discharge is operated in the Townsend mode after the electrical breakdown of the gas. When an infrared (IR) image is projected onto the cathode, a spatial modulation of the resistivity is produced in the semiconductor due to photoconductivity. It also manifests itself in the distribution of the current density of the discharge. As a result the light emission from the discharge in the visible range of the spectrum reproduces the IR image, which can be recorded with normal CCD cameras. Moreover, the IR converter is also suited for studying fast processes on the μs time scales when combined with a streak camera (see Astrov et al., 1993, and references therein).

Motivated by the pattern formation studies in the 1D gas discharges with semiconductor anodes, the IR-converter setup has also been used for pattern formation studies. Instead of projecting an image onto the semiconductor cathode, a homogeneous illumination is used as illustrated in Figure 3.14 (b). In most of the measurements, Si doped with deep impurities of Zn has been used. In contrast to a gap width of the order of 100 μm in the case of IR-converter, it is enlarged to a value typically above 0.5 mm. The
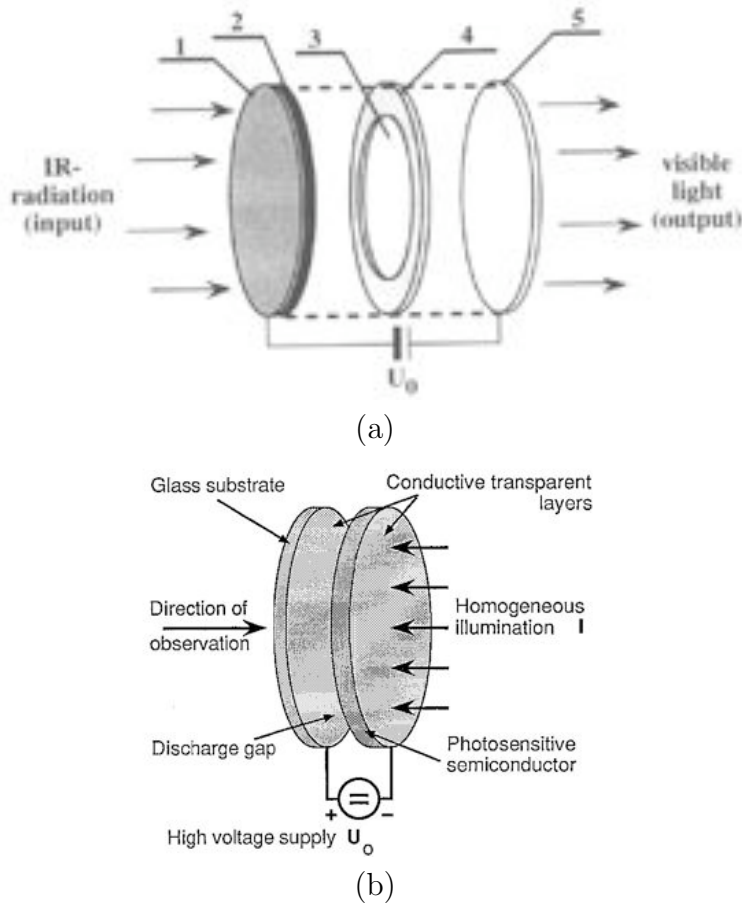
47

(a)

(b)

Figure 3.14: Schematic setup of the infrared-visible converter based on the semiconductor gas discharge (a) and its operation in pattern formation studies (b). 1. IR transparent electrical contact; 2. IR sensitive semiconductor, e.g. Si:Zn; 3. gas gap; 4. dielectric spacer; 5. glass plate coated with conductive Indium-Tin-Oxide film. (from Willebrand et al., 1994; Astrov et al., 1996, Fig. 1)

control parameters in this system are the source voltage U_0 and the intensity of the homogeneous illumination. In general, a prerequisite for obtaining self-organization is the destabilization of the spatially homogeneous state. In this case, the homogeneous state of the discharge loses its stability when the current density exceeds a certain threshold. The current density can be increased in two ways: either by increasing U_0 while keeping the illumination unchanged or by increasing the illumination at a constant U_0. In the original work on pattern formation using this setup by Astrov et al. (1996), generic patterns, i.e. stripes and hexagonal lattice of discharge spots, were observed (Figure 3.15). In that work, three kinds of scenarios were reported when the homogeneous state was destabilized. When U_0 is slightly above the breakdown voltage and the illumination is gradually increased, a transition from a homogeneous state to a stationary hexagonal pattern and then to non-stationary patterns occurs. It should be cautioned here that what was referred to as the stationary hexagonal pattern by Astrov et al. (1996) is in fact not stationary, but drifts coherently across the active area with a velocity of about 0.3 mm/s as revealed in the later work (Ammelt et al., 1998). When U_0 is fixed at a larger value than in the previous case, the hexagonal pattern changes first to a stationary
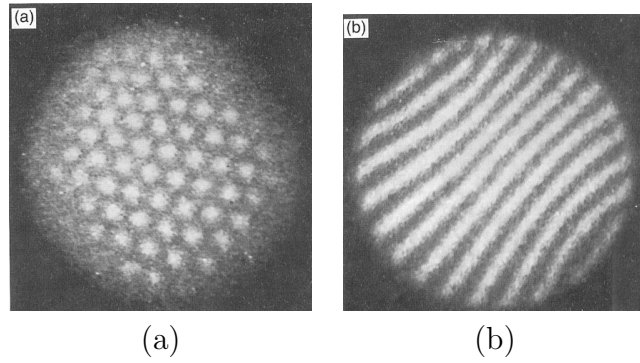
(a)   (b)

Figure 3.15: Hexagonal and striped pattern observed in the gas discharge system with a Si cathode. Experimental parameters: Si:Zn cathode; gas gap d = 0.8 mm; 120 hPa N_2; (a) U_0 = 1815 V; (b) U_0 = 1935 V. (from Astrov et al., 1996, Fig. 2).

stripe pattern and then to non-stationary patterns with increasing illumination. At a still higher constant U_0 the direct transition from the homogeneous state to the stationary stripe pattern is observed as the illumination is increased and finally to non-stationary patterns at sufficiently strong illuminations. Again, the stationary stripe pattern referred to by Astrov et al. (1996) is only quasi-stationary as the stripes drift with a constant speed of about 0.8 mm/s (Ammelt et al., 1997).

Stripes and zigzag instability

(a)   (b)
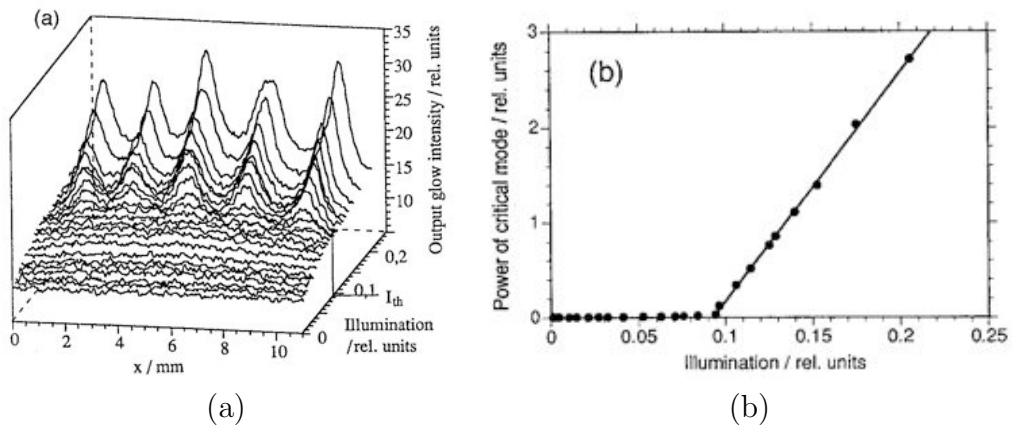
Figure 3.16: Evolution of spatial distribution of the luminosity along a line perpendicular to the stripes as the intensity of the illumination is increased (a) and related bifurcation diagram (b). Experimental parameters: Si:Zn cathode; gas gap d = 1.4 mm; 101 hPa N_2; U_0 = 2500 V. (from Astrov et al., 1996, Fig. 3).

As illustrated in Figure 3.16, the nature of the bifurcation from a homogeneous state to the striped state was investigated with a 1.4 mm gap filled with 101 hPa N_2. The intensity of the illumination was used as the bifurcation parameter. When the intensity exceeds the bifurcation point indicated by I_{th} in Figure 3.16 (a), the amplitude of the spatial modulation increases continuously. The wavelength is about 2.1 mm. The bifurcation diagram given in Figure 3.16 (b) was obtained by plotting the power of the

49

critical mode in the Fourier spatial spectrum of the striped pattern as a function of the bifurcation parameter. The linear dependence of the power on the deviation of the parameter from the bifurcation point showed that the bifurcation to stripes was of a supercritical nature.

Figure 3.17: Emergence of stripes as the mean current density rises as a result of the increasing intensity of illumination (a) and evolution of various characteristics of the stripes, (b) spatial wave number; (c) spatial orientation; (d) drifting velocity. Experimental parameters: Si:Zn cathode; gas gap d = 0.8 mm; 142 hPa N_2; U_0 = 2142 V. (from Ammelt et al., 1997, Fig. 5, 8, 9, 10).
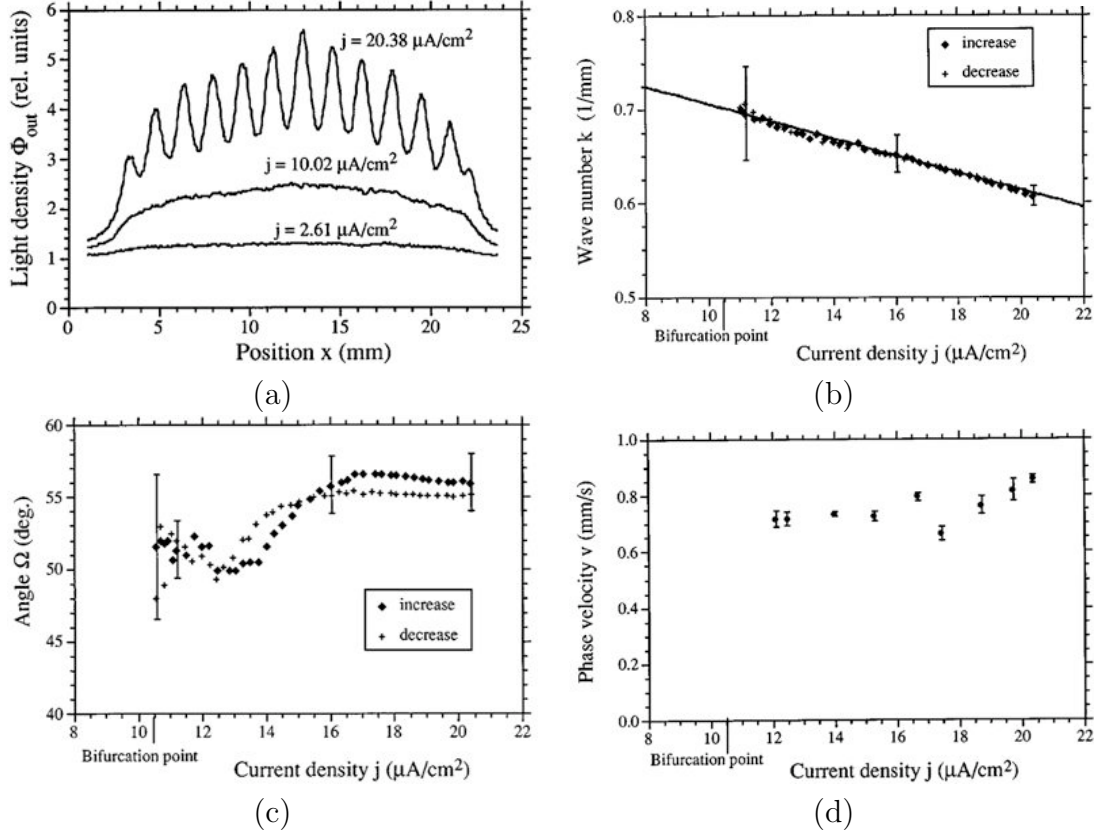
As mentioned above, the striped patterns are not strictly stationary. The dynamics of the stripe pattern close to the bifurcation point was investigated quantitatively in the gas discharge with a 0.8 mm gap filled with 142 hPa N_2 (Ammelt et al., 1997). Figure 3.17 (a) illustrates the luminosity distribution along a line across the center of the active area and perpendicular to the stripes. The discharge is uniform at current densities less than 10 $\mu A/cm^2$. The pincushion shape of the distribution is due to the configuration of the cryogenic cooling. The ring-shaped cold finger leads to a temperature gradient across the semiconductor. Under identical illuminations, the resistivity is lower in the central region due to higher temperatures. With current densities above 10 $\mu A/cm^2$, the uniform discharge loses its stability and striped modulations start to grow. The striped pattern is fully developed at 20 $\mu A/cm^2$. In parallel, the characteristics of the stripes, i.e. wave number, spatial orientation and drift velocity, also change during the process. As illustrated in Figure 3.17 (b), above the bifurcation point the wave number decreases continuously as the mean current density increases. For decreasing current density the

wave number increases again and there is no hysteresis. The spatial orientation of the stripes can be quantified by measuring the angle of the leading mode against the vertical axis in the Fourier space. The dependence of the angle on the mean current density is shown in Figure 3.17 (c). The stripes rotate slightly during the formation process and a hysteresis can be detected when the mean current density decreases. The drift velocity calculated from the phases of the leading mode in the Fourier space and its variation with increasing current density is given in Figure 3.17 (d). The drift velocity of the stripe varies only slightly during the formation process. It is also pointed out by Ammelt et al. (1997) that at higher pressures there is a tendency to form stationary stripes when the homogeneous state is destabilized.
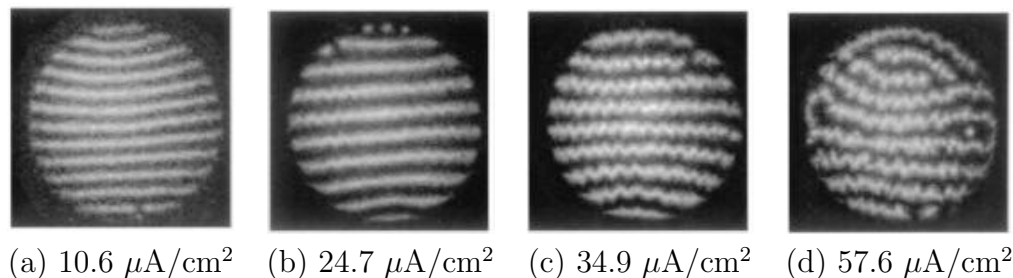

(a) 10.6 μA/cm^2 (b) 24.7 μA/cm^2 (c) 34.9 μA/cm^2 (d) 57.6 μA/cm^2

Figure 3.18: Zigzag instability of stripes as the intensity of the illumination is increased. Experimental parameters: Si:Zn cathode; gas gap d = 0.8 mm; 174 hPa N$_2$; U$_0$ = 2480 V. (Astrov et al., 1997).

(a)   (b)
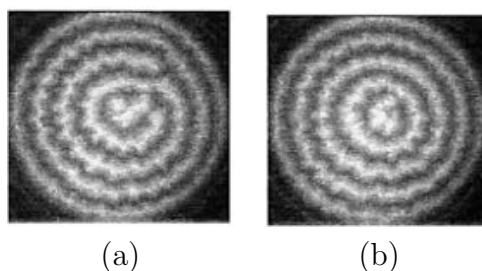
Figure 3.19: Snapshot of zigzag deformed spiral and target pattern. Experimental parameters: Si:Zn cathode ($\rho = 3.5 \times 10^8$ $\Omega \cdot$cm); gas gap d = 0.8 mm; 150 hPa N$_2$; U$_0$ = 2600 V. (Astrov et al., 1998).

It is known that in fluid systems the striped patterns formed through self-organization undergo secondary instabilities when the system is driven further from the primary bifurcation, e.g. Eckhaus, zigzag, skew-varicose, cross-roll and oscillatory instabilities in Rayleigh-Bénard convection (Cross and Hohenberg, 1993). In the present gas discharge system with Si cathode, zigzag instability for stripes was also observed by Astrov et al. (1997). The transition to zigzag destabilized stripes is illustrated in Figure 3.18 in the gas discharge with a 0.8 mm gap filled with 174 hPa N$_2$. A constant voltage of 2480 V was applied during the measurement and the intensity of the illumination was increased gradually. At a moderate mean current density of 10.6 μA/cm^2, a striped state was established (Figure 3.18 a). At 24.7 μA/cm^2, zigzag instability started to develop on some of the stripes. The pattern was dominated by zigzag destabilized stripes as the mean current densities was increased to 34.9 μA/cm^2. At higher current densities the

51

pattern showed complicated dynamics and a snapshot is given in Figure 3.18 (d). As illustrated in Figure 3.19, the zigzag deformation is also observed in spiral and target patterns (Astrov et al., 1998).

Figure 3.20: Dependence of the propagation velocity (left) and the wavelength (right) of the zigzag deformation along an isolated stripe on the total current at various source voltages, i.e. 2.7, 2.8 and 2.9 kV. Experimental parameters: Si:Zn cathode; gas gap d = 0.8 mm; 150 hPa N_2. (from Strümpel et al., 2000, Fig. 4).

In order to find out whether the zigzag instability results from the interactions between stripes, the phenomenon was investigated in the case where only a single isolated stripe was present. Such an isolated stripe was created artificially by illuminating only a 1.8×20 mm² rectangular zone of the Si cathode. The results confirmed that the zigzag instability occurred also in the case of an isolated stripe (Astrov et al., 1997). It was also found that the zigzag deformation was not stationary, but traveled along the isolated stripe. A quantitative study of the motion of the zigzag deformation was carried out with fast cameras by Strümpel et al. (2000). The propagation direction of the zigzag deformation was not predefined. In one measurement it was observed that the propagation direction changed twice in a period of 15 ms, which was the total recording time of the eight snapshots with a framing camera. In another example, it was observed that two zigzag deformations propagated in opposite directions at about 0.45 m/s and collided at some point close to the center of the isolated stripe. The dependence of the propagation velocity on the source voltage and the total current was studied systematically by introducing a small gradient of illumination along the stripe. In this way the zigzag deformation was forced to propagate in one direction and the uncontrolled random change of propagation direction could be avoided. The wavelength and the propagation velocity of the zigzag deformation along an isolated stripe were investigated when the total current was increased by increasing the intensity of illumination at three constant source voltages (Figure 3.20). At each constant voltage the propagation velocity increased with the current, but was almost independent of the source voltage. With increasing current, the wavelength of the zigzag deformation first increased and then reached a constant value. At very high currents, the zigzag deformed stripe broke up into bright discharge spots.

Hexagonal pattern and transition to stripes
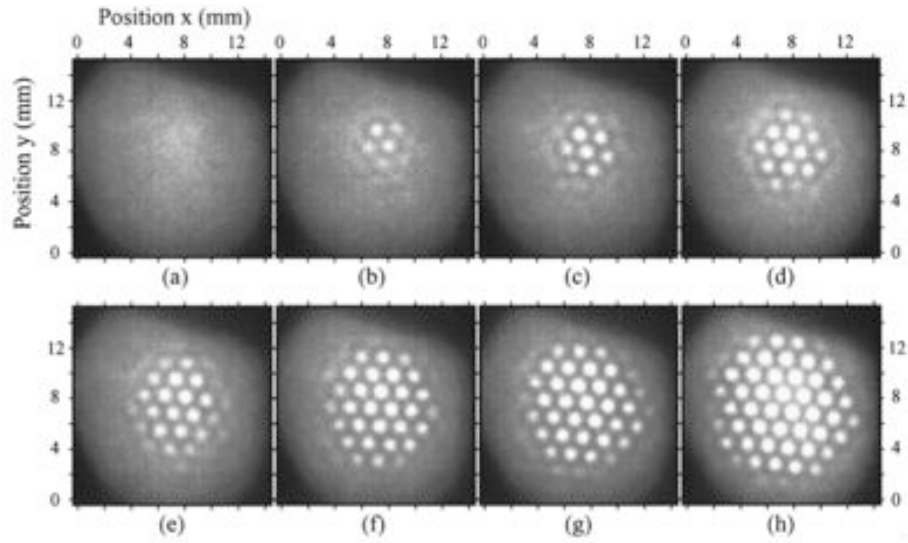
Figure 3.21: Emergence and growth of a hexagonal lattice of discharge spots on the uniform background at gradually increasing illumination. Experimental parameters: Si:Zn cathode; gas gap d = 0.8 mm; 142 hPa N_2; source voltage U_0 = 1886 V. (from Ammelt et al., 1998, Fig.2)
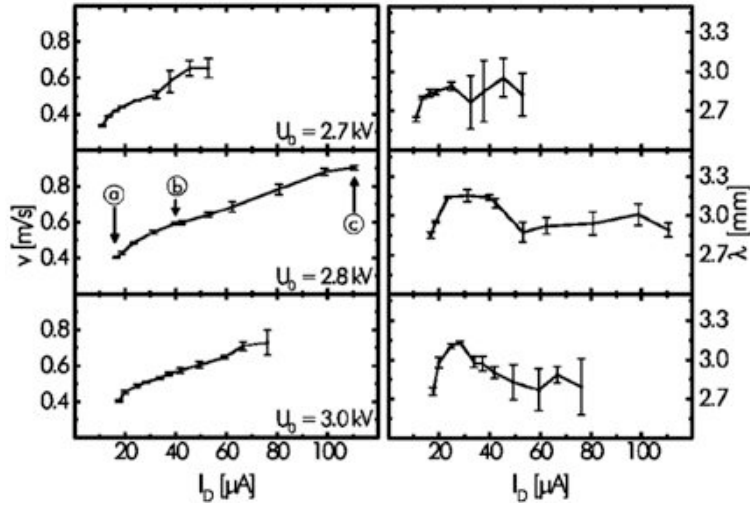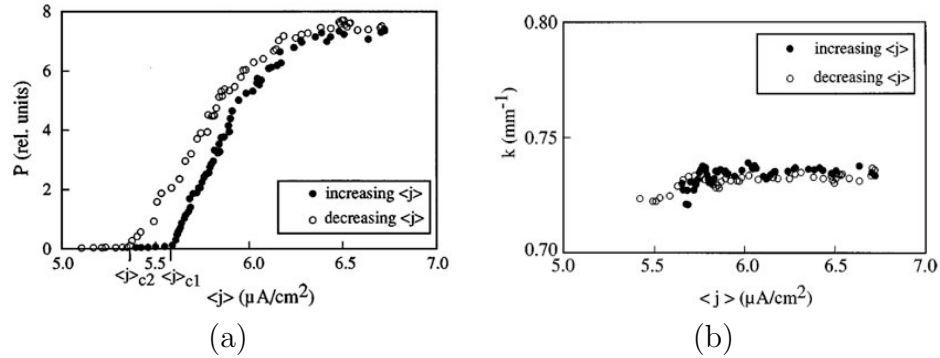

Figure 3.22: Dependence of the power (a) and the wave number (b) of the fundamental mode of the hexagonal pattern on the mean current density during the process of increasing and decreasing the intensity of the illumination. Experimental parameters: Si:Zn cathode; gas gap d = 0.8 mm; 142 hPa N_2; U_0 = 1886 V. (from Ammelt et al., 1998, Fig. 4, 5).

The emergence of a hexagonal lattice of discharge spots out of a uniform background shown in Figure 3.21 was observed with a Si:Zn cathode at about 90 K and a 0.8 mm gap filled with 142 hPa N_2 (Ammelt et al., 1998). The source voltage was kept at 1886 V and the mean current density $<j>$ increased with the intensity of the illumination. When $<j>$ was about 5.6 $\mu A/cm^2$, the discharge was uniform as illustrated in Figure 3.21 (a). When it exceeded a critical value $<j>_{c1}$, in this case about 5.7 $\mu A/cm^2$, the uniform discharge was destabilized and a hexagonal pattern started to develop. As the intensity of illumination was increased further, the hexagonal lattice grew from the center region

outward. Finally the lattice dominated the entire active area. The distance between the lattice spots was about 1.4 mm. The hexagonal lattice was not strictly stationary and drifted coherently across the active area with a velocity of about 0.3 mm/s. The Fourier spectrum power of the hexagonal pattern was calculated by integrating the intensity over a ring region defined by the radial interval covering the fundamental mode in Fourier space. The dependence of the power of the hexagonal pattern on the mean current density is given in Figure 3.22 (a). When $<j>$ is above $<j>_{c1}$ at increasing intensity of the illumination, the power of the hexagonal pattern increases continuously. At large values of the mean current density, the power reaches saturation. Starting from the fully developed hexagonal pattern, the power remains first at the saturation value in a small range of $<j>$ and then drops almost linearly with $<j>$ when the intensity of the illumination is reduced. Finally the system returns to a uniform state and the power of the hexagon pattern becomes 0 when another critical value $<j>_{c2}$ is reached. There is an obvious hysteresis in this process. The wave number of the hexagonal pattern is determined by averaging the center of mass of the six fundamental peaks in Fourier space. As shown in Figure 3.22 (b), the wave number of the hexagonal pattern is independent of the mean current density and there is no hysteresis increasing or decreasing the intensity of illumination.

(a) 1903 V	(b) 1940 V	(c) 2008 V	(d) 2145 V

Figure 3.23: Transition from a homogeneous state (a) to a hexagonal state (b) and then via a mixed state of hexagon and stripes (c) to a striped state as the source voltage is gradually increased. Experimental parameters: Si:Zn cathode; gas gap d = 0.8 mm; 142 hPa N_2. (from Ammelt et al., 1998, Fig. 7).

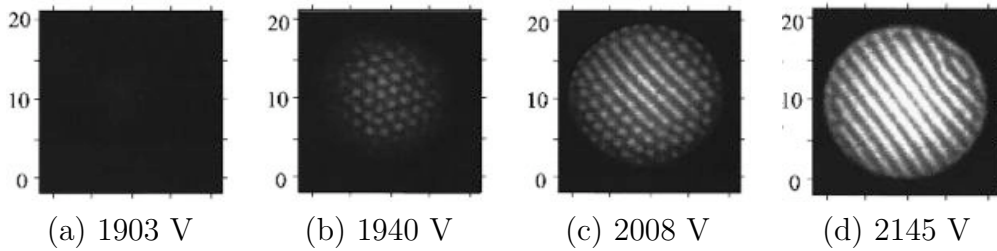In the experiment illustrated in Figure 3.23, the transition scenario in gas discharges with a 0.8 mm gap and 142 hPa N_2 was investigated by varying another control parameter, the source voltage U_0. When U_0 was raised from 1903 to 1940 V, the homogeneous state gave way to a hexagonal state. A further increase of U_0 led to the appearance of stripes which had the same wave number as that of the hexagon pattern. At 2145 V, the stripes prevailed. The spectral power of the fundamental mode for the hexagonal and striped patterns as a function of U_0 is shown in Figure 3.24 during the processes of increasing and decreasing the source voltage. During the process of increasing U_0, the transition to the hexagonal pattern occurs when U_0 exceeds a threshold value of about 1910 V. The power of the pattern increases linearly with the distance of the control parameter from the bifurcation point. At about 2000 V, there is a transition from the hexagonal pattern to periodic stripes. After the transition, the power of the striped pattern increases monotonically with U_0 and there is no significant sign of the transition in the bifurcation diagram. Above 2200 V the stripes are fully developed, and when the voltage is gradually decreased the striped pattern is stable until U_0 is reduced to about 2030 V, where the hexagonal pattern emerges. The hexagonal pattern is reestablished
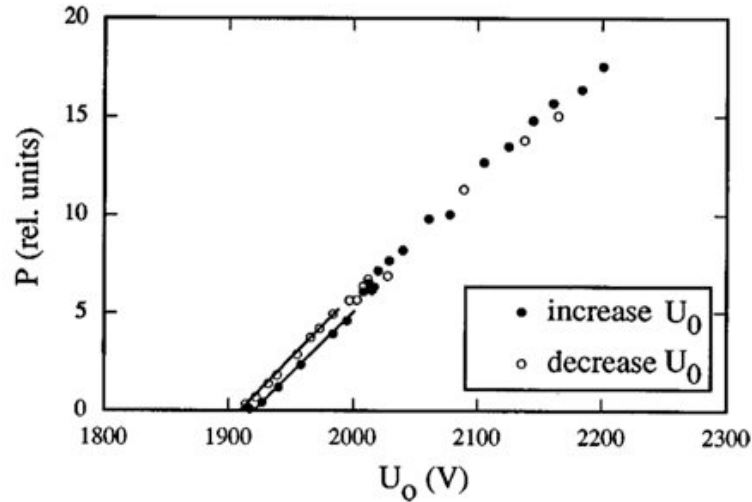
Figure 3.24: Spectral power of the fundamental mode for the hexagonal and striped state as a function of the source voltage during the increase and decrease of the source voltage. Experimental parameters: Si:Zn cathode; gas gap d = 0.8 mm; 142 hPa N_2. (from Ammelt et al., 1998, Fig. 9)

at lower U_0. As mentioned by Ammelt et al. (1998) both the hexagonal and the striped pattern drift across the active area with a velocity of about 0.3 mm/s.

General features of pattern formation in the gas discharge system with a Si:Zn cathode at about 90 K are summarized in the schematic diagram on the parameter plane of the source voltage U_0 and the conductivity of the semiconductor σ (Figure 3.25). The voltage U_{crit} corresponds to the breakdown voltage of the gas gap. Below this value the gap is insulating and in the dielectric state and it becomes conductive when U_0 is above U_{crit}. In the conducting state, the homogeneous state of the discharge, corresponding to region a in Figure 3.25, is stable at small σ. At each U_0 there is a critical σ for the homogeneous state, above which the spatial modulations start to grow. The amplitude of the spatially extended patterns is small compared to the uniform background. So far the regular patterns like hexagons and stripes discussed above belong to this class as indicated by region b in Figure 3.25. At higher σ the amplitude of patterns increases and the uniform background is suppressed. Finally, patterns consisting of the localized discharge spots with a rather high amplitude are common (region c in Figure 3.25). An example of the evolution of a hexagonal lattice consisting of discharge spots as a result of increasing σ is illustrated in Figure 3.26. In this measurement a large resistor $R_0 = 41$ MΩ in series with a 0.5 mm gap filled with 260 hPa N_2 was used. At low σ the discharge spots form a hexagonal lattice (Figure 3.26 a). As σ is increased, some spots start to detach from the lattice and move freely (Figure 3.26 b and c). At very high σ the lattice is destroyed and an ensemble of spots moves in the active area. The dynamics is very complicated and spots can be generated or disappear upon collisions. It is interesting to note the analogy of this transition with the typical phase transitions, i.e. melting and evaporation processes, of condensed matter.
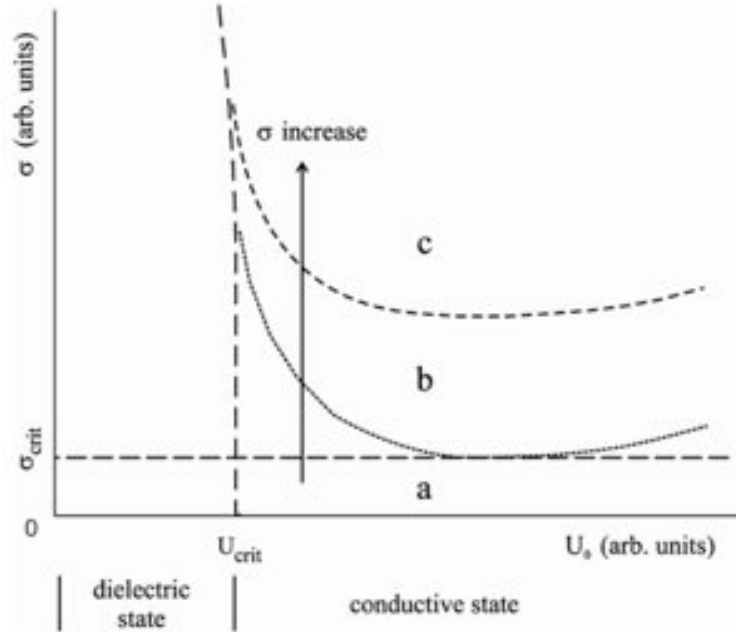
Figure 3.25: Schematic diagram on the parameter plane of the source voltage U_0 and the conductivity of the Si:Zn cathode. Region a in the diagram corresponds to the homogeneous state of the gas discharge; Region b corresponds to the spatially extended pattern of small amplitude; Region c corresponds to the localized discharge spots of large amplitude. (from Astrov and Purwins, 2001, Fig. 1)

Solitary discharge spots with particle-like characteristics

In the "gaseous" phase of an ensemble of solitary spots as illustrated in Figure 3.26 (d), various interesting phenomena are observed when two solitary spots get close to each other (Astrov and Purwins, 2001). In the simple case, the two spots come close to each other and then change their direction of motion and move apart. In the other case, two solitary spots come together and bound to each other. They move temporarily together as if a two-spot "molecule" is formed. After some time the "molecule" is destroyed and forms again in the course of time. In some cases a third spot can be generated by the collision of two spots. The generation of a new spot close to an existing spot is assumed to be related to the oscillatory tails of the localized spots. According to the activator-inhibitor model, a new solitary structure can be generated when the threshold of the self-activation is reached as a result of the superposition of activator side maximums of the tails. It is believed that the oscillatory tail of the solitary spot is also responsible for the formation of a hexagonal cluster via the self-completion scenario as illustrated in Figure 3.27. In Figure 3.27 (a), the localized structure consists of a bright spot surrounded by a ring. As the source voltage is increased, new spots appear on the ring (Figure 3.27 b-c). The further growth of the cluster is accompanied by the successive creation of new spots on certain lattice sites Astrov and Logvin (1997).

The experimental results obtained in the gas discharge system with N_2 and a Si cathode at about 90 K are summarized in Table 3.1. Although most of the experiments were made with Si:Zn, it was mentioned in some publications that the use of Si:Au or Si:Pt gave qualitatively the same phenomena. With the various choices of the pressure

56

(a)　　　　(b)　　　　(c)　　　　(d)
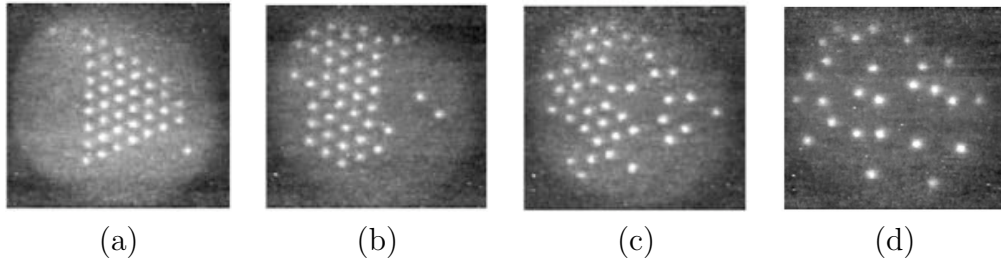
Figure 3.26: Transition from a solid-like lattice of discharge spots (a) to a "gaseous" ensemble (d) as the conductivity of the semiconductor is gradually increased. Experimental parameters: Si:Zn cathode; gas gap d = 0.5 mm; 260 hPa N_2; R_0 = 41 MΩ; U_0 = 2900 V. (from Astrov and Purwins, 2001, Fig. 2).

(a)　　　　(b)　　　　(c)

(d)　　　　(e)　　　　(f)

Figure 3.27: Growth of a hexagon cluster via the self-completion scenario as the voltage is slightly increased. Experimental parameters: Si:Zn cathode; gas gap d = 1.4 mm; 150 hPa N_2. (from Astrov and Logvin, 1997, Fig. 2).

and the gap width, a rich variety of the patterns and many interesting dynamic behaviors are observed.

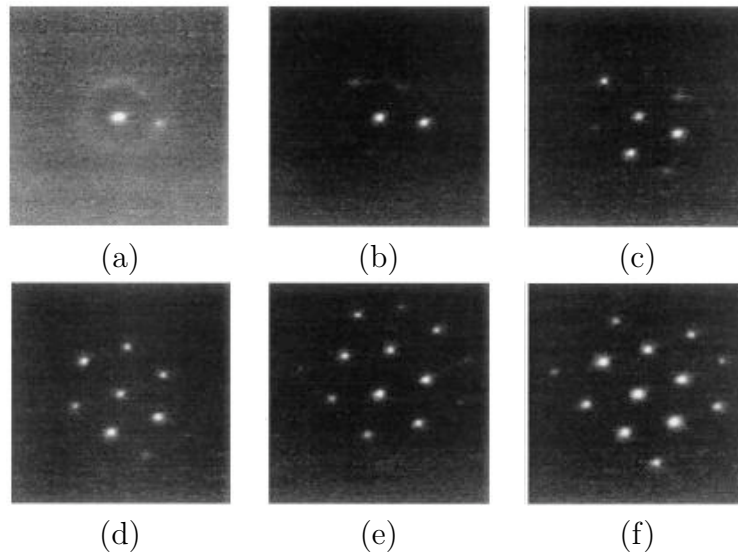| cathode	gap	N$_2$ pressure	parameters	phenomena	reference
Si:Zn (or Si:Au) $\varnothing$2 cm	0.8 mm	120 hPa	1815 V	hexagonal lattice	
			1935 V	stripes	
	1.4 mm	101 hPa	2500 V	supercritical bifurcation to stripes	Astrov et al. (1996)
Si:Zn $\varnothing$2 cm	0.8 mm	174 hPa	2480 V	transition from a uniform state to zigzag destabilized stripes	Astrov et al. (1997)
Si:Zn (or Si:Au) $\varnothing$2 cm	1.0 mm	168 hPa	2600-2800 V	hexagon formation via self-completion	
	1.4 mm	150 hPa	3200 V	self-completion	
	0.8 mm	130 hPa	1900 V	interaction between isolated spots and spot cluster	
		137 hPa	1900 V	interaction between spot clusters	Astrov and Logvin (1997)
Si:Zn (or Si:Au) $\varnothing$2 cm	0.8 mm	142 hPa	1886 V	hexagonal lattice	
			2142 V	bifurcation to drifting stripes	
		160 hPa	2530 V	drift direction of stripes	
	0.62 mm	190 hPa	2750 V	bifurcation to stationary stripes	
	1.50 mm	101 hPa	2500 V	influence of inhomogeneities on stripes	Ammelt et al. (1997)
Si:Zn (or Si:Pt) $\varnothing$3 cm	0.8 mm	150 hPa	2500-2900 V	high resistivity 1.6$\cdot$10^7 $\Omega\cdot$ m transition from hexagon to spirals	
			2500-2900 V	low resistivity 3.5$\cdot$10^6 $\Omega\cdot$ m transition from spots to zigzag spirals spiral-target-spiral transitions	Astrov et al. (1998)
Si:Zn (or Si:Au) $\varnothing$3 cm	0.8 mm	142 hPa	1886 V	growth of hexagonal lattice	
			1093-2145 V	transition to stripes via hexagons	
	0.75 mm	129 hPa	1900 V	hexagon	Ammelt et al. (1998)
Si:Zn (a strip of 1.8$\times$20 mm^2 illuminated	0.8 mm	160 hPa	2300 V	transition to zigzag stripe	
			2800 V	propagation of zigzag deformation along the isolated stripe	Strümpel et al. (2000)
Si:Zn $\varnothing$2 cm	0.5 mm	260 hPa	2900 V	"gaseous" ensemble of spots formation of spot "molecules"	

Table 3.1: Summary of experimental results in a gas discharge system with a Si cathode at about 90 K and a gap of about 1 mm filled with N_2.

3.3.2 GaAs cathode at room temperature

Besides the Si cathode doped with deep impurities, semi-insulating GaAs was also used as resistive cathode in the study of pattern formation. Whereas a cryogenic temperature is necessary in order to obtain a high resistivity with the Si cathode, the resistivity of GaAs is above 10^7 $\Omega\cdot$cm at room temperature. Therefore, the gas discharges with GaAs cathodes were investigated at room temperature in the initial work (Strümpel and Purwins, 2000; Strümpel et al., 2001, 2002). Later, the phenomena in gas discharges with GaAs samples of different material properties at various cryogenic temperatures were investigated by Gurevich (2004).
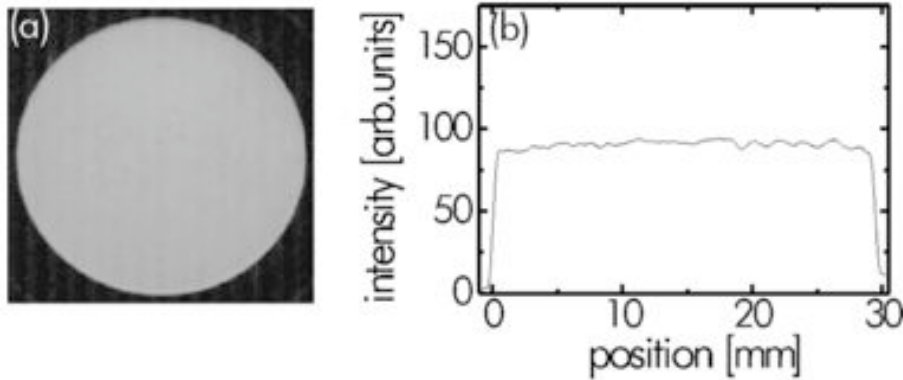

Figure 3.28: (a) Image of the stationary homogeneous state of the gas discharge; (b) Luminosity profile along a 30 mm diameter of the discharge area. Experimental parameters: GaAs cathode; gas gap d = 0.5 mm; 47 hPa N_2; U_0 = 533 V. (from Strümpel and Purwins, 2000, Fig. 2)

As in the case of the Si cathode, the major control parameters in this setup are the source voltage U_0 and the intensity of illumination. In the results given by Strümpel and Purwins (2000), the intensity of the illumination ϕ_L was normalized to the maximum intensity used in the experiments. Given a combination of the N_2 pressure and the gap width, the stationary homogeneous state is stable when the current is small, e.g. at small U_0 or at weak illuminations. As illustrated in Figure 3.28, there are no inhomogeneities in the entire discharge area and the luminosity profile along a 30 mm diameter of the active area is rather flat.

The stationary homogeneous state is destabilized when the current is raised by increasing U_0 or ϕ_L. The destabilization does not lead to the emergence of spatial modulations on the uniform background as in the case of the discharges with Si cathodes at cryogenic temperatures, but to a homogeneous oscillation. The spatial homogeneity of the oscillating state is illustrated in Figure 3.29. During the oscillation, the amplitude and frequency of the current oscillation are constant at fixed U_0 and ϕ_L. In the example given here, an oscillation with a frequency of 175 kHz is established in the discharge with a 1 mm gap filled with 40 hPa N_2 when U_0 and ϕ_L are 583 and 0.42 respectively. The photos taken with an image intensified camera at various stages during the time course of the current revealed the nature of the oscillation. During the period of a current pulse, a homogeneous light emission from the discharge is observed (image 1-3 in Figure 3.29 a). There is no light emission (image 4) when the current returns 0. In contrast
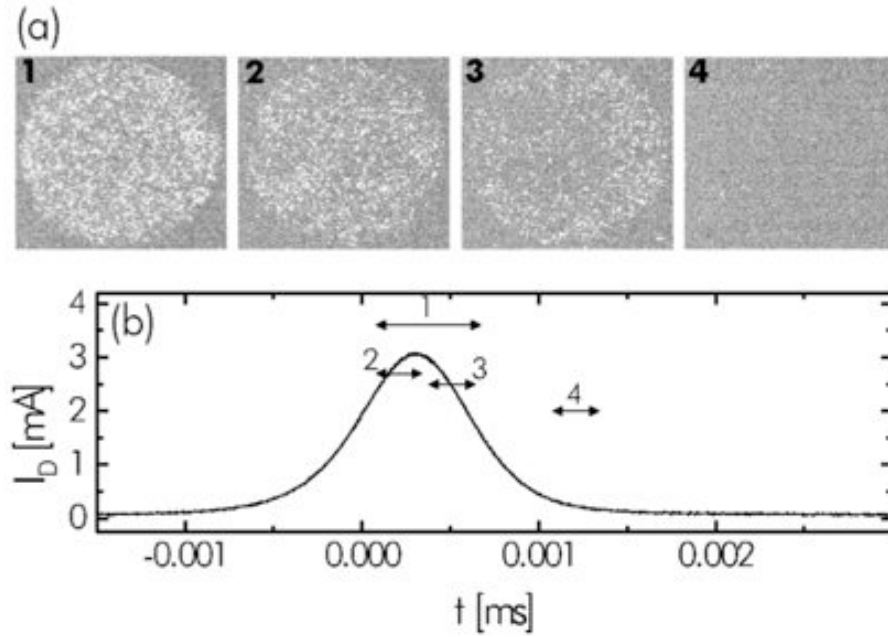
Figure 3.29: Photos (a) from an image intensified camera with short exposure times (630 ns for image 1; 300 ns for image 2, 3 and 4.) at different stages of a current pulse corresponding to the discharge (b). The position and duration of the exposure for the images are marked in the time course of the current. Experimental parameters: GaAs cathode; gas gap d = 1 mm; 40 hPa N_2; U_0 = 583 V. (from Strümpel and Purwins, 2000, Fig. 5)

Figure 3.30: Dependence of the amplitude and the fundamental frequency of the oscillation on the control parameters U_0 and ϕ_L. (a) and (b) correspond to the case of varying U_0 at a constant ϕ_L of 0.4 whereas (c) and (d) the case of varying ϕ_L at a constant U_0 of 528 V. Experimental parameters: GaAs cathode; gas gap d = 0.5 mm; 45 hPa N_2. (from Strümpel and Purwins, 2000, Fig. 8)

61

to the continuous discharge in the stationary homogeneous state, the discharge in the oscillatory mode is intermittent. The frequency and amplitude of the osci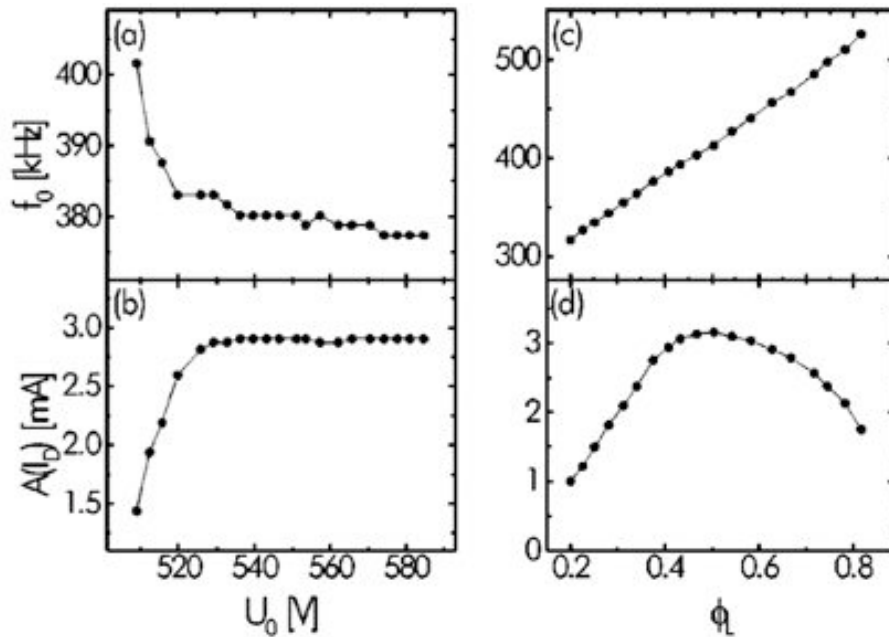llations are determined by the control parameters U_0 and ϕ_L at a given gas pressure and gap width. This dependence was investigated by varying U_0 at a constant $\phi_L = 0.4$ and by varying ϕ_L at a constant U_0 of 528 V. In the first case (Figure 3.30 a and b), the frequency decreases and the amplitude increases when U_0 is increased from the transition point. At larger U_0 the frequency and amplitude reach stable values, about 380 kHz and 3 mA respectively. In the second case, the fundamental frequency of the oscillation increases linearly with the illumination ϕ_L. In contrast, the amplitude of the oscillation first increases and then decreases as ϕ_L increases. The characteristics of the oscillation was also investigated at various pressures. In the case of 0.5 mm gap, the frequency and the amplitude vary very little when p is varied between 25 and 55 hPa. At p below 20 hPa, there is a significant drop in amplitude (50%) and a slight change of frequency (<5%). The gap width also has an effect on the frequency range of the oscillation. The frequency range from 250 to 600 kHz for a 0.5 mm gap changes to an interval between 100 and 250 kHz when a 1 mm gap is used.

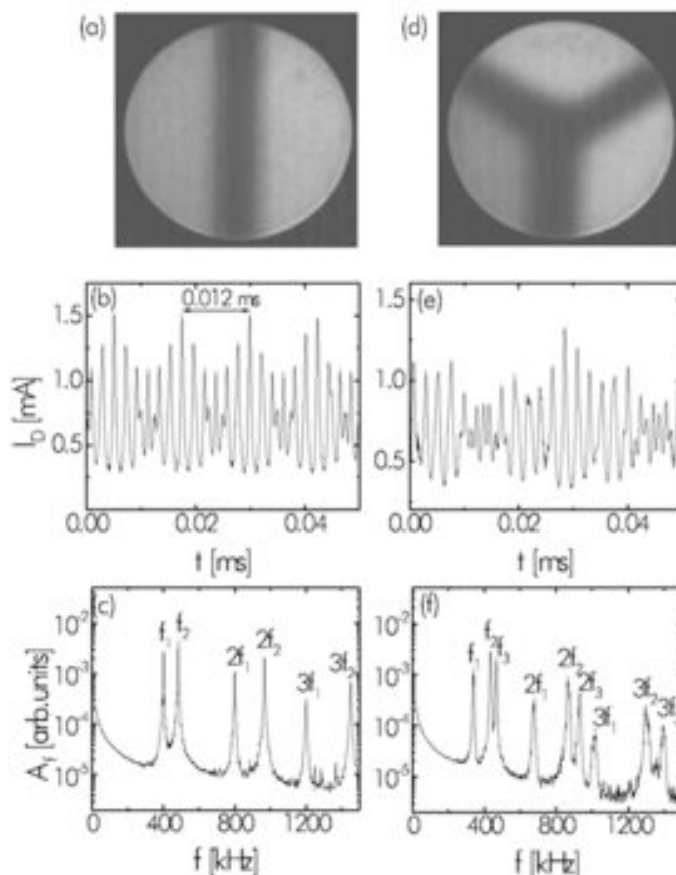Figure 3.31: Isolated domains oscillating at different frequency and amplitude and the corresponding current characteristics and their spectrum. (a) left $\phi_L = 0.39$ and right $\phi_L = 0.61$; (d) top $\phi_L = 0.55$, left $\phi_L = 0.32$ and right $\phi_L = 0.61$. Experimental parameters: GaAs cathode; gas gap d = 0.5 mm; 45 hPa N_2; $U_0 = 540$ V. (from Strümpel and Purwins, 2000, Fig. 9)

As discussed above, the frequency and the amplitude of the oscillations depend on the illumination. When the GaAs cathode is illuminated non-homogeneously, oscillation domains with different frequencies can be obtained. In the example given in Figure 3.31 (a), the cathode was divided into two domains separated by a strip area where the illumination was absent. The intensity of the illumination in the left part was attenuated to 64% with a filter and ϕ_L in the unfiltered right side is 0.61 and the value corresponding to the left side is thus 0.39. As seen in the spectrum of the current (Figure 3.31 c), there are two fundamental frequencies, 399 and 483 kHz, in the current oscillation. The beating of the two frequency can also be clearly recognized in Figure 3.31 (b). In the case illustrated in Figure 3.31 (d-f), three isolated domains oscillating at different frequencies are created. In the two cases described here where the domains are well separated by non-illuminated regions, the current characteristics is a simple linear superposition of two oscillations. When the width of the non-illuminated region is reduced, a nonlinear interaction between the two oscillations can be observed and additional frequency components, e.g. $f_1 + f_2$, $2f_1 - f_2$ and $3f_1 - f_2$ etc, are obtained in the spectrum of the current in the case of two oscillating domains. When there is no separation region, the two frequencies shift toward each other. This behavior of periodic pulling is typical for an incomplete entrainment of a nonlinear oscillator by an external harmonic driving. For more about the interactions between two oscillation domains, we refer to Strümpel and Purwins (2000).
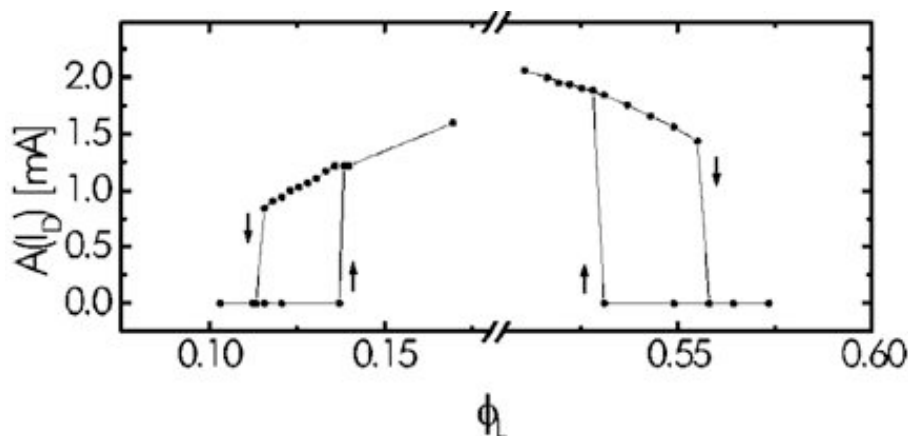
Figure 3.32: Transition between the stationary state and the oscillatory state as ϕ_L is varied. Experimental parameters: GaAs cathode; gas gap d = 0.5 mm; 40 hPa N_2; U_0 = 510 V. (from Strümpel and Purwins, 2000, Fig. 7)

The transition between the stationary and the oscillatory state as shown in Figure 3.32 has some interesting features. Increasing ϕ_L from a small value of about 0.1, the stationary state is stable up to a value close to 0.15 where the oscillatory state appears. When the ϕ_L is further increased to a value above 0.55 the oscillations disappear. Decreasing ϕ_L from a large value leads to the transition from the stationary state to the oscillatory state and then to the stationary state again. Two hysteresis loops of approximately the same width are observed in the transitions.

The region of existence for the homogeneous stationary state and the homogeneous oscillatory state is given on the plane of the control parameters U_0 and ϕ_L (Figure 3.33). At U_0-values below 530 V, the homogenous stationary state is obtained at very low
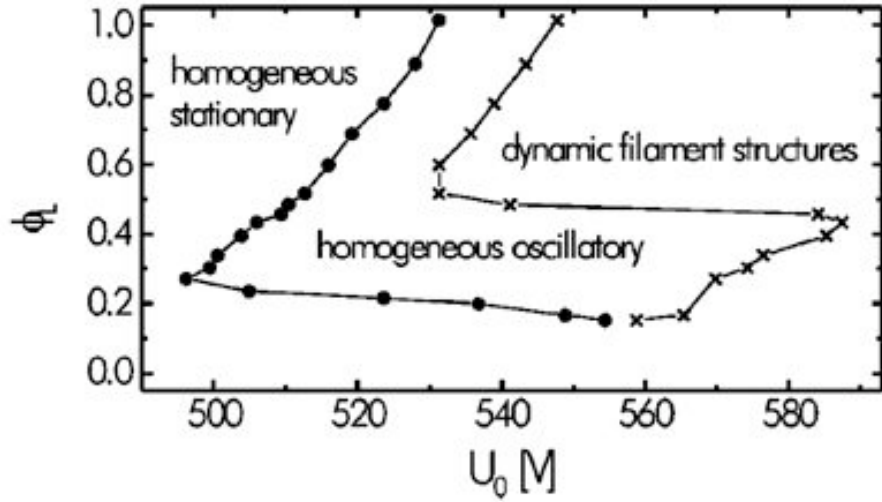
Figure 3.33: Region of existence for the homogeneous stationary state, the homogeneous oscillatory state and the dynamic filaments on the plane of U_0 and ϕ_L. Experimental parameters: GaAs cathode; gas gap d = 0.5 mm; 40 hPa N_2. (from Strümpel and Purwins, 2000, Fig. 6)
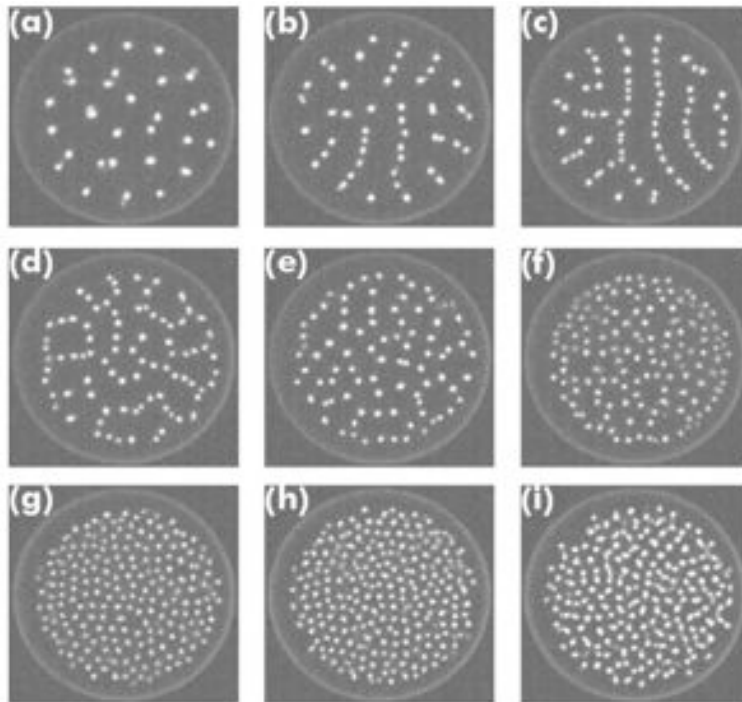
Figure 3.34: Snapshots (40 ms exposure time) of dynamic filaments as U_0 is increased: (a) 820 V; (b) 850 V; (c) 880 V; (d) 910 V; (e) 940 V; (f) 1000 V; (g) 1060 V; (h) 1120 V; (i) 1210 V. Experimental parameters: GaAs cathode ($\sigma = 0.65 \times 10^{-7}$ $(\Omega \cdot cm)^{-1}$); gas gap d = 0.5 mm; 42 hPa N_2. (from Strümpel et al., 2001, Fig. 3)

ϕ_L and at very high ϕ_L. At high U_0-values and high ϕ_L the homogenous oscillatory state gives way to a new form of structure, dynamic filaments. The evolution of the filamentary structure with increasing U_0 is illustrated in the snapshots taken with an exposure time of 40 ms (Figure 3.34). At 820 V (corresponding to Figure 3.34 a), the number of filaments is relatively small and they move randomly across the active area. The typical velocity of the motion is of the order of 3 mm/s. As U_0 is increased, the filaments tend to align and form parallel chains (Figure 3.34 b, c), which are, of course, not rigid objects. As the filaments in the chains move, they may bend and break and at the same time new chains are formed. The general features of the chain structure are, however, retained during the dynamics processes. When U_0 is increased further, the number of filaments increases accordingly and the chain structure changes to a net-like structure (Figure 3.34 d, e). The number of filaments is sufficiently large and the entire active area is densely packed (Figure 3.34 f-i). In this state, the increase of U_0 no longer leads to a significant increase of the filament number, but to an increase of their velocity.
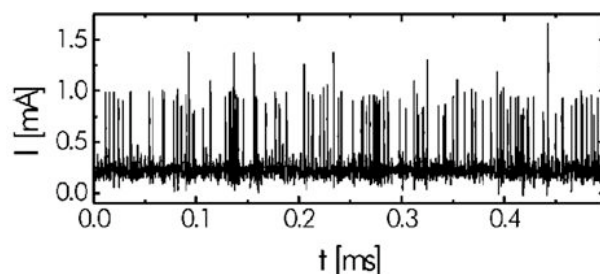
Figure 3.35: Time course of the total current of the discharge corresponding to the filament chains as illustrated in Figure 3.34 (c). Experimental parameters: GaAs cathode ($\sigma = 0.95 \times 10^{-7}$ $(\Omega \cdot cm)^{-1}$); gas gap d = 0.5 mm; 60 hPa N_2; $U_0 = 846$ V.(from Strümpel et al., 2001, Fig. 9)
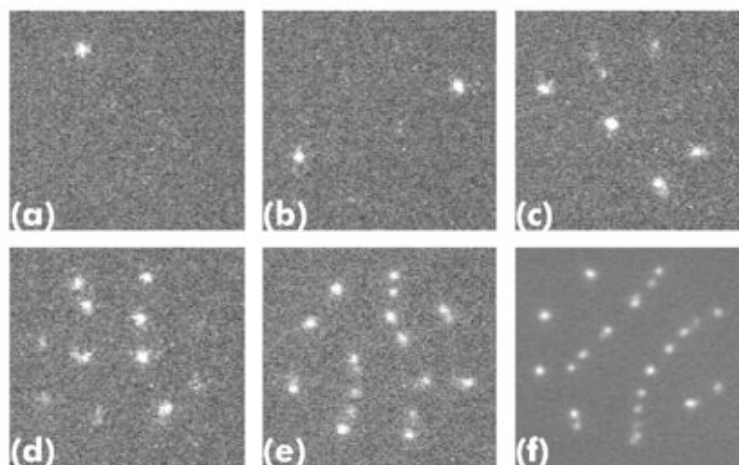
Figure 3.36: Images of the filamentary structures taken at various exposure times: (a), (b) 3 μs; (c) 10 μs; (d) 30 μs; (e) 300 μs; (f) 40 ms. Experimental parameters: GaAs cathode ($\sigma = 0.58 \times 10^{-7}$ $(\Omega \cdot cm)^{-1}$); gas gap d = 0.5 mm; 60 hPa N_2; $U_0 = 908$ V. (from Strümpel et al., 2001, Fig. 11)

The typical time course of the total current (Figure 3.35) consists of a succession of spikes when the filamentary structure is observed in the discharge. The spikes last for about 300 ns and have an amplitude of about 1 mA. As the number of filaments is increased with U_0, the frequency of the spikes rises accordingly. This kind of current characteristics suggests that the spike corresponds to the appearance of a single filament which exist only for a short period of time, e.g. about 300 ns. The images for the filamentary patterns taken with various exposure times are shown in Figure 3.36. As the average interval between two spikes ranges from 20 to 30 μs, only a small number of filament can be recorded with 3 μs exposure time, as in Figure 3.36 (a) and (b). In some cases no filament is recorded when the exposure time does not coincide with the current spikes. Increasing the exposure time to 10 or 30 μs makes more filaments appear in the image. The spatial distribution of the filaments seems to be random and there is no sign of correlations between the positions of the filaments from two successive spikes. With an exposure time of 300 μs the image shows effectively no qualitative difference from the image taken with video cameras which have a typical exposure time of 40 ms.
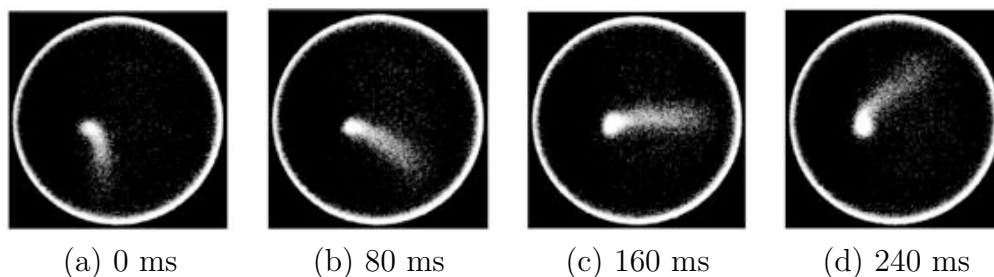

| (a) 0 ms | (b) 80 ms | (c) 160 ms | (d) 240 ms |

Figure 3.37: Rotating wave in N_2 discharge with a GaAs cathode at room temperature. Experimental parameters: GaAs cathode; gas gap d = 0.5 mm; 31 hPa N_2; U_0 = 500 V. (from Gurevich et al., 2003a, Fig. 2).

In the example shown in Figure 3.37, it is reported that a destabilization of the homogeneous stationary discharge leads to rotating wave (Gurevich et al., 2003a). The dynamics of the wave consists of a rotation around the tip and a drift of the tip across the active area. The rotation frequency is constant at fixed U_0 and illumination conditions. In the given example it is 1.4 Hz and decreases as U_0 is raised. In the voltage current characteristic of the 1.5 mm thick GaAs wafer there is a region of negative differential resistance when the voltage across the wafer ranged from 150 to 250 V. It is believed that the nonlinearity of the GaAs cathode is responsible for the appearance of the rotating wave.

The effect of the nonlinearity of GaAs on the form of the discharge was investigated with a 0.1 mm gap filled with 200 hPa Ar (Gurevich, 2004). By using this combination of the pressure and the gap width, the voltage-current characteristics of the gas discharge is monotonic and therefore should not contribute to the destabilization of the homogeneous stationary discharge. A typical voltage-current characteristics and the transition of different forms of the discharge at increasing voltage is illustrated in Figure 3.38. In the voltage range where the current increases monotonically, the gas discharge is homogeneous and stationary. In the range where negative differential resistivity appears, propagating waves with irregular dynamics can be observed. At voltages above 600 V the current rises again monotonically with voltage and filamentary structures become
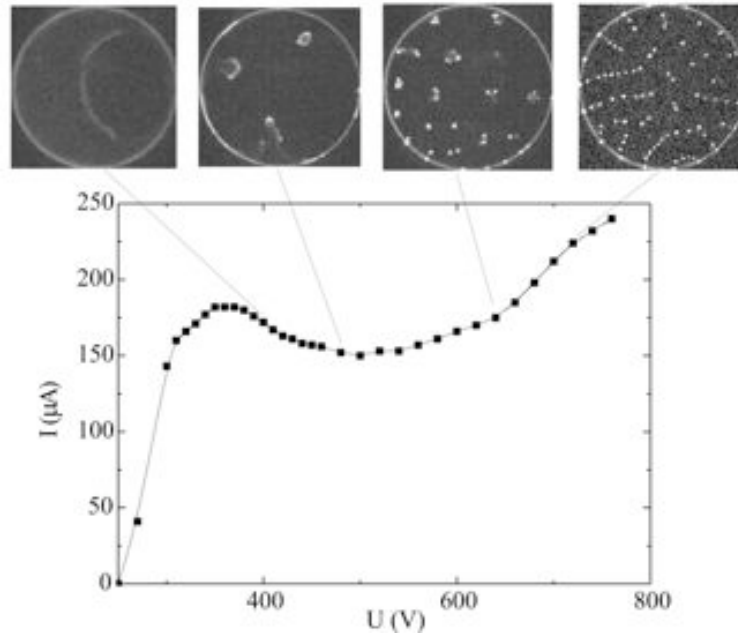
Figure 3.38: Voltage-current characteristics of the semiconductor gas discharge cell and the related form of the discharge. Experimental parameters: GaAs cathode; gas gap d = 0.1 mm; 200 hPa Ar. (from Gurevich, 2004, Fig. 5.10)

common.

Chapter 4

Experimental system

4.1 Experimental setup

The essential part of the experimental setup used in the study of pattern formation during gas discharges is a discharge cell (Figure 4.1) consisting of two planar electrodes (1 and 3) separated by a dielectric spacer (2). Throughout the measurements, various kinds of cathodes have been used, e.g. metal plates (1A), semiconductor wafers (1B) and semi-insulating materials (1C). In the case of semiconductor cathodes, a uniform electrical contact on one side of the wafer, which is transparent to illumination, is obtained either by depositing a thin gold film or by diffusing (or implanting) impurities at the surface of the semiconductor substrate. The electrical properties of the wafer, particularly the resistivity, can be varied when the wafer is illuminated by an incandescent lamp. The transparent anode (3) is a glass plate of which the entire surface is coated with a few hundred nm ITO (indium-tin-oxide) film which is conductive. The spacer (2) is made of hard PVC or synthetic resin. The lateral dimension of the electrodes, which typically have diameters between 30 and 50 mm, is much larger than the inter-electrode spacing, which is of the order of 1 mm.

Throughout the work, two variants of the setup have been used, depending on whether cryogenic temperature is required or not. In the simplest case where gas discharges are studied at room temperature, the setup consists of a discharge cell immersed in a gas chamber with two windows which are transparent to visible light (Figure 4.2 b). The discharge cell (1-3) mounted on the sample holder (5) is immersed in the chamber (6) which is filled with required gas. The pressure is regulated manually with the help of valves (7, 8, 10), an E2M2 high vacuum pump 9 (BOC Edwards, Sussex, UK), a bottle of industrial gas (11) and DI 2000 pressure gauges 12 and 13 (Leybold, Cologne, Germany). The electrical contact ring (4) and the sample holder (5) are connected to a high voltage power supply via two serial resistors R_0 and R_I. The purpose of R_0, which has a value of the order of 1 MΩ, is to limit the current flowing through the circuit. With the help of R_I (about 100 Ω), the time course of the current in the discharge circuit can be recorded with a digital storage oscilloscope. The PS350 constant voltage source (Stanford Research System Inc., Sunnyvale, USA) used in our measurements delivers a constant voltage of up to 5000 V with a current up to 5 mA. The LED display on the front panel shows the actual voltage and current values with an update frequency of 8 Hz. The current is thus an averaged value. In order to study the light emission from the
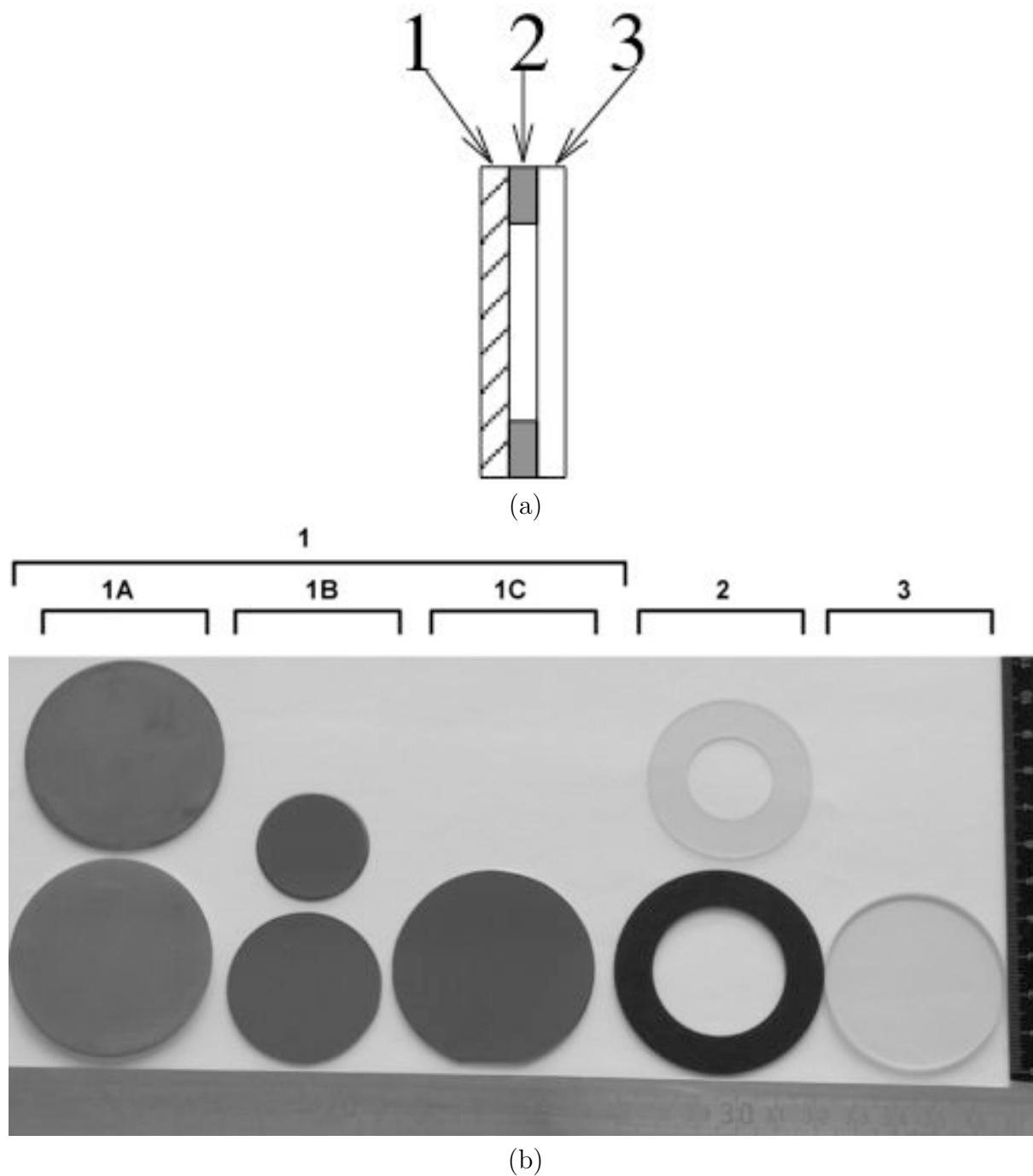
Figure 4.1: Schematic diagram of the discharge cell (a) and its components (b). 1 cathode; 1A metal plates made of copper (top) or nickel (bottom); 1B semiconductor wafers (top: Si:Pt, bottom: Si:Zn); 1C semi-insulating wafer made of GaAs:Cr; 2 dielectric spacer made of hard PVC (top) or synthetic resin (bottom); 3 transparent ITO glass anode;
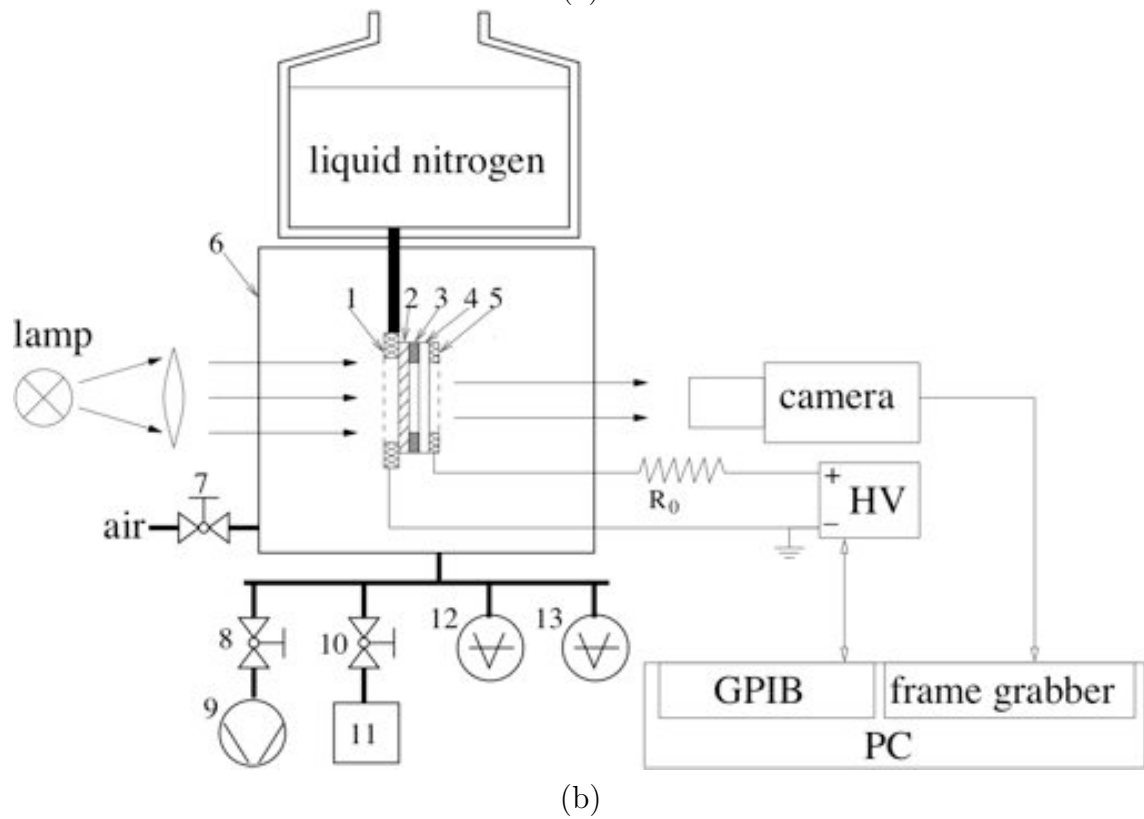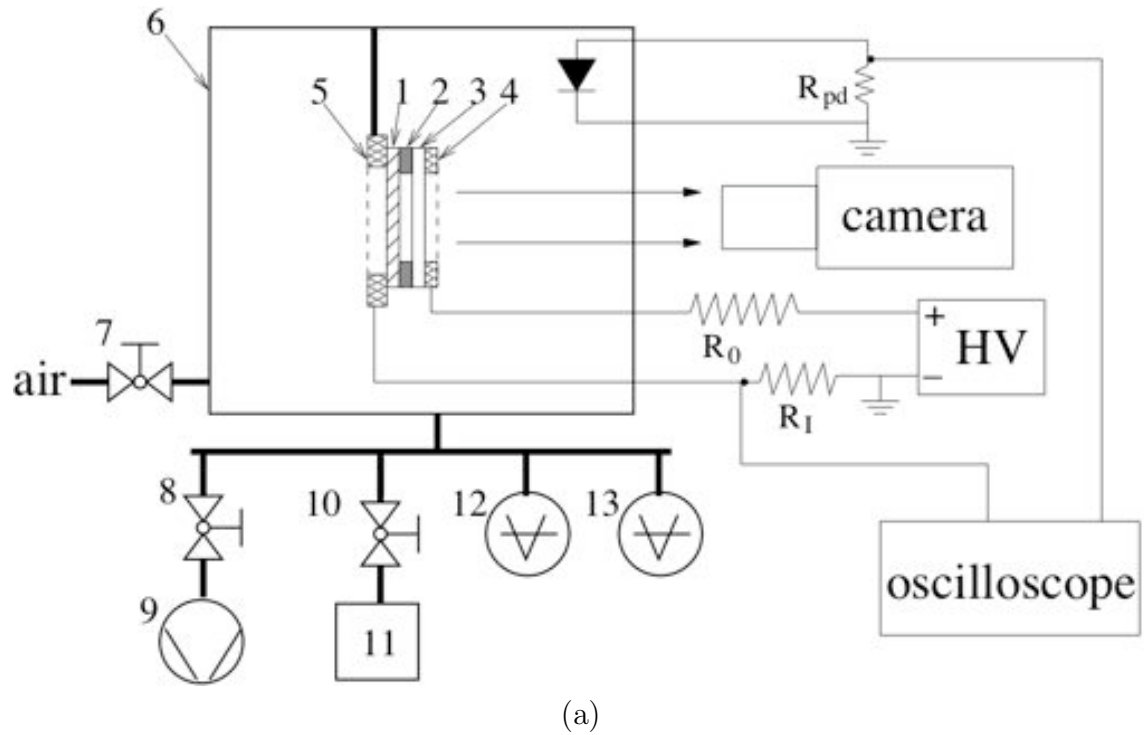
Figure 4.2: Schematic diagram of the experimental setup for studying gas discharges at room temperature (a) or at cryogenic temperature (b). 1 cathode; 2 dielectric spacer; 3 transparent anode; 4 contact ring; 5 sample holder/ cold finger; 6 gas chamber; 7, 8, 10 manual valve; 9 vacuum pump; 11 industrial gas bottle; 12, 13 pressure gauge.

discharge on a fast time scale, an OSD35-7 photodiode (OSI optoelectronics, Hawthorne, USA) with a load resistor R_{pd} was used. The circuit works in the photovoltaic mode where a photocurrent generated by the photodiode flows through the load resistor R_{ph} and results in a voltage drop. The voltage drop across R_{pd} recorded with an HP54602 digital storage oscilloscope (Agilent Technologies Inc., Palo Alto, USA) is a logarithmic function of the light intensity falling onto the active area of the photodiode. In our case where a 220 Ω R_{pd} was used, the rise time of the photodiode signal is about 450 ns. For recording the spatial distribution of the light emission, a CCD video camera or an image intensified camera are used. The VC45 CCD camera (PCO AG, Kelheim, Germany) delivers a video signal according to the CCIR or RS170 standard and the analog images are then converted to digital ones with a frame grabber installed inside a PC. The exposure time and frame rate are 40 ms and 25 fps (frames per second) respectively. For situations where shorter exposure time and/or higher frame rate are required, a MCP-PROXIFIER image intensified camera (PROXITRONIC, Bensheim, Germany) and a FASTCAM Super 10K readout unit (Photron Ltd., Tokyo, Japan) were used. The micro-channel plate intensifier (type: BV 2582 EX 5N from PROXITRONIC) controlled by a pulse generator (type: IG 5N from PROXITRONIC) allows exposure times down to 5 ns. The Super 10K readout unit supports frame rates up to 10000 fps. In practice, the frame rate and exposure time are chosen according to the intensity of the light emitted from the gas discharge and the dynamics of the phenomena of interest. The actual values used in measurements are usually far below the limits mentioned above.

The setup for studying gas discharges at cryogenic temperature has an origin in a special kind of infrared-visible image converter (Astrov et al., 1993). It turned out later that the system gave rise to spontaneous pattern formation under appropriate conditions (Astrov et al., 1996). The essential parts of the system (i.e. the gas chamber, liquid nitrogen cooling, illumination and the discharge cell etc.) have not changed much ever since. As illustrated in Figure 4.2 (c), the experimental system consists of a discharge cell (1-5) connected to a constant voltage source, a gas chamber (6) together with the pressure regulation subsystem (7-13), a liquid nitrogen container, a lamp for illuminating the semiconductor cathode and a camera.

The cell is mounted on the cold finger which is in contact with liquid nitrogen. Three variants of the coupling between the cold finger and liquid nitrogen were used throughout the present work (Figure 4.3). In the case of variants (a) and (b) where a solid copper cold finger is used, the liquid nitrogen (1) is inside a metal tube (2) terminated with a metal plate (4). An Indium seal (3) is used to prevent liquid nitrogen or impurity vapors from entering the gas chamber. A M-KK6 Pt-100 thermistor (7) from EPHY-MESS GmbH (Hofheim-Wallau, Germany) is mounted on the cold finger for temperature measurements. In one variant, there is an insulating foil (5) between the metal plate (4) and the cold finger (6) as illustrated in Figure 4.3 (a). Since the liquid nitrogen container and the gas chamber made of stainless steel are grounded, the current flows through R_I (see Figure 4.2 b), enabling the measurement of the time course of the current in the discharge circuit. However, this kind of coupling deteriorates the cooling effect and a temperature drift was observed due to the gas heating by the discharges. In order to improve the efficiency of cooling, the insulating foil (4) was removed in the other variant (Figure 4.3 b). As a result, R_I is short-circuited and the time course of the discharge current can no longer be directly registered. After removing the foil, the final stable

temperature of the cold finger decreases by about 10 K. When the chamber is filled with 250 hPa gas, for example, the lowest stable temperature is around 130 K in the case of variant (a) while it is about 120 K in the case of variant (b). In order to obtain lower temperatures and higher temperature stability, variant (c), a hollow cold finger made of steel in which the liquid nitrogen resides, was used. In this case, the lowest stable temperature is about 95 K.
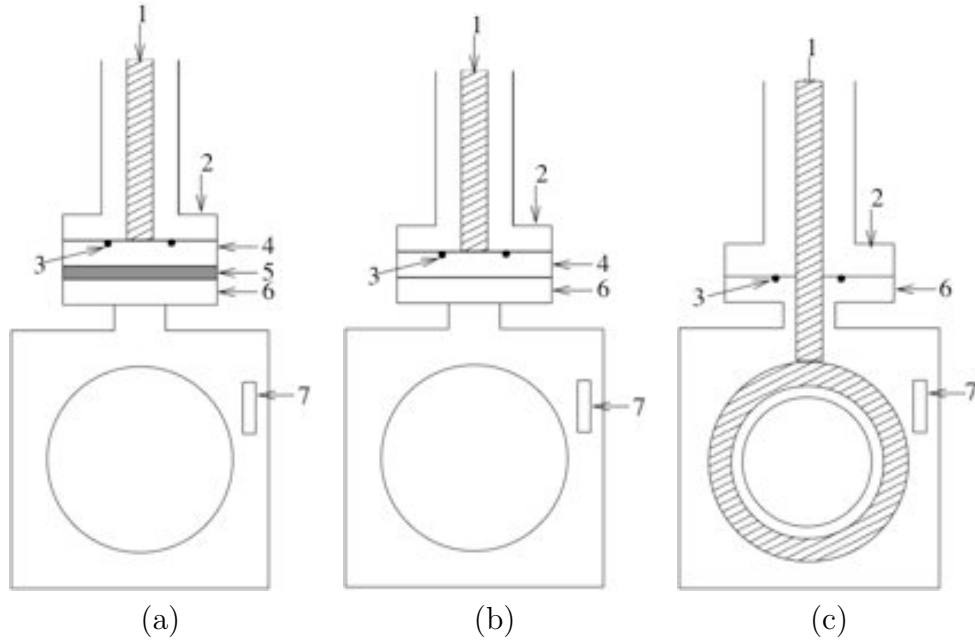

Figure 4.3: Schematic diagrams of various couplings between the cold finger and liquid nitrogen. 1 liquid nitrogen; 2 metal tube; 3 Indium seal; 4 metal plate; 5 insulating foil; 6 cold finger; 7 thermoresistor. (a) Coupling the solid copper cold finger with the liquid nitrogen via an insulating foil; (b) Direct coupling between the solid copper cold finger and the liquid nitrogen; (c) Hollow cold finger made of steel filled with liquid nitrogen.

The temperature of the cold finger is measured with a resistance (Pt-100 thermistor) calibrated to temperature values using the data from the specification. To check the relative error, the resistance values are measured at four temperatures: 20.4 Ω in liquid nitrogen (77 K); 101.3 Ω in cold water (276 K); 109.0 Ω in ambient air (294 K) and 113.0 Ω in warm water (307 K). As shown in Figure 4.4, these values are in good agreement with those given in the specification. The temperature is linearly related to the resistance between 70 and 340 K and can be calculated by:

$$T(K) = 2.46 \cdot R(\Omega) + 26.3 \tag{4.1}$$

An incandescent lamp driven with a constant current source is used to illuminate the wafer. With the help of a simple lens system, a relative homogeneous illumination onto the surface of the semiconductor cathode can be obtained simply by defocusing the lamp. The intensity of illumination is determined by the lamp power which can be varied between 6 and 200 W by changing the output current of the source from 3 to 15 A. Illumination can also be varied over a larger range through changes of the
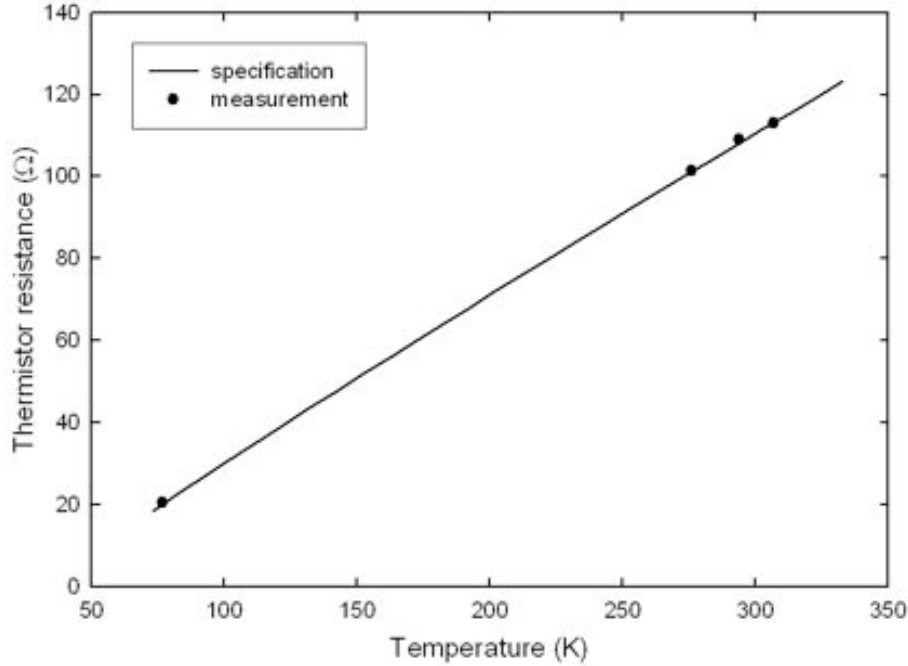
Figure 4.4: Calibration of the thermistor Pt-100, Specification and four measured values.

distance between the lamp and the wafer and the related optics. The usual lamp-to-wafer distance is about 1 m. In order to avoid saturation of the camera by the intense IR light penetrating the Si wafer, an IR filter is placed in front of the camera.

4.2 Materials

material	diameter (mm)	thickness (mm)
copper	52	1.5
nickel	52	4.0
Si:Zn(I)	40	1.0
Si:Zn(II)	30	1.0
Si:Pt	30	1.0
GaAs:Cr	51	1.5

Table 4.1: Material and geometry of various cathodes used in the present work.

In the present work, gas discharges with various cathode materials (i.e. metal, semi-conductor and semi-insulator) have been investigated. A copper plate and nickel plate were used as conductive cathodes. The surface of the plates was polished with 1 μm diamond polishing compound (Buehler, Lake Bluff, USA). For resistive cathodes, n-type Si compensated with Zn or Pt and semi-insulating GaAs compensated with Cr were chosen. According to the specification, the resistivity of the GaAs:Cr wafers (CrysTec GmbH, Berlin, Germany) is above 10^7 Ω·cm at room temperature. The Si:Pt wafers are produced through the following procedures: starting with an n-type Si with a resistivity of about 150 Ω·cm, Pt atoms are introduced through diffusion at 1280 °C for about 10

hours. A transparent ohmic contact layer (about 200 nm thick) on one side of the wafer is prepared by diffusing phosphor atoms. Two kinds of Si:Zn wafers are produced with n-type Si wafers with different resistivity, i.e. 20-30 Ω·cm and 100-150 Ω·cm. We shall refer to the former as Si:Zn(I) and to the latter as Si:Zn(II). The diffusion of Zn occurs at 1200 °C for 20 hours. In the case of Si:Zn(I) wafers, an ohmic contact layer is made by introducing boron atoms by ion implantation. For Si:Zn(II) wafers, a semi-transparent gold film is evaporated on one side of the wafer to form an electrical contact. The procedures of preparation of the semi-transparent gold film are described in Appendix A. The Si wafers with various dopants are produced by Megaimpulse (A. F. Ioffe Physico-Technical Institute, St. Petersburg, Russia). The resistivity of the wafers is of the order of 1 Ω·cm at room temperature and increases to above 10^{10} Ω·cm at 80 K.

4.3 Method

To carry out a measurement, the gas chamber is first evacuated with a rotary vane vacuum pump to a pressure below 0.1 hPa, and then filled with the gas from the bottle to the required pressure. There is no gas flow during the measurement. The discharge cell mounted onto the cold finger, which serves at the same time as sample holder, is immersed in the atmosphere of the working gas in the chamber. For measurements at room temperatures, the voltage is applied across the cell via a high-voltage feedthrough. The intensity distribution of the light emitted from the gas discharge is observed through the transparent ITO anode and the window of the gas chamber with a camera.
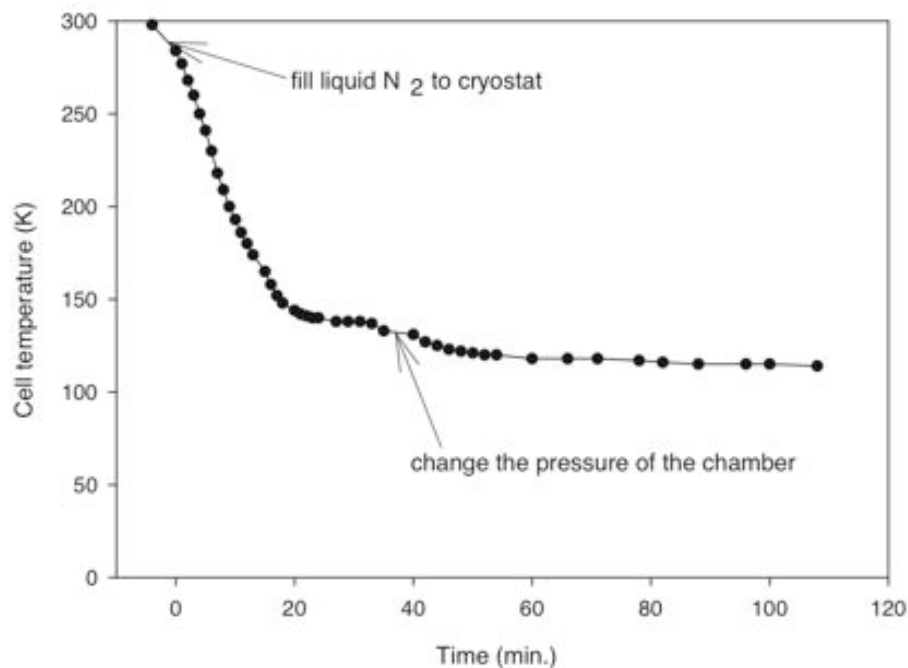

Figure 4.5: Evolution of the temperature of the cold finger during cooling.

For measurements using a semiconductor cathode at cryogenic temperatures, the coated side of the wafer is pressed onto the cold finger in order to achieve a good thermal and electrical contact. Liquid nitrogen is filled into the container after evacuating the

chamber and filling it with a working gas. After filling liquid nitrogen into the cryogenic container, the temperature of the cold finger decreases steadily as shown in Figure 4.5. It takes about 30 minutes to reach a stable value, the lowest temperature one can achieve with this setup. Although the cold finger is in contact with liquid nitrogen (77 K), the outer wall of the gas chamber is almost at room temperature. So heat flows continuously from the chamber wall to the cold finger through the gas in the chamber which is not a good thermal insulator at pressures of the order of hundred hPa. Consequently, the final stable temperature of the cold finger depends on the pressure inside the chamber as indicated in Figure 4.5. The final temperature of the cell depends on pressure. For example, the temperature is about 110 K when the chamber is filled with 20 hPa N_2, but increases to 125 K when the pressure is raised to 300 hPa. After the temperature is stabilized, gas discharges can be investigated as a function of various control parameters, e.g. gas pressure, illumination and source voltage.

4.4   Data and image acquisition

Pattern formation in the gas discharge system as of function of several experimental control parameters is the subject being investigated here. Important outputs of the system are the total current flowing through the external circuit and the spatial distribution of the light emission from the gas discharge, i.e. the distribution of the current. Due to the large aspect ratio of the system, the light intensity is integrated along the direction of the current flow, and a two-dimensional image is thus obtained. For image acquisition with video cameras and some image analysis, the program TGS (Dr. V. M. Marchenko, Institute of Applied Physics, University of Muenster) was used.

Since the source voltage is an important control parameter, in many measurements it is required to repeatedly change the output voltage, read the current and record an image of the discharge. With the help of the GPIB interface of the PS325 voltage source, it is possible to automate these tasks. A program was written by the author with LabView to control the output voltage and read out the values. A scan of U_0 over a certain range of voltages is implemented in the program. A flow chart of the program is given in Figure 4.6. The wait period after turning on the high voltage ensures that the recorded image corresponds to the stable state of the discharge after the transient POWER-ON effect. The wait period during which the high voltage is off can be chosen to avoid temperature rises due to the heating effect of the discharge. The user interface of the LabView program is shown in 4.7.
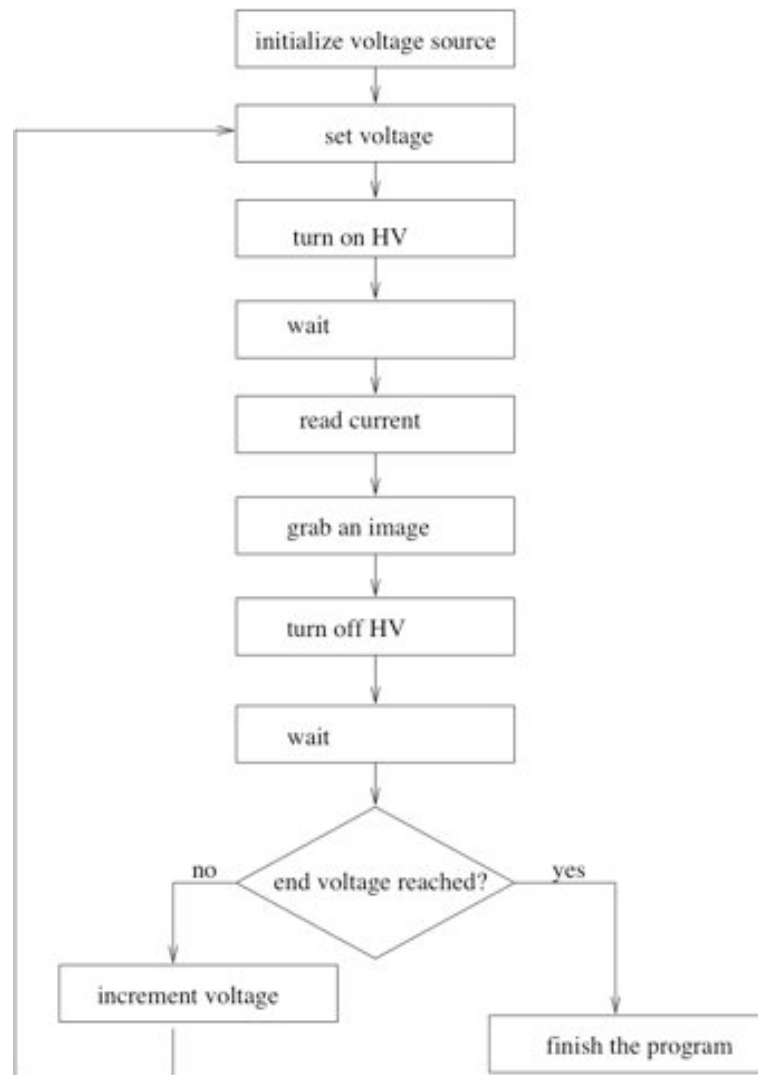
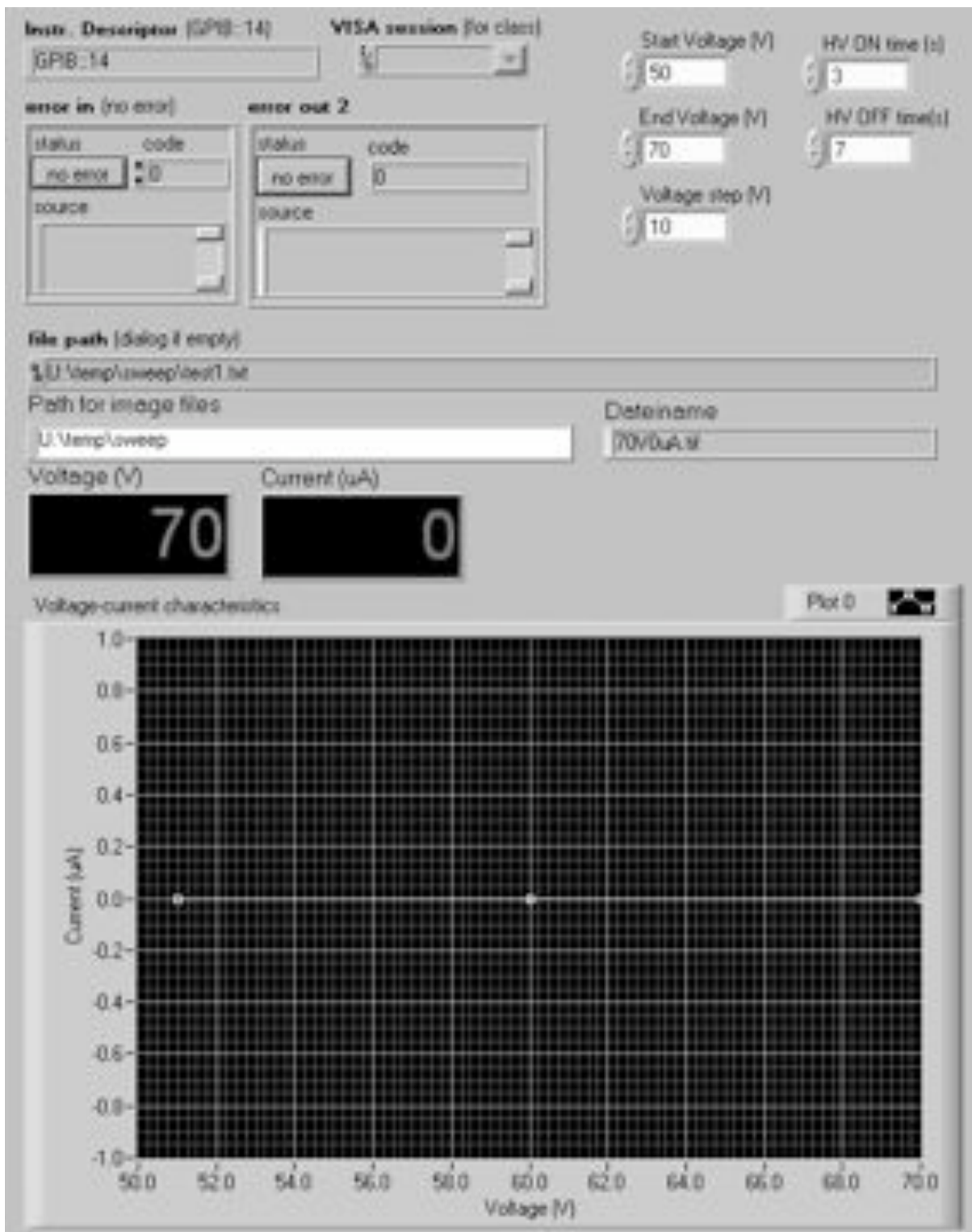Figure 4.6: Flow chart of the program for PS350 voltage source.

Figure 4.7: User interface of the GPIB program for the PS350 voltage source.

Chapter 5

Spots in micro-gap discharge systems with conductive electrodes

The motivation for a brief study on discharge phenomena in systems with conductive electrodes in the present work is twofold. First, the multiple glowing spots in the gas discharge with a Ni cathode reported by Nasuno (2003) seemed confusing since in the case of normal glow discharge, only a single spot with a well-defined normal current density can exist. The aim was to verify and extend the published results, as well as clarify the mechanisms. Secondly, the discharge parameters used in the present work for pattern formation, especially the sub-millimeter gap and the medium gas pressure, are quite different from those used in the traditional DC gas discharge with a typical tube geometry (tens or hundreds of cm long and filled with gases at pressures below 1 hPa). Moreover, the discharge cell is cooled down to about 120 K for studying pattern formation. Due to these differences, it is difficult to compare the measured values, e.g. the current density or voltage drop, with the literature values. In order to facilitate quantitative comparisons of the relevant quantities, measurements were made in systems with conductive electrodes under similar conditions to those used in the pattern formation studies.

5.1   Dynamic spot pattern

5.1.1   Intermittent discharge and multiple spots

The measurements in the work of Nasuno (2003) were made with a Ni cathode, a 100 μm thick gas gap filled with air and a ITO glass plate as anode. The serial resistor was 35.2 kΩ and the spot patterns were investigated in the pressure range between 45 to 60 hPa at room temperature for currents between 0.1 and 10 mA. As the first aim was to reproduce these results, similar parameters were chosen, i.e. a Ni plate as cathode and a 100 μm gap filled with 50 hPa air at room temperature. A constant voltage source was connected to the electrodes via a 80 kΩ serial resistor.

When a voltage of 600 V is applied across a 100 μm gap filled with 50 hPa air, a self-sustained discharge is obtained and the voltage source displays a steady averaged value 3.94 mA for the total discharge current (see section 5.1 for more about the voltage source). As shown in Figure 5.1, the light emission of the discharge were taken with an image intensified PROXITRONIC camera at different exposure times (see section 5.1
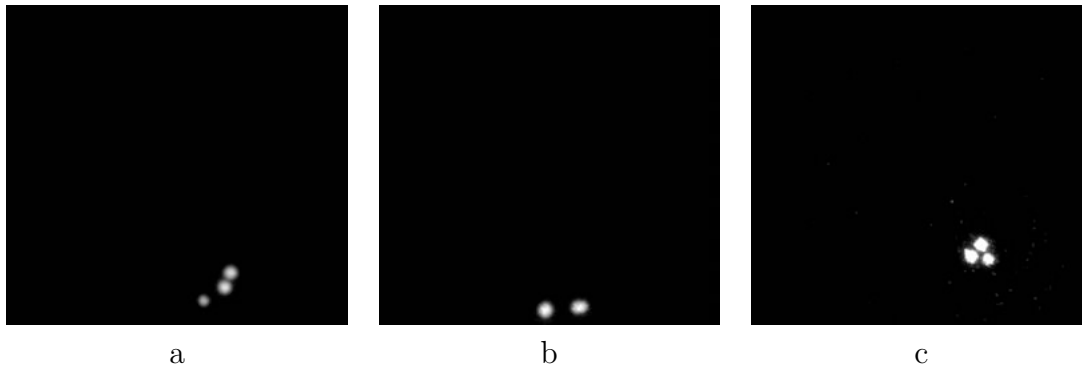
Figure 5.1: Spots in the discharge of a 100 μm gap filled with 50 hPa air and a Ni cathode photographed at different exposure times: (a) 100 μs; (b) 1 μs; (c) 10 ns. (Source voltage: 600 V; Averaged total current: 3.94 mA.)

for more about the camera). At exposure times of 1 μs and 100 μs, the photographs register multiple spots. As the time scale of the growth of a single Townsend avalanche (typically several ns) is much smaller than these exposure times, it is still possible that the observed multiple spots would result from a single spot jumping from one place to another. The image in Figure 5.1 (c) obtained with a 10 ns exposure time excludes that possibility because within this period it is impossible for the Townsend avalanche to change its position. This implies that the three light spots recorded in the image are due to light emission from separate avalanches occurring simultaneously at different places.
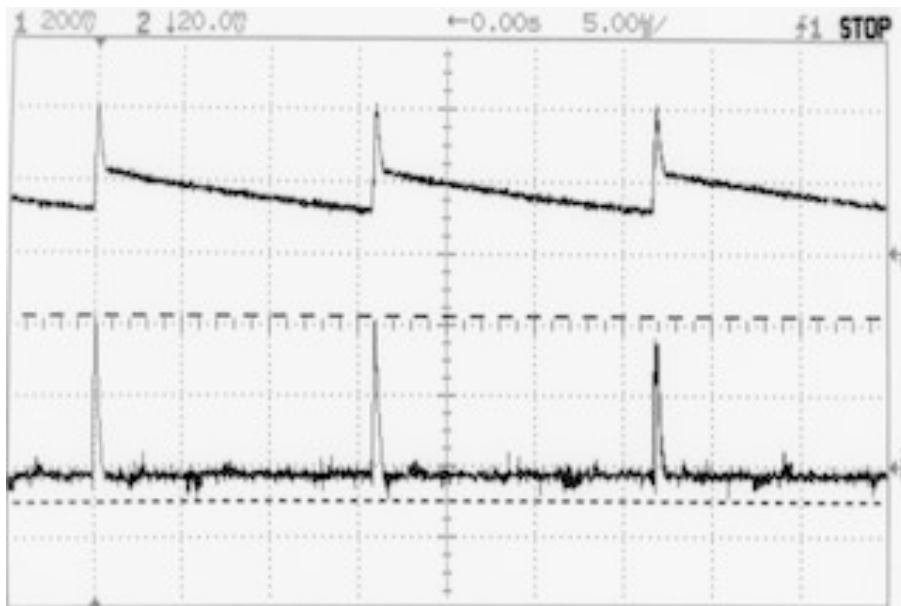
Figure 5.2: Typical time course of the current and the light emission from the gas discharge.

During the measurements, it was also noticed that not all images contain the bright spots, which indicates that the steady discharge is in fact intermittent. In order to verify it, the light emission of the discharge was monitored with a photodiode (see section 5.1 for more about the photodiode). The signals of the light intensity from the photodiode

and the total current in the circuit were recorded simultaneously with a digital storage oscilloscope (Figure 5.2). The current oscillates with a period of about 16 μs between two phases: a spike lasting about 1 μs and a slowly decaying tail. The spikes in the photodiode signal show that the light emission is intermittent. The light is only emitted when the current spikes appear and lasts also only for the duration of a current spike. This confirms that the discharge is indeed intermittent. The discharge phenomenon observed here can be understood as follows: the slowly decaying tail corresponds to the charging of the cell when the voltage is below the breakdown voltage of the gas and the spikes to the transient discharges of the cell when the voltage exceeds it. Within a single discharge of the cell, several avalanches may grow at different places in the gas where the electric field is sufficiently strong and seed electrons are available, leading to the appearance of multiple spots.

In order to confirm the above explanation, the characteristics of the decaying tail were studied in detail. During the charging phase of the oscillation, the circuit is effectively a simple RC circuit. This can be verified by studying the time constant of the circuit. The slowly decaying background corresponding to the charging current is an exponential function with a time constant $\tau = R_0 C$ where C is the effective capacitance of the circuit. The time constant are experimentally determined by fitting the decaying tail with an exponential function. As expected, it depends linearly on R_0 and is not influenced by the source voltage U_0 (Figure 5.3). The capacitance of the circuit is estimated to be about 255 pF. For an ideal parallel plate capacitor with a radius $r = 20$ mm and a gap $d = 100$ μm, the calculated capacitance ($C = \varepsilon_0 \pi r^2 / d$ where the vacuum permittivity $\varepsilon_0 = 8.85$ pF/m) is 110 pF. When the spacer thickness is changed to 200 μm, the capacitance determined from experimental data is 224 pF instead of the expected 55 pF. The discrepancy is probably due to the parasitic capacitance of the BNC cables (a 1m BNC cable with 50 Ω impedance has a capacitance of 100 pF).

This type of oscillation consisting of cycles of a charging and discharging phase is known as relaxation oscillation in nonlinear dynamics. It is characterized by a slow energy buildup and a sudden relaxation. The period of the relaxation oscillation is related to the threshold voltages (i.e. the extinction voltage of the discharge U_e and the breakdown voltage U_b) by:

$$T = R_0 C ln \frac{U_0 - U_e}{U_0 - U_b} \tag{5.1}$$

The dependence of the current oscillation on U_0 and R_0 is given in Figure 5.4. As U_0 is increased, the period of the oscillation decreases and the background as well as the peak value of the current increase. An average total current is obtained. Decreasing R_0 leads also to a rise of the total current, which is again realized by a higher charging and discharging current as well as a higher frequency of the cycle.

5.1.2   Transition to glow discharge

As described in the previous section, the period of relaxation oscillation decreases as the source voltage is increased. When it is below a certain threshold, the oscillation disappears and a constant current flows through the gas gap. This transition is illustrated in the measurement shown in Figure 5.5. In this case, the 200 μm gap is filled with 53 hPa air and a Cu plate is used as cathode. When U_0 is 1000V, the current oscillates between
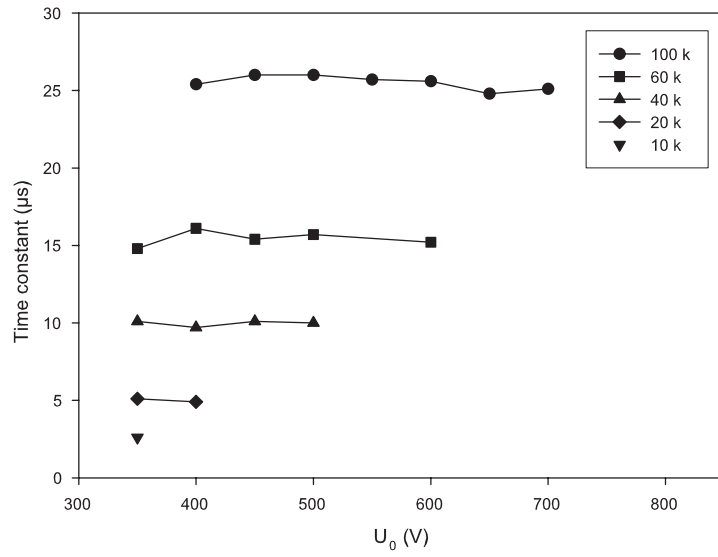
(a)
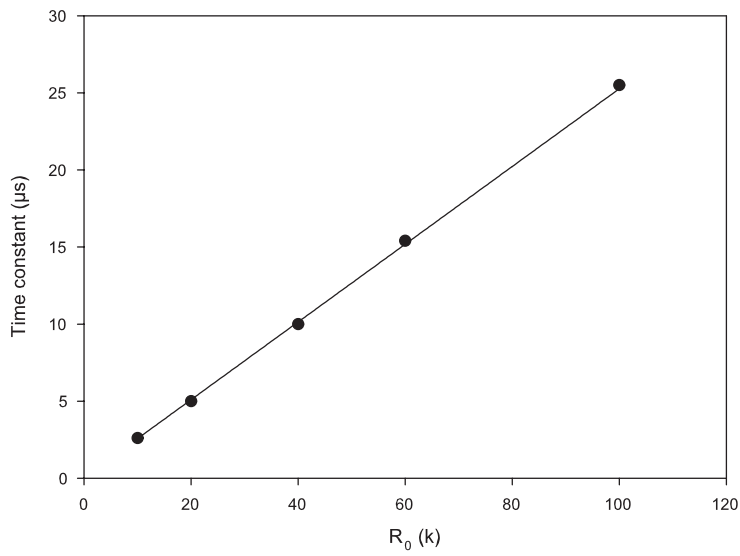
(b)

Figure 5.3: Time constant of the exponentially decaying part of the time course of the current in the discharge with a 100 μm gap filled with 50 hPa air.

(a)

(b)

Figure 5.4: Dependence of the period of the current oscillation in the discharge with a 200 μm gap filled with 53 hPa air on U_0 when $R_0 = 100$ kΩ (a) and R_0 when $U_0 = 500$ V (b).

about 5 (background) and 11 mA (spikes) with the typical characteristics of relaxation oscillation. At 1040 V, a constant current of 7.32 mA is obtained. The tran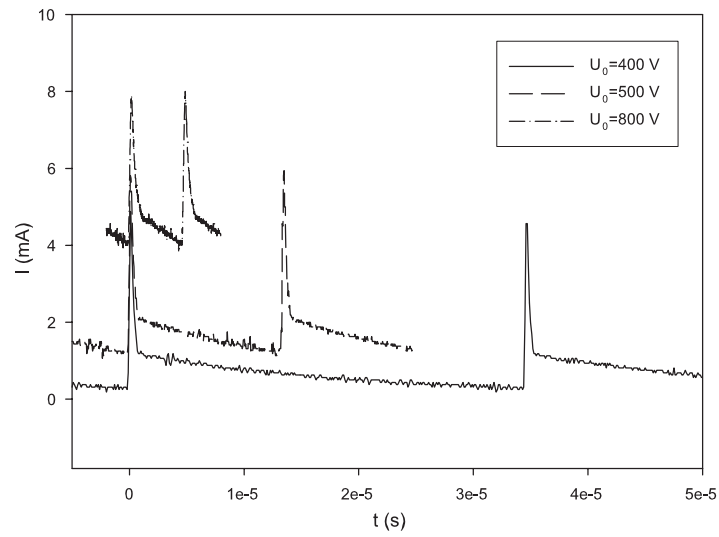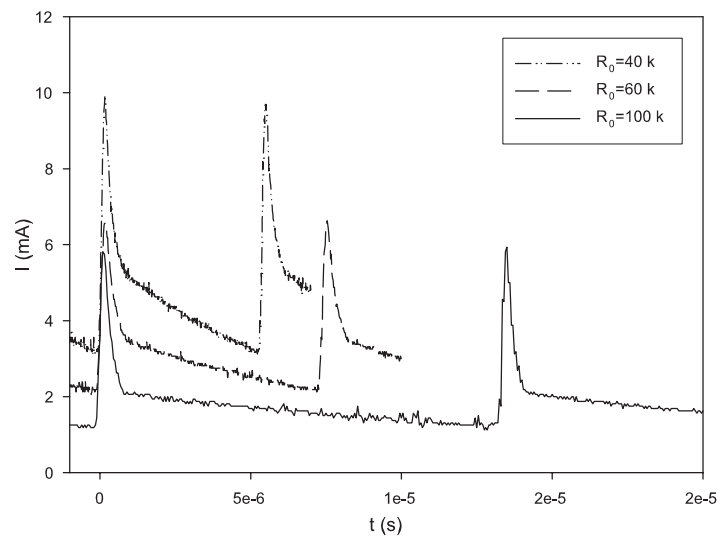sition also manifests itself in the appearance of the discharge spots. Before the transition, multiple spots with a rather diffuse border jump randomly in the discharge area. Thereafter either a stationary spot with a sharp boundary or a closed loop is observed with the unaided eye. The normal glow discharge is clearly obtained. It was noticed in several measurements that immediately before the disappearance of the oscillation the period decreases to a fixed value, e.g. about 3 μs for 186 hPa He in a 100 μm gap. This threshold is probably related to the ion transit time when considering the accumulation of space charges in the gas gap. The intermittent discharge occurs approximately within 1 μs, during which electrons and ions are created in Townsend avalanches. The electrons rapidly drift to the anode due to their higher mobility, while the ions drift much more slowly to the cathode. When the interval between two discharges is much longer than the ion transit time, no ions accumulate and the oscillation mode is stable. As the discharge frequency increases, the interval between successive discharges becomes comparable to the ion transit time, and ions start to accumulate close to the cathode where most of the electron impact ionizations occur. Once the cathode layer (i.e. a layer of positive ions in front of the cathode) is fully formed, the oscillation stops and the normal glow discharge is established.

The oscillations were also observed as a transient process immediately after applying a high voltage across the discharge gap. As an example, the breakdown processes of a 1 cm gap filled with 8 hPa air under 800 V were recorded (Figure 5.6). Due to the large overvoltage, in both cases the peak value of the initial spike, which corresponds to the first Townsend avalanche, is rather large compared to those of the following ones. The decreasing peak value of the following spikes implies a decreasing voltage drop across the gas gap, which results in avalanches at a smaller scale. The ever shorter interval between spikes indicates the accumulation of positive space charge. This is consistent with the statement in Druyvesteyn and Penning (1940) that the transition to normal glow discharge is often accompanied by an intermittent discharge. For more references on intermittent discharge and oscillations, see section 95 in Francis (1956).

5.1.3   Discharge spot in the glow mode

In the glow discharge mode there is only a single discharge spot as expected from the theory. In some cases the spot is stationary. Otherwise, as illustrated in Figure 5.7 it moves in a closed loop. It should be pointed out that the loop is closed when the image is taken with an exposure time longer than 200 μs, as in the case of unaided eye (integration time about 30 ms). In these images the trajectory of the spot is mostly attached to the boundary of the spacer. Nevertheless, a loop of irregular shape detached from the spacer was also observed. In this case, the inner diameter of the spacer is 30 mm and the time needed for the spot to run over a complete circle is about 240 μs. A rough estimation of the traveling velocity of the spot leads to a value of about 400 m/s. As this value is of the same order of magnitude with the speed of sound (331 m/s at room temperature), it is suspected that the motion of the glow spot is related to sound propagation in gas. The relatively higher speed of the spot is probably due to a slight heating effect, which is frequently the case for glow discharge.
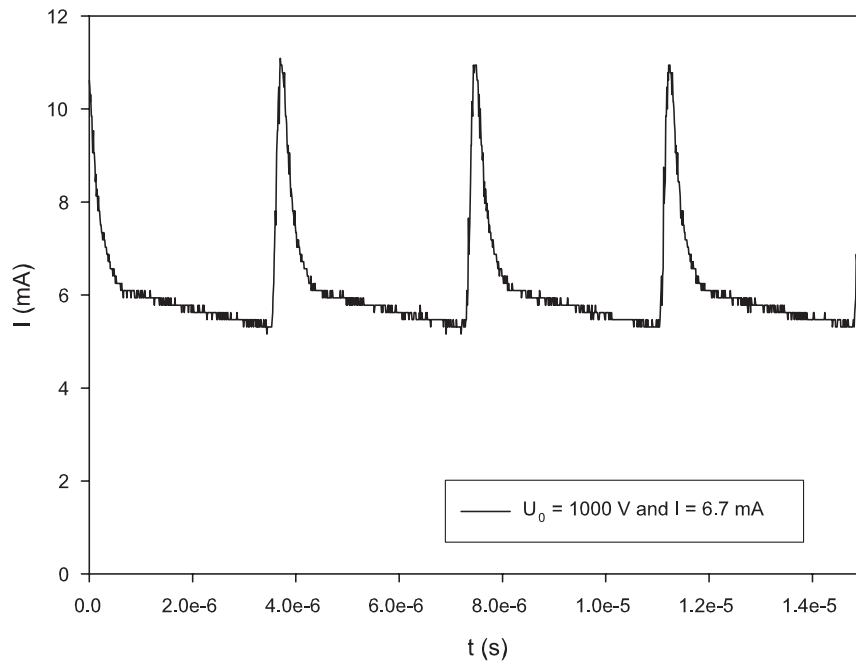
(a)
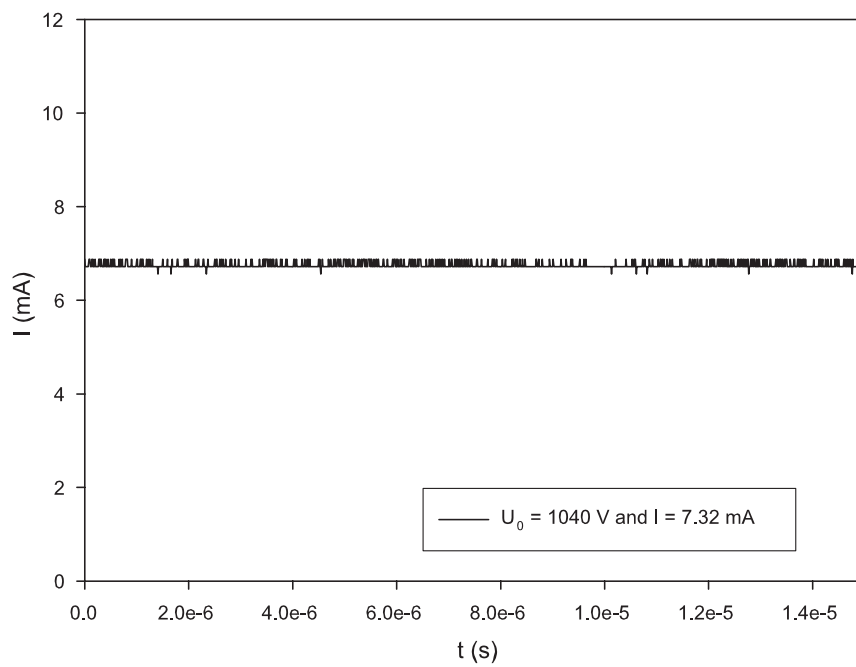
(b)

Figure 5.5: Transition from a current oscillation (a) to a constant current when the source voltage is increased from 1000 V to 1040 V in a discharge with a 200 μm gap filled with 53 hPa air (Cu cathode; $R_0 = 100$ kΩ; $R_I = 100$ Ω.).
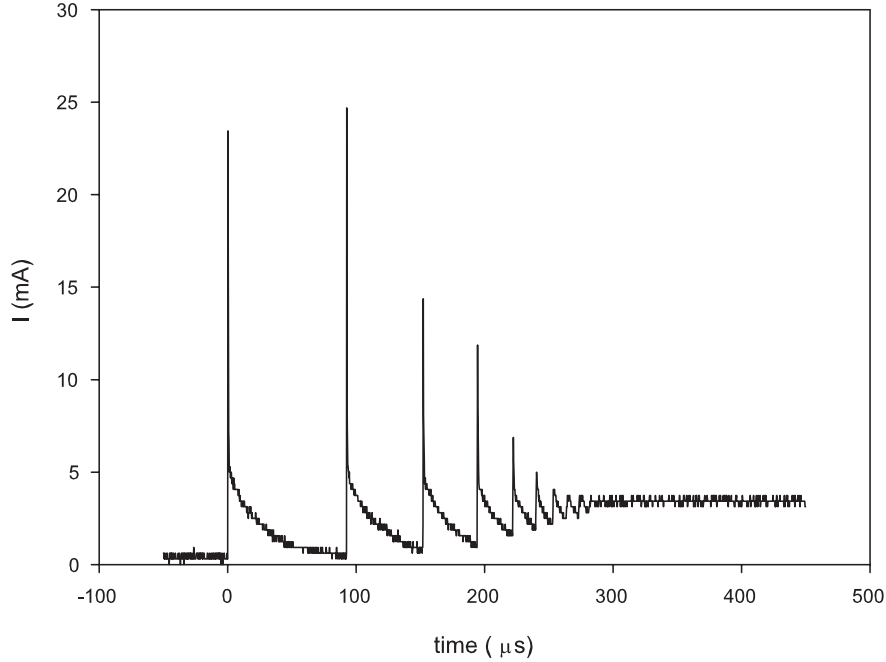
85

Figure 5.6: Transient oscillation during the POWER-ON stage of the glow discharge. ($U_0 = 800$ V; $R_0 = 1$ kΩ; $R_I = 100$ Ω)

5.1.4 Discussion

There are three different discharge modes when the gas gap is driven by a constant voltage source, i.e. Townsend discharge, intermittent discharge and glow discharge. In practice, the discharge gap filled with gas is always connected with the voltage source via a serial resistor. The mode of the gas discharge is not only determined by the gas pressure and gap size, but also by the external resistance, the capacitance and the driving voltage. For example, the relation between the ion transit time τ_i and the time constant of the circuit $R_0 C$ determines whether the discharge is intermittent. When $R_0 C$ is significantly large compared to τ_i, relaxation oscillation is observed. Otherwise, a steady current flows through the gas gap, depending on the source voltage and the R_0, either in the Townsend mode or in the glow mode.

It is interesting to note that the phenomena studied here are actually also of interest to certain applications. The relaxation oscillator consisting of a resistor, a capacitor and a gas discharge lamp (e.g. neon lamp) can be used as a flashing lamp or audio oscillator. The breakdown voltage and extinction voltage of a common NE-2 neon lamp are 110 V and 90 V respectively. According to Eq. 5.1, the frequency of the oscillator can be adjusted by choosing the appropriate combination of the resistance, the capacitance and the operation voltage.

There is also a mechanical counterpart to the electrical discharge system as far as the relaxation oscillation is concerned. As shown in Figure 5.8, the mechanical oscillator consists of a triangular bucket, a water reserve and a pump. The hanging point of the bucket is carefully chosen such that it tilts bit by bit as the water level is increased. After a slow buildup process of the water inside the bucket, it goes suddenly out of balance and

86
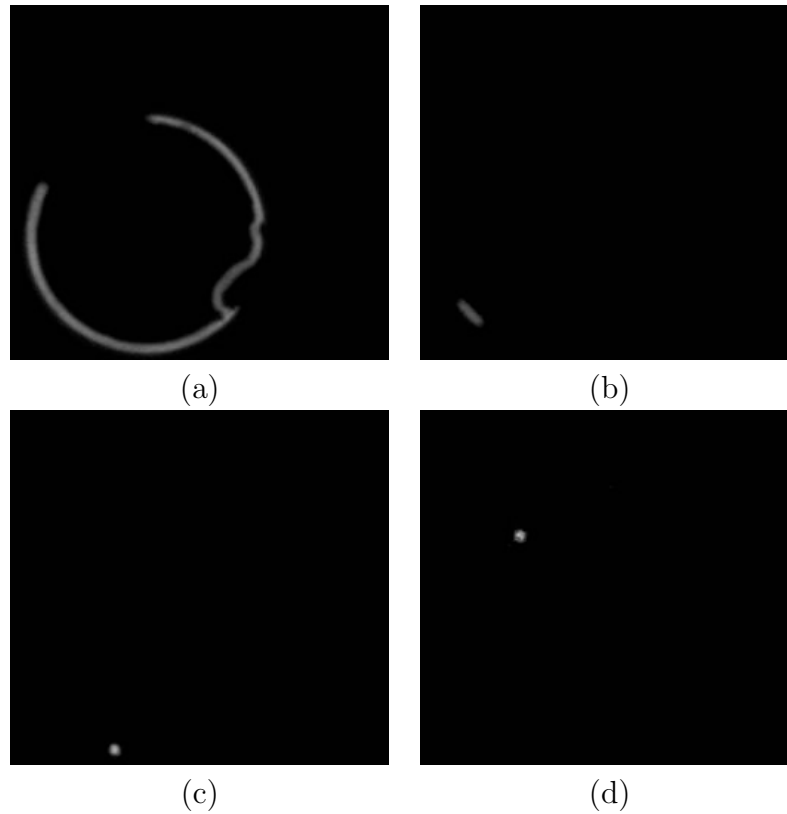
Figure 5.7: Traveling spot in the normal glow discharge of a 100 μm gap filled with 49 hPa air with a Ni cathode photographed at different exposure times: (a) 200 μs; (b) 10 μs; (c) 1 μs; (d) 50 ns. (R_0=80 kΩ, U_0=580 V, I=4.35 mA)
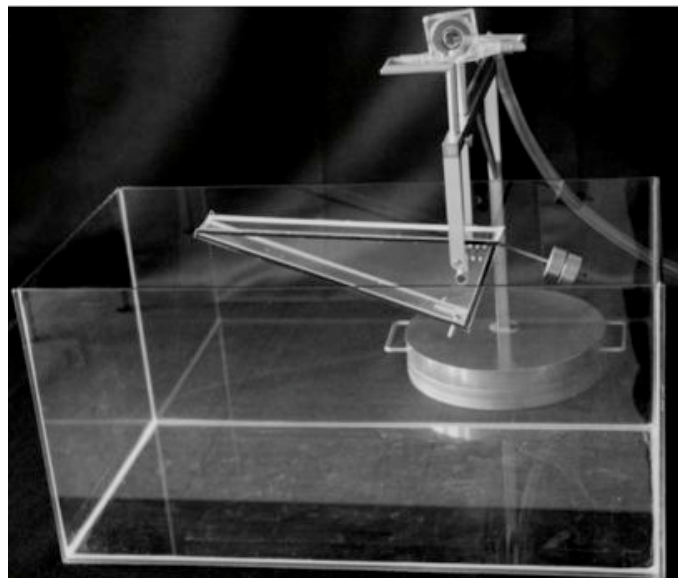
Figure 5.8: A mechanical relaxation oscillator. (Image source: http://www.uni-muenster.de/Physik.AP/Purwins/DE/Relaxationsschwinger-de.html)

its content pours down to the reserve beneath. Then the bucket returns to balance with an orientation corresponding to its residue water level. Water then starts to accumulate again in the bucket. With the help of a pump, the process of slow accumulation of water in the bucket and the fast release continue forever.

5.2 Current density of Townsend discharge and glow discharge

The spontaneous formation of regular patterns is related to the destabilization of the uniform state of the discharge. It is well-known that the uniform Townsend discharge will give way to glow discharge when the current density is gradually increased. This transition is driven by the space charge accumulated in the gas gap. The local current density is directly related to the density of charge carriers. Therefore, a measurement of the critical current density for the Townsend discharge under similar conditions (e.g. with small inter-electrode distance, at cryogenic temperatures) to those used in pattern formation studies is helpful for determining whether space charges play important role in pattern formation.
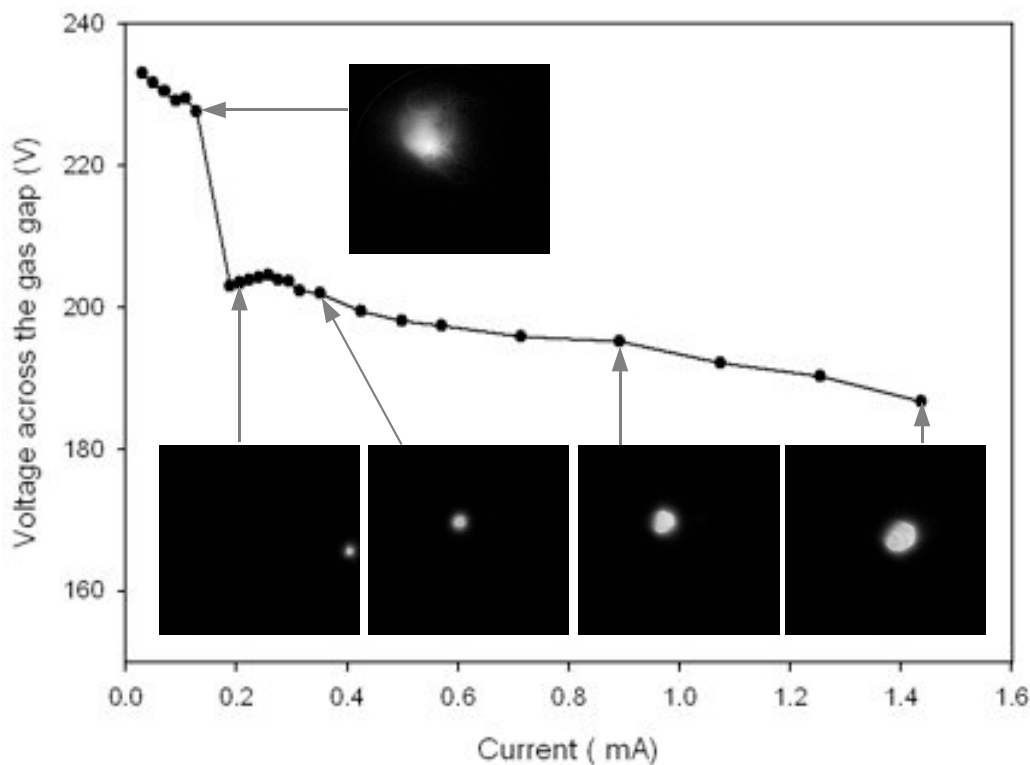
Figure 5.9: Transition from Townsend discharge to glow discharge. Images recorded with 40 ms exposure time with a CCD camera.

A measurement was made by using a Ni cathode and a 0.5 mm discharge gap filled with 19 hPa Ar. The discharge cell is cooled down to about 116 K. The serial resistor

R_0 is 566 kΩ and the source voltage U_0 is increased in steps of 10 V. The voltage-current characteristic and the form of the gas discharge are shown in Figure 5.9 (b). Electric breakdown of the gas occurs when the source voltage U_0 exceeds 250 V. A jump of the voltage drop across the gas occurs as the total current is increased with U_0. Before the transition, the lateral extension of the discharge is about 150 mm^2 and the current density is estimated to be about 0.8 A/m^2. The maintaining voltage of the discharge is about 230 V. The low current density and high maintaining voltage indicate that the discharge ovvurs in the Townsend mode. After the transition, the maintaining voltage decreases to about 200 V and a strong constriction of the discharge in the lateral dimension is observed. Moreover, the current density jumps to a value of the order of 100 A/m^2. As U_0 is further increased, the total current and the area covered by glow increase while the current density remains of the same order (i.e. 100 A/m^2 at a total current of 0.24 mA and 76 A/m^2 at 1.44 mA. This is one of the typical properties of normal glow discharge.

Chapter 6

Experimental investigation in gas discharge systems with Si:Pt cathodes

In this chapter a systematic study of the phenomenology of pattern formation in the dc-driven gas discharge systems with resistive semiconductor cathodes is presented. The control parameters chosen in the present study are the driving voltage U_0, the conductivity of the semiconductor σ (determined by the intensity of the illumination), the gas pressure p and the inter-electrode distance d. At the first stage, the phase diagram on the plane of U_0 and σ is experimentally determined for nitrogen and Si:Pt. During the measurement of each phase diagram, p and d are fixed. The reproducibility of the phase diagram is confirmed when using different samples under same conditions. The dependence of the phase diagram on p and d is then investigated. Subsequently, the investigation is extended to other gases, i.e. Ar, Ne and He.

6.1 Calibration of the conductivity as a function of the lamp power

Whereas the driving voltage U_0 is a direct control parameter, the conductivity σ of the semiconductor can only be varied indirectly by changing the intensity of illumination from an incandescent lamp. In our measurements the lamp is controlled by a constant voltage source. Therefore, the relationship between σ and the lamp voltage is required for the determination of the phase diagram. In order to determine σ, the discharge was operated in the homogeneous Townsend mode by choosing a rather small gap width, typically 60 μm. In this case, the conductivity can be calculated by $\sigma = d_{sc}/(A_{sc}R_{sc})$ where d_{sc} and A_{sc} are the thickness and area of the semiconductor. The resistivity of the semiconductor, R_{sc}, can be determined from the voltage-current curve of the hybrid semiconductor-gas layers at fixed illumination conditions. This calculation is only valid, however, when the current flow inside the semiconductor is homogeneous. This prerequisite is fulfilled in the present measurements and is confirmed by the observation that the light emitted from the discharge is homogeneous. Examples of the typical voltage-current curves under illuminations of different intensities are shown in Figure
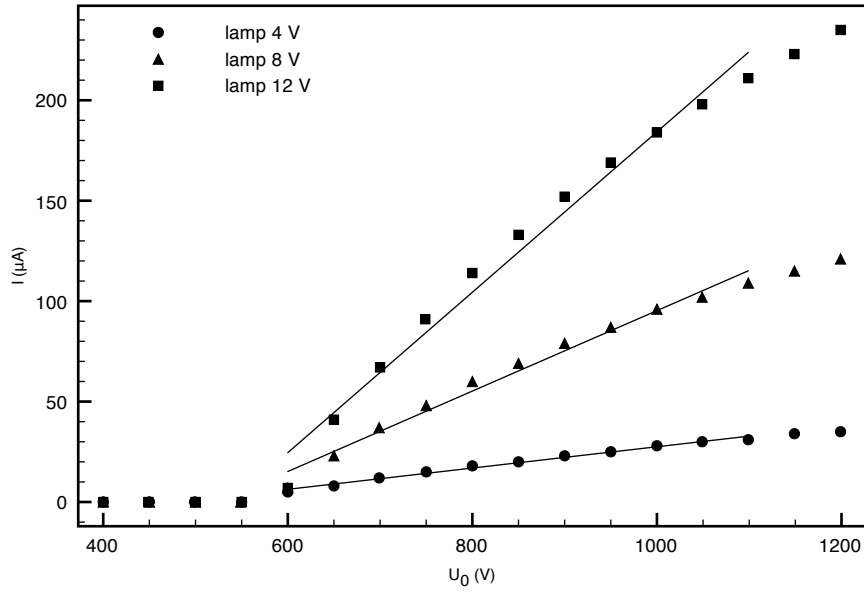
Figure 6.1: Voltage-current curves of the hybrid semiconductor-gas discharge cell under illuminations corresponding to lamp voltages of 4, 8 and 12 V. Experimental parameters: Si:Pt (label P4) at about 100 K; 160 hPa N_2 and 60 μm gap.

lamp voltage V	semiconductor resistivity MΩ	semiconductor conductivity $\times 10^{-9}$ ($\Omega \cdot$cm)$^{-1}$
4.0	18.7	1.29
4.5	15.7	1.53
5.0	11.9	2.02
5.5	10.2	2.36
6.0	8.8	2.74
6.5	7.4	3.26
7.0	6.1	3.95
7.5	5.5	4.38
8.0	4.9	4.92
8.5	4.5	5.35
9.0	4.0	6.02
9.5	3.7	6.51
10.0	3.3	7.30
11	2.9	8.31
12	2.5	9.64

Table 6.1: Conductivity values of a Si:Pt wafer (label P4) calculated with the resistance determined from the voltage-current curve of the Townsend discharge under illumination at different intensities.
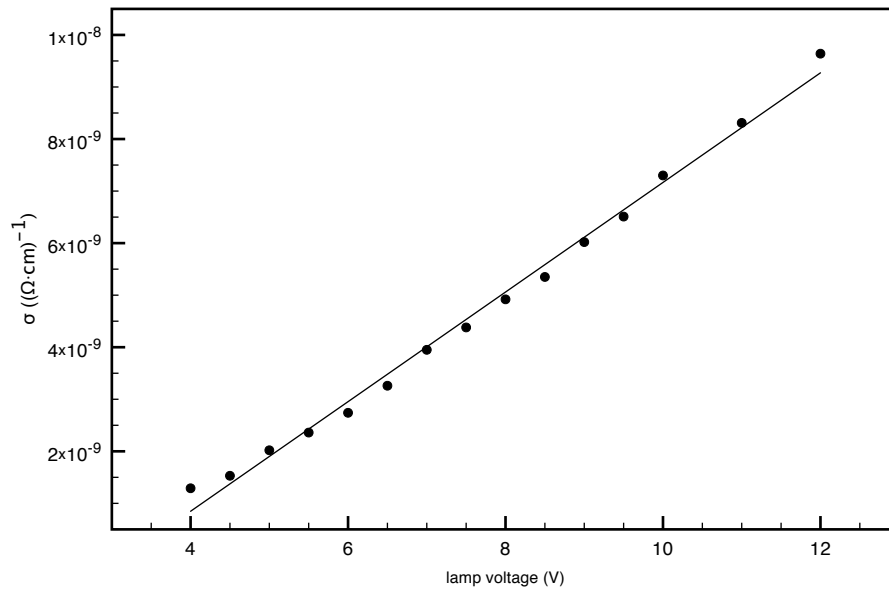
Figure 6.2: Linear dependence of the conductivity on the lamp voltage for a Si:Pt wafer under illumination.
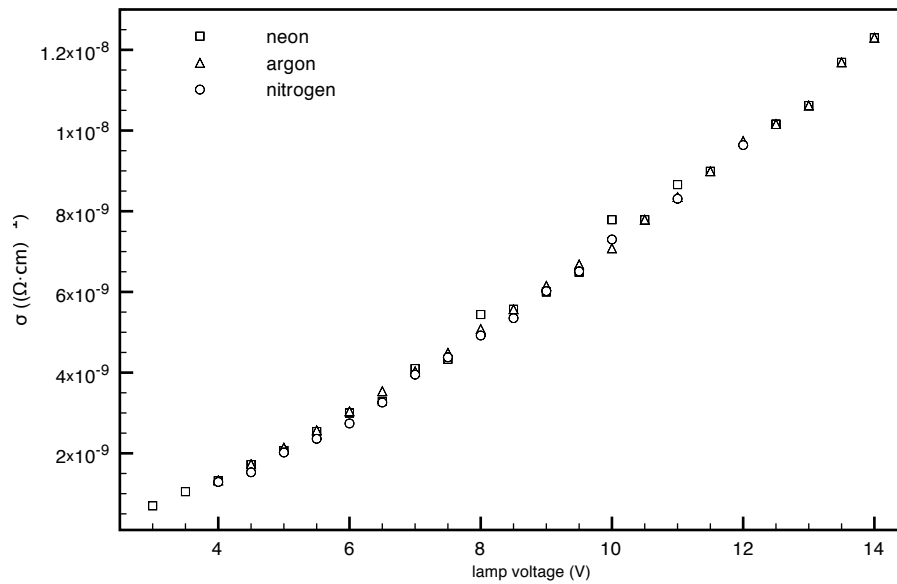
Figure 6.3: Conductivity of a Si:Pt wafer under illumination as a function of the lamp voltage determined from Townsend discharge with N_2, Ne and Ar.

6.1. At driving voltages below 500 V, the gas layer is insulating and no current flows through the discharge cell. As U_0 is increased above the breakdown voltage of the gas gap, a uniform Townsend discharge is established. Thereafter the current increases linearly with U_0. The linear fit in the figure is made with the data points corresponding to U_0 between 600 and 1100 V in this case. Since the sustaining voltage of Townsend discharge is a constant, the slope of the linearly rising part corresponds to the resistivity of the semiconductor. As seen in the curves, R_{sc} decreases as the lamp voltage is increased. As an example, the conductivity values of a 0.97 mm thick Si:Pt wafer ($\varnothing$ 23 mm) at different lamp voltages are listed in Table 6.1. Despite the complicated mechanism of the photoconductivity in the semiconductor, a simple linear relation between σ and the lamp voltage is obtained (Figure 6.2). A formula for the calibration can be obtained from a linear fit: $\sigma = (1.05 \cdot U_{lamp} - 3.36) \cdot 10^9$ where the unit for U_{lamp} and σ are V and $(\Omega \cdot cm)^{-1}$ respectively. Of course this method for the calculation of the semiconductor is only valid when the discharge with the chosen gas pressure is really operated in the Townsend mode. In our measurements, the current density flowing through the gas and the semiconductor is below 1 A/m^2. If we recall the measurements described in section 5.2, this value is of the same order of magnitude as the current density of Townsend discharge operated with a similar pd. Besides N$_2$, Ne and Ar were also used in the calibration measurements. As expected, the conductivity values under the same illumination are independent of the nature of the gas (Figure 6.3). This confirms that the conductivity as a function of the illumination (the lamp voltage in this case) is a property of the semiconductor alone and thus does not depends on the details of the discharge. The conductivity as a function
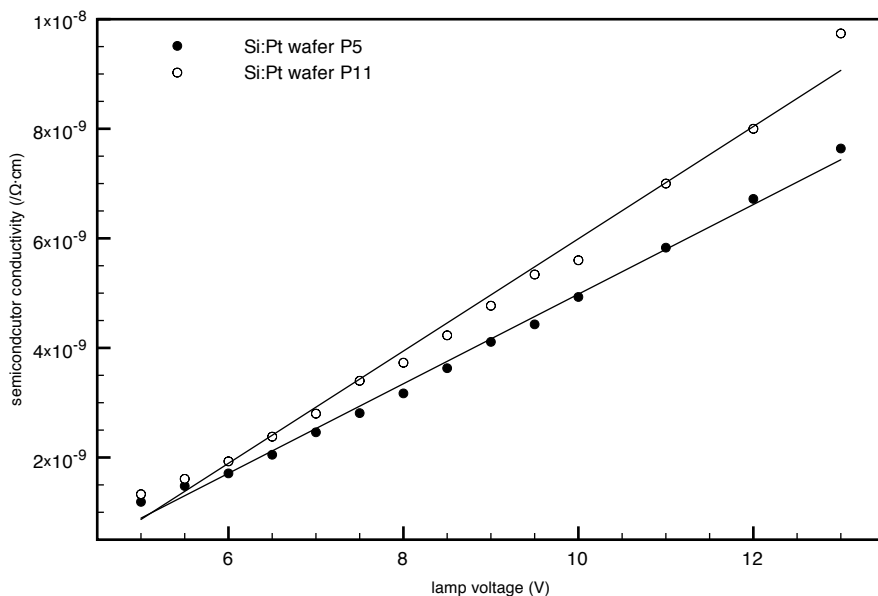

Figure 6.4: Linear dependence of the conductivity of two semiconductor wafers on the lamp voltage which corresponds to the intensity of the illumination onto the wafer. Experimental parameters: Si:Pt (label P5 and P11) at about 100 K; 160 hPa N$_2$ and 60 μm gap.

of the lamp voltage for two Si:Pt samples from the same batch during the production

94

was experimentally determined and the curves are given in Figure 6.4. At low lamp voltages the difference of the conductivity between the two samples is relatively small. It increases up to about 30% at higher lamp voltages. The linear fit gives the calibration relation $\sigma = (8.2U_{lamp} - 32) \times 10^{-10}$ $(\Omega \cdot cm)^{-1}$ for sample P5 and $\sigma = (U_{lamp} - 4.3) \times 10^{-9}$ $(\Omega \cdot cm)^{-1}$ for sample P11. The slope of the calibration line corresponds to the sensitivity of the semiconductor to the illumination. In this case, the difference of the sensitivity is about 20% between the two samples.

6.2 Pattern formation in N_2 discharge

6.2.1 Basic phenomenology

Given the gas pressure and the inter-electrode distance, the discharge gap is insulating and no current flows when the driving voltage U_0 is below the breakdown voltage U_b. This is referred to as the insulating state in the phase diagram. As U_0 is slightly above U_b, a uniform discharge is established in most cases (referred to as the uniform state). An example of the uniform discharge is illustrated in Figure 6.5 (a). The measurement was made with a 0.8 mm gap filled with 160 hPa N_2. The conductivity of the Si:Pt wafer is calculated to be 5.7×10^{-9} $(\Omega \cdot cm)^{-1}$, corresponding to a lamp voltage of 9V. The discharge is usually not absolutely homogeneous, but the spatial distribution of the luminosity is smooth compared to the patterned state. The current density is typically of the order of 0.1 A/cm^2. In addition, the luminosity is slightly higher at the center of the active area than at the boundary region. This results from the ring-shaped cold finger in our setup (see Chapter 3). In the centeral region the temperature is slightly higher and the conductivity is consequently higher. This explains the fact that when U_0 is increased the patterns appear first in the center as illustrated in Figure 6.5 (b). The hexagonal lattice consists of bright spots corresponding to higher current densities than the background. The spots observed here are not stationary, but drift along the line of reflection symmetry to the top right with a speed of about 0.5 mm/s. The spots emerge from the bottom left boundary of the cluster, drift across the cluster area and then disappear at the top right boundary. The coherent motion of the spots gives the visual effect that the hexagonal lattice drifts along one of its lines of reflection symmetry. A further increase of U_0 leads to the growth of the hexagonal cluster and the appearance of defects which destroy the coherent motion. The pattern illustrated in (b) and (c) are referred to as dynamic hexagonal spots. The transition from the uniform state to the hexagonal state is sharp. In the given example, the value is 2230 V with an uncertainty of 10 V. At still higher U_0 the spots pattern gives way to stripes with irregular dynamics and defects, referred to as dynamic stripes in the phase diagram. Here the transition voltage is 2300 V with an error of 20 V according to visual observation.

A direct transition from the uniform state to the dynamic stripes is observed when the conductivity of the Si:Pt wafer is lower. It is about 3.8×10^{-9} $(\Omega \cdot cm)^{-1}$ (lamp voltage 7.5 V) in the example shown in Figure 6.6. The discharge is initially uniform at $U_0 = 2340$ V and fluctuations start to grow when U_0 is above 2360 V. A striped pattern is established at higher voltages (images d, e, f in Figure 6.6). In this case, due to the relatively low conductivity the total current varies only by a few μA in response to the 20 V voltage steps. The transition is not sharp as U_0 is increased. As an example, a

(a) 2220 V, 13 μA (b) 2240 V, 20 μA (c) 2280 V, 34 μA

(d) 2300 V, 41 μA (e) 2320 V, 48 μA (f) 2340 V, 53 μA
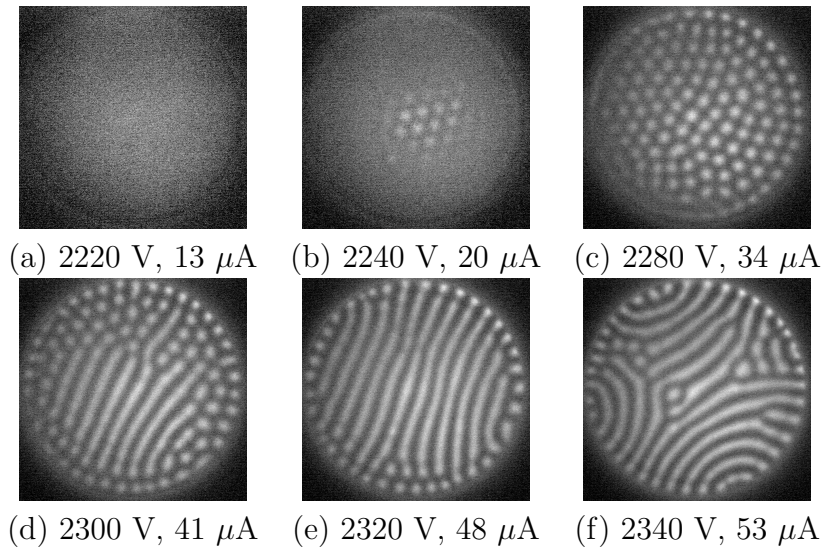
Figure 6.5: Transition from a uniform discharge to a hexagonal pattern and then to dynamic stripes with defects as U_0 is increased. The grayscale of each image is rescaled for better visualization. Experimental parameters: Si:Pt (label P4) at about 100 K; 160 hPa N_2 and 0.8 mm gap; lamp voltage 9 V.

(a) 2340 V, 29 μA (b) 2360 V, 31 μA (c) 2380 V, 35 μA

(d) 2400 V, 37 μA (e) 2420 V, 40 μA (f) 2440 V, 43 μA

Figure 6.6: Emergence of stripes out of the uniform background as U_0 is increased. The grayscale of each image is rescaled for better visualization. Experimental parameters: Si:Pt (label P4) at about 100 K; 160 hPa N_2 and 0.8 mm gap; lamp voltage 7.5 V.

transition voltage of 2400±20 V is determined based on the visual observation of the images.

6.2.2 Determination of a phase diagram on the σ-U_0 plane
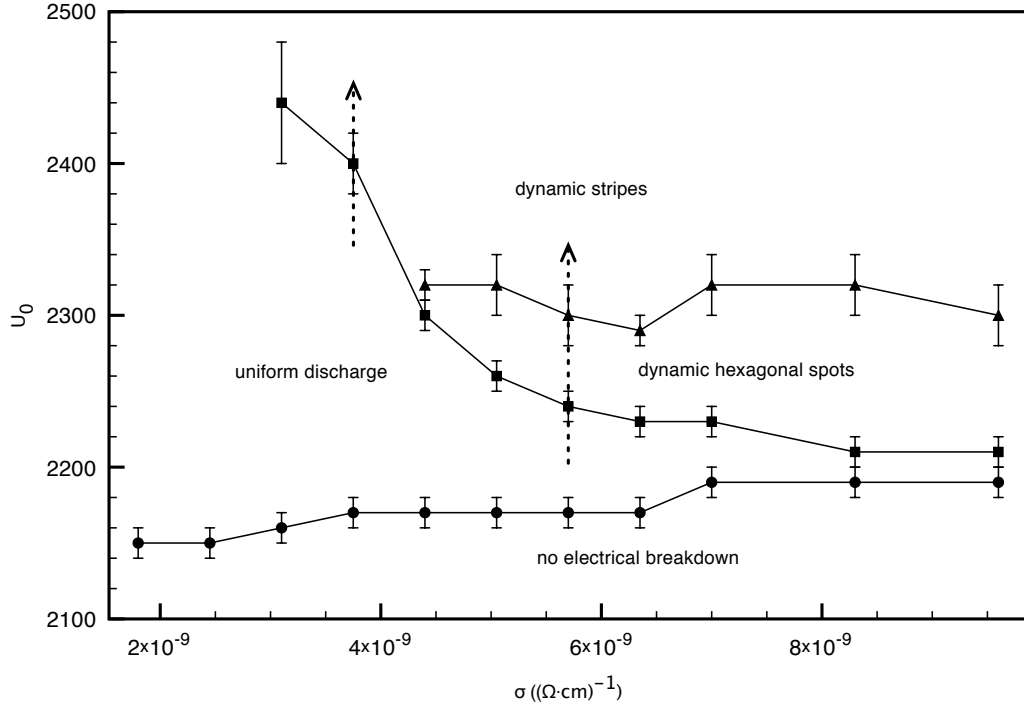
Figure 6.7: Typical phase diagram of different forms of patterns in the control parameter σ-U_0 plane. The left and right dashed lines with arrow correspond to the transition scenarios described in Figure 6.6 and 6.5 respectively. Experimental parameters: Si:Pt (label P4) at about 100 K; 160 hPa N_2 and 0.8 mm gap.

In order to produce a phase diagram on the σ-U_0 plane, the following procedure was carried out: First, the discharge cell with a Si:Pt wafer and the spacer of the expected thickness was installed onto the sample holder. Then the gas chamber was filled with the working gas to the required pressure. Thereafter, liquid nitrogen was added and the sample holder was cooled. After about 20 minutes, the temperature of the cathode reached a minimum value. Notice that the pressure in the chamber also decreased during the cooling process. The pressure after the cooling was given as an expe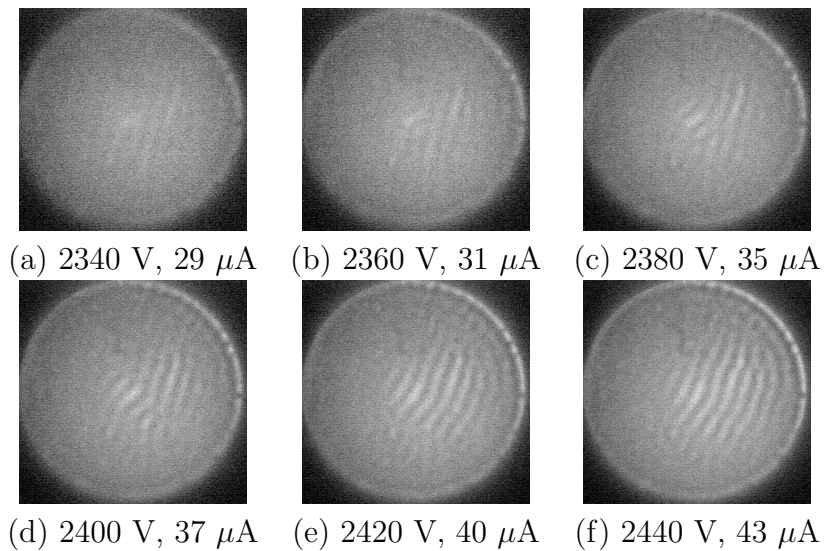rimental parameter in the results. After the temperature and the pressure were stabilized, a certain voltage for the lamp was set and the voltage U_0 across the discharge cell was increased in steps of typically 20 V from a value below the breakdown voltage up to a certain maximum. At each U_0, the current and the spatial distribution of the visible light emitted from the discharge were recorded. Then a different lamp voltage was set and the driving voltage was successively incremented. The recorded images and current values were used for determining the transition voltages for different forms of patterns.

Plotting the transition voltages at various conductivities of the semiconductor on the σ-U_0 plane gives the phase diagram. An example of such diagram shown in Figure 6.7

97

was obtained with a Si:Pt wafer and a 0.8 mm gap filled with 160 hPa N_2. The line at the bottom where the voltage values are below 2200 V corresponds to the breakdown voltage of the gas gap. Below this line the gas gap is insulating. Above it there is a region of uniform discharge, of which the upper boundary corresponds to the destabilization of this state and the emergence of patterns. Depending on the conductivity of the semiconductor, pattern formation can follow two scenarios, i.e. from the uniform to the striped state or to the hexagonal state. In the given example, the change of scenario occurs at a conductivity value of about 4.4×10^{-9} ($\Omega \cdot$cm)$^{-1}$.

6.2.3   Reproducibility of the phase diagram

The behavior of the system as a function of other parameters, e.g. gas pressure, gap size etc, is investigated further in section 6.2.4. Reproducibility of the diagram is essential for drawing any conclusions about its dependence on the different parameters. Two aspects of reproducibility were investigated. First of the all, the measurements are repeated with the same semiconductor sample and under the same experimental conditions in order to establish the spread of the experimental results. Subsequently, different semiconductor samples are used in measurements under the same condition. A comparison of the diagrams between different samples gives the information about the variability between samples.

Two phase diagrams obtained from separate measurements with the same semiconductor sample under the same experimental conditions are given in Figure 6.8. The empty symbols correspond to the data points determined from the first measurement while the filled symbols to the second. The four regions, i.e. the insulating state, the uniform state, dynamic hexagonal spots and dynamic stripes, are present in both diagrams, indicating that the different types of patterns are qualitatively reproducible. The two boundary lines separating the insulating state and the uniform state (i.e. the breakdown voltages of the gas gap) overlap within the uncertainties. There is a shift of the boundary corresponding to the destabilization of the uniform state, especially at a conductivity around 4×10^{-9} ($\Omega \cdot$cm)$^{-1}$. This is exactly the region where a change from the stripe-scenario to the hexagon-scenario occurs. At higher conductivities where only transition to dynamic hexagonal spots is observed, the difference between the two lines is getting smaller. The boundary of the transition from the dynamic hexagonal spots to dynamic stripes agrees rather well for the two measurements. Except the shift of the destabilization line of the uniform state along the conductivity axis, the spread of the data is in general of the order of the uncertainties.

Given the measurement spread of one sample, the second step is to compare the phase diagram obtained with different samples under the same conditions. The phase diagram in the $\sigma - U_0$ plane for the two samples were determined by operating the discharge with a 0.8 mm gap and N_2 at a pressure about 160 hPa (Figure 6.9). Both measurements were made by varying the lamp voltage up to 12 V. As a result of the different response of the samples to the illumination, the data points cover a smaller interval on the σ-axis for sample P5. The boundary between the insulating and the uniform state and that between the dynamic hexagonal spots and the dynamic stripes are well reproduced for the two sample. The boundary between the uniform state and the dynamic stripes is shifted by about 10^{-9} ($\Omega \cdot$cm)$^{-1}$ for sample P5 compared to the

Figure 6.8: Two Superimposed phase diagrams of the same semiconductor sample determined from two measurements repeated under the same experimental conditions. The empty and filled symbols correspond to the data points from each measurement. Experimental parameters: Si:Pt (label P4) at about 100 K; 160 hPa N_2 and 0.8 mm gap.

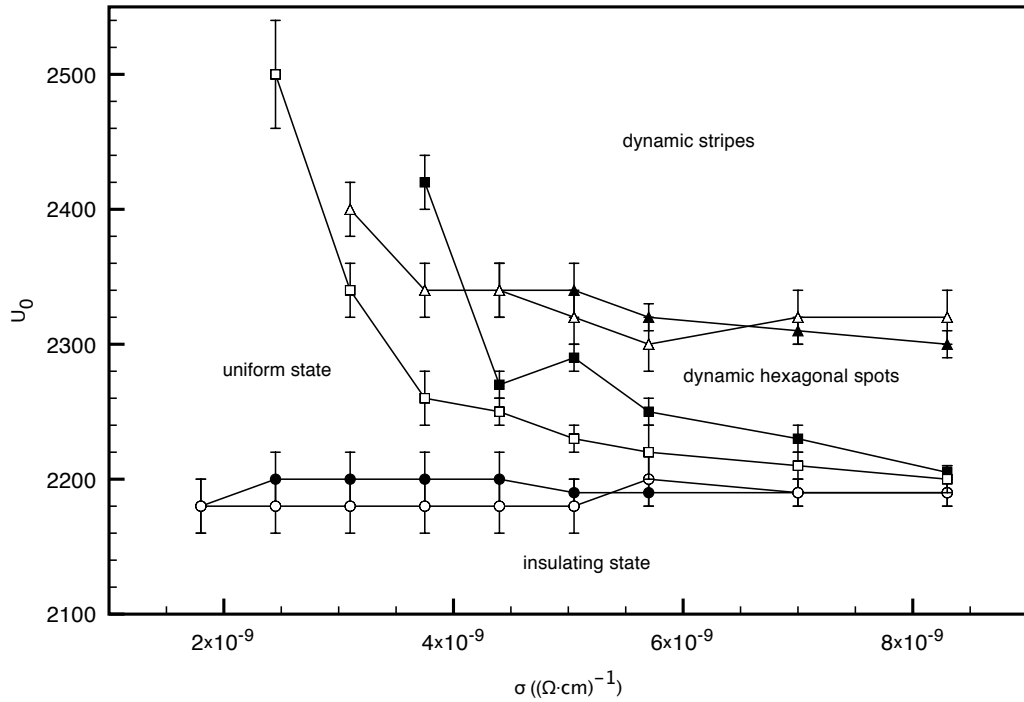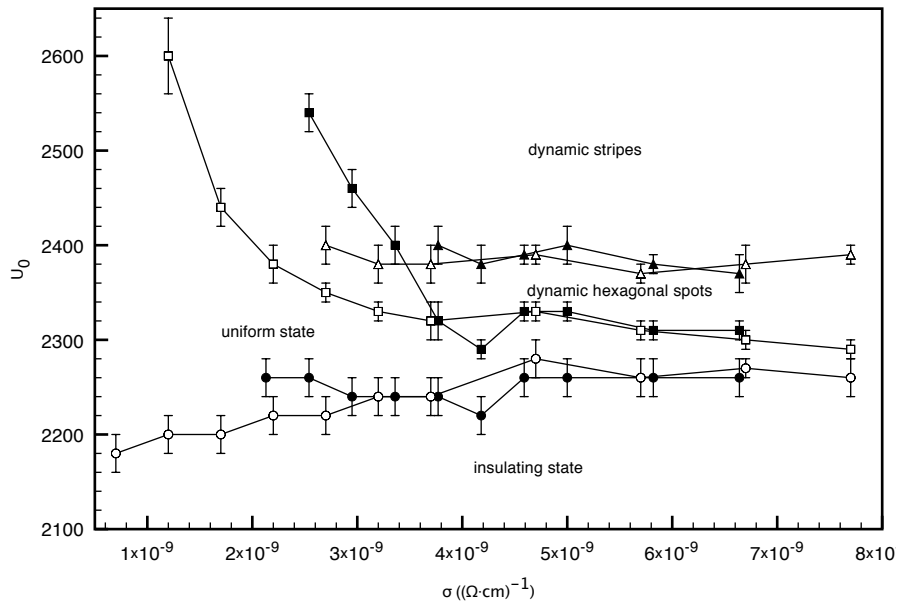Figure 6.9: Superimposed phase diagrams of two semiconductor samples obtained from measurements under the same experimental conditions. The empty and filled symbols correspond to the data points for sample P11 and P5 respectively. Experimental parameters: Si:Pt at about 100 K; 160 hPa N_2 and 0.8 mm gap.

case for sample P11. This kind of shift has also been observed when the phase diagram was determined from the repeated measurements with the same sample. Therefore, the shift does not result from the variations of the material properties between the samples, especially when considering the fact that the boundary between the uniform state and the dynamic hexagonal spots at higher conductivities overlaps very well for the two samples. In general, our results confirm a quantitative reproducibility of the phase diagram for different samples from the same batch during the material production. Therefore, the same sample P4 was used in the measurements for investigating the dependence of the phase diagrams on other control parameters.

6.2.4 Dependence of the phase diagram on p and d
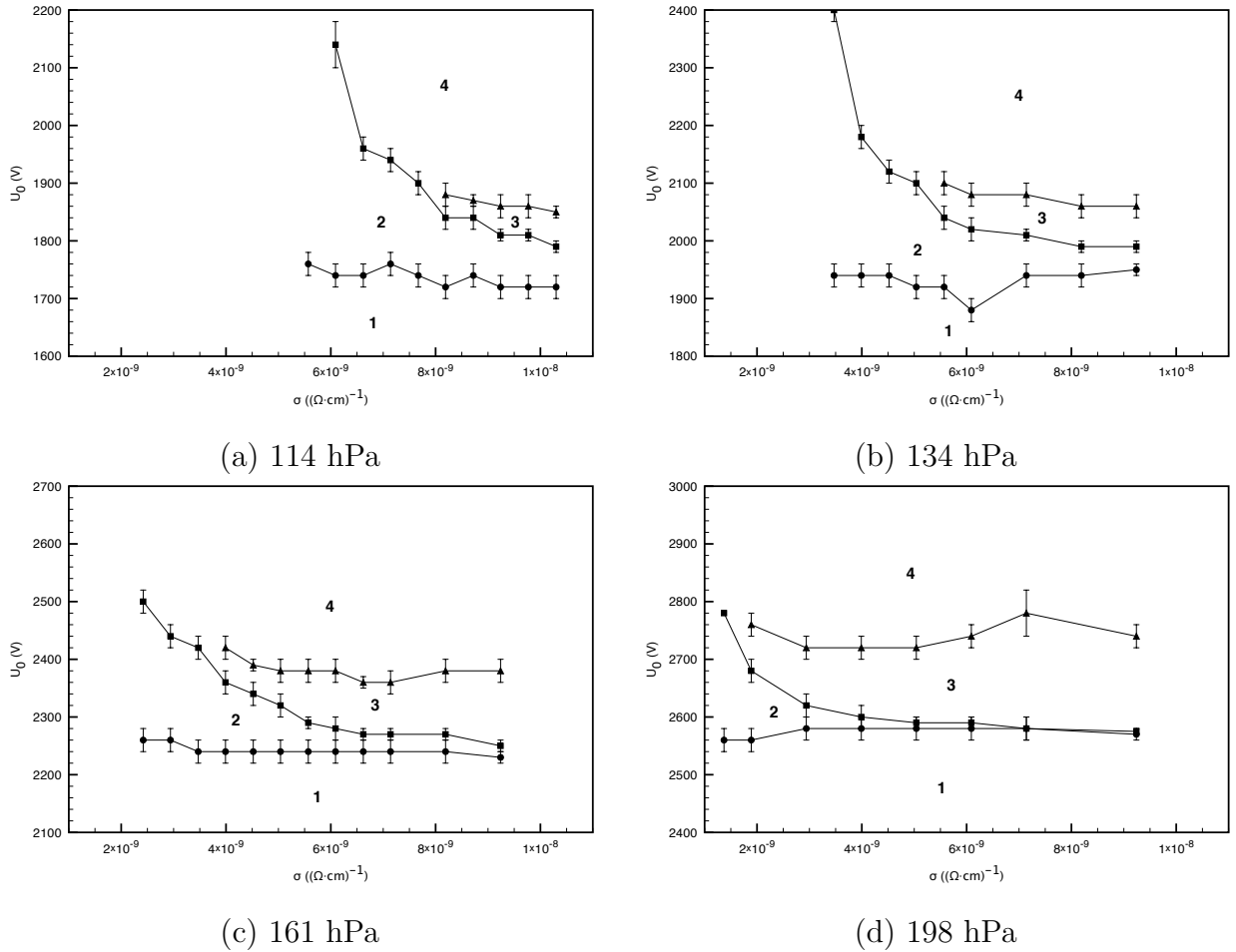
Figure 6.10: Phase diagrams obtained in gas discharges with a 0.8 mm gap at different pressures. 1 insulating state; 2 uniform state; 3 dynamic hexagonal spots; 4 dynamic stripes. Experimental parameters: Si:Pt (label P4) at about 100 K and N_2.

In order to investigate the pressure dependence of the phase diagram, a series of measurements were made in gas discharges with a 0.8 mm gap filled with N_2 of four pressures, i.e. 114, 134, 161 and 198 hPa. In order to facilitate the comparison, the U_0-axis covering an interval of 600 V and the σ-axis between 10^{-9} and $1.1 \cdot 10^{-8}$ $(\Omega \cdot cm)^{-1}$

are chosen to represent the phase diagrams obtained at different pressures (Figure 6.10). First, the breakdown voltage for the 0.8 mm gap increases with pressure p. This causes a shift of the diagram upwards along the U_0-axis as the pressure is increased. The topology of the phase diagram is independent of the pressure: at low conductivities (i.e. weak illumination), the transition from the uniform state (2) to the dynamic stripes (4) is observed whereas the transition from the uniform state (2) to dynamic hexagonal spots (3) is obtained at high conductivities. A pressure change shifts the boundary lines and varies the region of existence for the different phases. At p = 114 hPa, the uniform state dominates the diagram. The σ value corresponding to the change of the transition scenario is about $8 \cdot 10^{-9}$ $(\Omega \cdot cm)^{-1}$ and the region of existence for the dynamic hexagonal spots spans an interval of less than 100 V. At p = 198 hPa, the region of existence for the dynamics spots covers a significant region along both axes. With increasing p the uniform state at high conductivities, defined by the breakdown line and the boundary with the dynamics hexagonal spots, shrinks steadily. There is a clear tendency for the boundary corresponding to the destabilization of the uniform state to shift to the left along the σ-axis as p increases.

(a) 228 hPa   (b) 269 hPa
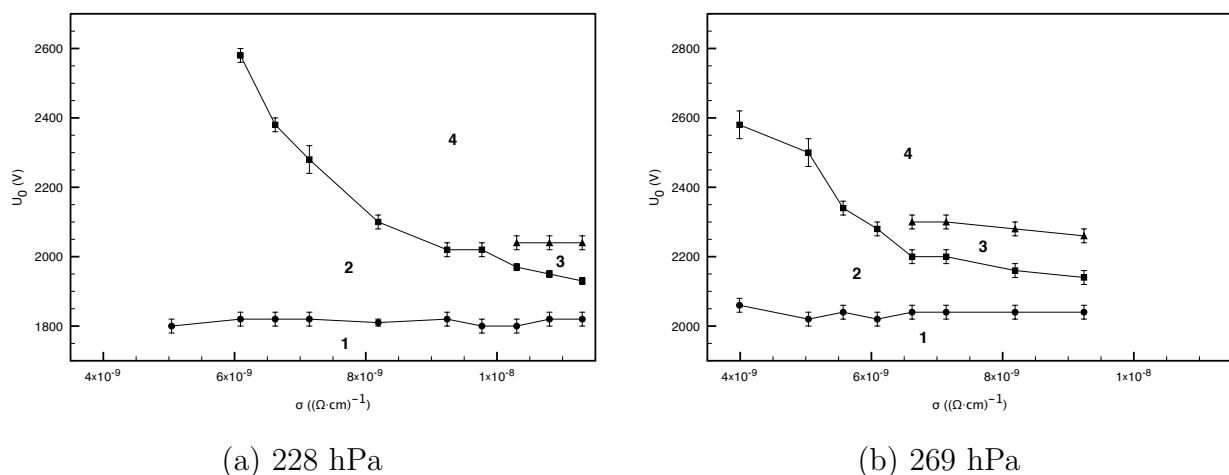
Figure 6.11: Phase diagrams obtained in gas discharges with a 0.4 mm gap size at pressures of 228 hPa and 269 hPa. 1 insulating state; 2 uniform state; 3 dynamic hexagonal spots; 4 dynamic stripes. Experimental parameters: Si:Pt (label P4) at about 100 K and N_2.

Two phase diagrams were determined in measurements with a 0.4 mm gap (Figure 6.11). When the gas pressure is below 200 hPa, the uniform discharge is stable within the regions on the σ-U_0 plane accessible with our experimental setup. Therefore, two pressures higher than that used with a 0.8 mm gap (i.e. 228 hPa and 269 hPa) are chosen in order to obtain the destabilization of the uniform state. At p = 228 hPa, the transition to dynamic stripes is observed in a large range of σ. Only at conductivities above 10^{-8} $(\Omega \cdot cm)^{-1}$, can a transition to dynamic hexagonal spots be found. As p is increased, the region of existence for dynamic hexagonal spots shifts to smaller conductivities. A similar behavior is also observed in the case of discharges with a 0.8 mm gap.

Finally, pattern formation was investigated in discharges with two different gap sizes, 0.6 and 1 mm. The pressures are chosen such that the product of the gas pressure p and the gap size d is 10.8 hPa·cm. As seen in the diagrams (Figure 6.12), the breakdown

voltage is about 2020 V for a 0.6 mm gap at 181 hPa and about 1940 V for a 1 mm gap at 108 hPa. Considering an uncertainty of 20 V for the values, the difference is below 5%. However, the feature of the phase diagram is dominated by the influence of the pressure. At high pressures the region of existence for dynamic hexagonal spots is large and shrinks as the pressure is decreased.
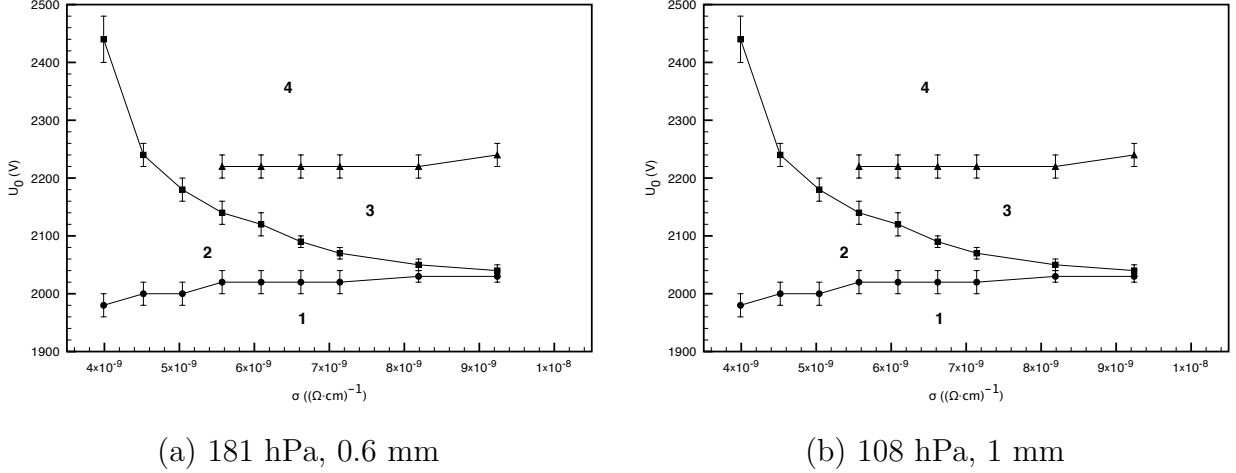

(a) 181 hPa, 0.6 mm

(b) 108 hPa, 1 mm

Figure 6.12: Phase diagrams obtained in gas discharges with a 0.6 mm gap at 181 hPa and a 1 mm gap with 108 hPa. 1 insulating state; 2 uniform state; 3 dynamic hexagonal spots; 4 dynamic stripes. Experimental parameters: Si:Pt (label P4) at about 100 K and N_2.

6.3 Pattern formation in discharges with noble gases

At the second stage of the investigation, the study was extended to the use of noble gases. The phenomenology in Ar discharges is qualitatively different from that in N_2 discharge. In the following sections, a basic phenomenology and the typical phase diagram are described. The investigation of the dependence of the phase diagram on pressures and gap size is then presented. Finally, results obtained in discharges with other noble gases, i.e. He or Ne, are discussed.

6.3.1 Typical phase diagram and its reproducibility

The transition scenario observed in Ar discharge is completely different from that in N_2 discharge when the uniform state is destabilized. The images shown in Figure 6.13 illustrate a typical scenario of pattern formation in discharges with a 0.8 mm gap filled with 255 hPa Ar. In this case, the lamp voltage is kept at 9.5 V and the driving voltage U_0 is increased gradually. At 880 V, the discharge is uniform in the active area. A 20 V increase of U_0 leads to the emergence of three sets of stripes which cross at 60° with respect to each other. This results in a hexagonal pattern consisting of dark spots where the current density is smaller than the current density in the striped region and in the uniform background. On the contrary, the discharge spots in the hexagonal pattern observed in N_2 discharges have current densities larger than that in the background

(a) 880 V, 29 μA　(b) 900 V, 36 μA　(c) 920 V, 42 μA

(d) 940 V, 50 μA　(e) 960 V, 57 μA　(f) 980 V, 62 μA
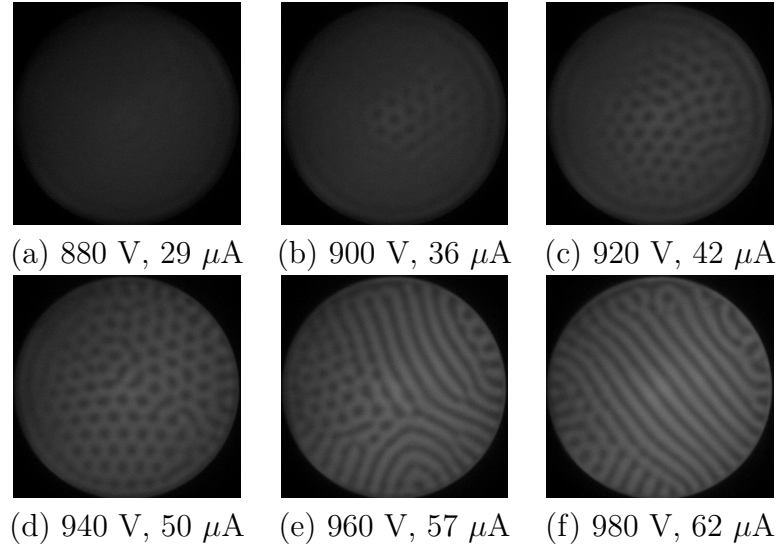
Figure 6.13: Transition from a uniform state to hexagonally woven stripes and then to stripes as U_0 is increased. Experimental parameters: Si:Pt (label P4) at about 100 K; 255 hPa Ar and 0.8 mm gap; lamp voltage 9.5 V corresponding to a conductivity of 6.8×10^{-9} $(\Omega \cdot \text{cm})^{-1}$.
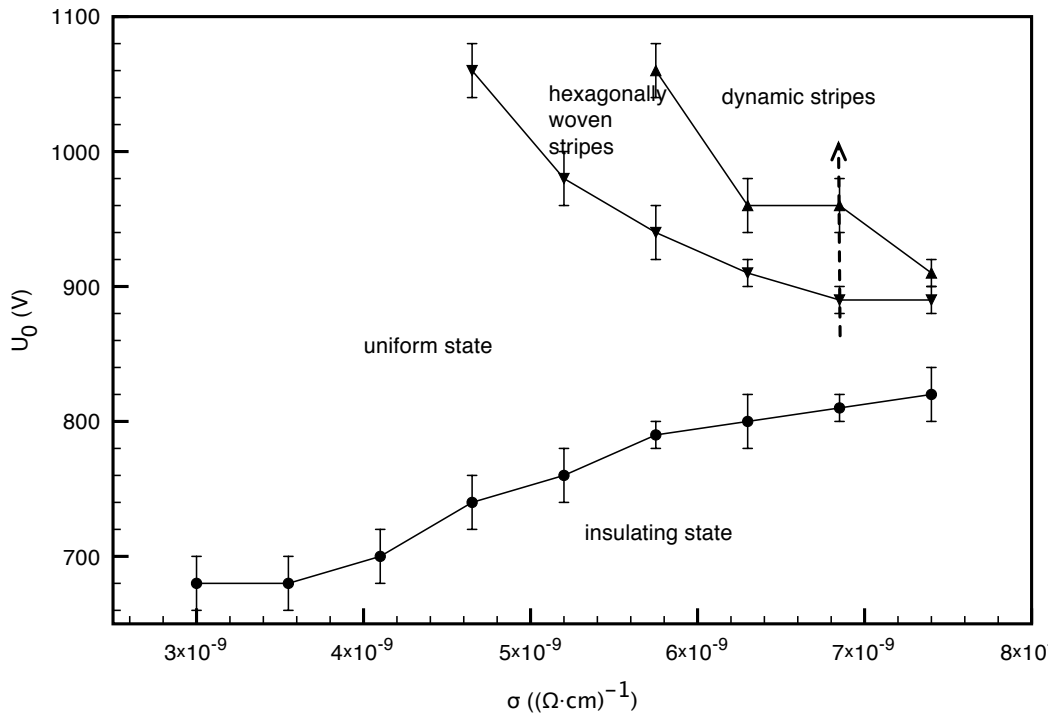
Figure 6.14: Typical phase diagram of various types of patterns in the σ-U_0 control parameter plane. The dashed line with arrow corresponds to the transition scenarios described in Figure 6.13. Experimental parameters: Si:Pt (label P4) at about 100 K; 255 hPa Ar and 0.8 mm gap.

region. A further increase of U_0 leads to the expansion of the patterned region and the appearance of defects. At 960 V oriented stripes start to be dominant and a well-formed striped pattern is obtained at 980 V. A phase diagram on the σ-U_0 plane is obtained by determining the transition voltages in measurements at several lamp voltages (Figure 6.14). In this case, only the scenario described above, i.e. the transition from the uniform state to hexagonally woven stripes and then to stripes, is observed. In contrast to the case in N_2 discharge, a direct transition from the uniform state to a striped state has not been observed. The monotonic change of the breakdown voltage is probably due to the surface cleaning effect of the argon ions. A modification of the surface condition of the chathode changes the coefficient of the secondary emission of electrons and thus the breakdown voltage.
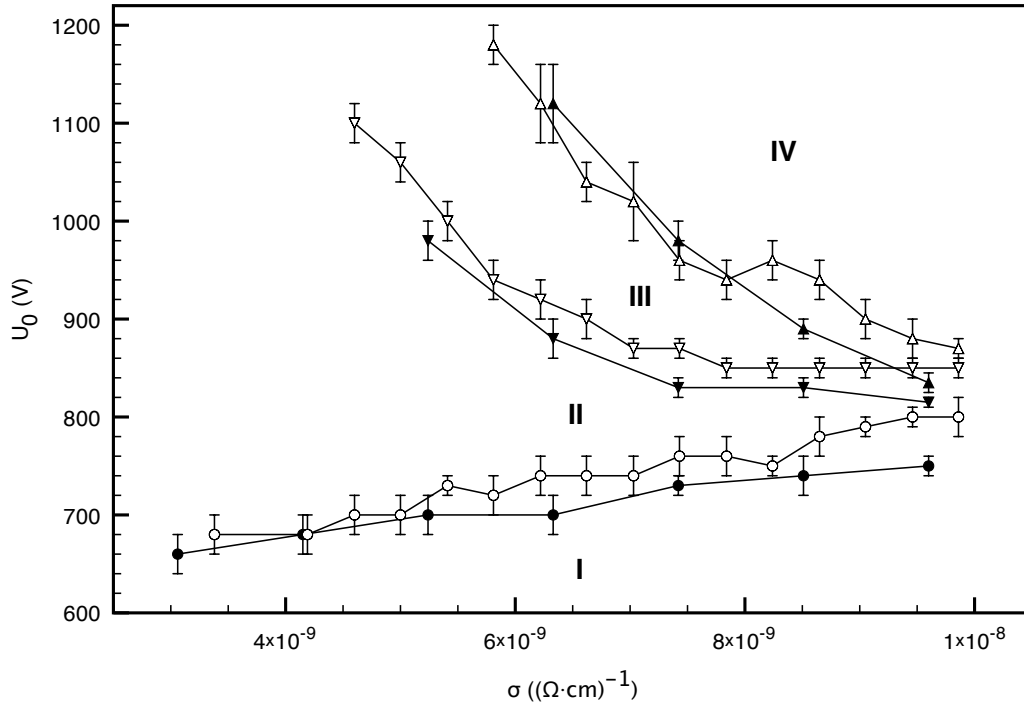
Figure 6.15: Superimposed phase diagrams of two semiconductor samples P4 and P5 obtained from measurements under the same experimental conditions. The filled and empty symbols correspond to the data points for sample P4 and P5 respectively. I insulating state; II uniform state; III hexagonally woven stripes; IV dynamic stripes. Experimental parameters: Si:Pt at about 100 K; 242 hPa Ar and 0.8 mm gap.

The reproducibility of the phase diagram was checked by making measurements with two samples under the same experimental conditions. The two phase diagrams are superimposed in Figure 6.15. Four different states of the system, i.e. the insulating state, the uniform state, hexagonally woven stripes and dynamic stripes, are present in the phase diagram for both samples. The general feature of the boundaries between various states are the same for both samples. At σ-values below $8 \cdot 10^{-9}$ $(\Omega \cdot \text{cm})^{-1}$, the boundary lines can be quantitatively well reproduced. At higher conductivities where the existence interval on the U_0-axis is less than 100 V, the quantitative reproducibility is lost. Nevertheless, the qualitative features remains the same for both samples.
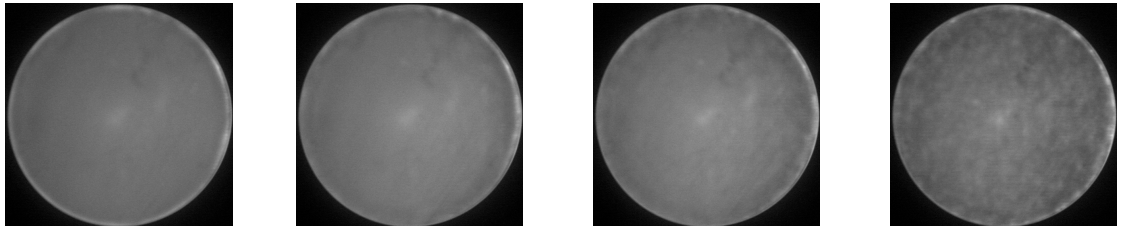
(a) 1000 V, 43 μA (b) 1080 V, 133 μA (c) 1139 V, 168 μA (d) 1200 V, 277 μA

Figure 6.16: Transition from a uniform state to irregular spatiotemporal oscillation. Experimental parameters: Si:Pt (label P4) at about 100 K; 162 hPa Ar and 0.8 mm gap; lamp voltage 10 V corresponding to a conductivity of 7.4×10^{-9} $(\Omega \cdot cm)^{-1}$.

When the Ar pressure is low, a new type of destabilization of the uniform state is observed. The transition is illustrated in the images given in Figure 6.16. The initially uniform discharge at $U_0 = 1000$ V lose its stability at 1080 V where the irregular oscillations start to appear close to the spacer. The region of oscillation grows as U_0 is increased and finally occupies the entire active area at 1200 V. The measurement at high conductivity indicates that this kind of irregular spatiotemporal oscillations compete with spatially ordered patterns like the hexagonally woven stripes. The oscillations destroy these patterns when U_0 is sufficiently high. An example of this scenario is illustrated in Figure 6.17. At 700 V the discharge is uniform. Oscillations start to appear close to the boundary at 800 V, but the center region remains stationary and uniform. At 840 V, hexagonally woven stripes emerge at the center region, coexisting with the oscillations. The spatiotemporal oscillations finally destroy the ordered pattern and dominate the entire discharge area at 940 V.
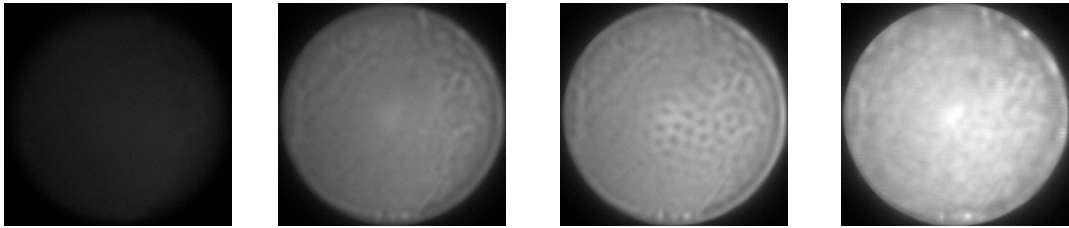
(a) 700 V, 43 μA (b) 800 V, 133 μA (c) 839 V, 168 μA (d) 940 V, 277 μA

Figure 6.17: Transition from a uniform state to the mixed state of hexagonally woven stripes and irregular spatiotemporal oscillation and finally to irregular spatiotemporal oscillation. Experimental parameters: Si:Pt (label P4) at about 100 K; 162 hPa Ar and 0.8 mm gap; lamp voltage 16 V corresponding to a conductivity of 1.4×10^{-8} $(\Omega \cdot cm)^{-1}$.

A phase diagram obtained with a 0.8 mm gap filled with 162 hPa Ar is illustrated in Figure 6.18. The dashed boundary of the uniform state II corresponds to the appearance of the spatiotemporal oscillations and the oscillatory state V stands for the fully developed oscillations which occupy the entire active area. In the transition region from II to V the uniform state coexisting with the oscillation state at σ-values below 1.2×10^{-8} $(\Omega \cdot cm)^{-1}$. At high σ-values, hexagonally woven stripes which coexist with the oscillation state can be observed.
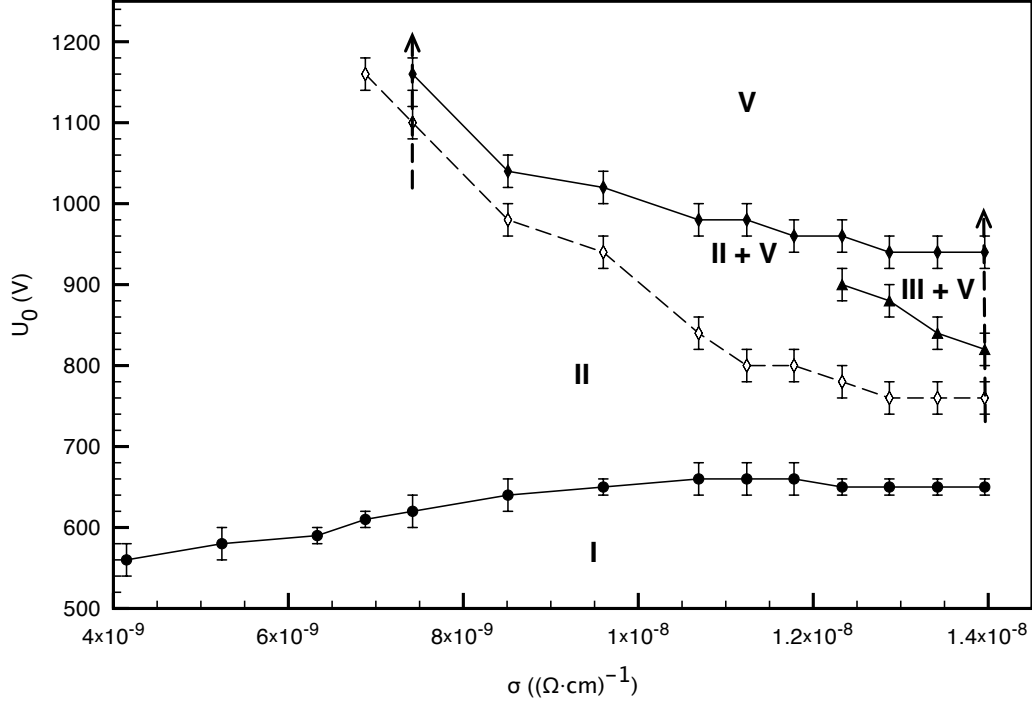
Figure 6.18: Phase diagram of various forms of patterns in the control parameter σ-U_0 plane at low gas pressure. I insulating state; II uniform state; III hexagonally woven stripes; V spatiotemporal oscillation. The left and right dashed lines with arrow correspond to the transition scenarios described in Figure 6.16 and Figure 6.17. Experimental parameters: Si:Pt (label P4) at about 100 K; 162 hPa Ar and 0.8 mm gap.

6.3.2 Dependence of the phase diagram on p and d

The phase diagrams given in Figure 6.19 were obtained with a 0.8 mm gap filled with Ar at various pressures. At 181 hPa, the spatiotemporal oscillation state V is observed when the uniform state is destabilized as U_0 is increased when σ is small. At large σ-values the oscillation state competes with spatially ordered patterns: hexagonally woven stripes III and dynamics stripes V. The oscillations destroy the dynamic stripes in the region where U_0 is above 900 V and σ above 1.1×10^{-8} $(\Omega \cdot cm)^{-1}$. When the pressure is increased to 214 hPa, there is a significant change in the phase diagram. The boundary lines between II and III and between III and IV shift to smaller σ-values. At the same time the boundary line corresponding to the appearance of oscillations shift upwards along the U_0-axis. It lies most probably in the regions of higher U_0 and σ, beyond the parameter range investigated in this measurement. As the pressure is further increased, a tendency for the transition lines to shift to smaller σ-values is evident.

The shift of the boundary lines in the phase diagram as the pressure is varied can best be illustrated in the measurements with a 1 mm gap (Figure 6.20). At p = 228 hPa, the highest pressure in this series of measurement, the same transition scenario is observed in a wide range of σ. With increasing U_0, the uniform state II gives way to hexagonally woven stripes III which then change to the state of dynamic stripes. The stripes IV are finally destroyed by spatiotemporal oscillations V. The voltage interval

106

(a) 181 hPa

(b) 214 hPa

(c) 242 hPa

(d) 278 hPa

Figure 6.19: Phase diagrams obtained in Ar discharges with a 0.8 mm gap size at different pressures. I insulating state; II uniform state; III hexagonally woven stripes; IV dynamic stripes; V spatiotemporal oscillation. Experimental parameters: Si:Pt (label P4) at about 100 K; 0.8 mm gap and Ar.

corresponding to the coexistence of IV and V is about 50 V independent of σ. As p is decreased, the boundary lines for the oscillation state V shift to smaller U_0 with respect to the line corresponding to the breakdown voltage. At the same time, the boundary line separating II and III and that between III and IV move to higher σ-values. As a result, the region of existence for the state of spatial patterns III and IV becomes smaller with decreasing p. At p below 171 hPa, the direct transition from the uniform state II to the oscillation state V is obtained when σ is below 7×10^{-9} $(\Omega \cdot cm)^{-1}$

Another series of measurements was made with a 0.6 mm gap. The phase diagrams shown in Figure 6.21 illustrate the complicated nature of the phenomenology when the boundary lines shift with respect to each other with changing gas pressures. At p = 220 hPa, the dashed transition line corresponding to the appearance of oscillations in part of the active area is below the boundary line for hexagonally woven stripes III. A destabilization of the uniform state II leads thus to the appearance of oscillations when U_0 is increased gradually. At high conductivities hexagonally woven stripes can emerge in the discharge area where the oscillation is absent, resulting in a region of coexistence of III and V. As the pressure is increased to 261 hPa, the dashed boundary line is above

(a) 147 hPa

(b) 171 hPa

(c) 197 hPa

(d) 228 hPa
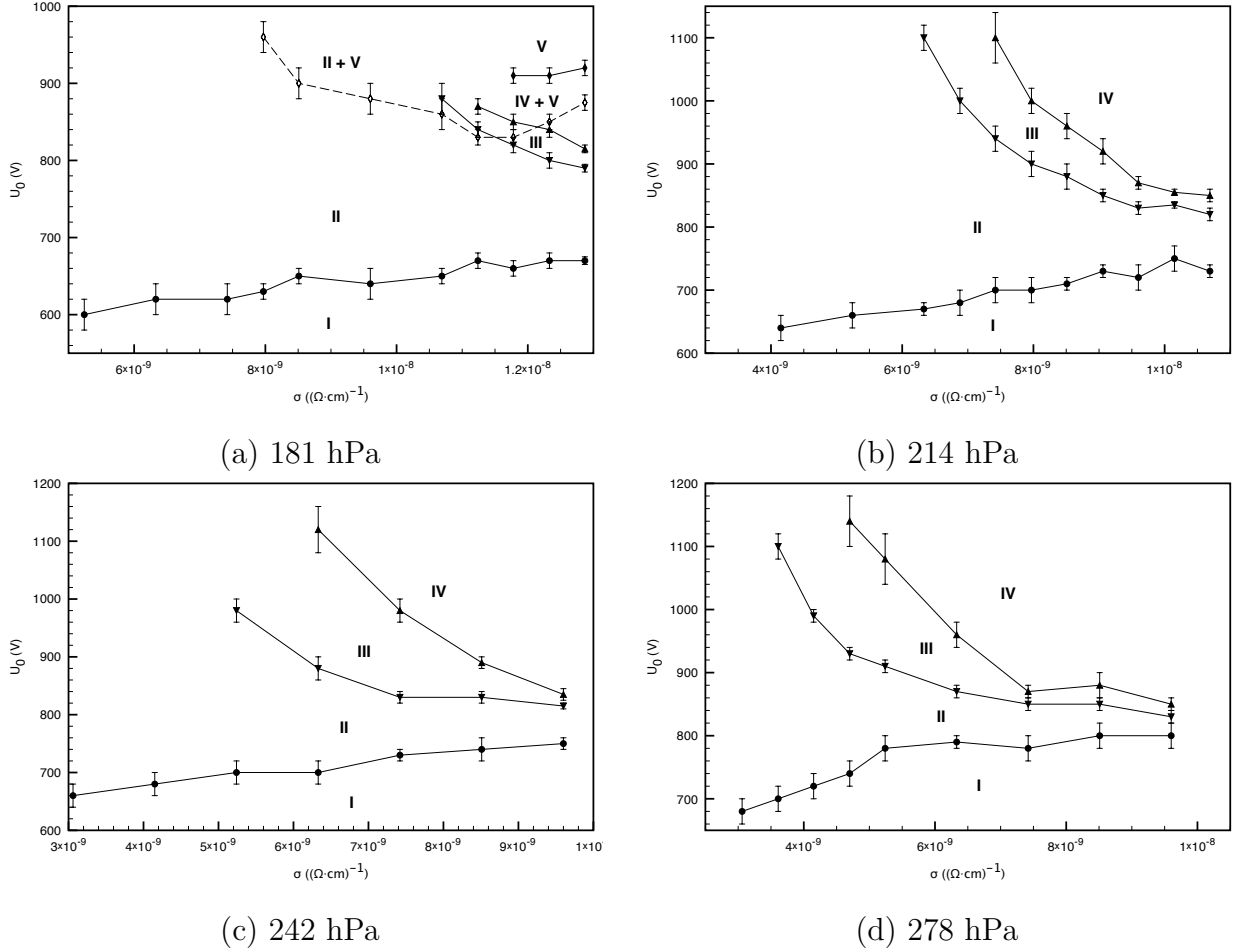
Figure 6.20: Phase diagrams obtained in Ar discharges with a 1 mm gap at different pressures. I insulating state; II uniform state; III hexagonally woven stripes; IV dynamic stripes; V spatiotemporal oscillation. Experimental parameters: Si:Pt (label P4) at about 100 K; 1 mm gap and Ar.

the boundary lines for the spatially ordered patterns III and IV. In this case the scenario of transition with increasing U_0 is qualitatively different from the case at lower pressure. A transition from the uniform state to the oscillation state via spatial patterns will be observed. At 290 hPa the dashed boundary line moves further above the boundary line between III and IV.

6.3.3 Phenomena in gas discharges with Ne and He

Besides Ar, two other noble gases, Ne and He, were used in the study on pattern formation. In the case of Ne, a measurement was initially made with a 0.8 mm gap filled with 234 hPa. In the range of the σ-U_0 plane investigated in our experiments, the uniform state was stable and neither spatial patterns nor oscillations were observed. The pressure was increased to 306 hPa and the uniform discharge remained stable. Finally the trials were extended to higher pressure and larger gap sizes, i.e. 1 mm gap filled with 326 hPa Ne and 1.5 mm gap filled with 328 hPa Ne. In both cases, the discharge was investigated with σ in the interval between 3×10^{-9} and 1.4×10^{-8} $(\Omega \cdot cm)^{-1}$ and voltages up to 500
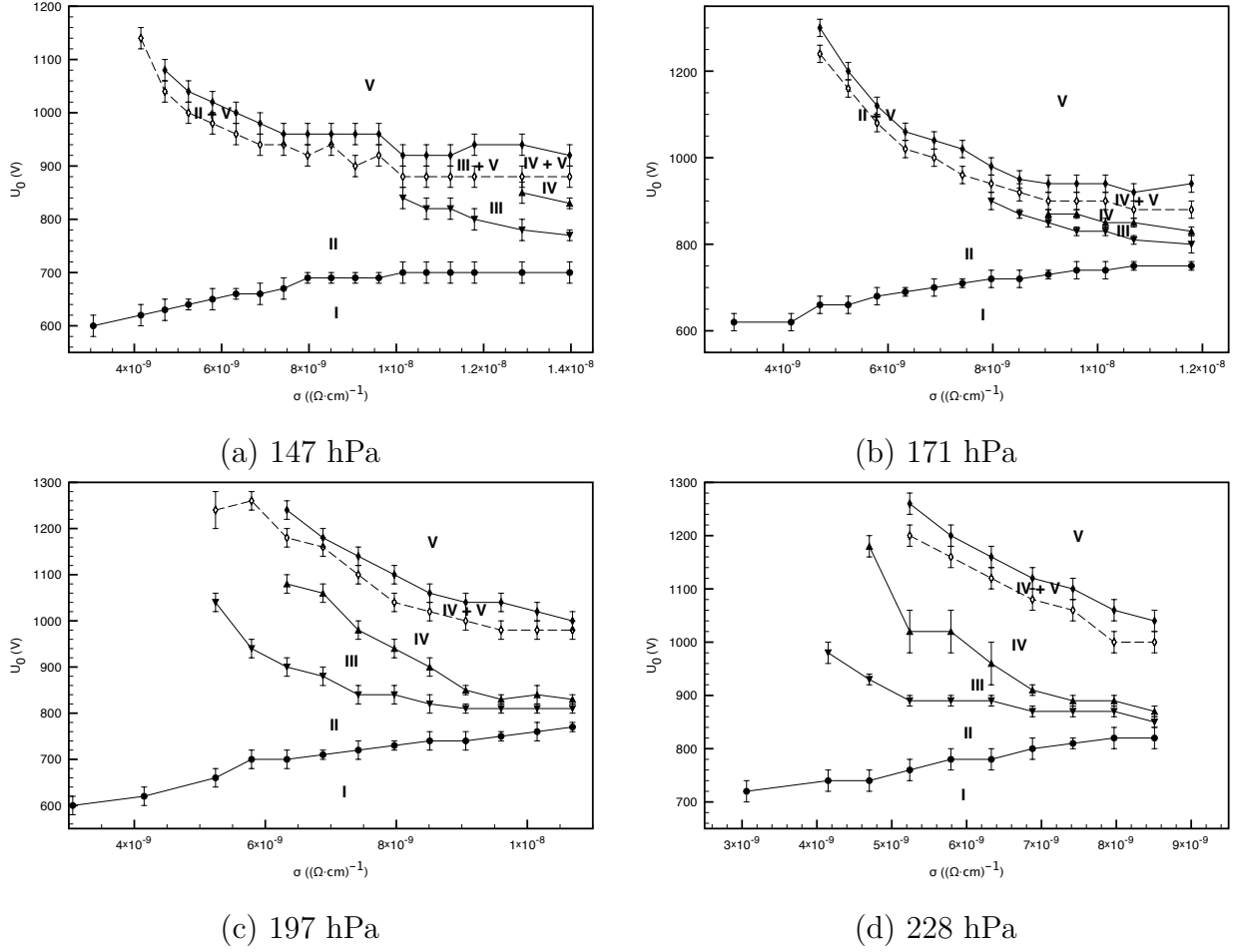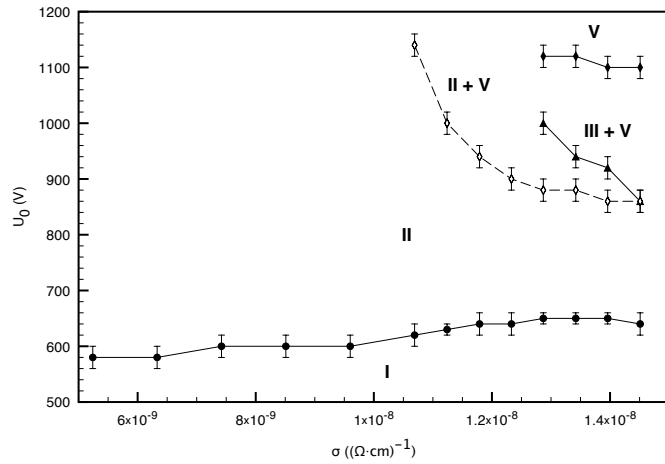
(a) 220 hPa

(b) 261 hPa
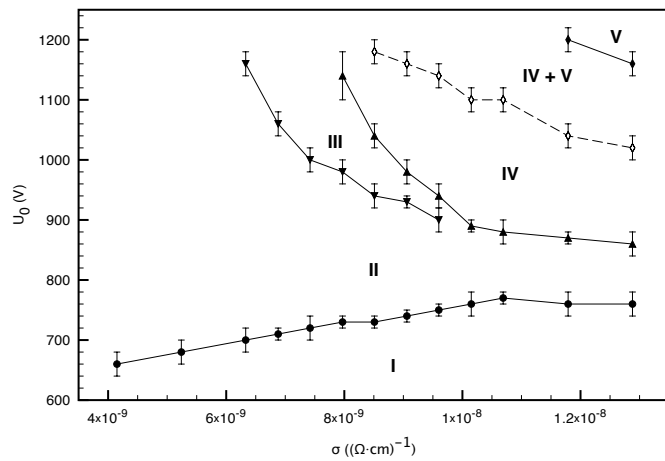
(c) 290 hPa

Figure 6.21: Phase diagrams obtained in Ar discharges with a 0.6 mm gap at different pressures. I insulating state; II uniform state; III hexagonally woven stripes; IV dynamic stripes; V spatiotemporal oscillation. Experimental parameters: Si:Pt (label P4) at about 100 K; 0.6 mm gap and Ar.
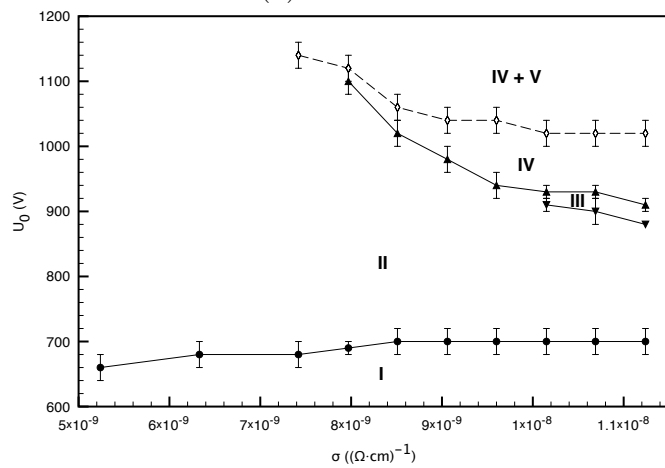
V above the breakdown voltage. In all these measurements, only the uniform state was observed.

(a) 800 V, 0.95 mA   (b) 700 V, 1.2 mA   (c) 700 V, 3.3 mA
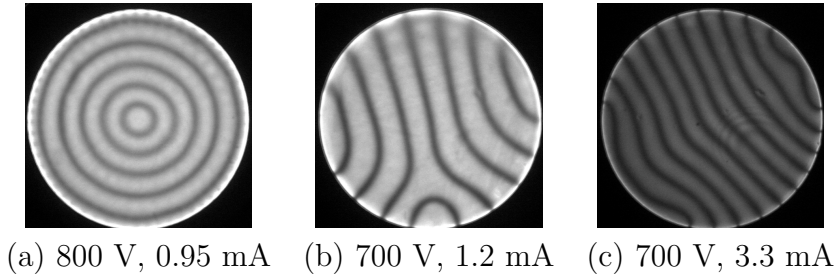
Figure 6.22: Patterns observed at high pressure and high conductivity of the semiconductor during the warming up phase of the setup. (a) 524 hPa, 0.8 mm gap; (b) 367 hPa Ne, 1 mm gap; (c) 369 hPa Ne, 1 mm gap. The cathode Si:Pt (label P4) was used and the temperature was not measured in those measurements.

It is, however, suspected that pattern formation should be observed in a different parameter range, e.g. higher pressure and high conductivity etc. This opinion is based on the observation of patterns during the warming up phase of our setup. Examples of the patterns observed in this kind of situation are given in Figure 6.22. When the liquid nitrogen was used up, the temperature of the cold finger increased gradually and the gas pressure in the chamber increased accordingly. At temperatures above 100 K the conductivity of Si:Pt rises rapidly. The total current corresponding to the images given here, ranging from 1 to 3 mA, is significantly higher than the discharge current in the case of Si:Pt cathode at 100 K, which is typically less than 0.3 mA.

In the experiments with He, a 1 mm gap filled with 206 hPa and a 1.5 mm gap filled with 203 hPa were investigated. In the former case, the discharge remains uniform at σ = 1.1×10^{-8} $(\Omega \cdot cm)^{-1}$ when U_0 is increased to 1500 V, which is 1000 V above the 500 V breakdown voltage. In the latter case, a destabilization of the uniform state was also not observed in the investigated parameter range.

Chapter 7

Observations in gas discharge systems with other semiconductors

In this chapter, the influence of the semiconductor material on the phenomenology of pattern formation is addressed. Besides Si:Pt wafers, we investigated Si:Zn wafers and semi-insulating GaAs wafers compensated with Cr. The two kinds of Si:Zn wafers produced with different starting materials are referred to as Si:Zn(I) and Si:Zn(II) in section 5.2, where the difference between the material is described in detail. Measurements with Si:Zn wafers were carried out in two periods. During the first period, the cold finger shown in Figure 4.3 (c) was used and the temperature was about 100 K. During the second period, the cold finger was changed to the one shown in Figure 4.3 (b) which is adapted to the size of Si:Zn(II) wafers. In this case, the temperature of the cathode was about 120 K.

7.1 Gas discharge system with Si:Zn cathode (first period)

7.1.1 Electrical property of Si:Zn under illumination

An attempt was made to calibrate the conductivity of the wafer as a function of the lamp power using the procedure described in section 6.1.1. The method for calculating the conductivity is based on measuring the voltage-current characteristics of the discharge in Townsend mode. For this purpose, a 60 μm gap filled with 239 hPa Ar was chosen in the measurements with a Si:Zn(I) wafer (label 14-D2) and a Si:Zn(II) wafer (label Z99). The temperature of the semiconductor cathode in these measurements was about 100 K. The voltage-current curves for both wafers under illuminations corresponding to various lamp voltages are given in Figure 7.1. As the voltage drop across the Townsend discharge is constant, which is close to the breakdown voltage, the voltage current characteristics of the hybrid semiconductor gas discharge cell reflects actually that of the semiconductor. The curves are shifted along the voltage axis by a value corresponding to the breakdown voltage of the gas gap, about 200 V in this case. In contrast to the linear voltage-current characteristics of Si:Pt wafers, both type of Si:Zn wafers give a nonlinear curves. There is a significant difference in the sensitivity of the semiconductor to illumination. The Si:Zn(I) wafer displays a high sensitivity. At a lamp voltage of 2 V, the total current
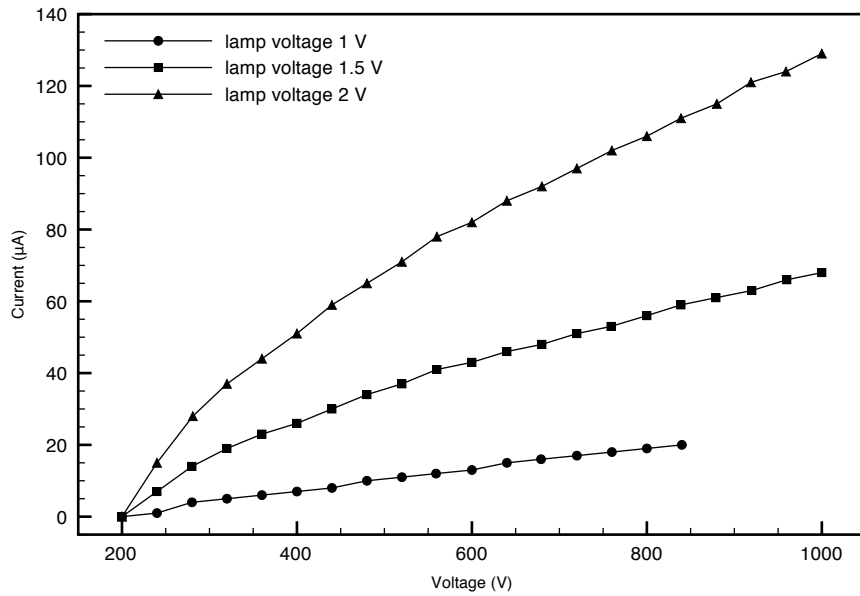
(a)
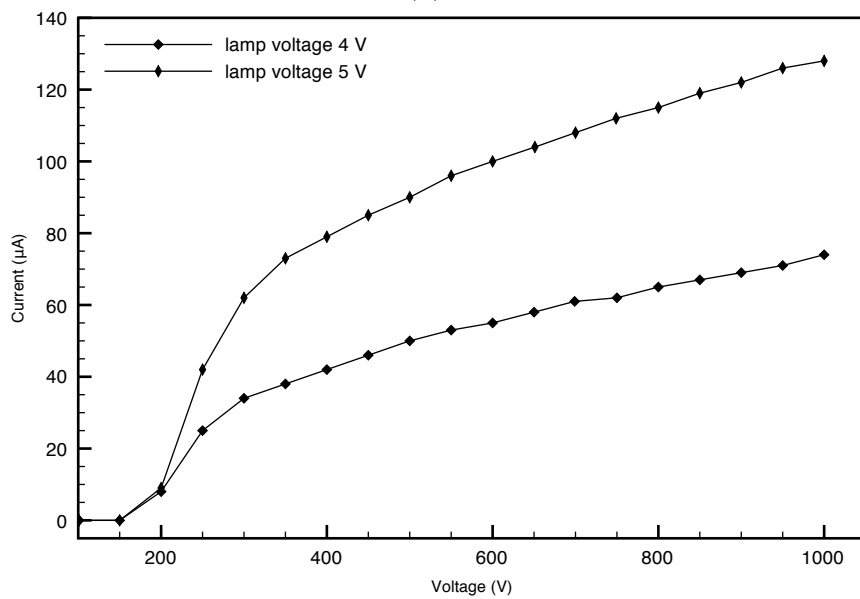
(b)

Figure 7.1: Voltage-current characteristics of the hybrid semiconductor-gas discharge cell with a Si:Zn(I) wafer (label 14-D2) and a Si:Zn(II) wafer (label Z99) under various illumination conditions. Experimental parameters: Si:Zn at about 100 K; 240 hPa Ar and 60 μm gap.

reaches about 120 μA at 1000 V whereas a stronger illumination (i.e. lamp voltage of 5 V) is necessary for the Si:Zn(II) wafer to reach comparable current values at 1000 V. The voltage-current curve of SiZn(I) at a lamp voltage of 1.5 V is in general comparable to that of SiZn(II) at 4 V lamp voltage. Only under very weak intensity of illumination (e.g. lamp voltage below 1 V) can a linear voltage-current characteristics be observed. In that case, for example, the dark conductivity of SiZn(I) is calculated to be about 5×10^{-10} $(\Omega\cdot\text{cm})^{-1}$. At moderate lamp voltages, the voltage-current curve is nonlinear and a constant conductivity is not defined. A quantitative calibration of the conductivity as a function of the lamp voltage is thus not possible here. In this respect, Si:Zn wafers are not suitable for a systematic quantitative study of pattern formation. Therefore, a phenomenological approach was taken in this part of the work and a quantitative study of the reproducibility was not pursued.

7.1.2 Discharge patterns
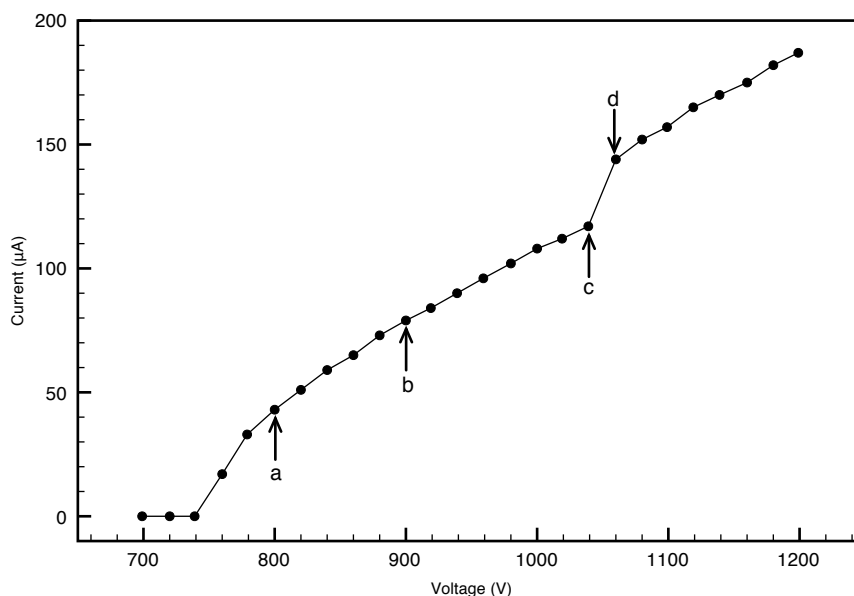
Figure 7.2: Voltage-current characteristics of the hybrid semiconductor-gas discharge cell where patterns are observed. Experimental parameters: Si:Zn (label 14-D2) at about 100 K; 240 hPa Ar; 0.8 mm gap; lamp voltage 2.5 V.

Pattern formation in the gas discharge with a Si:Zn(I) wafer (label 14-D2) was studied with a 0.8 mm gap filled with 240 hPa Ar. The voltage-current characteristics of the discharge cell at a lamp voltage of 2.5 V and the patterns corresponding to the points marked with arrows are given in Figure 7.2 and 7.3 respectively. With a voltage of 800 V, which is slightly above the breakdown voltage, spatial patterns appear amid the uniform background. The spatial patterns dominate the entire active area as the voltage is increased to 1040 V. A further increase of 20 V leads to a jump of the total current, accompanied by a dramatic change of the form of the discharge. Before the transition, the pattern is spatially extended whereas after it the discharge shrinks to form bright

(a) 800 V, 43 μA (b) 900 V, 79 μA (c) 1040 V, 117 μA (d) 1060 V, 144 μA
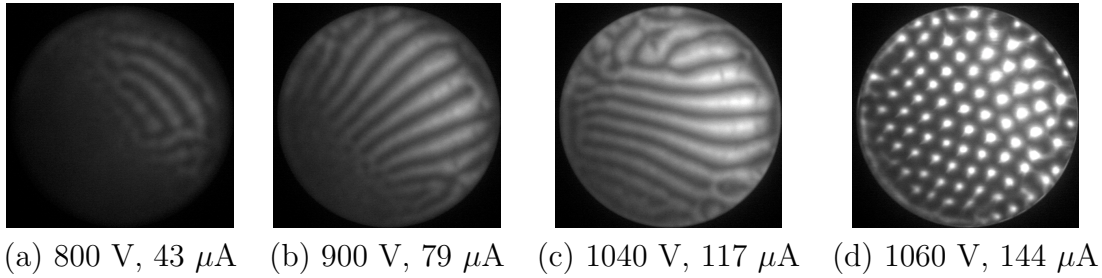
Figure 7.3: Abrupt transition from spatially extended patterns to filament lattice. Experimental parameters: Si:Zn(I) wafer (label 14-D2) at about 100 K; 240 hPa Ar and 0.8 mm gap; lamp voltage 2.5 V.

spots which arrange themselves in a hexagon-like lattice. Considering the size of the spots and the width of the gap which is 0.6 mm and 0.8 mm respectively, the bright spot is in fact a discharge filament across the gap. With higher lamp voltages, the transition to a filament lattice is also observed.

(a)   (b)   (c)   (d)
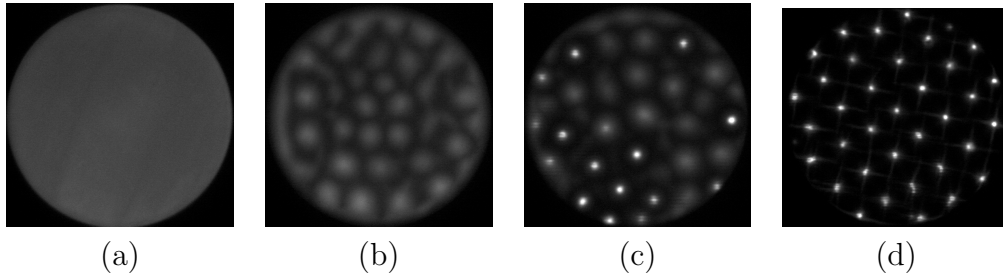
Figure 7.4: Various discharge types observed in Ar discharge with a Si:Zn(II) cathode. (a) uniform state (lamp voltage 3 V, 1120 V and 25 μA); (b) spatially extended pattern (lamp voltage 6 V, 940 V and 123 μA); (c) coexisting spatial pattern and filaments (lamp voltage 6.5 V, 1100 V and 179 μA); (d) square filament lattice (lamp voltage 8 V and 1000 V 370 μA). Experimental parameters: Si:Zn(II) wafer (label Z99) at about 100 K; 240 hPa Ar and 0.8 mm gap.

As seen in Figure 7.1, the electrical property of both types of Si:Zn material display qualitatively the same general features. Various types of discharge observed with a Si:Zn(II) wafer at about 100 K and a 0.8 mm gap with 240 hPa Ar are illustrated in Figure 7.4. The uniform state, the spatial pattern and the filament lattice pattern observed in the system with a Si:Zn(I) cathode can be reproduced with a Si:Zn(II) cathode at different parameters. The competition between the filament state and the spatial patterned state can also be investigated with the Si:Zn(II) material thanks to the existence of coexisting filaments and spatial patterns over a large range of control parameters (Figure 7.4 c). The origin for the difference of the details of the patterns, e.g. the square lattice observed with Si:Zn(I) in contrast to the hexagonal-like one with Si:Zn(I) (Figure 7.3 d), is still not identified and requires further study.

The Si:Zn(I) cathode was also tried in one measurement where a 0.8 mm gap was filled with 158 hPa N_2. During the measurement, the voltage was kept constant and the intensity of illumination , i.e. the lamp voltage, was gradually increased. The typical patterns observed in N_2 discharges with a Si:Pt cathode, i.e. the uniform state, dynamic

hexagonal spots and dynamic stripes, are all reproduced here. However, it was observed that the discharge is not stable at currents above 80 μA. The total current increased continuously even when all the control parameters were kept unchanged. Some kind of positive feedback must be responsible for the instability. As there is no significant heating problem in N_2 discharges with Si:Pt cathodes at currents of several hundred μA, the instability observed here should not be attributed to gas heating. Considering the extremely high sensitivity of Si:Zn(I) to illumination, the positive feedback is most probably a result of the interplay of the light emitted from the gas discharge and the photoelectric effect inside the semiconductor.
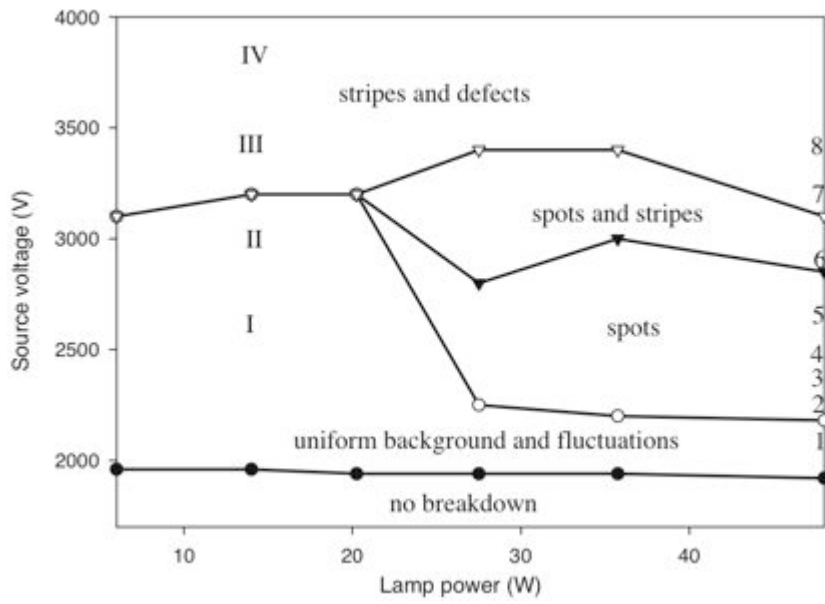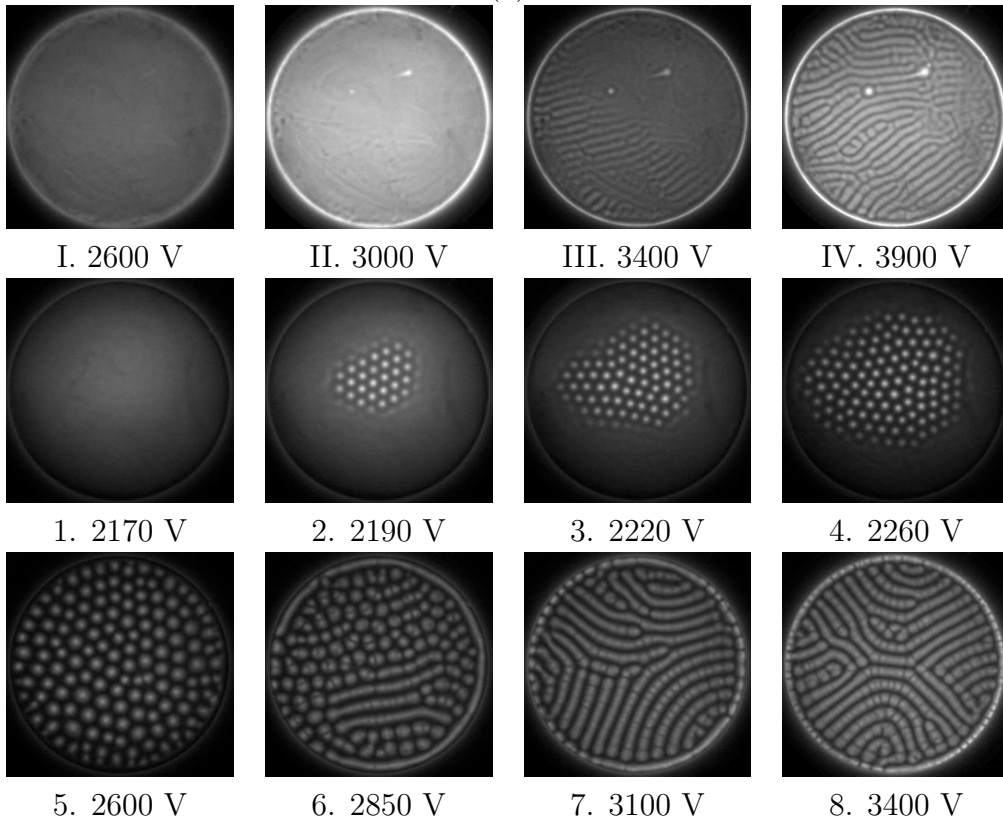
7.2 Gas discharge system with Si:Zn(II) cathode (second period)

The diameter of the Si:Zn(II) wafers is larger than that of the Si:Pt or Si:Zn(I) wafers and the cold finger shown in Figure 4.3 (c) does not fit well. Therefore, the cold finger shown in Figure 4.3 (b) was made. However, the unintentional change from a cold finger with liquid nitrogen inside to one made of a copper block introduces a temperature change. Whereas a temperature of 100 K could be achieved by the first cold finger, the temperature is about 120 K when the second one was used. At this temperature the dark conductivity of the Si:Zn(II) is about 10^{-7} (Ω·cm)$^{-1}$. This is significantly higher than that at 100 K, which is below 10^{-10} (Ω·cm)$^{-1}$. This value is also large compared to that of Si:Pt wafers at 100 K where spatial patterns are observed (i.e. of the order of 10^8 (Ω·cm)$^{-1}$). Due to the smaller resistance of the semiconductor, a serial resistor, typically 1 MΩ, was used in the following measurements. In contrast to the Si:Zn(I) wafers which have a transparent ohmic contact on one side, there is no such layer on the surface of the Si:Zn(II) wafers. In order to obtain a homogeneous electrical contact, a thin semitransparent gold film was evaporated onto one surface of the wafer. The transmittance of the gold film varies between 30% and 60% for irradiation with wavelengths ranging from 350 nm to 850 nm. Considering the details of these differences in the setup, a direct comparison of the phenomenology is not possible. Nevertheless, the patterns observed in systems with Si:Pt or Si:Zn(I) cathodes were reproduced in systems with Si:Zn(II) cathodes.

A series of measurements were made with the Si:Zn(II) wafer labeled Z99 and a 0.8 mm gap filled with 180 hPa N_2. The surface of one side of the wafer was coated first with 3.4 nm Cr and then 23 nm Au where the use of Cr is to enhance the adhesion between Au and the polished surface of the wafer. The phase diagram on the plane of the source voltage U_0 and the power of the lamp, as well as typical patterns are shown in Figure 7.5. The breakdown voltage is about 1960 V, below which the gas is insulating and there is no current flowing through the gas gap. In general, a uniform discharge is established at a U_0-values slightly above the breakdown voltage, which is subsequently destabilized at increasing U_0 and spatiotemporal patterns emerge. Depending on the intensity of illumination (i.e. the lamp power), two destabilization scenarios were observed. When the illumination is weak, i.e. the lamp power below 20 W, a direct transition from the uniform state to a striped state is obtained at a rather high U_0 (above 3000 V in this case). The transition is illustrated in the image sequence I-IV in Figure 7.5 (b). The

(a)

| I. 2600 V | II. 3000 V | III. 3400 V | IV. 3900 V |

| 1. 2170 V | 2. 2190 V | 3. 2220 V | 4. 2260 V |

| 5. 2600 V | 6. 2850 V | 7. 3100 V | 8. 3400 V |

(b)

Figure 7.5: Phase diagram on the parameter plane of the source voltage and the lamp power (a) and the patterns observed with parameters marked by the numbers I-IV and 1-8 (b). Experimental parameters: Si:Zn(II) wafer (label Z99) at about 120 K; 180 hPa N_2 and 0.8 mm gap.

stripes are not stationary, but show irregular dynamics where line defects are created and destroyed constantly. A different scenario of the transition, illustrated in the sequence 1-8, was observed when the lamp power is high. At $U_0 = 2170$ V, the uniform state (image 1) is stable. An increase of U_0 to 2190 V leads to the emergence of hexagonal lattice consisting of bright spots from the uniform background (image 2). The whole lattice drifts coherently along a well-defined direction with a velocity of the order of 1 mm/s. With a further increase of U_0 to 2200 V, the area covered by hexagonal lattice grows and breaks into domains separated by grain boundaries (image 3). The arrangement of the spots becomes disordered at still higher U_0 (image 4). After the spots cover the entire active area, stripes start to appear as U_0 is increased. Finally stripes prevail at U_0 above 3000 V.
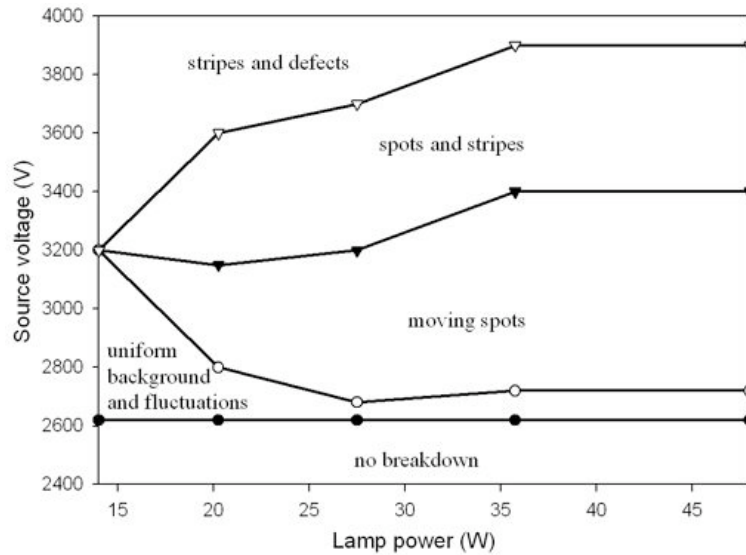
Figure 7.6: Phase diagram on the parameter plane of the source voltage and the lamp power. Experimental parameters: Si:Zn(II) wafer (label Z99) at about 120 K; 260 hPa N_2 and 0.8 mm gap.

The phase diagram shown in Figure 7.6 is obtained in gas discharge with a higher pressure, 260 hPa. Compared to the phase diagram at 180 hPa (Figure 7.5 a), general features for both diagrams are qualitatively the same. Two scenarios for the destabilization of the uniform state are present. As in the measurement with 180 hPa N_2, under strong illuminations the form of the discharge evolves from the uniform state to a state of dynamic hexagonal spots, then to a mixed state of spots and stripes, and finally to a state of stripes with moving defects as U_0 is increased gradually. Under weak illuminations a transition directly from the uniform state to a striped state occurs. However, the region of existence for dynamic spots and coexisting spots and stripes is shifted to smaller lamp powers and is expanded compared to that at 180 hPa.

As can be seen in the phase diagram, when the wafer is appropriately illuminated hexagonal lattice forms spontaneously. Once formed, the spots in the hexagonal lattice are not stationary, but drift coherently to a certain direction. The evolution of the hexagonal lattice with changing U_0 and its coherent motion were investigated in the measurements made with N_2 at a pressure of 210 hPa and a lamp power of 28 W (Figure 7.7). The breakdown voltage in this case is 2300 V and the source voltage U_0 is varied

117
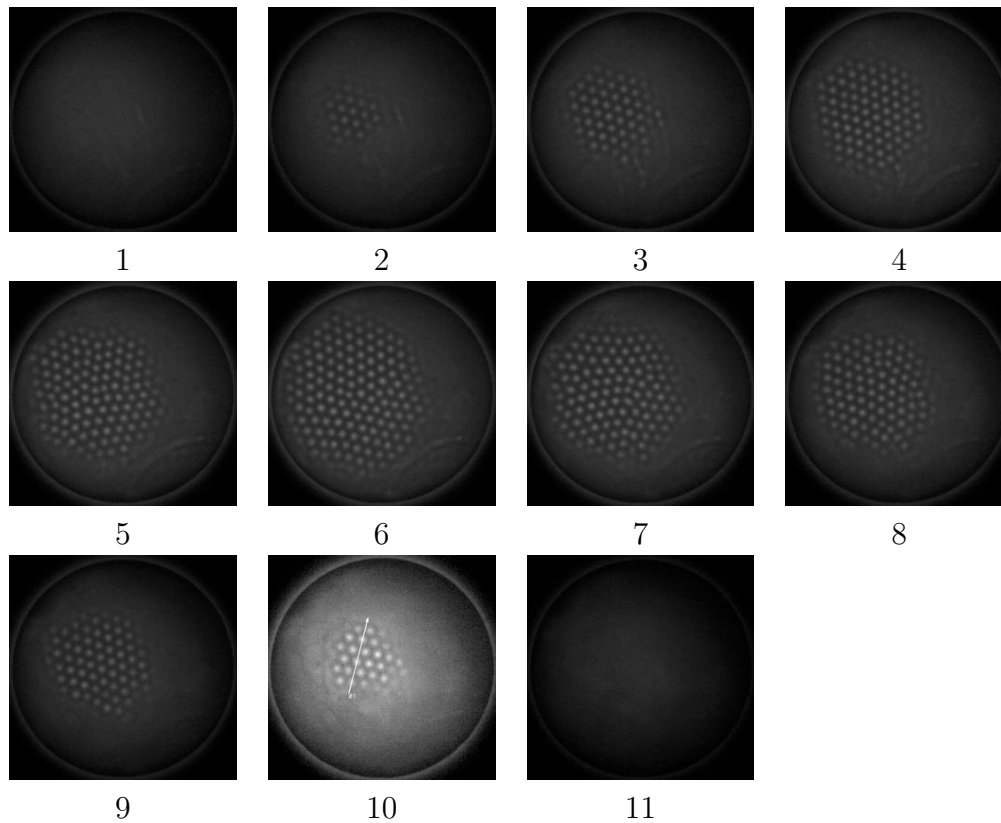
Figure 7.7: Evolution of the hexagonal patterns with increasing and decreasing source voltage. Experimental parameters: Si:Zn(II) wafer (label Z99) at about 120 K; 260 hPa N_2 and 0.8 mm gap.

between 2400 and 2500 V in 20 V steps. A uniform discharge is established after the breakdown and remains stable when U_0 is increased to 2400 V. The faint circle is due to the light reflected at the inner boundary of the transparent PVC spacer, which is 34 mm in diameter. At 2420 V a cluster of luminous spots forming a hexagonal lattice emerges out of the uniform background. The lattice observed here belongs to the 2D space group p6m and each primitive cell consists of a single luminous spot. The lattice parameter is about 2 mm and the size of the spot determined from the FWHM (full width at half maximum) is about 0.7 mm. The spot cluster is not stationary, but drifts along the line of reflection symmetry to the top right as indicated in Figure 7.7 image 10. The speed is estimated to be 0.5 mm/s. The spots emerge from the bottom left boundary of the cluster, drift across the cluster and then disappear at the top right boundary. It was observed in other measurements that the direction of the coherent drift was not pre-defined by the experimental setup, but a result of competition between directions along two different reflection symmetry lines. An increase of U_0 leads to a growth of the cluster. The number of spots in the cluster increases, but the spots do not move coherently along a direction any more. Some spots disappear as they collide (image 5-6 in Figure 7.7). When decreasing U_0 the phenomena occurred in the reverse order. Finally the spot cluster disappears when U_0 is reduced to 2400 V and the uniform discharge dominates.

The evolution of patterns when the system is driven far from the primary bifurcation

Figure 7.8: Evolution of patterns in a wide range of source voltage U_0. The grayscale of images 1-4 is rescaled for better visualization. Experimental parameters: Si:Zn(II) wafer (label U1) at about 120 K; lamp power 48 W; 200 hPa N_2 and 1 mm gap.

point was investigated with a 1 mm gap filled with 200 hPa N_2. The lamp power was 48 W. In this case, the breakdown voltage is 2820 V and th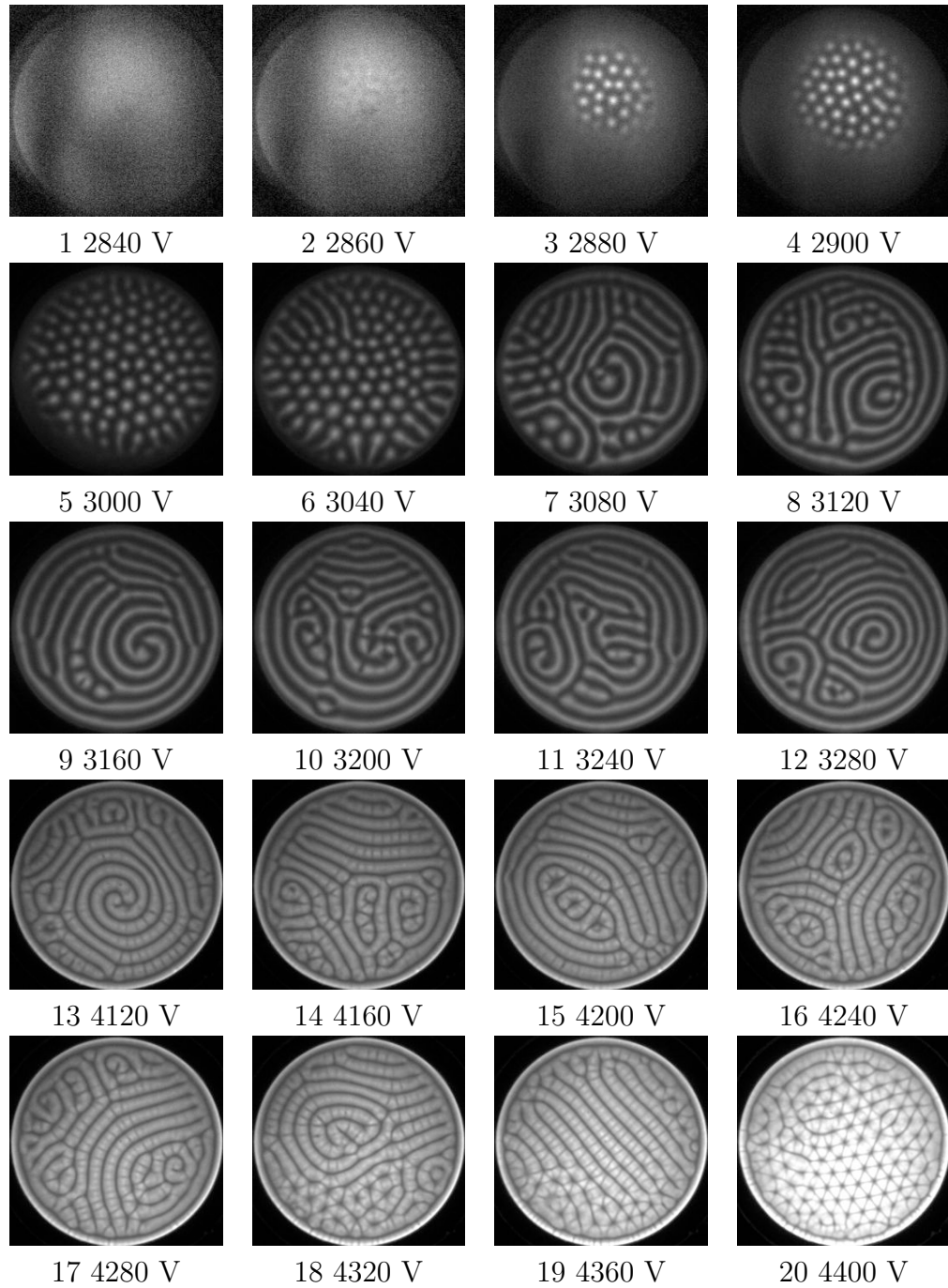e primary bifurcation occurs at $U_0 = 2880$ V. The source voltage U_0 is increased up to 4400 V in steps of 20 or 40 V depending on the voltage range. With U_0 slightly above the breakdown voltage the discharge is uniform as illustrated in image 1 and 2 in Figure 7.8. A further increase of U_0 by 20 V to 2880 V leads to the emergence of a spot pattern from the smooth background. The transition occurs at a current of 30 μA and the power dissipated into the system is less than 0.1 W. As U_0 is increased, the area covered by spots increases (image 4) and the spot pattern finally dominates the entire discharge area (image 5). It is then replaced by a labyrinthine pattern at voltages above 3080 V (image 7). The labyrinthine pattern evolves erratically and spirals can be observed occasionally (image 9 and 12). When U_0 is above 4000 V, the lines in the labyrinthine pattern become segmented and dark spots with arms start to form. At 4400 V the dark spots arrange themselves into a regular hexagonal network. The transition from segmented lines to the hexagonal network accompanying a steep current rise with U_0. This is probably related to the effect of gas heating because the power dissipated into the discharge cell at 4400 V is about 2.9 W and the temperature of the cold finger increases by 4 K in a few minutes.

7.3 Gas discharge system with GaAs:Cr cathode

Compared to the discharge phenomena with conductive metal cathodes, the use of resistive semiconductor cathodes is essential for pattern formation in the gas discharge systems. So far it is not clear whether other properties of the Si material, besides the high resistivity, also play important roles. In this context, the gas discharge system with a GaAs wafer compensated with Cr was investigated. The GaAs:Cr wafer (CrysTec GmbH, Berlin, Germany) is 2 inches in diameter and 1.5 mm thick. The specific resistivity given in the specification is above 10^5 $\Omega \cdot$m at room temperature. In order to measure the time course of the total current, the cold finger shown in Figure 4.3 was used and the stable temperature which can be obtained is about 130 K. The unpolished side of the wafer is coated with a semitransparent gold film as a homogeneous electrical contact and the polished side is in contact with gas.

In order to study the electrical properties of the GaAs:Cr wafer, its voltage-current characteristics at about 130 K under various illumination conditions were measured with a sample coated with gold film on both sides. The voltage-current curves in Figure 7.9 are monotonic in a voltage range up to 800 V and are linear at voltages below 250 V. The specific resistivity is calculated from the resistance determined by a linear fit of the voltage-current curves at small voltages. The dark resistivity of GaAS:Cr at 130 K is estimated to be of the order of 10^7 $\Omega \cdot$m. As the intensity of the illumination is increased, the specific resistivity decreases and finally approaches a value of the order of 10^5 $\Omega \cdot$m.

In this system the typical spatial patterns like dynamic hexagonal spots and dynamic stripes were not observed. In contrast, solitary discharge spots are observed when the uniform state is destabilized. The properties of this kind of discharge spot are different from the spots observed in the intermittent discharge with conductive electrodes. The solitary spots observed here are generated or destroyed on a ms time scale and can be stable for a period of up to minutes. The behavior of the solitary spots is illustrated in Figure 7.10 from a measurement with a 0.5 mm gap and 258 hPa N_2. The current
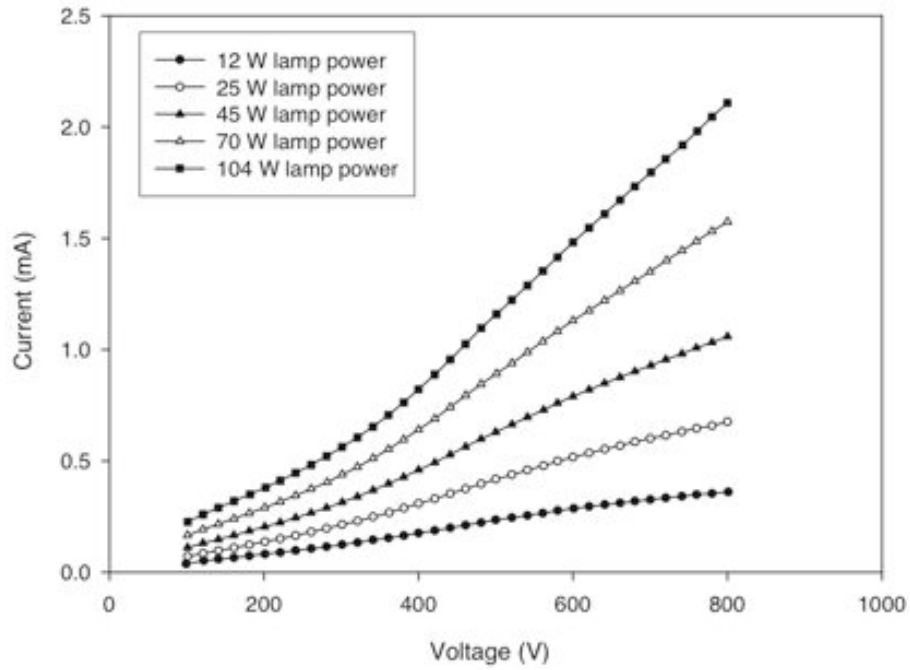
Figure 7.9: Voltage-current characteristics of a GaAs:Cr wafer at about 130 K.

| t = 0 ms | t = 8 ms | t = 16 ms | t = 24 ms |

| t = 32 ms | t = 40 ms | t = 48 ms | t = 60 ms |
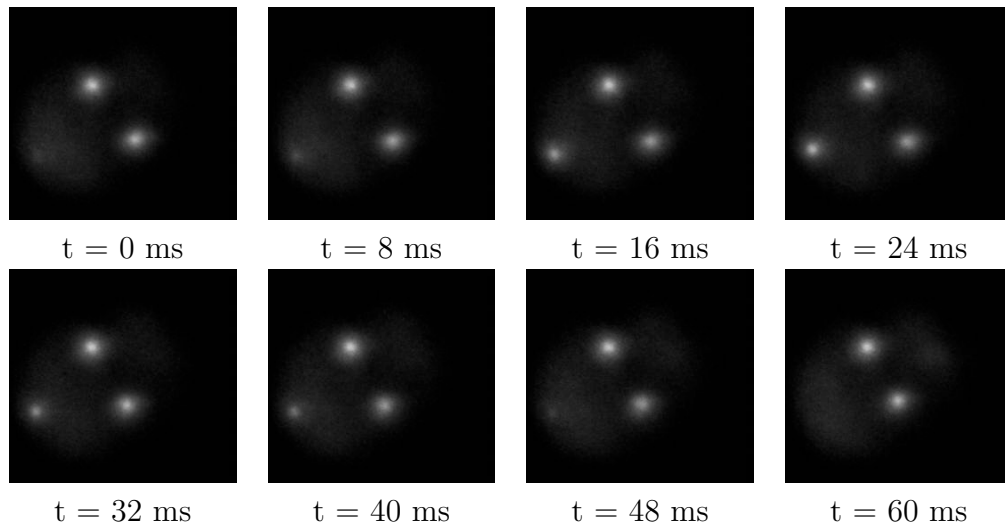
Figure 7.10: Generation and annihilation of a discharge spot. The images were taken with an exposure time 3.9 ms. Experimental parameters: GaAs:Cr wafer at about 130 K; lamp power 70 W; 258 hPa N_2 and 0.5 mm gap.

density of the spot is about 18 A/m^2 in this case, which is significantly higher than the typical current density of below 1A/m^2 in the case of a Townsend discharge under similar conditions. This indicates that a normal glow discharge is probably established inside the solitary spots. The mechanism of their generation, annihilation and irregular motion is still not understood.

Chapter 8

Summary and outlook

8.1 Summary

The essential part of the present work consists of an extensive review of self-organized structures in gas discharge systems and a systematic investigation of pattern formation in the DC driven systems with various semiconductor materials as cathodes at cryogenic temperatures. The present review focuses on the self-organization in the lateral direction which is perpendicular to the direction of the current flow. In the case of conductive electrodes, various dynamic patterns consisting of glowing spots have been observed in systems of large aspect ratio. In the glow discharge, the luminous spots can be due to the self-organization in the cathode layer or in the anode layer. In these cases, the spots carry constant current and their spatial configuration can be understood as a result of the repulsive Coulomb interaction. In the case of the intermittent discharge, the discharge spots exist in fact only for a brief period of the order of μs, which corresponds to the duration of a micro-discharge. In the quasi-one-dimensional gas discharge systems with Si anodes, glow discharge is normally established as a result of the low resistivity of the Si electrode (typically of the order of 1 kΩ·cm). There are two kinds of structures observed in this system, i.e. the solitary discharge filaments and the spatially periodic structure. The multiplication of the filaments is accompanied by oscillations in current and discontinuities in the voltage-current characteristics of the discharge. In contrast, the periodic structures emerge from the background via a supercritical bifurcation. In the quasi-two-dimensional gas discharge systems with a semiconductor cathode, the resistivity of the Si:Zn cathode is of the order of 10^{10} Ω·cm when it is cooled down to a temperature around 100 K. Due to the very high resistivity, the discharge is established in the Townsend mode when the electrical breakdown of the gas gap occurs. Destabilization of the uniform state of the discharge leads to the emergence of the spatially periodic structures, notably stripes and a hexagonal lattice of luminous spots. The primary transition from the uniform state to the striped state occurs via a supercritical bifurcation. Zigzag instabilities of the stripes are observed as the system is driven further from the primary bifurcation point. Besides the spatially extended patterns, solitary filaments showing particle-like characteristics are also observed. In a slightly modified system, semi-insulating GaAs is used as cathode and the discharge is operated at room temperature. In this case, the destabilization of the initially established homogeneous stationary state of the gas discharge leads not to spatially ordered patterns, but to homogeneous

oscillations. Dynamic filaments take the place of the homogeneous oscillatory state when the control parameter is increased further. As in the case of the intermittent discharge with conductive electrodes, the time course of the current consists of a succession of spikes and the filaments correspond to micro-breakdowns of the gas gap.

The experimental part of the present work focuses on the spatially extended patterns. The phenomenology of pattern formation at about 100 K is first investigated systematically in the N_2 discharges with Si:Pt cathodes by varying the control parameters: the conductivity of the semiconductor σ, the source voltage U_0, the gas pressure p and the gap width d. The advantage of Si:Pt lies in its linear voltage-current characteristics at a constant intensity of the illumination (i.e. the lamp voltage) so that a σ value can be defined in the range of voltages of interest. As σ is only an indirect control parameter, the necessary calibration relation between σ and the lamp voltage can be obtained by fitting the σ values at several lamp voltages. In a typical phase diagram on the σ-U_0 plane, the primary bifurcation gives rise to dynamic hexagonal spots or dynamic stripes depending on σ. The quantitative reproducibility of the phase diagram is investigated by repeating the measurement with the same Si:Pt sample under identical conditions and by using two different samples under the same conditions. In both cases, the boundaries lines in the phase diagram overlap rather well within the error bars. The change of p and d does not change the topology of the phase diagram, but only shifts the boundaries between various patterns. The investigation is then extended to other gases, i.e. He, Ne and Ar. In the case of Ar discharge, the basic phenomenology is qualitatively different from that of N_2 discharge. In the typical σ-U_0 phase diagram, the dynamic hexagonal spots are absent and a new form of pattern, hexagonally woven stripes, comes into play. Moreover, irregular spatiotemporal oscillations are observed to compete with spatially ordered patterns. The change of the gas pressure or the gap width affects the relative position of the boundary lines and thus determines the observed transition scenarios. When He or Ne is used as the working gas, the uniform state of the gas discharge is stable within the investigated range of the parameters. However, there are signs that spatial patterns could be obtained with a very high current. Besides the Si:Pt cathode, two types of Si:Zn wafers with slightly different material properties are used as cathode in the gas discharge. The two types of Si:Zn show different sensitivities to illumination but otherwise give qualitatively the same behavior. As the voltage-current characteristics of Si:Zn is nonlinear, a unique σ is not defined for each illumination condition. Consequently, a phenomenological approach is taken and a quantitative reproducibility is not pursued. In the measurements with N_2, typical patterns like dynamic hexagonal spots and dynamic stripes are observed. Moreover, spirals, segmented stripes, and negative hexagonal network are obtained at very high voltages. In the gas discharge with a semi-insulating GaAs cathode at cryogenic temperatures, the spatially ordered patterns are not observed. In contrast, the destabilization of the uniform discharge leads to the appearance of solitary spot structures.

8.2 Directions for future research

The gas discharge systems with resistive semiconductor electrodes are, among others, interesting experimental systems for studying pattern formation in dissipative systems. So far only some, mainly phenomenological, aspects of the systems have been investigated,

i.e. obtaining various kinds of patterns, determining their properties and studying the nature of the bifurcation etc. There is less work on identifying the physical mechanism of the instability, which is important for building quantitative models. From the experimental point of view, it would be important to clarify the role of space charge in the instability of Townsend discharge and the effect of UV radiation on pattern formation.

Space charge effects influence the distribution of the electric field along the direction of the current flow, which can be calculated numerically given the voltage drop across the gas gap and the current density. A study of the field distribution in the case of the uniform state of the discharge (i.e. just below the bifurcation point) gives information about the deformation of the electric field. A strong deformation of field distribution as a result of space charge would directly confirm that the transition from the uniform state to a patterned state of the discharge is driven by space charge.

Until now, gas discharge systems with resistive semiconductor electrodes are modelled with reaction diffusion equations. The basic assumption is that the spatial coupling perpendicular to the applied field in the gas discharge results from diffusion only. Emission and subsequent absorption of UV radiations represent a form of spatial coupling which differs from diffusion. Consequently, a clarification of the effect of UV radiation on pattern formation is important for the selection of models. It is known from research on gas-filled X-ray detectors that quenching gases (e.g. CO_2) mixed with Ar can avoid the spatial coupling due to UV radiation (Sauli, 1977). Experiments on discharges using Ar mixed with a quenching gas could thus give information on the effect of non-diffusive coupling in space on the formation of patterns.

In self-sustained discharges driven by a DC source, the cathode plays an essential role and its surface condition has a strong effect on the discharge. The external circuit (i.e. the capacitance, the serial resistance etc) also plays a role in the dynamical behavior of the discharge. In order to avoid the complications related to the cathode and the circuit, the study gas discharges in the non-self-sustained regime would be interesting. X-ray gas detectors could provide a conceptually simple system for studying pattern formation under these conditions (Petrascu et al., 1998). The relevant processes, i.e, multiplication of electrons through Townsend avalanche and inhibitory effect of space charge, occur in the gas volume only and no electrode processes are involved. The discharge is controlled by the incident X-rays and the effect of external circuit can be eliminated. So far very little is known about pattern formation in such systems which certainly provide a direction for future research.

Appendix A

Preparation of semi-transparent gold film on semiconductor wafers

The surface of the semiconductor wafer is polished with 1 μm diamond polishing compound (Buehler Ltd. Lake Bluff, USA). After polishing the following cleaning process is carried out: First, the wafer is immersed in chloroform (>99%, Merck KGaA, Darmstadt, Germany) and cleaned in an ultrasonic bath for 15 minutes. Then the same cleaning procedure is repeated in acetone (>99%, Carl Roth GmbH, Karlsruhe, Germany) to remove the residual chloroform. After that isopropanol (>99%, Merck KGaA, Darmstadt, Germany) is used to remove residual acetone. Finally the wafer is cleaned in deionized water, dried in air and installed on the sample holder (4) of a PVD (physical vapor deposition) device shown in Figure A.1. This instrument is essentially a high vacuum chamber (1) where gold is heated and evaporates. The chamber is first evacuated to a pressure of about $4 \cdot 10^{-5}$ hPa with the help of a DUO 012A rotary vane pump (9) and a TC 600 turbomolecular pump (8) (Pfeiffer Vacuum GmbH, Asslar, Germany). The carrier (5) made of Tungsten is connected to a power supply which delivers a current up to 20 A. The purity of gold used in the deposition is 99.9% and the diameter of the gold wire is 0.25 mm. A 1 or 2 cm long wire is put on the Tungsten carrier, which is placed about 10 cm below the sample holder (wafer). The gold vapor will deposit on the wafer surface when a high current of about 20 A passes through the Tungsten carrier.

The deposition of gold onto a glass substrate is made under the same conditions. Two transmittance spectra of the thin gold film of different thickness measured with an Ultrospec 3000 Pro UV/Visible spectrophotometer (Biochrom Ltd., Cambridge, UK) are given in Figure A.2. A thinner film is obtained when a 1 cm long gold wire is used during the deposition process. The transmittance varies between 30% and 60% in the range of visible light. When the film was obtained using a 2 cm long gold wire, the transmittance was systematically lower by about 10%. On average the gold films deposited on the wafer surface have a transmittance around 40%.
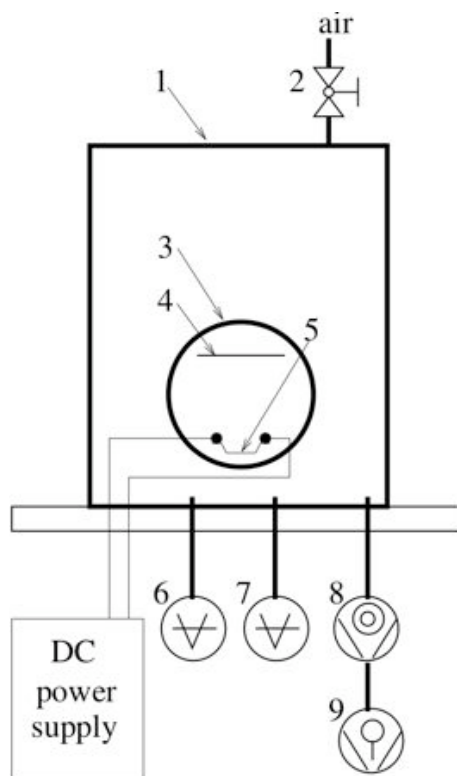
Figure A.1: Schematic setup for physical vapor deposition (PVD). 1 vacuum chamber; 2 manual valve; 3 window; 4 sample holder; 5 Tungsten carrier for gold wire; 6, 7 pressure gauges; 8 turbomolecular pump; 9 rotary vane pump.
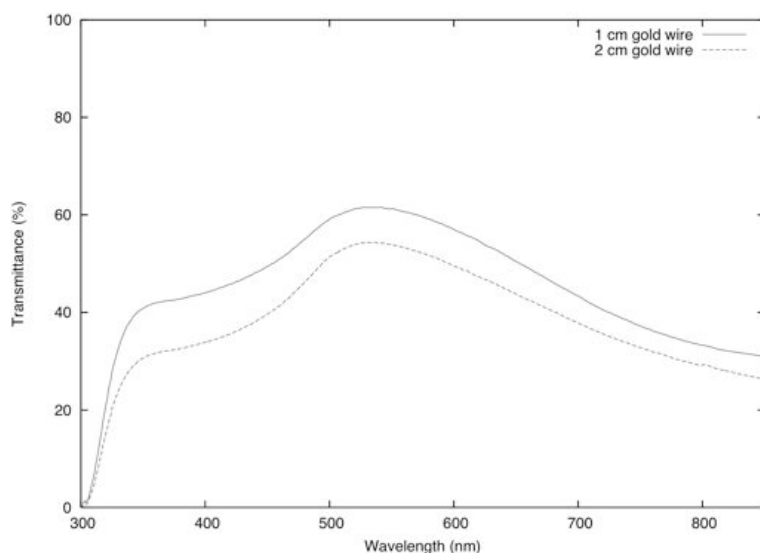

Figure A.2: Transmittance spectra of thin gold films deposited on a glass substrate.

Bibliography

T. Ackemann and W. Lange. Optical pattern formation in alkali metal vapors: Mechanisms, phenomena and use. *Appl. Phys. B*, 72:21–34, 2001.

E. Ammelt, H. Willebrand, and H.-G. Purwins. Periodically self-excited moving striations in a low-temperature gas plasma. *Contrib. Plasma Phys.*, 32:3–14, 1992.

E. Ammelt, D. Schweng, and H.-G. Purwins. Spatio-temporal pattern formation in a lateral high-frequency glow discharge system. *Phys. Lett. A*, 179:348–354, 1993.

E. Ammelt, Yu. A. Astrov, and H.-G. Purwins. Stripe Turing structures in a two-dimensional gas discharge system. *Phys. Rev. E*, 55:6731–6740, 1997.

E. Ammelt, Yu. A. Astrov, and H.-G. Purwins. Hexagon structures in a two-dimensional DC-driven gas discharge system. *Phys. Rev. E*, 58:7109–7117, 1998.

Yu. Astrov, L. M. Portsel, S. P. Teperick, H. Willebrand, and H.-G. Purwins. Speed properties of a semiconductor-discharge gap IR image converter studied with a streak camera system. *J. Appl. Phys.*, 74:2159–2166, 1993.

Yu. Astrov, E. Ammelt, S. Teperick, and H.-G. Purwins. Hexagon and stripe Turing structures in a gas discharge system. *Phys. Lett. A*, 211:184–190, 1996.

Yu. A. Astrov and Yu. A. Logvin. Formation of clusters of localized states in a gas discharge system via a self-completion scenario. *Phys. Rev. Lett.*, 79:2983–2986, 1997.

Yu. A. Astrov and H.-G. Purwins. Plasma spots in a gas discharge system: birth, scattering and formation of molecules. *Phys. Lett. A*, 283:349–354, 2001.

Yu. A. Astrov, E. Ammelt, and H.-G. Purwins. Experimental evidence for zigzag instability of solitary stripes in a gas discharge system. *Phys. Rev. Lett.*, 78:3129–3132, 1997.

Yu. A. Astrov, I. Müller, E. Ammelt, and H.-G. Purwins. Zigzag destabilized spirals and targets. *Phys. Rev. Lett.*, 80:5341–5344, 1998.

K. M. S. Bajaj, J. Liu, B. Naberhuis, and G. Ahlers. Square patterns in Rayleigh-Bénard convection with rotation about a vertical axis. *Phys. Rev. Lett.*, 81:806–809, 1998.

K. M. S. Bajaj, N. Mukolobwiez, N. Currier, and G. Ahlers. Wave number selection and large-scale-flow effects due to a radial ramp of the spacing in Rayleigh-Bénard convection. *Phys. Rev. Lett.*, 83:5282–5285, 1999.

J. Bechhoefer, A. J. Simon, A. Libchaber, and P. Oswald. Destabilization of a flat nematic-isotropic interface. *Phys. Rev. A*, 40:2042–2056, 1989.

J. Berkemeier, T. Dirksmeyer, G. Klempt, and H.-G. Purwins H.-G. Purwins. Pattern formation on a nonlinear periodic electrical network. *Z. Phys. B-Condensed Matter*, 65:255–258, 1986.

E. Bodenschatz, J. R. de Bruyn, G. Ahlers, and D. S. Cannell. Transitions between patterns in thermal convection. *Phys. Rev. Lett.*, 67:3078–3081, 1991.

D. G. Boyers and W. A. Tiller. Plasma bubble domains: A magnetic bubble analog. *Appl. Phys. Lett.*, 41:28–31, 1982.

I. Brauer, E. Ammelt, and H.-G. Purwins. Double breakdown in a pattern forming dielectric barrier discharge system. In *XXIV International conference on physics of ionized gases*, pages 141–142, Warsaw, Poland, 1999.

I. Brauer, M. Bode, E. Ammelt, and H.-G. Purwins. Traveling pairs of spots in a periodically driven gas discharge system: Collective motion caused by interaction. *Phys. Rev. Lett.*, 84:4104–4107, 2000.

W. Breazeal, K. M. Flynn, and E. G. Gwinn. Static and dynamic two-dimensional patterns in self-extinguishing discharge avalanches. *Phys. Rev. E*, 52(2):1503–1515, 1995.

S. C. Brown. *Basic data of plasma physics: the fundamental data on electrical discharges in gases*. AIP Press, New York, 1993.

C. J. Campbell, E. Baker, M. Fialkowski, A. Bitner, S. K. Smoukov, and B. A. Grzybowski. Self-organization of planar microlenses by periodic precipitation. *J. Appl. Phys.*, 97:126102–1–3, 2005.

V. Castets, E. Dulos, J. Boissonade, and P. De Kepper. Experimental evidence of a sustained standing Turing-type nonequilibrium chemical pattern. *Phys. Rev. Lett.*, 64 (24):2953–2956, 1990.

M. C. Cross and P. C. Hohenberg. Pattern formation outside of equilibrium. *Rev. Mod. Phys.*, 65:851–1112, 1993.

J. R. de Bruyn, B. C. Lewis, M. D. Shattuck, and H. L. Swinney. Spiral patterns in oscillated granular layers. *Phys. Rev. E*, 63:041305–1–12, 2001.

T. Dirksmeyer, R. Schmeling, J. Berkemeier, and H.-G. Purwins. Experiments on the formation of stationary spatial structures on a network of coupled electrical oscillators. In D. Walgraef and N. M. Ghoniem, editors, *Patterns, Defects and Materials Instabilities*, NATO ASI Series E: Applied Sciences, pages 91–107. Kluwer Academic Publishers, 1990.

L. Dong, Y. He, Yin Z., and Chai Z. Experimental observation of travelling hexagon patterns in dielectric barrier discharge. *Chin. Phys. Lett.*, 20:1524–1526, 2003a.

L. Dong, Yin Z., L. Wang, G. Fu, Y. He, and Chai Z. Square pattern formation in a gas discharge system. *Thin Solid Films*, 435:120–123, 2003b.

L. Dong, Y. He, Z. Yin, and Z. Chai. Hexagon and stripe patterns in dielectric barrier streamer discharge. *Plasma Sources Sci. Technol.*, 13:164–165, 2004.

L. Dong, F. Liu, S. Liu, Y. He, and W. Fan. Observation of spiral pattern and spiral defect chaos in dielectric barrier discharge in argon/air at atmospheric pressure. *Phys. Rev. E*, 72:046215–1–8, 2005.

L. Dong, W. Fan, Y. He, F. Liu, S. Li, R. Gao, and L. Wang. Square superlattice pattern in dielectric barrier discharge. *Phys. Rev. E*, 73:066206–1–4, 2006.

M. J. Druyvesteyn and F. M. Penning. The mechanism of electrical discharges in gases of low pressure. *Rev. Mod. Phys.*, 12:87, 1940.

S. Facsko, T. Dekorsy, C. Koerdt, C. Trappe, H. Kurz, A. Vogt, and H. L. Hartnagel. Formation of ordered nanoscale semiconductor dots by ion sputtering. *Science*, 285: 1551–1553, 1999.

G. Francis. The glow discharge at low pressure. In S. Flügge, editor, *Handbuch der Physik*, volume XXII, pages 53–203. Springer-Verlag, Berlin, 1956.

M. Gleiche, L. F. Chi, and H. Fuchs. Nanoscopic channel lattices with controlled anisotropic wetting. *Nature*, 403:173–175, 2000.

E. L. Gurevich. *Experimental investigations on pattern formation in semiconductor-gas discharge systems*. PhD thesis, Westfälische Wilhems-Universität Münster, 2004.

E. L. Gurevich, A. S. Moskalenko, A. L. Zanin, Yu. A. Astrov, and H.-G. Purwins. Rotating waves in a planar dc-driven gas-discharge system with semi-insulating gaas cathode. *Phys. Lett. A*, 307:299–303, 2003a.

E. L. Gurevich, A. L. Zanin, A. S. Moskalenko, and H.-G. Purwins. Concentric ring patterns in a dielectric barrier discharge system. *Phys. Rev. Lett.*, 91:154501–1–4, 2003b.

H. Haken. *Synergetics, An introduction. Nonequilibrium phase transitions and self-organization in physics, chemistry and biology.* Springer-Verlag, Berlin, 1983.

C. Harrison, D. H. Adamson, Z. Cheng, J. M. Sebastian, S. Sethuraman, D. A. Huse, R. A. Register, and P. M. Chaikin. Mechanisms of ordering in striped patterns. *Science*, 290:1558–1560, 2000.

H. M. Jaeger, S. R. Nagel, and R. P. Behringer. Granular solids, liquids, and gases. *Rev. Mod. Phys.*, 68:1259–1273, 1996.

B. Jüttner. Cathode spots of electric arcs. *J. Phys. D - Appl. Phys.*, 34:R103–R123, 2001.

A. Kudrolli and J. P. Gollub. Patterns and spatiotemporal chaos in parametrically forced surface waves: a systematic survey at large aspect ratio. *Physica D*, 97:133–154, 1996.

K. Maginu. Reaction-diffusion equation describing morphogenesis i. waveform stability of stationary wave solutions in a one dimensional model. *Math. Biosc.*, 27:17–98, 1975.

H. Meinhardt. *Models of biological pattern formation.* Academic Press, London, 1982.

F. Melo, P. B. Umbanhowar, and H. L. Swinney. Hexagons, kinks, and disorder in oscillated granular layers. *Phys. Rev. Lett.*, 75:3838–3841, 1995.

M. Moselhy and K. H. Schoenbach. Excimer emission from cathode boundary layer discharges. *J. Appl. Phys.*, 95:1642–1649, 2004.

I. Müller, E. Ammelt, and H.-G. Purwins. Interaction of filaments in an a.c.-driven planar gas discharge system. In *XXIII International conference on physics of ionized gases*, volume 2, pages 182–183, Toulouse, France, 1997.

I. Müller, E. Ammelt, and H.-G. Purwins. Self-organized quasiparticles - breathing filamements in a gas discharge system. *Phys. Rev. Lett.*, 82:3428–3431, 1999a.

I. Müller, C. Punset, E. Ammelt, H.-G. Purwins, and J. P. Boeuf. Self-organized filaments in dielectric barrier glow discharges. *IEEE Trans. Plasma Sci.*, 27:20–21, 1999b.

K. G. Müller. Structures at the electrodes of gas discharges. *Phys. Rev. A*, 37:4836–4845, 1988.

S. Nasuno. Dancing atoms and molecules of luminous gas discharge spots. *Chaos*, 13(3): 1010–1013, 2003.

G. Nicolis and I. Prigogine. *Self-organization in non-equilibrium systems.* Wiley, New York, 1977.

Q. Ouyang and H. L. Swinney. Transition from a uniform state to hexagonal and striped turing patterns. *Nature*, 352:610–612, 1991.

A.-M. Petrascu, M. H. J. Koch, and A. Gabriel. A beginner's guide to gas-filled proportional detectors with delay line readout. *J. Macromol. Sci.-Phys.*, B37:463–483, 1998.

G. J. Pietsch. Peculiarities of dielectric barrier discharges. *Contrib. Plasma Phys.*, 41 (6):620–628, 2001.

H.-G. Purwins and C. Radehaus. Pattern formation in analogue parallel networks. In H. Haken, editor, *Neural and synergetic computers*, Springer Series in Synergetics. Springer-Verlag, 1988.

C. Radehaus, T. Dirksmeyer, H. Willebrand, and H.-G. Purwins. Pattern formaiton in gas discharge systems with high impedance electrodes. *Phys. Lett. A*, 125:92–94, 1987.

C. Radehaus, H. Willebrand, R. Dohmen, F.-J. Niedernostheide, G. Bengel, and H.-G. Purwins. Spatially periodic patterns in a dc gas-discharge system. *Phys. Rev. A*, 45: 2546–2557, 1992.

Yu. P. Raizer. *Gas discharge physics.* Springer-Verlag, Berlin, 1991.

F. Rothe. Some analytical results about a simple reaction-diffusion system for morphogenesis. *J. Math. Biol.*, 7:375–384, 1979.

F. Sauli. Principles of operation of multiwire proportional and drift chambers. Technical report, CERN, 1977.

M. Seul and D. Andelman. Domain shapes and patterns: The phenomenology of modulated phases. *Science*, 267:476–483, 1995.

L. Stollenwerk and H.-G. Purwins. Drift bifurcation of dissipative solitons in barrier gas discharge. *Europhys. Lett.*, 70:22–28, 2005.

C. Strümpel and H.-G. Purwins. Nonlinear interaction of homogeneously oscillating domains in a planar gas discharge system. *Phys. Rev. E*, 62:4889–4897, 2000.

C. Strümpel, Yu. A. Astrov, E. Ammelt, and H.-G. Purwins. Dynamics of zigzag destabilized solitary stripes in a DC-driven pattern forming semiconductor gas-discharge system. *Phys. Rev. E*, 61:4899–4905, 2000.

C. Strümpel, H.-G. Purwins, and Yu. A. Astrov. Spatiotemporal filamentary patterns in a dc-driven planar gas discharge system. *Phys. Rev. E*, 63:026409–1–9, 2001.

C. Strümpel, Yu. A. Astrov, and H.-G. Purwins. Multioscillatory patterns in a hybrid semiconductor gas-discharge system. *Phys. Rev. E*, 65:066210–1–5, 2002.

N. Takano and K. L. Schoenbach. Self-organization in cathode boundary layer discharges in xenon. *Plasma Sources Sci. Technol.*, 15:109–117, 2006.

G. I. Taylor. Stability of a viscous liquid contained between two rotating cylinders. *Phil. Trans. Roy. Soc. Lond. A*, 223:289, 1923.

A. M. Turing. The chemical basis of morphogenesis. *Phil. Trans. Roy. Soc. Lond. B*, 327:37–72, 1952.

P. B. Umbanhowar, F. Melo, and H. L. Swinney. Localized excitations in a vertically vibrated granular layer. *Nature*, 382:793–796, 1996.

A. von Engel. *Ionized gases*. AIP Press, New York, 1993.

H. Willebrand. *Strukturbildung in lateral ausgedehnten Gasentladungssystemen*. PhD thesis, Westfälische Wilhems-Universität Münster, 1992.

H. Willebrand, C. Radehaus, F.-J. Niedernostheide, R. Dohmen, and H.-G. Purwins. Observationn of solitary filaments and spatially periodic patterns in a dc gas-discharge system. *Phys. Lett. A*, 149:131–138, 1990.

H. Willebrand, K. Matthiessen, F.-J. Niedernostheide, and R. Dohmen. Experimental observation of simultaneously existing moving and standing patterns in a gas-discharge system. *Contrib. Plasma Phys.*, 31(57-68), 1991a.

H. Willebrand, F.-J. Niedernostheide, E. Ammelt, R. Dohmen, and H.-G. Purwins. Spatio-temporal oscillations during filament splitting in gas discharge systems. *Phys. Lett. A*, 153:437–445, 1991b.

H. Willebrand, T. Hünteler, F.-J. Niedernostheide, R. Dohmen, and H.-G. Purwins. Periodic and turbulent behavior of solitary structures in distributed active media. *Phys. Rev. A*, 45:8766–8774, 1992.

H. Willebrand, Y. Astrov, L. Portsel, T. Gauselmann, and H.-G. Purwins. Excitation of wave patterns in an infrared-visible converter. *J. Phys. D - Appl. Phys.*, 27:2354–2362, 1994.

A. L. Zanin, A. W. Liehr, A. S. Moskalenko, and H.-G. Purwins. Voronoi diagrams in barrier gas discharge. *Appl. Phys. Lett.*, 81:3338–3340, 2002.

A. L. Zanin, E. L. Gurevich, A. S. Moskalenko, H. U. Bödeker, and H.-G. Purwins. Rotating hexagonal pattern in a dielectric barrier discharge system. *Phys. Rev. E*, 70: 036202–1–9, 2004.

Lebenslauf

Name:	Weifeng Shang
Geburtsdatum:	08 Dez. 1978
Geburtsort:	Henan, Volksrepublik China
Staatsangehrigkeit:	chinesisch
Eltern:	Laifu Shang (Vater) und
	Xiaoying Ma (Mutter)

Schulbildung:

09.1984 – 08.1989	Grundschule in Henan, China
09.1989 – 08.1992	Mittelschule in Henan, China
09.1992 – 08.1995	Oberschule in Henan, China
07.1995	Allgemeine Hochschulreife

Studium:

09.1995 – 07.1999	University of Zhejiang, China, Department of materials science and engineering, Bachelor,
10.2001 – 09.2003	Imaging Physics an der Universität Siegen, Master of Science

Promotionsstudium

11.2003	Beginn der Dissertation am Institut für Angewandte Physik an der WWU Münster
	Unter der Betreuung von Prof. Dr. H.-G. Purwins

Ttigkeiten:

08.1999 – 08.2001	Programmierer bei der Firma Hangzhou TorrenSoft Co., China
11.2003 – 12.2005	Stipendiat des Graduiertenkollegs "Untersuchung nichtlinearer kontinuierlicher Systeme mit numerischen, qualitativen und experimentellen Methoden" an der WWU Münster
01.2006 – 05.2007	Wissenschaftliche Mitarbeiter am Institut für Angewandte Physik der WWU Münster

Münster, den   _____